Development of Microwave/Droplet-Microfluidics Integrated Heating and Sensing Platforms for Biomedical and Pharmaceutical Lab-on-a-Chip Applications

by

Gurkan Yesiloz

A thesis
presented to the University of Waterloo
in fulfillment of the
thesis requirement for the degree of
Doctor of Philosophy
in
Mechanical and Mechatronics Engineering

Waterloo, Ontario, Canada, 2017

Examining Committee Membership

The following served on the Examining Committee for this thesis. The decision of the Examining Committee is by majority vote.

External Examiner	Dr. Michel Godin Associate Professor
Supervisor(s)	Dr. Carolyn L. Ren Professor
Internal Member	Dr. James Tung Asst. Professor
Internal-external Member	Dr. Raafat Mansour Professor
Internal-external Member	Dr. Marios Ioannidis Professor

AUTHOR'S DECLARATION

I hereby declare that I am the sole author of this thesis. This is a true copy of the thesis, including any required final revisions, as accepted by my examiners.

I understand that my thesis may be made electronically available to the public.

Abstract

Interest in Lab-on-a-chip and droplet-based microfluidics has grown recently because of their promise to facilitate a broad range of scientific research and biological/chemical processes such as cell analysis, DNA hybridization, drug screening and diagnostics. Major advantages of droplet-based microfluidics versus traditional bioassays include its capability to provide highly monodispersed, well-isolated environment for reactions with magnitude higher throughput (i.e. kHz) than traditional high throughput systems, as well as its low reagent consumption and elimination of cross contamination. Major functions required for deploying droplet microfluidics include droplet generation, merging, sorting, splitting, trapping, sensing, heating and storing, among which sensing and heating of individual droplets remain great challenges and demand for new technology. This thesis focuses on developing novel microwave technology that can be integrated with droplet-based microfluidic platforms to address these challenges.

This thesis is structured to consider both fundamentals and applications of microwave sensing and heating of individual droplets very broadly. It starts with developing a label-free, sensitive, inexpensive and portable microwave system that can be integrated with microfluidic platforms for detection and content sensing of individual droplets for high-throughput applications. This is, indeed, important since most droplet-based microfluidic studies rely on optical imaging, which usually requires expensive and bulky systems, the use of fluorescent dyes and exhaustive post-imaging analysis. Although electrical detection systems can be made inexpensive, label-free and portable, most of them usually work at low frequencies, which limits their applications to fast moving droplets. The developed microwave circuitry is inexpensive due to the use of off-the-shelf components, and is compact and capable of detecting droplet presence at kHz rates and droplet content sensing of biological materials such as penicillin antibiotic, fetal bovine serum solutions and variations in a drug compound concentration (e.g., for Alzheimer's Disease).

Subsequently, a numerical model is developed based on which parametrical analysis is performed in order to understand better the sensing and heating performance of the integrated platform. Specifically, the microwave resonator structure, which operates at GHz frequency affecting sensing performance significantly, and the dielectric properties of the microfluidic chip components that highly influence the internal electromagnetic field and energy dissipation, are studied systematically

for their effects on sensing and heating efficiency. The results provide important findings and understanding on the integrated device operation and optimization strategies.

Next, driven by the need for on-demand, rapid mixing inside droplets in many applications such as biochemical assays and material synthesis, a microwave-based microfluidic mixer is developed. Rapid mixing in droplets can be achieved within each half of the droplet, but not the entire droplet. Cross-center mixing is still dominated by diffusion. In this project, the microwave mixer, which works essentially as a resonator, accumulates an intensive, nonuniform electromagnetic field into a spiral capacitive gap (around 200 μm) over which a microchannel is aligned. As droplets pass by the gap region, they receive spatially non-uniform energy and thus have non-uniform temperature distribution, which induces non-uniform Marangoni stresses on the interface and thus three-dimensional (3D) chaotic motion inside the droplet. The 3D chaotic motion inside the droplet enables fast mixing within the entire droplet. The mixing efficiency is evaluated by varying the applied power, droplet length and fluid viscosity.

In spite of various existing thermometry methods for microfluidic applications, it remains challenging to measure the temperature of individual fast moving droplets because they do not allow sufficient exposure time demanded by both fluorescence based techniques and resistance temperature detectors. A microwave thermometry method is thus developed here, which relies on correlating fluid temperature with the resonance frequency and the reflection coefficient of the microwave sensor, based on the fact that liquid permittivity is a function of temperature. It is demonstrated that the sensor can detect the temperature of individual droplets with ±1.2 ℃ accuracy.

At the final part of the thesis, I extend my platform technology further to applications such as disease diagnosis and drug delivery. First, I develop a microfluidic chip for controlled synthesis of poly (acrylamide-co-sodium acrylate) copolymer hydrogel microparticles whose structure varies with temperature, chemical composition and pH values. This project investigates the effects of monomer compositions and cross-linker concentrations on the swelling ratio. The results are validated through the Fourier transform infrared spectra (FTIR), SEM and swelling test. Second, a preliminary study on DNA hybridization detection through microwave sensors for disease diagnosis is conducted. Gold sensors and biological protocols of DNA hybridization event are explored. The event of DNA hybridization with the immobilized thiol-modified ss-DNA oligos and complimentary DNA (c-DNA) are monitored. The results are promising, and suggests that microwave integrated Lab-on-a-chip platforms can perform disease diagnosis studies.

Acknowledgements

First, I gratefully acknowledge the guidance of my supervisor, Dr. Carolyn L. Ren, from whom I learned a lot during my PhD studies. Useful and exciting discussions with Dr. Ren are always inspiring.

Next, I would like to thank Dr. Michel Godin, Dr. Raafat Mansour, Dr. James Tung and Dr. Marios Ioannidis for serving as my PhD committee members. Their suggestions, time and contribution to my thesis are much appreciated.

My experience and PhD study would not have been so fruitful and colorful without the current and former members of the Waterloo Microfluidics Laboratory, who worked as a cooperative team and are good friends. Special thanks to Dr. M. Said Boybay for insightful recommendations during my early stage of PhD study. Many thanks to Dr. Caglar Elbuken, Dr. Zeyad Almutairi, Dr. Tom Glawdel and Dr. Mostafa Shameli, and also great thanks to other lab members who worked with me closely, Dizhu Tong, David Wong, Sahil Kashyap, Anna Thu Nguyen, Pegah Pezeshkpour, Matthew Courtney, Dr. Cody Chen, Ning Qin, Alexander Brukson and Weijia Cui.

I would also like to deeply thank my family: my dear spouse (Ezgi) and our lovely daughter (Elif Ece), my dear parents (Zeliha and Ramazan Yesiloz), my sister and brother (Berna and Volkan), my mother in law (Sevil Karaer), my grandmother and grandfather (Nimet and Ali Yesiloz). Their encouragement, support and love have been always the greatest source of my strength and motivation. I love you all.

Dedication

To my Grandmother (Nimet Yesiloz) and Grandfather (Ali Yesiloz), who have supported me all of my life.

To my loving wife (Ezgi Yesiloz) and my daughter (Elif Ece Yesiloz), who are always supporting me now.

Table of Contents

List of Figures

List of Tables

CHAPTER 1

INTRODUCTION

1.1 RESEARCH BACKGROUND AND MOTIVATION

The term ‘laboratory’ can be interpreted as a facility in which analysis, measurements, scientific research or experiments are carried out in controlled conditions. The term Lab-on-a-chip (LOC), sometimes called micro total analysis systems (μTASs), refers to a device technology that integrates and operates multiple laboratory functions on a single chip (see Figure 1.1[1]). More importantly, LOC platforms scale down these functions and processes into a miniaturized format[2,3] which provides great advantages, such as low reagent consumption, better process control, faster analysis, reduced cost and portability. Because of its many potential benefits, investigations intersect a wide range of interdisciplinary areas, from nanotechnology, biotechnology and biochemistry to fluid mechanics, medicine, applied physics and material science in order to develop new platforms for multiple processes[4-6].

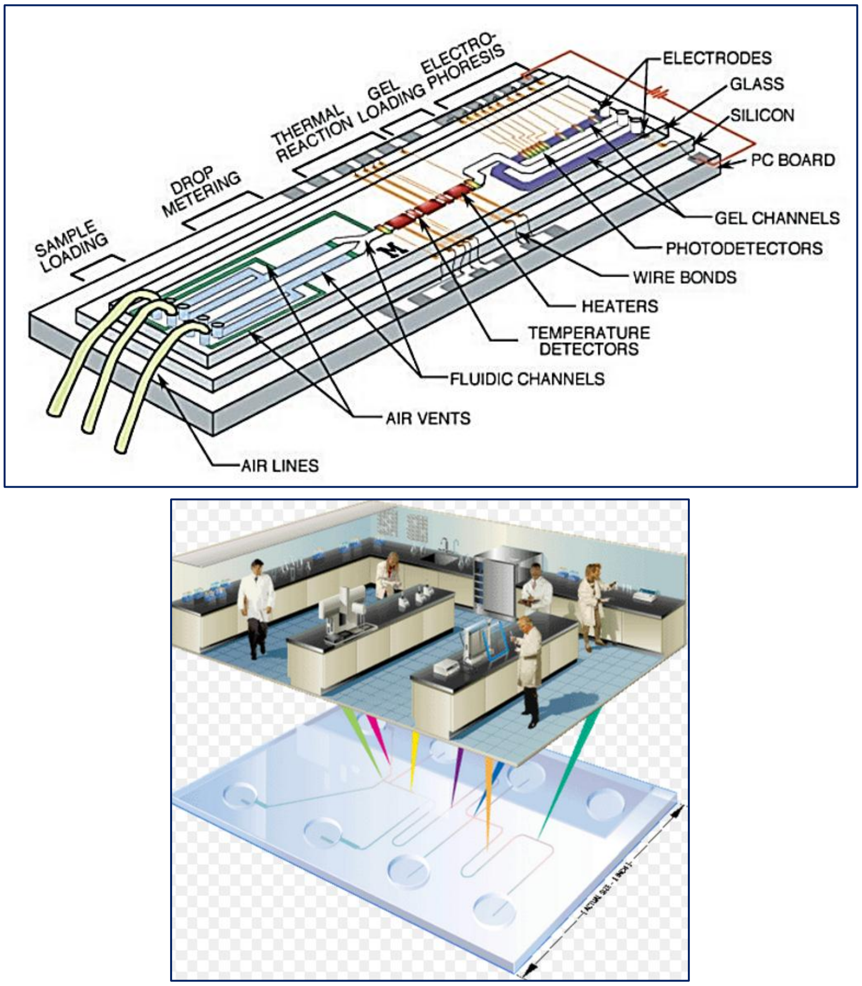

Figure 1.1. Example of components of Lab-on-a-chip platform for carrying out multiple tasks (top image)[7]. Schematic description of miniaturization of traditional laboratory processes onto an integrated Lab-on-a-chip device (bottom image)[1].

To perform multiple analysis tasks, LOC devices draw from various roots, such as fabrication technologies, fluid manipulation/control, assay preparation, manipulation and processing. In general, LOC devices rely on microfluidics (see Figure 1.1[7]) for sample transport and manipulation, which, fundamentally, deals with the physics, behavior and manipulation of fluids at small volumes such as nano to pico-liter. However, scaling down brings its own advantages and challenges in terms of the characteristics of physical-system behavior at small scales. For example, micro-and nano-scale systems provide a high surface-to-volume ratio, which helps thermal management, and on the other side, interfacial forces become important leading capillarity, which brings challenges in surface chemistry into fluid manipulation. Nevertheless, flow at micro-and nano-scale results in laminar flow nature leading poor mixing capability[8-11]. Rapid mixing of reagents such as enzymes, biomolecules or drug components in LOC systems is essential in preparing or initiating reactions. In the early development of microfluidics, single phase microfluidics which relies on miscible fluids to carry and manipulate samples was primarily employed. Slow diffusive mixing and large residence time characteristic to single-phase microfluidics have been detrimental for the quality and performance of LOC systems. Cross contamination between different assays and Taylor dispersion that gives rise to low resolution for protein or DNA separation[12-14] are additional challenges that prompted a number of excellent studies towards the improvement of single phase microfluidics (see Figure 1.2[15]).

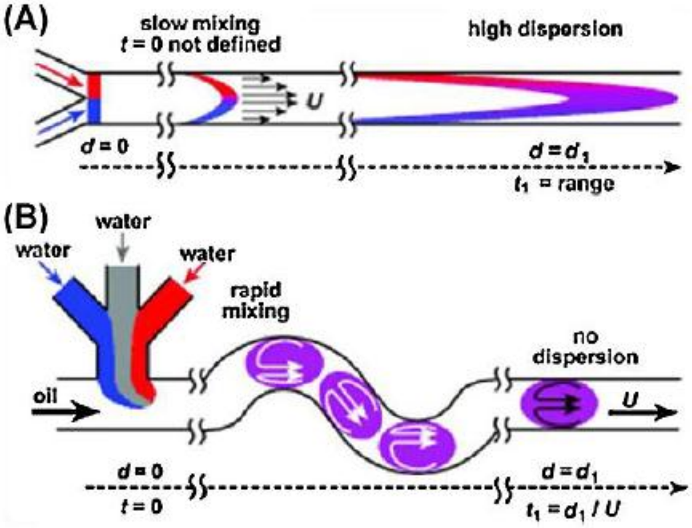

Figure 1.2. Comparison of single phase (A) and droplet microfluidics (B). In single-phase flow slow mixing and high dispersion happens, whereas in droplet microfluidics, rapid mixing occurs and droplets prevent dispersion of reagents[15].

In order to address the major limitations of single-phase microfluidics, droplet-based microfluidics emerged as an alternative in the early 2000s [16-22]. In the last decade, droplet microfluidics has attracted ever-increasing attention from both academia and industry because of its capability for combinatorial high throughput screening analysis. Droplets can be formed from a continuous liquid within a second immiscible carrier fluid at a several kHz rate meaning that ideally millions of droplets can be analyzed in a couple of minutes[12,13,23]. Nano to picoliter-sized droplets are fully compartmentalized by the immiscible carrier fluid which prevents cross contamination and enhance reaction. Almost instantaneous mixing occurs within each half of the droplets and full mixing could be realized by pumping droplets through serpentine channels. With these advantages and potentials, droplet microfluidics has found many applications in disease diagnosis, material synthesis and drug discovery [2,3,24-30].

Besides droplet formation which in general is the first step, in order to realize the full potential of droplet microfluidics based Lab-on-a-chip devices, new functions need to be added to the system. Droplet manipulations in microfluidic chips such as splitting, coalescence, valving, pumping, and sorting operations have been performed so far to some extent. These techniques and operations may be sufficient to conduct a certain number of processes such as preparing biological and chemical samples and producing some materials. However, many Lab-on-a-chip applications require more-complex features, measurement capabilities and external disturbances/triggers in order to outperform in addition to simple fluid manipulations[3]. For example, one of the important aspects of Lab-on-a-chip platform technology is point-of-care (POC) diagnostics. Improved and appropriate POC applications and diagnostics have critical roles in health care worldwide. Early and proper treatments, safe blood analysis, fast detection of clinical symptoms and diseases are some of the objects of this field, which requires miniaturized, portable and fast on-site sensing systems. Another side of the issue is that while, for instance, droplet generation is relatively easy to perform at the several kHz level, lack of ability to sense those droplet’s contents or analyze them at the same detection rates due to the lack of proper fast-response and portable detection platforms is a challenge, and a limiting factor. Moreover, the trend of LOC platform technology is continuously moving towards integrating complex and sophisticated analysis with the help of new fabrication technologies. From a broader perspective, the development of functional devices and systems for biomedical, pharmaceutical and clinical applications has become more significant. More specifically, potential new uses of microfluidics and LOC systems need the development of tools for studying cells and tissues, hydrogel-based microfluidics, particle fabrication, proteomics, genomics, organic synthesis in micro/nano-channels and efficient point-of-care devices[2,3,31-34]. Implementing challenging tasks in these research fields first requires indispensable rapid, portable, sensitive and efficient sensing and heating functionalities be developed or improved and added to Lab-on-a-chip platforms. The above reasons highly suggest alternative technologies to be developed and electrical techniques for sensing and heating have the potential to address the challenges. Among the commonly used electrical detection methods such as resistance, impedance and microwave techniques, microwave technique has unique advantages benefiting from its high operating frequency, but not as yet to be fully explored for droplet microfluidics and LOC applications. For this reason, this thesis research focuses on developing novel microwave/droplet-microfluidics integrated heating and sensing platforms for multi-purpose Lab-on-a-chip applications such as in the biomedical and pharmaceutical fields.

Microwave sensors/resonators have versatile features for both sensing and heating, and the implementation of droplet microfluidics and microwave technologies is a rather new approach to integration of both. In the scope of the thesis work, both the localized, sensitive, selective and miniaturized heating and sensing functions of electrically small microwave resonators are used, along with droplet microfluidics. In addition to developing label-free, high-throughput, portable miniaturized sensing platforms, and studying the fundamental behavior and characteristics of the integrated system for superior performance, several applications are employed practically such as screening drug compounds for treating Alzheimer's disease, sensing of biomaterials, synthesis of hydrogel micro particles, preliminary detection of DNA hybridization event, developing droplet temperature measurement thermometry for Lab-on-a-chip platforms, and investigating the mixing phenomena inside droplets. This broad, fundamental, and application-based research have been conducted in the thesis, which provides enabling tools and functionalities to be incorporated in new Lab-on-a-chip platforms. It is intended to give a contribution for carrying out more complex and sophisticated LOC analysis in the field, and advance the development of new analytical processes.

1.2 THESIS OUTLINE

Chapter 2 discusses the relevant work described in the literature to date, and presents fundamentals related to the physical phenomena involved in this thesis. First, examples of droplet based LOC platforms in biomedical, chemical, medicine and pharmaceutical fields are provided, which gives an insight and inspiration to enlarging the applications and utilizing them suitably. Next, it provides the fundamentals of two-phase flow in regards to droplet-based microfluidics, knowledge that is important for improving and operating such systems. Later, generation and manipulation of droplets by active and passive means, sensing, detection and heating in droplet microfluidics in general and by means of microwaves are reviewed, and the rational need of microwaves are discussed. Lastly, the microwave sensing and heating systems available for microfluidics are reviewed, with a brief explanations of the physical mechanism of microwave dielectric heating and sensing.

Chapter 3 introduces the experimental facility used throughout the thesis research, with a detailed explanation of each component. The methodology, fluids and chemicals, fabrication by means of soft-lithography and protocols for surface treatment of the microfluidic channels are provided as well. Also, the steps of microwave resonator fabrications with both gold and copper electroplating in combination with lithography techniques are demonstrated.

The research carried out for the thesis starts with Chapter 4, with a description of development of a label-free, sensitive, inexpensive and portable microwave system that can be integrated with microfluidic platforms for detection and content sensing of individual droplets for high-throughput applications. For future point-of-care application purposes, cost-effective off-the-shelf components for developing the circuitry have been chosen. The system is shown to have a detection limit of several kilohertz (kHz). Additionally, an Alzheimer’s disease (AD) drug assay is used to demonstrate its bioapplications where the concentrations of an inhibitor are screened through the microwave sensing system, and droplet content sensing is performed using biomaterials.

Chapter 5 presents a parametrical analysis using numerical simulation tools in order to understand better the performance of the integrated platform. Specifically, the microwave resonator structure and the behavior of the dielectric properties of the microfluidic chip components on sensing and heating efficiency are investigated. Since the sensor is operating at high frequencies, the design of the system is very sensitive to these parameters, such that any improper design may cause sharp performance damping than the actual capability of the device. In order to control the microwave sensing and heating functionalities for an appropriate Lab-on-a-chip platform development, a comprehensive study is performed in this chapter by investigating the effects of different parameters.

In Chapter 6, recognizing the challenge and difficulty of mixing in micro-and nano-scale systems, a microwave-based microfluidic mixer is developed to allow rapid and efficient mixing within individual droplets. Mixing in microfluidics is challenging due to its laminar flow nature and is often dominated by molecular diffusion. In this chapter, the spiral design of the microwave resonator is designed through numerical simulation and used as a localized and selective heater that provides spatially non-uniform energy and thus result in non-uniform temperature distribution inside droplets. The non-uniform temperature distribution induces non-uniform Marangoni stresses on the interface, which results in three-dimensional chaotic motion inside the droplet and thus fast mixing. The physical mechanism of mixing, mixing index, effect of excitation power and droplet length are investigated.

Chapter 7 demonstrates a temperature measurement platform for single-phase and droplet based microfluidics. In this work, a microwave thermometry method that is non-intrusive and requires minimal external equipment is developed which relies on the correlation of fluid temperature with the resonance frequency and the reflection coefficient of the microwave sensor that operates at a GHz frequency range based on the fact that the permittivity of liquids is a function of temperature.

Chapter 8 describes extended studies of the developed platform on pharmaceutical drug delivery and biomedical disease diagnosis purposes. In this chapter synthesis of poly (acrylamide-co-sodium acrylate) hydrogel micro particles and preliminary DNA hybridization sensing are demonstrated.

Chapter 9 compiles the results, findings, conclusions and contributions of the thesis work. In addition, it makes recommendations for future academic studies based on the knowledge, experience and observations gained throughout the thesis. Finally, possible future work is suggested including application and development of advanced LOC platforms for various areas such as bioengineering, nanotechnology, pharmacology, biomedical research, chemical synthesis and thermo-fluid mechanics in terms of physical micro-nano scale phenomena.

Nomenclature

LOC	Lab-on-a-Chip
μTAS	Micro Total Analysis System
PCR	Polymerase chain reaction
AD	Alzheimer’s disease

Chapter 2

LITERATURE REVIEW

As pointed out above in Chapter 1, Lab-on-a-chip technology combines multiple laboratory functions into small scale miniaturized systems that open up a novel window for developing devices and analysis systems for a wide range of fields, with many valuable advantages. From this perspective, droplet microfluidic systems have been receiving great attention as an enabling tool to achieve the exciting goals of these platforms. To provide fundamental information about the research area; to review the work done so far; and most importantly, to provide the underlying vision needed to interpret contribution, need and novelty of the thesis research, this chapter is organized as follows. First, droplet based systems are introduced with examples of their implementation in various applications in bioengineering, pharmaceutical, biomedical, chemical and medical fields. These examples have inspired researchers to expand the applications and discover new ideas to build platforms that will contribute to society. Later, the fundamental physics of two-phase flows in droplet microfluidics is reviewed, being crucial for understanding, operating, designing, developing, improving and controlling those platforms and devices. Subsequently, droplet generation and manipulation methods in microfluidics are presented. Droplet generation is the initial step, and is well understood so far. After generation, these droplets must then be properly transported and manipulated inside microchannels, and of these prevalent techniques are described. However, because of ongoing demands to solve current challenges in the field, and the need to realize new applications for carrying out diagnosis, synthesis, screening and biochemical analysis, new functions must be added and developed in order to realize the full potential of Lab-on-a-chip technology. Thus, corresponding to the focus of the thesis, as emphasized previously, the rational need for integration of microwave sensors/heaters is discussed. Thereafter, available microwave sensing and heating systems in microfluidics are reviewed, with a brief discussion of the physical mechanism of microwave dielectric heating and sensing. Lastly, the chapter is briefly summarized.

2.1 DROPLET MICROFLUIDICS FOR BIOMEDICAL, CHEMICAL, BIOLOGICAL AND PHARMACEUTICAL APPLICATIONS

Droplet microfluidics show a great potential for various applications in a wide spectrum of fields. Droplet based microfluidic platforms have been implemented in chemical reactions, imaging, drug delivery, diagnostics, drug discovery, cell biology, molecule synthesis and many others[35]. The fundamental feature, and the reason for droplet microfluidics being an attractive platform, is that droplet systems demonstrate a high level integration, and have the ability to provide a low amount of reagent use, an isolated and a well-controlled environment, short analysis times, high-throughput screening and improved sensitivity[36]. For example, droplet microfluidics establishes a powerful platform for drug delivery purposes since each individual droplet can be taken as a cargo or drug delivery vehicle. Drug molecules either can be carried or transported by droplets, or the production of new drugs can be performed inside of droplets[37-39]. Likewise, cell studies have been widely employed in droplets. Droplets provide a sterile and an isolated environment into which cells can be encapsulated with a robust and controlled approach. Also, the content of droplets can be adjusted appropriately by merging or splitting droplets. In comparison with traditional cell studies, cell and reagent consumption are decreased dramatically. Studies using yeast, human, mammalian, bacterial cells or microorganisms like C. Elegans have been implemented through droplet microfluidics[25,29,40-41]. In this regard, in a recent study, D. Weitz’s group [42] reported a droplet barcoding technique for single-cell transcriptomics, which is applied to embryonic stem cells. They developed a droplet-microfluidic approach for barcoding RNA from thousands of individual cells for

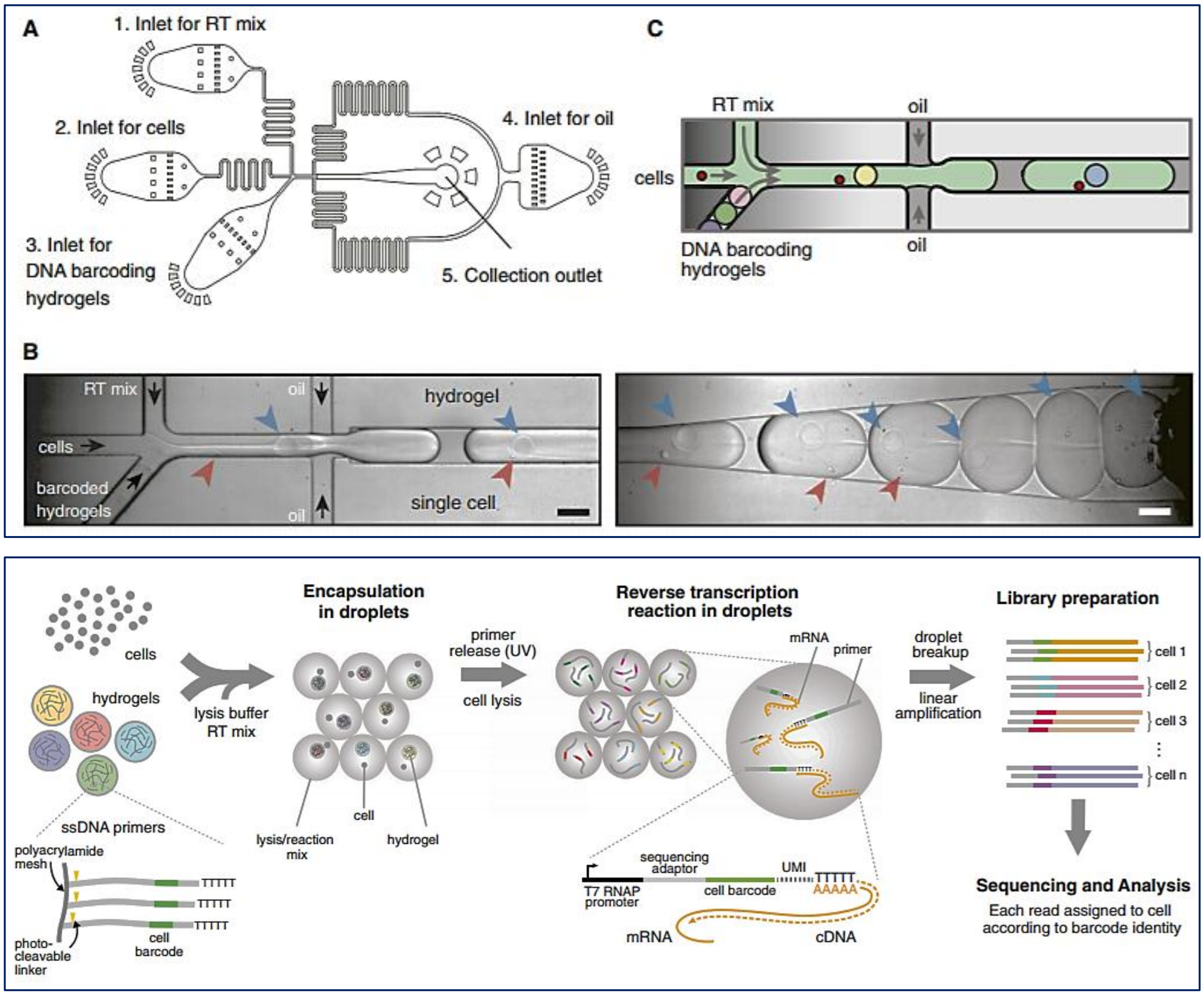

Figure 2.1. Microfluidic device design (top image); (A) shows details of the design, (B) and (C) describes encapsulation and collection modules, arrows indicate cells (red), hydrogel (blue) and flow direction (black). Barcoding platform (bottom image); cells are encapsulated into droplets with lysis buffer and hydrogel microspheres carry barcoded primers[42].

subsequent analysis by next-generation sequencing. Obtained single-cell data allowed to deconstruct cell populations and infer gene expression relationships. In their study, droplet microfluidics served as an efficient platform in order to capture and barcode cells in nanoliter volume droplets, and each droplet hosts hydrogel photo-cleavable combinatorially barcoded primers. Then the mRNA of thousands of mouse embryonic stem cells are sequenced. In Figure 2.1 the microfluidic device design and barcoding of cells are described. In another study, Weitz et al. [43]demonstrated portable microtissues in individual droplets for an “organ in a droplet” application. They used water–water–oil double emulsions as templates to spatially assemble hepatocytes in the core and fibroblasts in the shell, forming a 3D liver model in a drop. Through the highly monodispersed droplets, controlled assembly of heterotypic cells showed biocompatible 3D core–shell hydrogel scaffolds. Thousands of monodisperse microtissues, each in an individual drop, are achievable using this microfluidics technology, and each maintains enhanced liver-specific functions (see Figure 2.2).

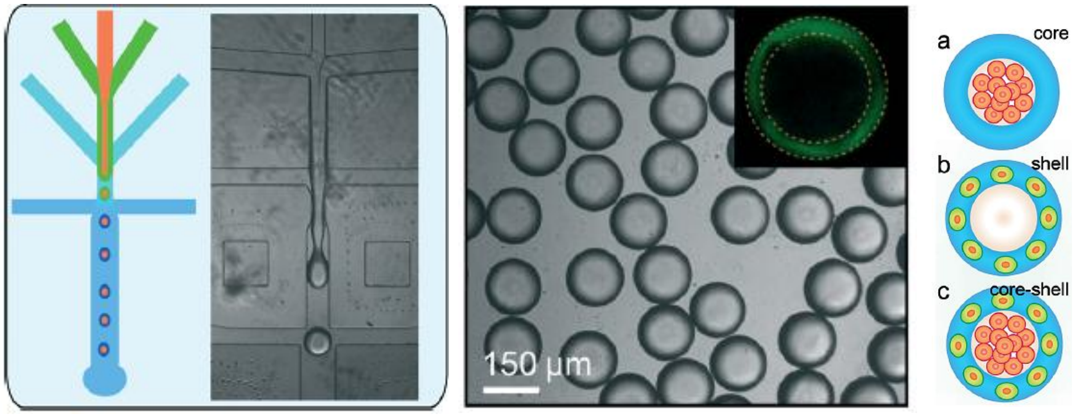

Figure 2.2. Top images demonstrates the construction of the 3D scaffold in a drop consisting of an aqueous core and a hydrogel shell. Fabrication of core–shell droplets using w/w/o double emulsions as templates. Bottom image illustrates the spatial assembly of different cells in the 3D core–shell scaffold. As can be seen, cells are confined in the core by the hydrogel shell (a), fibroblasts are immobilized in the shell (b) and the assembly of the structure forms an artificial liver in a drop (c) [43].

A modular Lab-on-a-chip system designed for cultivation of mammalian cells and delivery into microdroplets were demonstrated by Hufnagel et al.[28]. It was shown that cells can be reproducibly cultivated over a period of seven days and maintain their health morphology. Also, via gas permeable perfluorocarbon oil keeps the cells alive for several days. Wang et al. [44] presented an anticancer drug testing study with a microfluidic droplet-based method for the formation of multicellular tumor spheroids using alginate and matrigel mixed hydrogel beads. Mixed hydrogel beads with different volume ratios between alginate and matrigel are obtained through changing the flow rate of the two hydrogel solutions on-chip. Meanwhile, human cervical carcinoma (HeLa) cells are encapsulated in the mixed hydrogel beads, and it was shown that the viability of cells encapsulated in the mixed hydrogel beads was more than 90%. These results indicate that the microfluidic device might be an efficient tool for the preparation of multicellular tumor spheroids, which could be used in a variety of cancer studies such as cell–cell interactions, oncotherapy, and high-throughput screening of anticancer drugs.

Polymerase chain reaction and amplification of DNA has also been proven in droplet microfluidics. Using conventional microfluidic systems for PCR offers the advantages of performance, miniaturization and operational flexibility. However, there are still challenges like reproducibility of amplification and the adsorption of polymerase enzymes to the channel walls. PCR in confined droplets, on the other hand, facilitates the further reduction of reagents, and because of reduced thermal mass, it provides more precise amplification and shorter reaction times[45]. Wang et al.[46] designed a droplet-based micro oscillating-flow PCR chip. Three different temperature zones of denaturation, extension and annealing temperatures were integrated with a single microchannel to form the chip's basic functional structure. Lien et al.[47] conducted a study with an integrated microfluidic system performing four reverse transcription polymerase chain reaction processes simultaneously for fast diagnosis of aqua cultural diseases. Another key field where droplet-based microfluidic platforms can be applied is conducting enzyme assays. Enzyme kinetics, by mixing and merging droplets of alkaline phosphatase with fluorescein diphosphate in a microfluidic device, were carried out by Miller et al.[26]. An alternate biological application is the use of immunoassays with droplet microfluidics. An immunoassay is a biochemical test that measures the presence or concentration of a macromolecule in a solution through the use of an antibody[48]. A droplet based magnetic bead immunoassay has been reported to detect insulin[49].

On another side, each compartmentalized droplet can be used as individually addressable microreactors for chemical applications. This provides many promising applications and benefits for chemical synthesis. For applications ranging from protein expression to organic compound synthesis, performing reactions in the microscale reduces the cost of expensive reagents, reduces the risk of exposure to hazardous chemicals, and also allows multiple reactions to be carried out in highly parallelized experiments[50]. In large chemical processes, significant amounts of heat might be released when exothermic reactions occur, which give rise to potential risks. However, scaling down reactions into microreactors minimizes the risk. As well, reactions can be performed much faster because of the advantages of droplets in terms of the mixing (vortex circulation inside droplet) and heat transfer efficiency. Schachschal et al.[51] described the synthesis of poly (N-isopropylacrylamide) microgel particles, in water/oil inverse emulsions, used as carriers for enzyme encapsulation. The potential application of these enzymes is to be used in biotechnological applications, using their ability to be immobilized on polymer colloidal carriers. The polymerization process occurred via radical initiation in aqueous droplets in the presence of the comonomer vinylimidazole and the crosslinker N,N-methylene-bis-acrylamide at room temperature. Another example of synthesis was reported by Chan et al.[52] for high temperature synthesis of CdSe nanoparticles using microdroplet reactors. Millman et al.[53] synthesized a wide variety of micro-particles, including capsules and semiconducting microbeads. In addition, droplet-based reactions can be implemented for protein crystallization[54] (Figure 2.3).

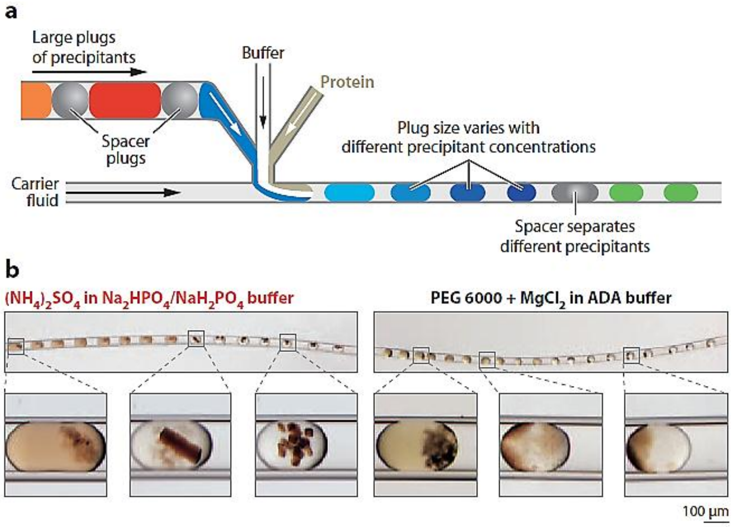

Figure 2.3. A droplet-based microfluidic hybrid approach to screen crystallization conditions using the microbatch method[54].

2.2 TWO-PHASE FLOW PHYSICS IN DROPLET MICROFLUIDICS

As listed some examples of the droplet microfluidic applications as an enabling platform above, applications and requirements of the device operation might be very broad. In order to design, control, improve and manipulate droplet microfluidics properly for those analytical tasks, it is important to understand the underlying physics of the device operation principles. In this section, fundamental physics of two-phase flows in droplet microfluidics is reviewed for this purpose.

2.2.1 FORCES

A multiphase flow can be regarded as the flow that contains at least two different fluids, with different chemical compositions, such as liquid/liquid or gas/liquid forms. The dynamical response of two-phase flows is characterized by fluid properties and dimensional parameters. Fluids are continuum materials, and forces on fluid elements originate from fluid stresses $\boldsymbol{\sigma}$ (forces per unit area) applied on surfaces in addition to the body forces $\boldsymbol{f}$ applied on the bulk of the fluid elements. For a Newtonian fluid, Navier-Stokes equation, which depicts the continuum version of $\boldsymbol{F}=m.\boldsymbol{a}$ per unit volume, is employed:

$$\rho\left(\frac{\partial \mathbf{u}}{\partial \mathrm{t}}+\mathbf{u}.\nabla \mathbf{u}\right)=\nabla \boldsymbol{\sigma}+\mathbf{f}=-\nabla \mathrm{p}+\mu \nabla^2 \mathbf{u}+\boldsymbol{f}_{\boldsymbol{\gamma}}+\mathbf{f} \qquad (1)$$

where the left and right side of the equation demonstrate the inertial acceleration and forces, respectively, and $\boldsymbol{f}$ denotes body forces. Also it should be noted that it is necessary to include the interfacial effects (γ) into the flow equation. On the micro and nanoscales, equation (1) reduces to the Stokes equation since inertial force becomes smaller in comparison to viscous force,

$$\rho \frac{\partial \mathbf{u}}{\partial \mathrm{t}}=\nabla \boldsymbol{\sigma}+\mathbf{f}=-\nabla \mathrm{p}+\mu \nabla^2 \mathbf{u}+\boldsymbol{f}_{\boldsymbol{\gamma}}+\mathbf{f} \qquad (2)$$

and the mass conservation equation,

$$\frac{\partial \rho}{\partial \mathrm{t}}+\nabla(\rho \mathbf{u})=0 \qquad (3)$$

for nearly constant fluid density gives the incompressibility condition $\nabla\mathbf{u}=0$. In such fluidic systems, tensor stress $\boldsymbol{\sigma}$ has both tangential and normal components. For instance, pressure (as force per unit area) is applied normal to any surface, viscous stress ($\sim\mu\nabla\mathbf{u}$) includes both shear and normal components, and capillary (interfacial) stress ($\sim\gamma/R$) is applied normal direction to the surface while Marangoni stress (interfacial tension gradient, $\sim\nabla\gamma$) is applied tangential to the surface [10], [55].

Two-phase flows in the micro scale are governed by these bulk and surface phenomena exerted on fluid molecules, as well as variations on fluid properties such as in density and viscosity. To characterize the microfluidic two-phase flows, four fundamental forces (viscous, interfacial, inertial and buoyancy) and competition among them are analyzed. The relative importance of the forces are described by non-dimensional numbers [56]. Table 1 provides important dimensionless numbers with the scaling factors that are used in micro and nanofluidics multiphase systems. In micro and nanoscale flows, the flow velocities are low and the surface to volume ratio is high that it causes inertia, buoyancy and gravitational forces to be inconsequential compared to the interfacial and viscous forces. For this reason, Weber, Bond and Grashoff numbers are generally not considered as important parameters to control and design the fluidic process, while Capillary becomes more significant. To discuss these forces and non-dimensional numbers further, for instance, Bond number

Table 2.1. Relevant dimensionless numbers in multiphase micro and nanofluidics with characteristic length scale.

Dimensionless number	*Abbreviation*	*Description*	*Equation*	*Scale*
Capillary number	Ca	Viscous/interfacial	$\frac{\mu U}{\gamma}$	0
Reynolds number	Re	Inertia/viscous	$\frac{\rho L U}{\mu}$	1
Weber number	We	Inertia/interfacial	$\frac{\rho U^2 L}{\gamma}$	1
Bond number	Bo	Gravitational/interfacial	$\frac{\Delta \rho g L^2}{\gamma}$	2
Grashof number	Gr	Buoyancy/viscous	$\frac{g \rho^2 \beta \Delta T L^3}{\mu^2}$	3

(Bo) compares the gravitational force acting on the fluid, where Δρ is the fluid density difference (kg/m^3), g is the gravitational acceleration (m/s^2), L represents a characteristic length-scale (m) (e.g., the diameter of a droplet), and γ is the surface or interfacial tension of the two fluids in contact (N/m). To analyze the relative importance of gravitational force (body force) and interfacial tension, the value of the ratio of these two expressions allows for a judgment on whether the body force (gravity) dominates the interfacial tension (for $Bo>1$) or, conversely, the gravitational force is weaker than the interfacial force (for $Bo<1$). At the microscale, the Bond number is far smaller than 1. Thus, the interfacial forces dominate the gravitational forces.

Reynolds number depicts the relative importance of inertial forces to viscous forces. Since fluid flow inside microfluidic devices essentially operates at low Reynolds number, the viscous effects dominate the inertial effects.

The dimensionless capillary number, Ca, plays a key role in determining droplet dynamics, and is the most important interfacial non-dimensional number. It compares the viscous stresses with the interfacial forces. In microfluidic systems, the capillary number can change over a wide ranges of values. The value of the capillary number determines the mechanism of formation of droplets and bubbles. Generally, capillary number is calculated from the properties of the continuous phase.

Lastly, Weber (We) may be introduced, and it describes the relationship between the inertial and interfacial tension forces of the aqueous phase. In determining droplet formation dynamics, Weber number is usually paired with the Capillary number. We and Ca numbers demonstrate the relative importance of inertial, viscous and interfacial tension forces. Plotting the aqueous-phase Weber number against the oil-phase Capillary number provides a droplet formation regime map, and it highlights the critical Weber and Capillary numbers that mark the transition from steady droplets to jetting. At small aqueous and oil flow rates (We<<1 and Ca<<1), the aqueous fluid forms pulls apart an aqueous neck to minimize surface energy, yielding monodisperse droplets. At larger aqueous flow rates (We~1 or greater), inertial forces begin to dominate interfacial tension forces. At a critically high Weber number, the aqueous neck moves downstream as a wide unstable 'jet' of aqueous fluid from the nozzle. A transition from dripping to jetting also occurs as oil flow rates increase (Ca~1 or greater). At a critically large Capillary number, viscous drag forces from the outer carrier oil pull on the aqueous flow enough to overcome interfacial tension forces, causing the inner aqueous fluid to stretch into long, thin streams[13,20,57-58],[57].

2.2.2 SURFACE WETTING AND CONTACT ANGLE

Due to the intermolecular interactions and the force balance between adhesive and cohesive forces, wetting describes the ability of a liquid to keep contact with a solid surface. Wetting properties of liquids (i.e., phases; such as aqueous and oil) in two-phase microfluidic systems influence the droplet formation process, flow conditions and the capillary effect. It is very crucial to control the surface features and surface wetting characteristics of working fluids along with the contact angle which shows the tendency of a drop to spread out on the wall (surface) or rolling up that is the inverse measure of the wetting. Concave and convex interfaces can be obtained upon filling the microchannels with hydrophilic and hydrophobic fluids, as presented in Figure 2.4.

The contact angle occurs when a liquid droplet contacts both a solid and a gas (or a second immiscible liquid and a solid, as is the case in droplet-microfluidics). Here, the curvature originates from the differences of interfacial tensions, and Young's equation describes the force balance among the phases[11]:

$$\sigma_{sg} = \sigma_{sl} + \sigma_{lg} cos\theta \qquad (4)$$

Figure 2.4. Wettability on free surfaces (A) and channels (B) [11].

where σ (N/m) denotes the interfacial tension between two phases, and the subscripts g, l, s shows gas, liquid and solid, while θ represents contact angle. In droplet microfluidics, in order to form stable droplets and manipulate them properly inside the microchannels, the continuous phase should wet the walls in preference to aqueous phase. This case causes a thin film surrounding the droplet and isolates it from the walls. On the other scenario, both the aqueous and continuous phases partially wet the walls, and droplets can stick to the wall. This disturbs the operation of the device and the transportation of the droplet along the channel[59-66]. In Figure 2.5 Wetting and non-wetting of channel surfaces by aqueous droplets are shown.

2.2.3 INTERFACIAL PHENOMENA AND SURFACTANTS

Interfaces in microfluidic two-phase flows include interactions between fluid-wall and fluid-fluid[20], and understanding the wetting properties of the fluid-wall interactions are crucial to figure out whether ordered or disordered flow patterns occur[62]. It is usually observed that the size of droplets and the formation frequency depend on external parameters such as flow rates of the dispersed and continuous phases, the channel dimensions, as well as physical quantities such as the viscosities of the dispersed and continuous phase, the interfacial tension γ between both fluid phases, and the wettability of the channel walls.

The primary modification that droplets introduce to the single phase microfluidic flows comes through the swap-in of interfacial tension. Interfacial tension can be thought of in two complementary ways. First, it is a force per unit length which pulls the interface with a magnitude γ (N/m). Any imbalance in the value of γ will cause a flow along the interface from high to low interfacial tension regions. This phenomenon is also known as Marangoni stress. Second, interfacial tension can be thought of as the energy per unit area (J/m^2) which tries to minimize the total surface area in order to reduce the free energy of the interface. The minimum area for a given volume is a sphere for isolated

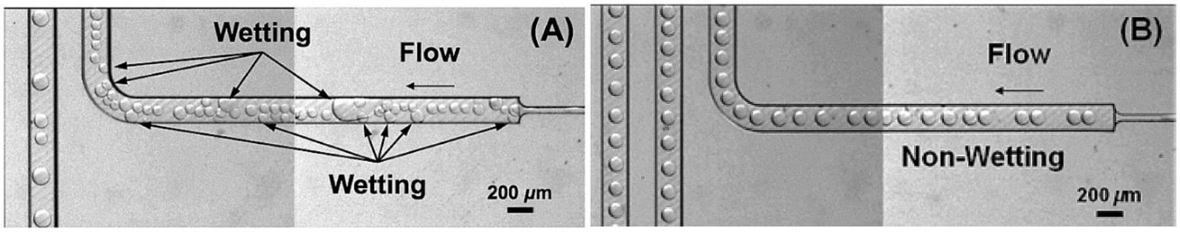

Figure 2.5. Wetting and non-wetting of channel surfaces by aqueous droplets [66].

droplets and for confined channels, droplets adjust their shape to the wall while curving their interface. This generates a pressure jump between the inside and outside of the droplet, which plays an essential role in flow conditions[67-68]. The existence of the interface separates two immiscible fluids such as oil and water, or a liquid and a gas, such as water and air. Interfacial effects become dominant and significant when the length scale is reduced to micrometer scale. When two immiscible fluids are brought into contact in the microchannel, two interfaces, between fluid-fluid and fluid-wall, arise. The wetting properties of the fluid-wall interface are enormously important in determining whether ordered or disordered flow droplets occur, as mentioned above. When the continuous phase (e.g., oil, in water-in-oil droplets) completely wets the microchannels, stable droplets can be obtained. While, if the wetting is partial, irregular or unstable, droplets are produced. In order to form water-in-oil droplets, walls must be hydrophobic and, for oil-water droplets, hydrophilic. In other words, the continuous phase needs to wet the walls preferentially, so that the dispersed phase is always separated from the walls of the channels by at least a thin film of the matrix liquid [20]. PDMS is mostly used for microfluidic chip fabrication, and is naturally hydrophobic. However, after plasma bonding, the channel surfaces become hydrophilic. The contact angle can be adjusted by heat treatment, chemical modification by surface treatment or adding surfactants at different concentrations[69]. For example, heat treatment can be performed on PDMS, at over 1900C for 24 h, to change the surface from hydrophilic to hydrophobic.

Surfactants, on the other hand, are mostly used for generating stable droplets, and to stabilize droplets against coalescence (Figure 2.6). The value of the interfacial tension can be lowered by the addition of surfactants. Most surfactants form a molecular solution in the liquid in which they are dissolved, but only up to a critical concentration (termed the critical micelle concentration, or CMC). Above this CMC they aggregate (micelles) and, below the CMC, the interfacial tension depends on the concentration of the surfactant[23]. To work with a constant and stable surface tension value, the CMC should be above the critical value.

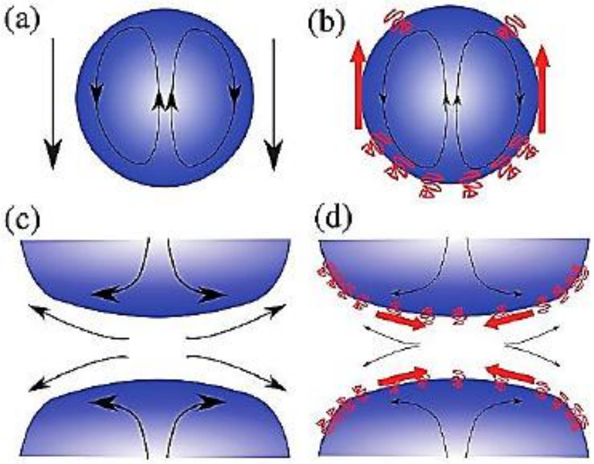

Figure 2.6. Marangoni effects in the presence of surfactant. (a) The flow pattern in the absence of surfactant. (b) In the presence of surfactant, causing a Marangoni stress (c) Upon collision of droplets, the continuous phase has to be drained before droplets coalesce. (d) In the presence of surfactants, the gradient of surface density of the surfactant generates a Marangoni stress against coalescence[23].

2.2.4 DYNAMICS OF DROPLET MOTION AND TRANSPORT

Transport of droplets along the microchannels after they are generated is another important point to tackle. As emphasized previously, for many Lab-on-a-chip processes droplets serve as vehicles for drug assays, cells or reagents that are supposed to be travelled from one location to the other, for the purpose of, for example, sensing or heating for measurements or analysis. Although different flow characteristics may occur with different channel aspect ratios, flows at bifurcations, flows under various capillary number conditions or under external forces, herein slug shape droplet flow in rectangular microchannels is considered to look at the flow. Detailed information on the hydrodynamics of those topics can be found elsewhere[17,70-78]. As droplets flow in microchannels, a thin lubrication film of the continuous phase is collected between the channel walls and the droplet. This can be thought of as the balance of shear stress from the channel walls against the capillary pressure in the droplet. Due to the viscous force, the carrier (continuous phase) liquid is pulled back, opposite to droplet direction, which deposits the thin film between the droplet and the walls. Besides, the pressure inside the droplet is higher than the pressure in the continuous phase, which causes a Laplace pressure jump at the interface[68]. Also, the competition of capillary pressure and viscous drag induces the thickness of the thin oil film. Therefore, the capillary number of the flow plays an important role in the thickness of the film. And, the film thickness effects the velocity of the droplets.

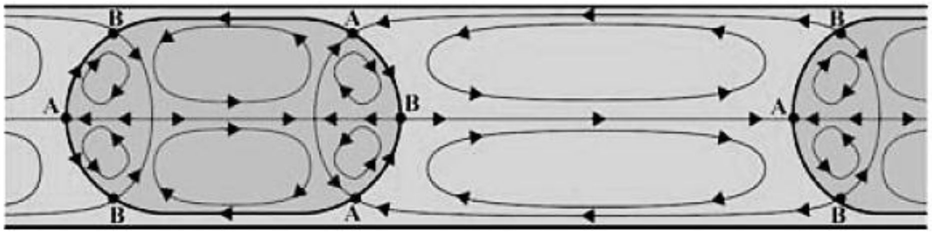

Figure 2.7. Topology of the counter-rotating recirculation zones induced by the presence of the interface[68].

While in single-phase microfluidic flows, the flow is constituted by a Poiseuille-like profile. In this case, at the centerline of the channel, the velocity is maximum. However, in droplet microfluidics, this is not the case, and it behaves differently since there is an interface, and the continuous and disperse phase liquids cannot mix. Thus, because of relative velocity difference between the carrier fluid, viscous drag and pressure difference, the fluid motion inside the droplet takes different forms than that of continuous phase (see Figure 2.7).

2.3 DROPLET FORMATION AND MANIPULATION

There are many methods have been reported by researchers in literature. Droplets can be formed by using active and passive methods. While active droplet generation may be driven by using electric fields, thermally induced, acoustic forces or piezoelectric actuators, passive techniques include flow focusing, T-junction or co-flowing configurations.

Droplet generation is a first step for droplet-based microfluidic systems. So as to develop microfluidics and Lab-on-a-chip devices with droplets and realize complex applications, they must be well-controlled and manipulated properly. As well, more importantly different functions must be added to microfluidics. Even though several methods have been depicted, microwave technology as a versatile technique provides challenging functionalities to LOC/microfluidics. Examples, methodology and explanations on droplet generation and manipulation techniques are presented below. First, active droplet generation techniques will be reviewed, then passive techniques and manipulation approaches will be introduced in turn.

2.3.1 ACTIVE DROPLET GENERATION

To generate a droplet from a liquid phase in an immiscible second continuous liquid phase, energy needs to be exerted to the interface so that some of the energy is converted to surface energy. At the liquid/liquid interface, an energy imbalance leads to instability, and causes droplet pinch-off. This energy might come from an external source or from the hydrodynamic pressure of the flow. In the former case, the droplet generation process that occurs due to locally added external energy is called “active droplet formation” and, in the latter case, “passive droplet formation” occurs without external input[79]. While active methods require additional components to be added to the system, they are able to provide more control and flexibility. Passive methods are simpler in this manner, yet the control of the process is complicated, and requires hydrodynamic modelling for robust droplet breakup. Depending on the Lab-on-a-chip or microfluidics application, either of the droplet generation techniques can be chosen.

Here, in this report, essential approaches are taken into account, and recent review articles are referred to such as Zhu and Wang’s (2017) and Chong et al. (2016) papers, (ref. [80] and [79] respectively) for further information.

2.3.1.1 THERMAL

The important parameter of thermally induced droplet generation is the heating source or heating approach. For example, lasers or resistive heaters have been used for this purpose. Although it has not been presented yet, and is not reported in this thesis, microwave resonator heaters which provide localized and selective heating fit well for droplet generation task by thermal means, and provide unique advantages. Preliminary results have been obtained for droplet generation through the microwave heater used in the thesis, and the approach will be studied in detail later.

Using resistive heaters to manipulate droplet size was first introduced by Nguyen’s group[81-82]. To control both droplet size and droplet generation regimes, microheaters and temperature sensors were employed. The heater and sensor were insulated from the fluids with a thin PDMS passivation layer. The droplet formation process is based on the temperature dependency of fluid properties such as interfacial tension and viscosity. They provided a correlation between normalized droplet diameter and thermophysical fluid properties as follows[79,81],

$$D^{*}(\Delta T) \propto \frac{\gamma^{*}(\Delta \mathrm{T})}{\mu^{*}(\Delta T)} = e^{0.02\Delta T} \qquad (5)$$

where D^*, γ^* and μ^* show the diameter, interfacial tension and viscosity which are normalized values at a reference temperature. Ismagilov[83] and Whitesides[84] provided similar dependence of size drops that are inversely proportional to the Capillary number. Results showed that with a temperature increase from 25 ^{o}C to 70 ^{o}C, the diameters of the droplets increased about 2 times. However, it should be emphasized that the exponential scaling presented in that study does not describe the complex nature of thermal control, and is specific and valid to the parameters used in the study. But, the initial attempt of those results are valuable to propose and study the problem. Spatial temperature distribution, surfactant concentration if used, Marangoni effect and flow rate ratios should be considered for further analysis.

The droplet generation work was later extended to investigate the effects of nanoparticles added to the fluid. 15 nm diameter TiO_2 caused an interfacial tension decrease, and experiments showed that the size of the droplets increased about 15% in comparison to cases without nanoparticles [85-87].

In another study, Stan et al.[84] used two heat exchangers to heat an entire microfluidic chip. One if the heat exchanges heated the upstream part (variable between 0-90 ^{o}C), and the other one heated the downstream part to keep it at room temperature (Figure 2.8). Their method controlled the volume and the velocity of drops generated in a flow-focusing device dynamically and independently by simultaneously tuning the temperature of the nozzle of the device and of the flow rate of the continuous phase. Increasing the temperature of the flow-focusing nozzle from 0 to 80 ℃ increased the volume of the drops by almost 2 orders of magnitude.

On the other hand, localized heating near the droplet generation location can be a better approach to control the temperature of the interface. Focused laser beam is a method to achieve this and Baroud et. al [88] demonstrated a work on laser heating and droplet generation. An argon-ion laser with a wavelength of 514 nm was focused slightly downstream of a cross junction. The disadvantage of lasers for this type of task is that the heating is manipulated at a spot, but selective heating only for the disperse phase which pinches off a droplet is more promising in terms of the control of temperature at the whole surface. Likewise, Park et al.[89] used a pulse laser on a stable water–oil interface to generate water droplets on demand with a valve. They observed that the laser beam caused localized heating with boiling and the rapid formation of a cavitation bubble. The bubble injects a droplet from the interface into the surrounding oil phase.

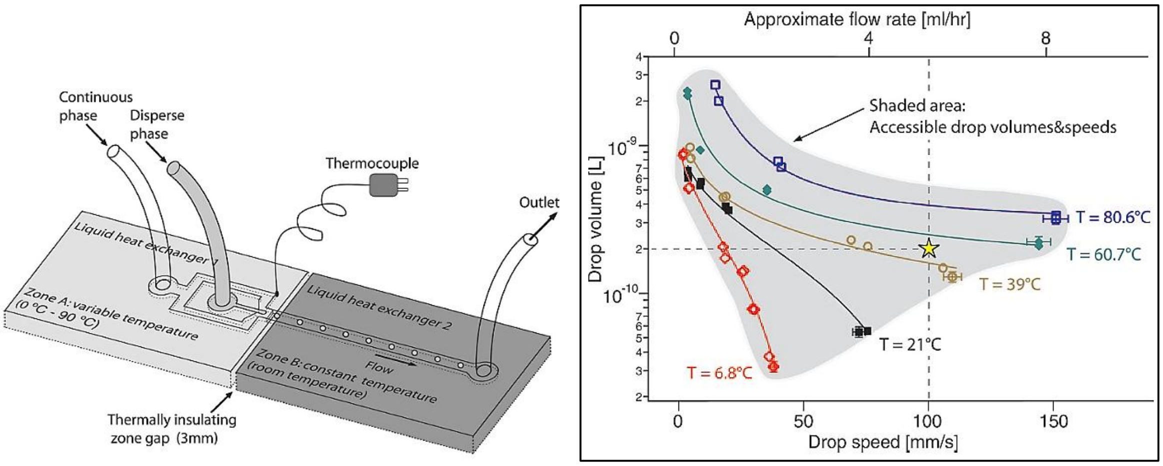

Figure 2.8. The microfluidic device presented by Stan et al.[84] and the behaviour of independent tuning of the drop volume and drop velocity using simultaneous variation of temperature and flow rate.

2.3.1.2 ELECTRICAL

The combination of geometry and electrical forces is also implemented to generate droplets. For this purpose both AC and DC control were applied. To apply an electric field, a microfluidic device is embedded with electrodes, one or pairs of which are connected to the high voltage, and the others are grounded. The migration and accumulation of charges at the water-oil interface can be induced by exerted electric fields. Then the interaction between surface charges and the electric field with proper field distribution can be used to control the droplet generation[80,90-91]. For example, the control of droplet sizes by an AC voltage applied across microelectrodes patterned around a flow-focusing junction was demonstrated by Tan et al.[91] (Figure 2.9). The authors concluded that the effective voltage at the tip of the liquid to be dispersed controls the droplet formation process. Also, several regimes of droplet generation were monitored through the electric fields, and at low voltages below 600 V, droplets were in the dripping regime. At voltages above 600 V, droplet jets were observed.

2.3.1.3 MECHANICAL ACTUATION

Droplet generation can be controlled through physical deformation of the liquid/liquid interface by means of mechanical actuation such as hydraulic, pneumatic or piezoelectric. Hydraulic and pneumatic controls are generally implemented by valves combined with the microfluidic chip, and usually made of elastic materials like PDMS[79]. By applying pressure (hydraulic) or compressed air (pneumatic), the liquid filled valve can be disturbed to cause droplet breakup. However, due to faster response and flexibility on control, piezoelectric actuation is more favorable than other mechanical methods. Figure 2.10 shows a mechanical vibrator used by Zhu et al. [92]. Other examples of mechanical actuation techniques can be found in [93-96].

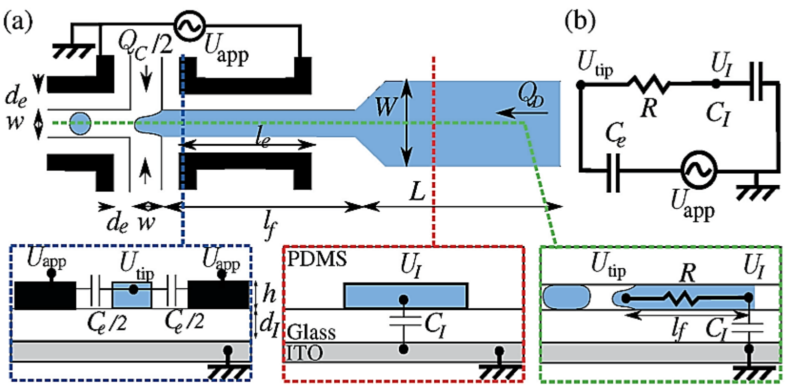

Figure 2.9. Microfluidic flow focusing device in an AC electric field (a). The electrodes are presented in black, and the aqueous phase in blue. The blue, green and red cuts illustrate the parameters used to derive the equivalent circuit of the system (b) [91].

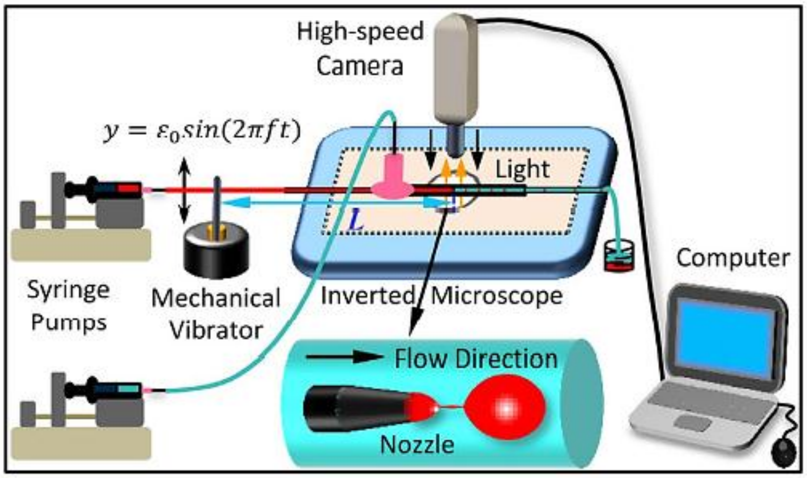

Figure 2.10. Pinch-off of droplet by mechanical perturbation presented by Zhu et al.[92].

2.3.1.1 MAGNETIC

Another approach to generate droplets by active means is the use of magnetic fields. A ferrofluid, which is type of nanofluid containing nanometer-sized magnetic particles, can be magnetized or demagnetized with an applied magnetic field[80]. By varying the applied magnetic field and filling the disperse phase with ferrofluids, controlled droplet breakup can be achieved[97-98].

2.3.2 PASSIVE DROPLET GENERATION

2.3.2.1 T-JUNCTION

T-junction design is one of the most common techniques, and droplets in microfluidic channels have been generated mostly by this design. The first easily controlled monodisperse droplet generation in microfluidic channel was introduced by using a T-junction channel geometry by Thorsen et al.[74] in 2001. Since then many studies were performed using T-junction geometries to achieve a better understanding of the droplet formation mechanism and the role of several physical parameters[22,73,99-102], as well as to develop various applications[103-106]. The size of the droplets depends on the flow rates of the two liquids, the dimensions of the channels, the relative viscosity between the two phases, the channel wall wettability, and surfactants and their concentrations[12]. In T-junctions, the disperse phase and the continuous phase are injected from two branches, and the disperse phase microchannel perpendicularly intersects the main continuous phase channel. Droplets of disperse phase are produced as result of the shear force and interfacial tension at the fluid-fluid interface. The break-up of disperse phase is caused by shear from the cross flow of the immiscible continuous phase[67,103]. The general geometry of T-junction is shown in Figure 2.11 [107]. Three regimes could be identified for T-junction droplet generators. When the capillary number is large enough, droplets are dispatched before they can block the main channel, and the formation is entirely due to the effect of shear stress. This regime is called as dripping regime, where the droplet pinches off when the viscous shear stress overcomes the interfacial tension. The other regime is called squeezing regime, and it is observed when capillary number is low enough, as described by Garstecki et al.[22]. In this regime, droplets obstruct the main channel as they are growing, and they restrict the flow of the continuous phase. This prevents the continuous phase from flowing through the channel, causing a dramatic increase in the dynamic pressure upstream of the droplet and, thus, this pressure difference forces the interface to neck and pinch off as a droplet[68]. The third regime could be identified at very high flow rates of continuous and dispersed phase, and is the so-called jetting regime. The jetting regime is characterized by the formation of long threads of the dispersed phase before droplet break-up. Additionally, a stable co-flow regime can be achieved with higher continuous phase flow rates, where all interfacial instabilities are deferred to downstream (Figure 2.11)[107].

T-junctions are widely used in droplet based microfluidics as they are easy to fabricate, easy to operate, and allow for synchronized droplet formation. Thus, it is a good choice if the demands on the homogeneity of the generated droplet size are not too high[67].

2.3.2.2 FLOW-FOCUSING

Droplet flow focusing geometry was first proposed by Anna et al.[108] and Dreyfus et al.[62]. As can be seen from Figure 2.11, this design consists of three inlet channels which converge into a main channel with a narrow orifice. The disperse phase takes place in the middle channel, and the continuous phase flows from two opposing side channels so that it squeezes the disperse phase. Both phases pass through the narrow orifice that is located downstream of the three channels. Later, the stream of disperse phase becomes narrow and breaks into droplets due to the occurrence of a singular high shear stress at the orifice. In flow focusing devices, droplet size is determined by the viscosities of the two phases[109-110], channel geometries[111], and flow rate ratio[112-113]. In order to improve the control over the size and size distribution of the droplets, several variations of the basic flow focusing device geometry have been developed[114-117].

Similar to T-junction, flow focusing designs operate at different regimes depending on flow conditions: dripping, jetting, and stable co-flow, as illustrated in Figure 2.11. In flow-focusing design, after droplet pinch-off, the remaining interface does not recoil back, as in the T-junction design, and it instead stays fixed in the orifice. Breakup occurs due to a combination of capillary instabilities combined with viscous drag effects on the emerging droplet. Compared to T-junctions, flow focusing typically offers better monodispersity and superior frequency up to about several kHz of the droplet generation[67].

2.3.2.3 CO-FLOWING

Another method to generate monodisperse droplets by passive manner in microchannels is the co-flowing design. In this technique, droplets are formed when the disperse phase is launched via a needle or a capillary into the co-flowing continuous phase[118-120]. Similar to the flow focusing device, droplets can be formed in the dripping and jetting regime. Dripping happens at lower flow rates, while jetting occurs at higher flow rates. In Figure 2.11 co-flowing device geometry and flow regimes are shown.

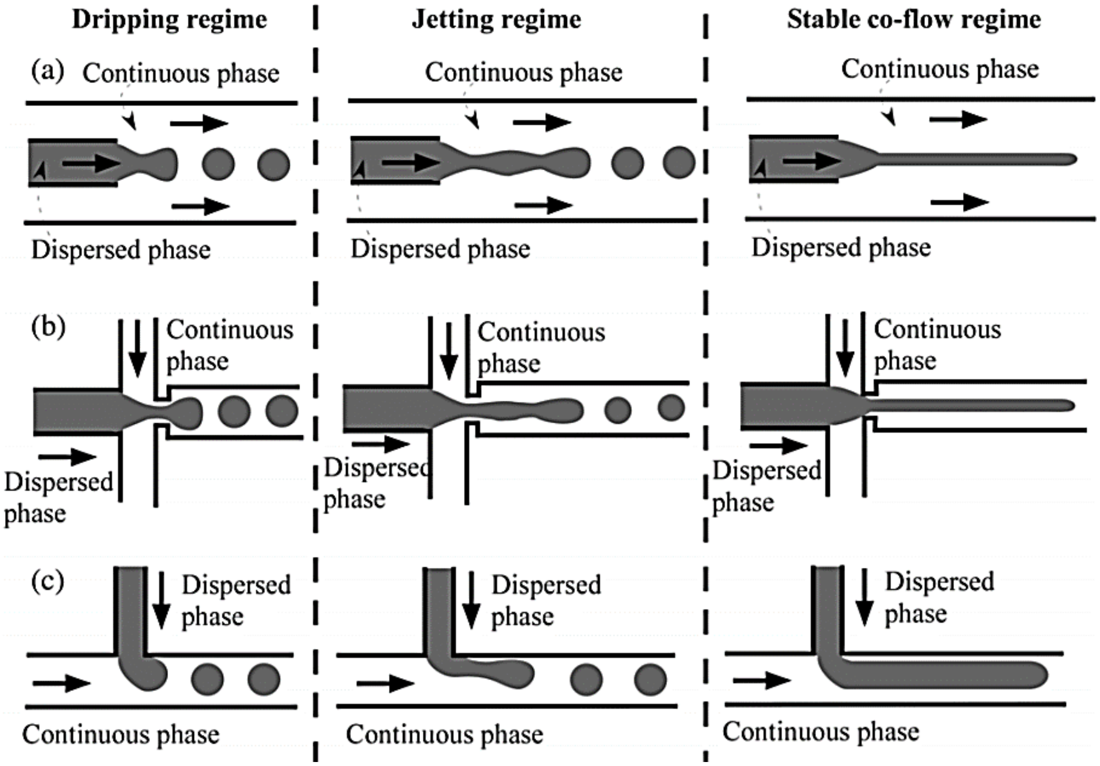

Figure 2.11. Schematic of different flow regimes in (a) coaxial, (b) flow-focusing and (c) T-junction microfluidic devices. Solid arrows indicate the flow direction [107].

2.3.3 DROPLET SORTING

After the review made on active and passive droplet generation approaches and techniques, it is now useful to overview the droplet manipulation methods in microfluidics. These techniques help to properly transport and manage droplets for different applications or reactions to be carried out in Lab-on-a-chip platforms.

Droplet sorting, in this scope, is a fundamental function in high-throughput applications so as to isolate specific droplets from the bulk population. Additionally, sorting facilitates an array of functions including segregation of a heterogeneous mix of droplets, purification of synthesized samples and enables individual control of single droplet. Droplets can be sorted passively[121-122], or actively[123-124] based on their properties or contents. Usually, passive techniques allow for the addressing and sorting of droplets through hydrodynamic effects[125-128], and are essentially governed by flow field properties. On the other hand, active methods use external fields, such as electric or magnetic fields, which can be switched on or off in order to actuate possible sorting by means of droplet electrorheological, magnetic or dielectric properties[129-145]. Also, temperature gradients induced by microwave heating or laser beams, can be employed to create flows and to control droplets via the thermocapillary effect.

Active sorting is mostly achieved by electrical based schemes, is the primary method for active manipulation of droplets. Ahn et al.[132], demonstrated a design where electrodes are placed beneath PDMS microfluidic channels to manipulate water droplets in hexadecane. The electric field created between the electrodes provides the force to steer the droplets into designated downstream channels. The position and shape of the electrodes are designed to maximize the field gradient and effectiveness in deflecting the droplets (Figure 2.12).

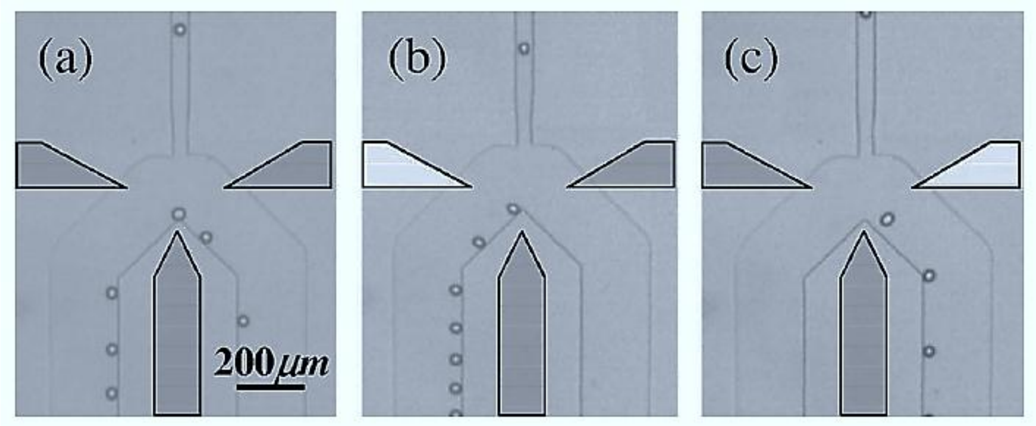

Figure 2.12. Droplet sorting via electric fields. (a) Droplets flow to both directions in the absence of electric field. (b) Droplets flow to left channel when left electrode is actuated. (c) Droplets flow right channel when right electrode is actuated[132].

A recent modification of the dielectrophoretic method in microfluidics is optically induced dielectrophoresis (ODEP), which is applied by coating the sides of the microfluidic device with electrically and photo conductive materials[133-135]. In this technique, virtual electrodes, generating the dielectrophoretic forces on dielectric droplets, are formed by optically projecting the electrode images onto the photoconductive material, in order to generate non-uniform electric fields, which enables to individually sort droplets. The shortcoming of this method is that it requires special device fabrication and a laser system. It is also worthwhile to mention that there are many other strategies that have been employed for droplet sorting. Thermocapillary effect can be used to realize from Marangoni stress. This is based on the fact that interfacial tension is a function of temperature, and influencing the interfacial tension can be used to manipulate droplets[88,137]. Mechanical valves embedded in microchannels are employed to rapidly change and stop liquid streams or to inject the desired substances[138-140]. Generating ultrasound waves by piezoelectric transducers can direct cells or droplets in channels by ultrasonic force fields[96,141-142]. Additionally, electrorheological fluids can also be used for droplet sorting since the viscosity of such fluids can be changed by applying an electric field. Electrorheological fluids can even exhibit solid-like behavior, and they can sustain shear stress in the direction perpendicular to the applied electric field, which can be utilized to control droplets[143-145].

2.3.4 DROPLET COALESCENCE AND SPLITTING

Individual droplets can be used as distinct microreactors for many chemical and biological applications. For instance, screening of biomedical diagnostics, chemical synthesis, kinetics studies, and cell morphology, can benefit from the use of microreactors. In such applications, merging of two droplets is important step[12]. The practical conditions for droplet merging are to first contact each other, and secondly, to overcome the stabilizing forces caused by surface tension and lubrication. For this task, different designs have been performed to bring droplets together[127-128,147-151]. As well, in order to overcome the stabilizing forces, both the presence of surfactant at the interface, and the viscosity ratio of two-phase fluids, have to be considered. The best volume and reaction control is likely ensured by coalescing two formerly individual droplets, with a precisely adjusted volume, containing different reactants. Essentially, four main droplet merging approaches could be identified: droplet coalescence using liquid properties, channel geometry, thermocapillary effect, and electro-coalescence[67]. These methods differ in experimental requirements and specific demand.

The easiest technique may be droplet merging with a properly designed channel geometry. Nevertheless, this method is mainly used for surfactant-free droplet devices, or for liquid interfaces which are only very weakly stabilized via surfactants. The primary task here is to decrease the spacing between droplets and bring them into contact. Channel geometries can be properly designed so that the fluid resistance in a channel, enlarged by a narrow section, can be used for this purposes. It will cause stopping of the leading droplet, and it gives enough time for the subsequent droplet to catch up and come into contact with the leading droplet[152-153]. Alternatively droplets can be stopped and trapped by enlargement of the channel, through pillars[146-149], or colliding them in a T-junction[148]. These examples can be seen in Figure 2.13.

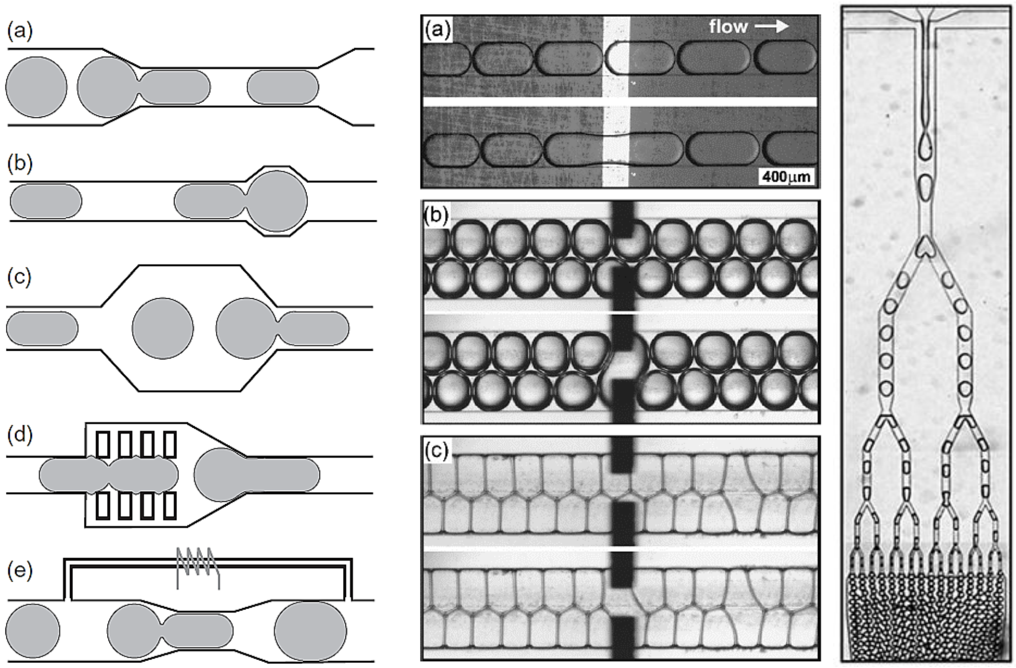

Figure 2.13. Mechanical droplet trapping and sorting (a-e)[67] (left image). Targeted electro-coalescence of droplets in a microchannel. When a low potential pulse is applied (50–100 ms, 1–3 V dc), pairs of droplets coalesce at the gap between the electrodes(a-c)[154] (middle image). Droplets splitting arrays for production of monodisperse emulsions at high throughput [164](right image).

Another method for droplet coalescence is called electro-coalescence which relies on electric fields[90,154-157]. Generating electric field in the range of 1-100kV/m induces dipoles, when droplets are close proximity to each other, and leads to an attractive Coulomb force between them. This will eventually lead to droplet merging. Priest et al. [154] studied the mechanism of electrofusion, where electric fields destabilize the interface, and this can cause liquid bridge and merging. Nevertheless, setting up a detailed model for the interactions between an electric field and the interface is hard due to the strong feedback between them. Their approach is illustrated in Figure 2.13, where applying a short pulse of 100 ms, with 1 V dc between the electrodes, induces local coalescence of droplet pairs arriving at the electrodes. A different strategy for droplet coalescence is by heating (thermo-capillary effect). One method is to use a focused laser to produce localized heating, and this heating effect changes the surface tension of two adjacent droplets leading to fusion[158]. Another heating method was reported by Luong et al. [159], where the authors investigated the phenomenon of thermo-coalescence of two droplets in a chamber with a microheater.

Increasing the temperature leads to lower viscosity and surface tension, and it results in a higher thermo-capillary force. The induced temperature field slows down droplets, and it eventually merges them at a critical value.

On the other hand, for various microfluidic processes, it is not only aimed at coalescing droplets, but also to split droplets into several smaller compartments for incubation or screening purposes, or to increase the droplet production frequency. Several methods have been demonstrated to effectively break up droplets to desired sizes (Figure 2.13). Most of the attempts have used shear force techniques to elongate the droplet until it splits[160-166].

2.4 SENSING AND DETECTION IN DROPLET MICROFLUIDICS

Sensing and detection techniques for droplets play critical roles in the development and application of droplet-based microfluidic systems. Many methods have been developed and used to control and manipulate droplets, as pointed out above. It is crucial to add functionalities to microfluidics because the early designs of the microfluidic systems were embodied mostly with monolithic miniaturized components such as microvalves, micropumps, and micromixers. With further improvement, compact and integrated microfluidic systems were realized, which were made up of multiple elements to achieve specific functions. The sensing and detection of droplets is very necessary for improving LOC systems. Since droplet-based microfluidic devices are increasingly being used to perform complex reactions, measurements and assays for chemical and biological applications, controlled manipulation and tracking of individual droplets is desirable. This is also required in order to realize a fully automated and integrated on-chip droplet operation. So far, a great number of approaches have been demonstrated in literature, ranging from capacitive measurements and temperature variations to optical signals. Each of the described methods is based on a particular system, and has its own advantages and drawbacks. However, the ideal technique should include features such as; easy integration with Lab-on-a-chip systems, cost-effectiveness, fast response, scalability, no need to bulky off-chip equipment and non-invasiveness.

In this review, first, examples of optical and electrical detection techniques for microfluidics are introduced, and the rational need for microwave sensing in microfluidics is discussed. Later on, available microwave detection methods in microfluidics are presented.

2.4.1 OPTICAL

The greater part of the techniques for controlling and monitoring microfluidic operations rely on optical measurements. And mostly, optical methods are comprised of a high-speed camera and an optical microscope. For further detailed analysis, fluorescence microscopy with fluorescent dyes are used to distinguish between different materials, observe sorting or track the reaction[167-169]. Physical basis for the optical sensing lies in the information provided by the light's changes as it travels through the sensing medium, including changes in absorption, fluorescence, luminescence, scatter or refractive index[170] (Figure 2.14).

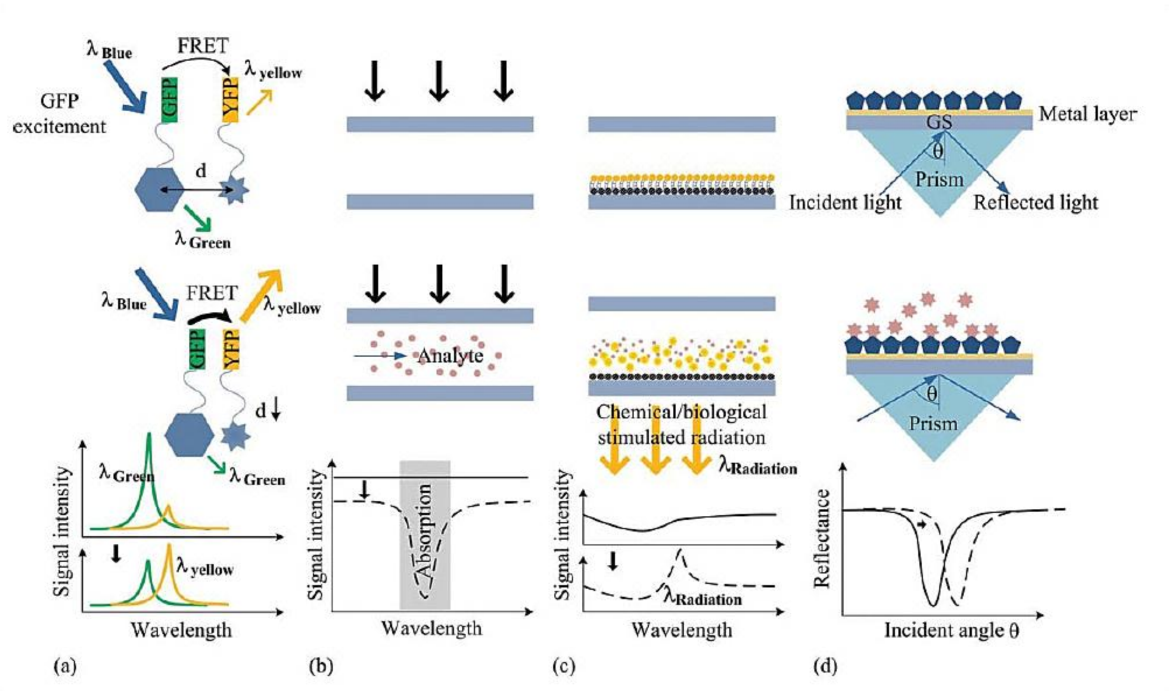

Figure 2.14. Typical optical methods. (a) Fluorescence, (b) absorbance, (c) luminescence, (d) surface plasmon resonance-based optical detection.

Microscopes are well-equipped in routine microfluidic and biological laboratories, and imaging with a microscope is the most straightforward and convenient way for droplet analysis. In droplet-based biological applications, it is important to quantitatively read the information of a specific compound, and fluorescence microscopy fulfills this task. He et al.[171] described a droplet-based method to study the enzymatic activity of a single cell. The single cell was encapsulated into a droplet, and the enzyme activity was measured by the fluorescence intensity of the enzyme-catalyzed product. Roach et al.[172] investigated protein adsorption on droplet-oil interfaces with fluorescently labeled proteins. One of the limitations of fluorescence imaging is that the CCD camera frame rate is usually lower than the droplet frequency, and is thus limited to high-throughput screening and sorting[21]. Additionally, an expensive fast camera is required to capture data from a single fast-moving droplet. Alternatively, Guo et al.[173] reported an optical fiber-based detection method. Their approach is based on detecting the fluorescence intensity using photomultiplier tubes (PMTs). Their detection limit was 2000 droplets per second. The fiber-based optical detection system includes two optical fibers: an input fiber which brings the excitation light from a blue laser (488 nm) to the detection point, and a detection fiber which collects the fluorescent emission from the excited droplets and directs it to an off-chip PMT (Figure 2.15). Here, one intrinsic drawback of detection is the need of fluorescent labeling, and the need of complicated laser and PMT setup.

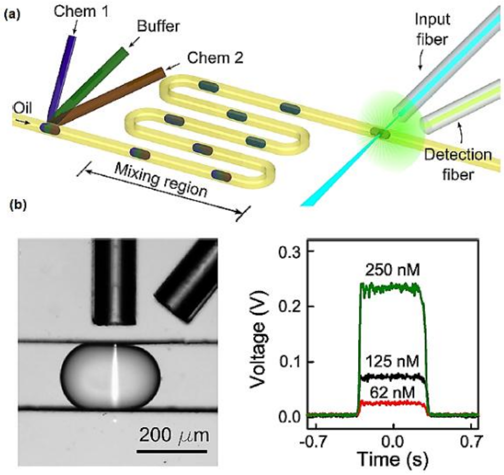

Figure 2.15. A fiber-based optical detection unit (a), electric signal and microscopic snapshot (b)[173].

Raman spectroscopy is another method, and is a label-free sensing technique. In this technique, the analyte can be recognized by the fingerprint of the Raman shift, and quantified using the corresponding peak intensity[174-178].

2.4.2 ELECTRICAL

Droplets can also be detected by electrical methods, which are mainly based on capacitance measurements and electrical signal information. Aqueous droplets passing over electrodes induce a change in the measured voltage, capacitance or impedance. This enables droplet detection to be done using multiple electrode pairs[179-183]. Elbuken et al.[184] presented a capacitive detection device for droplet size and speed detection. They used an interdigital capacitor with commercially available sensors, and calculated the maximum theoretical detection throughput of the proposed system as 15 droplets/s. Ernst et al.[185] demonstrated an open-plate capacitor to droplet detection technique, and determined the volume. Niu et al implemented capacitive method for real-time droplet detection, control and sorting in combination with electrorheological fluids. Recently, Kemna et al. [186] reported a microfluidic chip for fast (>100 Hz) and label-free electrical impedance-based detection of cells in droplets. The microfluidic glass-PDMS device consisted of two main components, the droplet generator and the impedance sensor. They tried to discriminate between viable and non-viable cells in a buffer. Electrochemical response can also be used to detect droplets. Luo et al.[187] reported using an electrochemical technique to measure droplet size and ion concentration based on the impedance difference of droplets and carrier. Liu et al.[188] presented an electrochemical method for the detection and characterization of aqueous droplets. Their method was based on the chronoamperometric analysis of an electro-active compound in carrier phase. They indicated that thismethodology was able to discriminate droplet formation, and the corresponding droplet size, up to a droplet frequency of 60 Hz. Magnetic methods are also another strategy for microfluidic sensing by using nanoparticles to interrogate droplets[189-191].

2.4.3 RATIONAL OF THE NEED FOR MICROWAVE

As can be seen from the above examples, although successful sensing aand detection approaches have been implemented by optial or electrical means, there are challenges and disadvantages when using these techniques. Optical methods usually require bulky and expensive components, and electrical systems usually work at low frequencies that make high-throughput applications difficult. In this regard, developing a miniaturized microwave sensor integrated with microfluidics is important to achieve verstaile Lab-on-a-Chip applications, label-free and high-througput detection purposes. Microwave sensors principally work in GHz frequency range, which increases the detection throughput, response time and sensitivity significantly. Below, examples of microwave sensing techniques in microfluidics are presented. Later, in the core chapters in the thesis, the newly developed microwave sensors and applications are demonstrated in detail.

2.5 REVIEW OF MICROWAVE SENSING AND DETECTION TECHNIQUES IN MICROFLUIDICS

2.5.1 FUNDAMENTALS OF MICROWAVE SENSOR STRUCTURES

In this section essentials of microwave sensing structures and some basic principles will be overviewed. Microwave sensing has many advantages over other techniques in terms of low-power requirements, scalability, non-invasiveness, no direct physical contact or use of labels on the processed materials, electronic integration possibility, portability, versatility (e.g., multiple tasks such as heating and sensing simultaneously) and compatibility with biological environments. First, some microwave structures will be given, and then sensor applications in literature will be presented. To begin with, transmission lines and planar structures are useful in terms of designing microwave sensors. Transmission lines in microwave circuits are normally used to carry information, or energy, from one point to the other, or for the coupling of energy. As a fact of matter, early microwave systems mostly relied on waveguides and coaxial lines. Waveguides have the advantages of high power handling capability and low loss, but they are bulky and expensive. On the other hand, planar transmission lines were used much later and provided very suitable configurations for microwave sensors and circuits, and also for easy fabrication processes. Planar transmission lines include microstrip, stripline, coplanar, slot lines and other structures. The advantages of planar transmission lines are their easy integration in the form of planar structure, compactness and low cost. For non-microwave frequencies, e.g. below 1 GHz, parallel wire lines or coaxial cables can be employed. When entering the microwave frequency region, it is no longer possible to use such structures because of radiation losses. Coaxial structures cannot be used above a few gigahertz as it becomes a bulky structure, and is therefore unsuitable. Hence, planar structures provide a good alternative[192],[193].

Geometry of Special Planar Transmission Structures

There are a number of geometries which are formed on different substrates. These can be listed as;

(i) Microstrip line

(ii) Slot line

(iii) Coplanar line or waveguide (CPW)

(iv) Coplanar strip (CPS)

(v) Inverted and suspended microstrip

(vi) Microstrip with overlay

(vii) Fin line

Transmission structures can be further categorized into (i) open, (ii) side-open or closed. The open microwave integrated configurations are not resistant to perturbations, and the closed ones are not affected by external fields. Generally speaking, if small size (miniaturization) is needed integrated planar structures are useful; and for high power and Q factor, the conventional designs are better (Figure 2.16). As well, worthy to note that newer fabrication technologies, e.g. micro and nano-fabrication, helped the growth of integrated sensors and circuits.

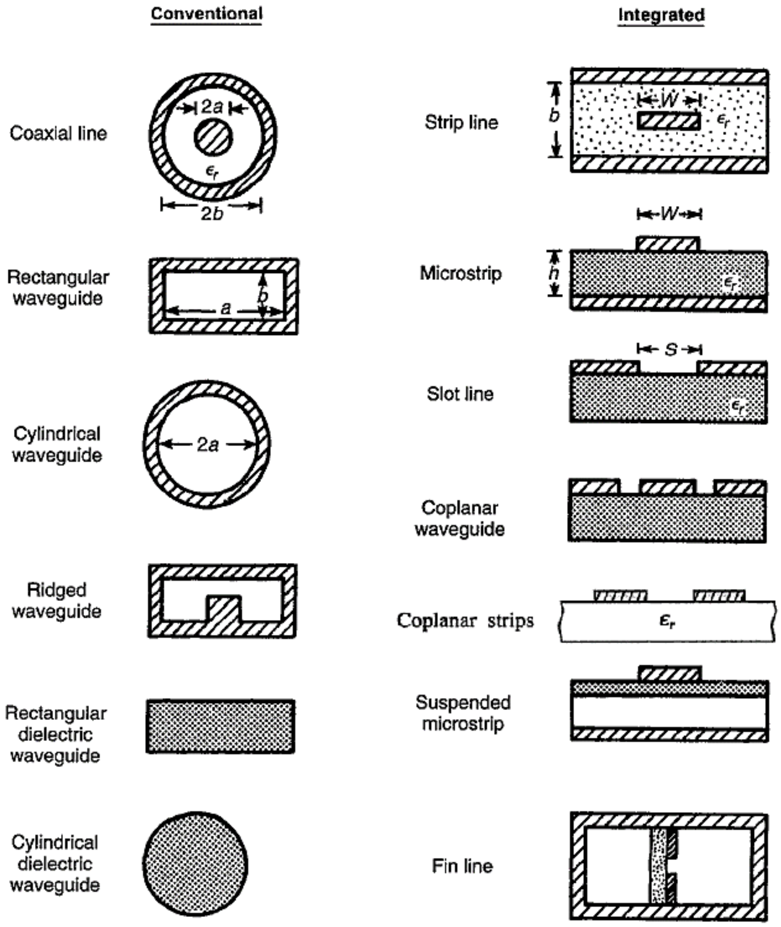

Figure 2.16. Conventional and planar transmission structures[192],[193].

Each of these planar structures have specific features; for instance, microstrip lines have a higher Q factor compared to others, suspended microstrip lines have a lower conductivity loss, and coplanar waveguides (CPW) have a higher integration and design flexibility. For microfluidics, integrated studies frequently use coplanar strips, coplanar waveguide or microstrip designs. However, since microstrip lines require a ground plane at the bottom, it is difficult to use this structure with microscopes, which are generally used for the observation and control of fluid flow in microchannels. Electric and magnetic field distributions are also demonstrated in Figure 2.17 for these structures[194].

Microwave sensors principally operate on the electromagnetic field interactions. Properties and information for the desired medium are extracted and analyzed with such interactions. Extracting material or liquid parameters such as permittivity, permeability and conductivity are used for detecting or sensing purposes. For instance, microwave sensing systems directly translate the presence of certain analyte (e.g., biomolecules, cells and viruses) into an electronic signal.

Different microwave topologies and sensor structures have been developed for various objectives. However, these methods have their own advantages and drawbacks. In many microwave sensing devices, resonant structures are essential elements because they allow for the localization of high field areas. At the resonance frequency, the electric and magnetic energy densities are enhanced dramatically at certain locations in the resonator. They are very efficient in the frequency band for which they were designed, since the signal-to-noise ratio in a resonator structure increases with resonator quality factor (Q). This increase in sensitivity and field strength is accompanied by a narrower frequency band, with the drop in amplitude depending on Q, which results from the shift in resonant frequency with different environments. Typical microwave devices use resonant structures, for instance, strip- and microstrip-line resonators, coaxial-cavity, and coaxial-line resonators. A detailed description of such structures can be found in review articles[195-196]. Recently, open planar LC resonators have been suggested for microwave sensing[197-198]. Furthermore, to achieve a high sensitivity, a resonator sensor needs to have a sharp resonance in its frequency response, and the electric field has to be confined to the portion of the sensor on which the sample substance is deposited. As a consequence, the resonance feature is more preferred in the design of sensors. On the other hand, resonators are usually regarded as detrimental in wide band applications.

The resonance approach has been widely adopted as a method for obtaining permittivity data at microwave frequencies, especially for polar liquids. Using a resonator that can be excited in many distinct modes opens up the possibility of resonant dielectric spectroscopy. The motivation for employing dielectric spectroscopy is that it yields useful information for applications across a large

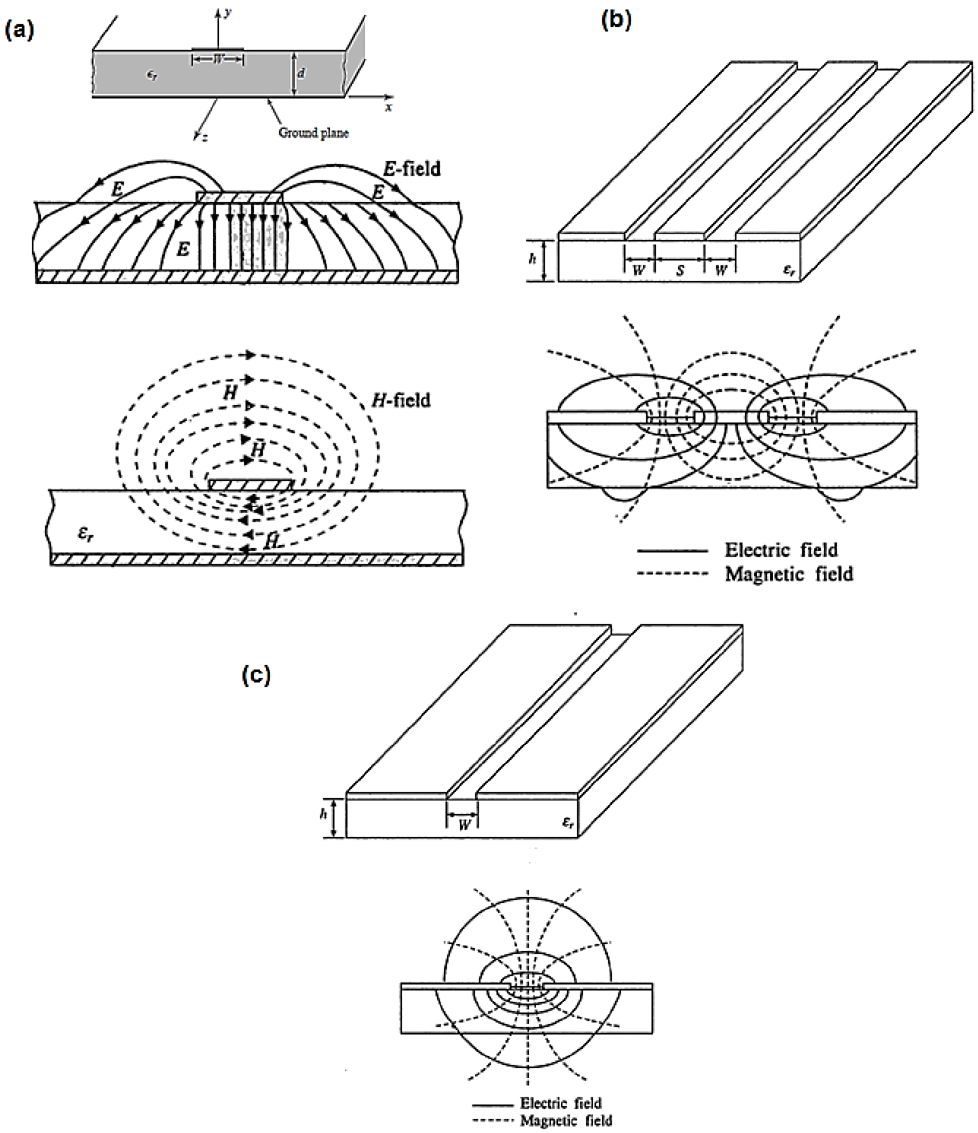

Figure 2.17. Electric and magnetic field patterns (a) microstrip line, (b) coplanar waveguide, (c) Slot line[192],[194].

range of scientific and engineering disciplines[199]. Indeed, measuring the dielectric property change with microwave devices is of great interest in the development of microwave sensors, due to the fact that it provides a relatively simple electronic way to gain information about the subject under investigation without a need for labeling, chemical modification or physical intrusion. Permittivity is a frequency dependent feature that reflects how a material interacts with an electric field. Molecules of a liquid in an oscillating electric field polarize and align, and dissipate some power. The real component of permittivity indicates the polarization ability of molecules, while the imaginary component presents information on how much power the molecules can dissipate when they align with the polarizing electric field. At microwave frequencies, specific molecular dipolar relaxations dominate, and ,therefore, this dielectric property can be used for identifying the chemical composition or changes in the liquid environment[200]. The use of a resonator allows measurements at multiple discrete frequencies throughout the permittivity spectrum. This is preferable to the continuous spectra of equivalent broadband techniques because of increased accuracy and reduced uncertainty[200]. Several groups have demonstrated the usefulness of dielectric measurement techniques for various applications[201-202] and development of resonant techniques at microwave frequencies[203]. Additionally, as an example of a reason why sensing with dielectric properties in the microwave frequency regime has become very attractive, bio-molecules exhibit rather large and distinct dielectric properties, and, in some matters, the ionic conductivity of water in most systems is greatly changed. For instance, it has been reported that tumoral cells exhibit larger values of electrical conductivity and permittivity than normal cells, which allows direct label- free sensing of the target molecules in their native environment using dielectric features[204].

It is also worthy to discuss that one type of most common microwave sensors is metamaterial structured split ring resonators, which was first introduced by Pendry et al. in 1999 [205-206]. The artificially constructed materials based split ring resonators (SRRs) have interesting electromagnetic properties and have received growing interest in recent years. Moreover, the resonance frequency shift of this material is extraordinarily sensitive to the changes in the capacitance of SRR, which makes SRR suitable for microwave sensing applications[207]. There are widely investigated studies in literature on split-ring resonators; flexible SRR metamaterial structure[208], applications of SRR to biomolecule sensing[209] and magnetic response of SRR[210]. Since these topics are broadly investigated by electromagnetics community at various structural features, attention here will be given to microfluidics related studies.

2.5.2 APPLICATIONS OF MICROWAVE SENSORS IN MICROFLUIDICS

Coplanar waveguide (CPW) based microwave sensors also have been found in a broad range applications. The structure is composed of a coplanar transmission line and ground plane separated with slots. The configuration provides a volumetric interaction between the fields and the medium. For example, for microfluidic integrated designs, about half of the electrical field is located in the fluidic channel, whereas the rest is positioned in the substrate. This design is resistant to losses and interferences induced from external sources[211]. A coplanar waveguide sensor was used by Grenier et al.[212] for biological analysis. Authors evaluated the relative effective permittivity of human cells. The working principle of the sensor is common as when the fluid (which may include biological samples) is incorporated in the fluidic channel, the transmitted signal is modified due to the relative permittivity of the fluid, which is strongly different from the substrate[213]. The drawback of their system is that this method only allows for the measurement of cell-suspended solutions, and it cannot provide proper measurements for single cells or sensing of individual droplets. Also, the structure is not convenient to use as a resonator. In Figure 2.18, examples of coplanar waveguide sensor configurations are provided.

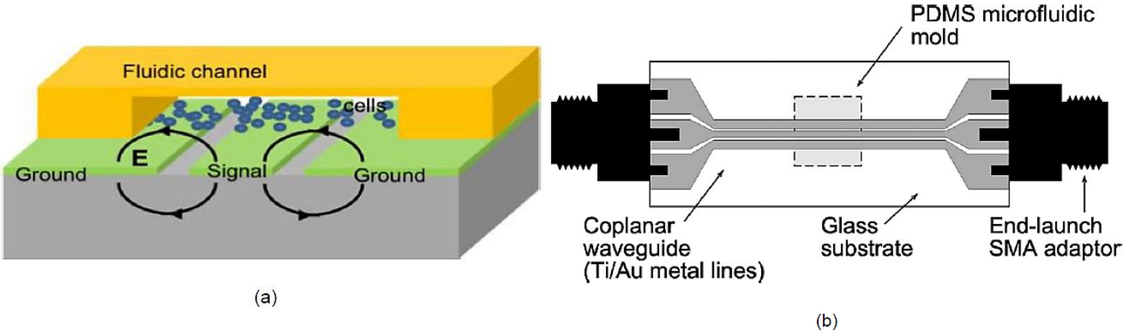

Figure 2.18. Examples of coplanar waveguide sensor configurations. (a) Schematic view of high frequency interaction[212], (b) CPW device showing wave-guide and microfluidic sample containment[201].

In a slightly different design, Dalmay et al.[214] investigated cell discrimination using glial cells through impedance spectroscopy analysis at microwave frequencies. They showed a proof of concept study through measuring sensor frequency response before and after cell deposition[215-218]. A resonant co-planar sensor was recently presented by Mason et al.[219] in order to distinguish the solutions with various glucose concentration levels at microwave frequencies. Even though they incorporated a fluidic channel onto the sensor, the sensor dimensions are relatively large and not applicable for visualization. Microwave sensor applications with coplanar waveguides can also be found with interdigital capacitors[220], liquid concentration measurement[203] and biomolecule detection[221-222].

Lee et al.[209,223-224] proposed a split-ring resonator at the microwave regime for DNA sensing, i.e., DNA hybridization. In this study, authors located a single resonator at close proximity to the microstrip line, which provides excitation with a time-varying magnetic field (Figure 2.19). Here, the microstrip line behaves as an open conduit for wave propagation so that the electromagnetic fields are not entirely confined under the signal line. Mainly, the SRR structure is excited by the field components. The resonator becomes resonant at a wavelength significantly larger than the diameter of the rings, which reduces the requirement of half-wavelength that could be an issue if the rings were closed. Additionally, a second split ring is placed inside the outer ring for the purpose of increasing the capacitance in the small gap field between the rings so that the resonance frequency decreases as well as confines more electric field in the small area. The fact that the interaction between electromagnetic waves and resonant medium; the surface currents which is dependent on resonant properties of the structure is triggered by the time-varying magnetic field components parallel to the resonator axis. Magnetic fields that propagate from the current of the resonator might either enhance or oppose the incident field, and the associated magnetic field pattern from the resonator is in a dipolar pattern[209]. With this configuration the resonator principally behaves as a resonant LC circuit and they estimated resonance as the following equation:

$$\omega_o \approx \frac{2}{\pi r_o LC} \qquad (6)$$

where r_0 is the average distance between the inner and the outer rings. As can be seen from Eq. 6, it is obvious that the resonant frequency can be controlled by changing the inductance and/or capacitance. This feature is very useful for various biological or chemical reactions to utilize as a biosensor because different reactions or compositions generate different capacity and permittivity change ranging from microwave to terahertz frequencies.

In a similar recent study, Withayachumnankul et al.[225] presented a metamaterial based single split-ring resonator (SRR) microfluidic sensor for dielectric characterization. The SRR is made of a metal loop with a square shape, and has a split on one side. By using a microstrip line, microwave is launched into an end, which excites the quasi-TEM mode of wave propagation. Quasi-TEM mode is depicted by an oscillating current on the microstrip, and by a magnetic field which is circulating around the strip. They propose that, in the quasi-static limit, the system of an SRR and transmission line can be modelled by fundamental circuit elements, as illustrated in Figure 2.20. The capacitance Cs is generated by the gap, and inductance Ls by the SRR loop. The authors described the characteristics of the structure; by omitting the effect of the mutual inductance M, they showed the impedance of the resonator as;

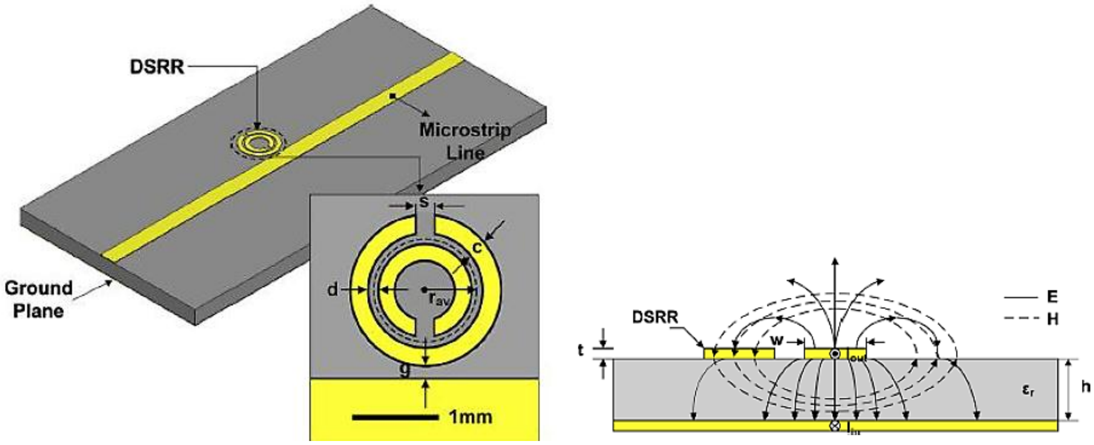

Figure 2.19. (a) The topology of SRR, (b) Cross section of microstrip transmission line with SRR and schematic electromagnetic field distribution[209].

$$Z_s = R_s + j\omega L_s + \frac{1}{j\omega C_s} \qquad (7)$$

And for the capacitance affected by the dielectric material around the gap, they used an approximation of;

$$C_s = C_o + \varepsilon_{sample} C_c \qquad (8)$$

where C_0 includes the capacitive effect from the dielectric substrate, channel walls, and surrounding space, excluding the channel cavity. ε_{sample} is the complex permittivity of the sample (ε_{sample}= ε'_{sample}+jε''_{sample}), and the term $\varepsilon_{sample}C_c$ describes the contribution from the loaded liquid sample with C_c for the capacitance of an empty channel. By substituting Eq. (7) into Eq. (6), the total resistance R_t and capacitance C_t of the SRR are a function of the sample permittivity,

$$R_t = F_R(\varepsilon'_{sample}, \varepsilon''_{sample}) \qquad (9)$$

$$C_t = F_C(\varepsilon'_{sample}, \varepsilon''_{sample}) \qquad (10)$$

Both R_t and C_t are the factors that determine the resonance characteristics, i.e., the resonance frequency,

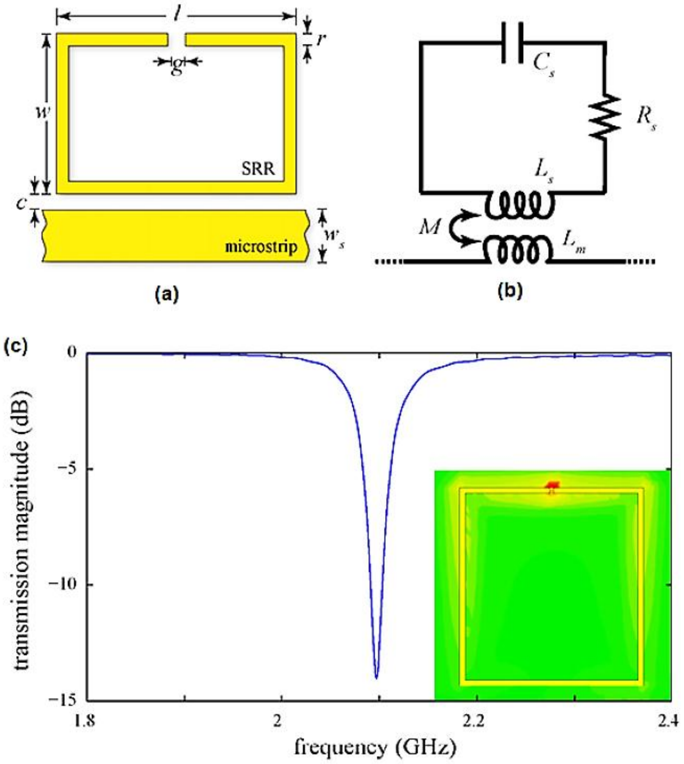

Figure 2.20. (a) microstrip coupled split-ring resonator, (b) equivalent circuit model, (c) numerically solved loaded microstrip[225].

$$f_o = \frac{1}{2\pi\sqrt{L_s C_t}} \qquad (11)$$

and Q factor,

$$Q = \frac{1}{R_t}\sqrt{\frac{L_s}{C_t}} \qquad (12)$$

Thus, from Eqs. 9-12, the SRR resonance is dominated by the complex permittivity of the sample. By analyzing this dependency, dielectric characteristics of the liquid sample can be extracted from the measurable transmission resonance[225]. Authors used this methodology for binary mixtures of ethanol and water in order to obtain complex permittivity. However, this sensor structure and their approach are not convenient for droplet microfluidics.

On the other hand, although coaxial and cavity resonators are not as flexible and compact as other sensors mentioned above for microfluidics, some examples can be given[199,226-228]. Rowe et al.[199] studied analyzing the chemical composition of single and multiphase solvent flows with a coaxial resonator operating at microwave frequencies. The coaxial sensor was embedded in a compression-sealed polytetrafluoroethylene microfluidic chip. Ferrier et al.[226] investigated mechanical analysis of cells through a cavity resonator.

Even though a large amount of work has been performed for various microwave sensors, there are few studies showing the integration of these sensors with microfluidics. As a matter of fact, most of them require expensive and bulky off-chip components, and lack high-throughput. Additionally, for droplet-based studies visualization and manipulation of individual droplets are key factors. In this regard, high-throughput, portable and inexpensive microwave-microfluidics integrated devices are highly needed.

2.6 HEATING IN MICROFLUIDICS

2.6.1 AVAILABLE HEATING METHODS AND THEIR PROS/CONS

Development of Lab-on-a-chip devices requires the integration of multiple functions within a compact platform. As mentioned in the droplet manipulation review of this report, integrated microfluidic devices necessitate a number of functionalities such as sensing, detection, sorting, pumping, splitting and merging. Other functionalities also include heating and temperature control. Indeed, the regulation of temperature is a vital factor in managing many physical, biological and chemical applications, but it still remains a challenge for microfluidic devices. Prominent examples of applications requiring temperature control are polymerase chain reactions (PCR)[229-231], temperature gradient focusing for electrophoresis[232-233], digital microfluidics[234-237] control and measurement of enzymatic activity[238-239] and mixing[240]. Most heating methods use external bulk heating sources such as macroscopic peltier elements[241-242] Joule (resistive) heating[243-245] lasers[246-247] and IR-mediated heating[248]. These approaches facilitate temperature regulation and heating for the whole microfluidic chip (i.e., large area). Therefore, the lack of localization, and the difficulty with integrating them on Lab-on-a-chip platforms, limits potential applications of heating manipulation on a single chip. In addition, the inertial effects of heating, as in the case of resistive or peltier heating, are not proper for droplet heating. When the heating element is switched on or off, the system has a long response time. For example, switching off of a resistive heater does not immediately stop heat release. Moreover, none of the mentioned heating techniques provide selective heating.

2.6.2 RATIONAL NEED FOR MICROWAVE HEATING

Microwave dielectric heating, on the other hand, provides many benefits and usefulness compared to conventional techniques. Microwave dielectric heating has the ability to selectively (i.e., only the target liquid heats up, like a droplet, and the other components do not get heated) and precisely control the temperatures of fluid volumes up to sub-nanoliters in microfluidics, and also offers enhanced thermocycling rates. Additionally, it offers a reduction in the reaction times because of the inertialess nature of microwave heating[249-250]. As well, most of the methods described above require physical contact between the heating surface and the fluid medium in order to deliver heat energy. On the contrary, microwave heating can be designed as contactless, and can directly provide volumetric delivery of heat.

2.7 MICROWAVE HEATING

2.7.1 PHYSICAL MECHANISM OF MICROWAVE DIELECTRIC HEATING

Microwave dielectric heating relies on the ability of a particular material to absorb energy and convert it into heat. Microwaves are electromagnetic waves which consist of an electric and a magnetic field component. The microwave frequency ranges from 0.3 to 300 GHz, corresponding to wavelengths of 1mm to 1m [251], and the range lies between infrared and radio frequencies. Microwaves are electromagnetic waves consisting magnetic and electric field components (see Figure 2.21)[252]. Heating is caused by the electric component of the electromagnetic field, and it has two main mechanisms: ionic conduction and dipolar polarization (see Figure 2.22). To be able to generate heat when exposed to microwave irradiation; a liquid must have a dipole moment. Under microwave frequencies, such dipoles align in the applied electric field. Since the field is oscillating with microwave frequency, the dipole field tries to realign itself with the alternating electric field. In this process, energy in the form of heat is lost through molecular friction and dielectric loss. Here, heat generation is affected by the ability of liquid molecules to align themselves with the frequency of the applied field.

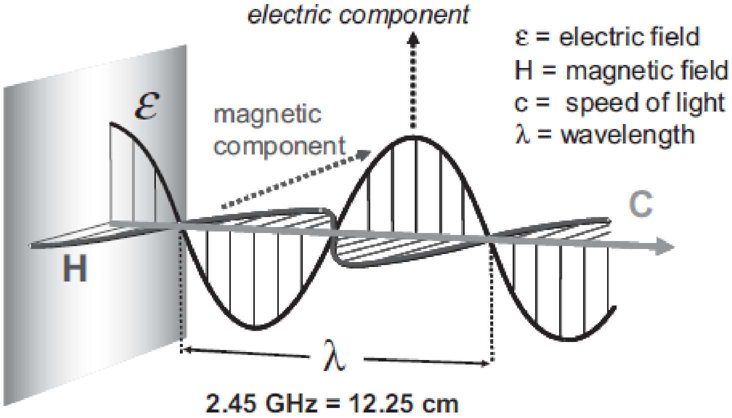

Figure 2.21. Electric and magnetic field components in microwaves[252].

If the frequency is too high, dipoles do not have enough time to realign. In contrast, if frequency is low, they reorient too quickly, and no heating occurs. As the dipole reorients to align itself with the electric field, the oscillating electric field forms a phase difference between the orientation of the dipole and the field. Thus, this phase difference results in energy being lost by collisions and molecular friction, and leads to dielectric heating. Namely, heat is generated by frictional forces arising between the polar molecules whose rotational velocity has been increased by coupling with the microwave irradiation. On the other hand, it should also be noted that gases cannot be heated under microwave irradiation since the distance between the rotating molecules is too far[251,253-254].

The second main heating mechanism is the ionic conduction mechanism (Figure 2.22). In this scenario, the dissolved charged particles in liquid oscillate back and forth under the microwave effect. They collide with their neighboring molecules, and heat is generated. If we compare two liquid examples containing the same amount of tap water and distilled water at a fixed microwave power, the tap water sample is heated more rapidly because of its ionic content. In general, the conductivity principle has a much stronger effect than the dipolar alignment and rotation mechanisms.

The dielectric properties of a liquid determine the microwave heating characteristics. The ability of a liquid to convert electromagnetic energy into heat, at a given frequency and temperature, is identified by its loss tangent, tan δ. Loss tangent is defined as tan $\delta = \varepsilon''/\varepsilon'$, where is the dielectric loss indicates the efficiency of electromagnetic energy converted into heat, and ε’ is the dielectric constant that shows the ability of the molecules to become polarized in the electric field. This means high tan δ is

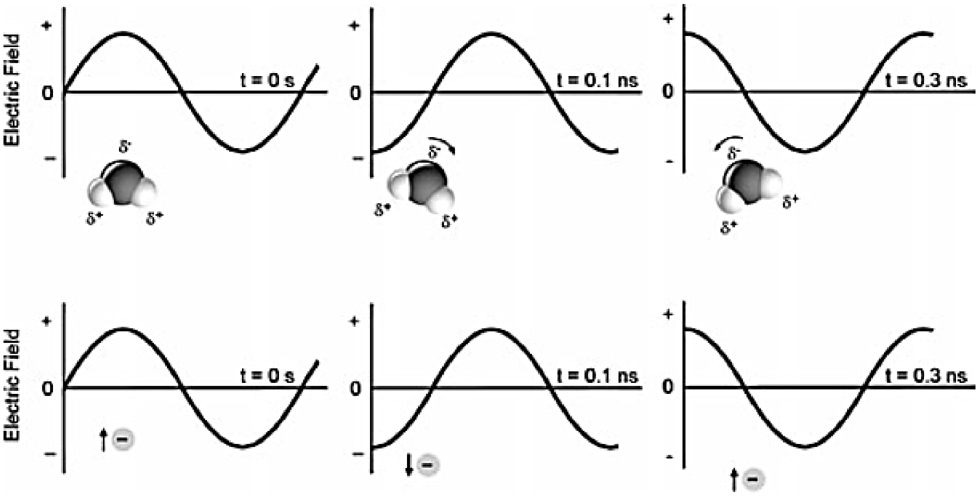

Figure 2.22. Dipolar polarization mechanism. Dipolar molecules try to align with an oscillating electric field (top). Ionic conduction mechanism. Ions in solution will move in the electric field (bottom)[251].

better for fast heating and energy absorption. However, liquids with a high dielectric constant do not automatically have a high loss tangent. For example, ethanol (ε’=24.3 at 25 °C) is heated much more rapidly than water (ε’=80.4 at 25 °C) because it has a higher loss tangent (ethanol tan δ=0.941, water tan δ=0.123). Also, it is important to note that the loss tangent is both a frequency and temperature dependent feature (see Figure 2.23)[252-254].

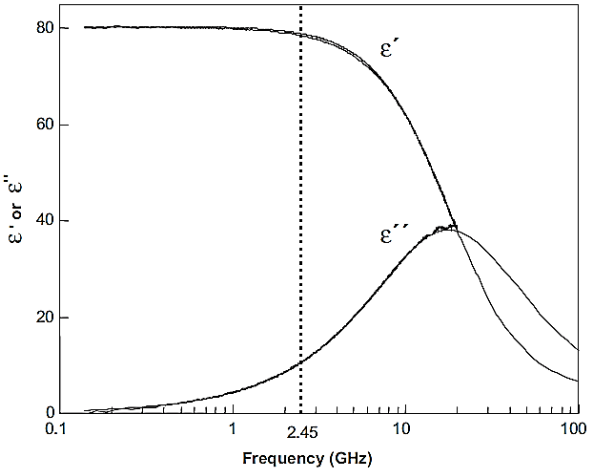

Figure 2.23. Dielectric properties of water as a function of frequency at 25 °C[252].

In addition, microwave power absorbed per unit volume in a dielectric material is given by:

$$P = \sigma \mathrm{E}^2 \qquad (13)$$

where

$$\sigma = 2\pi f \varepsilon_0 \varepsilon'' \qquad (14)$$

is the dielectric conductivity of the material, f is the frequency in Hz, ε_o is the permittivity of free space, ε" is the imaginary part of the complex permittivity of the material, and E is the electric field strength in V/m within the material. The ε" is given by:

$$\varepsilon'' = [(\varepsilon_s - \varepsilon_\infty)\omega\tau]/(1 + \omega^2\tau^2) \qquad (15)$$

where τ is the relaxation time, ω = 2πf is the angular frequency, ε_s is the static field permittivity, and ε_∞ is the optical domain permittivity at frequencies much greater than the relaxation frequency (1/τ)[255].

2.7.2 MICROWAVE DIELECTRIC HEATING IN MICROFLUIDICS

Only recently, microwave energy has been applied to microfluidics systems for utilizing heating purposes. Microwave power at several GHz is delivered to the channel by transmission lines integrated in the microfluidics device. In most cases, a coplanar waveguide configuration is used. Shah et al.[249] carried out a study where a microchannel fabricated in PDMS was aligned with a thin-film microwave transmission line in a coplanar waveguide (CPW) configuration. A schematic of the device is shown in Figure 2.24. The CPW was comprised of a 140 μm wide signal conductor separated by a 25 μm gap on either side from 300 μm wide ground conductors. The CPW conductors, 1.5 cm long, were formed by thermally evaporating Cr/Au (10 nm/500 nm) on a 0.5 mm thick glass wafer, and then using a standard lift-off metallization process. The device is characterized by the scattering (S) parameter and the temperature. The S-parameters are the transmission and reflection coefficients. The fluid temperature is obtained by measuring the temperature dependent fluorescence intensity of a dilute fluorophore, Rhodamine B that is added to the fluid. They observed a 0.88 ℃.mW^{-1} temperature rise at 12 GHz, and a 0.95 ℃.mW^{-1} temperature rise at 15 GHz. In a later study Shah et al.[256] described the on-chip microwave generation of spatial temperature gradients with a microstrip transmission line configuration. The transmission line was fabricated photo-lithographically on commercially available adhesive copper tape.

They achieved a nonlinear sinusoidally shaped gradient along a 7 mm distance. Temperature extremes of 31 ℃ and 53 ℃, at the minimum and maximum of the sinusoid, were established within 1 s. The sinusoid also produced a quasi-linear temperature gradient along a 2 mm distance with a slope of 7.3 ℃.mm^{-1}. Kempitiya et al.[257] demonstrated a microwave heating device via a copper transmission line in a microstrip configuration. They used a 130 μm copper strip line on top of a 1 mm thick polycarbonate substrate with a 2.3 mm diameter drilled well. Their test chamber volume corresponded to 4.1 μL. In their work, they achieved temperatures up to 72 ℃ with 400 mW power applied at the input of the transmission line. The microwave power reflection coefficient and temperature measurements were performed to characterize the power coupled to the chamber, and the rate of change in temperature. A recent and similar manner was reported by Marchiarullo et al.[250] for micro-chip based PCR (Figure 2.25). They controlled temperature by two ways; varying microwave power or frequency. This was an improvement upon their previous design, where the temperature was not sufficient for successful PCR thermal cycling. They controlled the PCR with a temperature program of 95 ℃ initial denaturation for 120 s, 95 ℃ denature for 15 s and 68 ℃ anneal for 30 s, and ended with a final extension at 72 ℃ for 120 s.

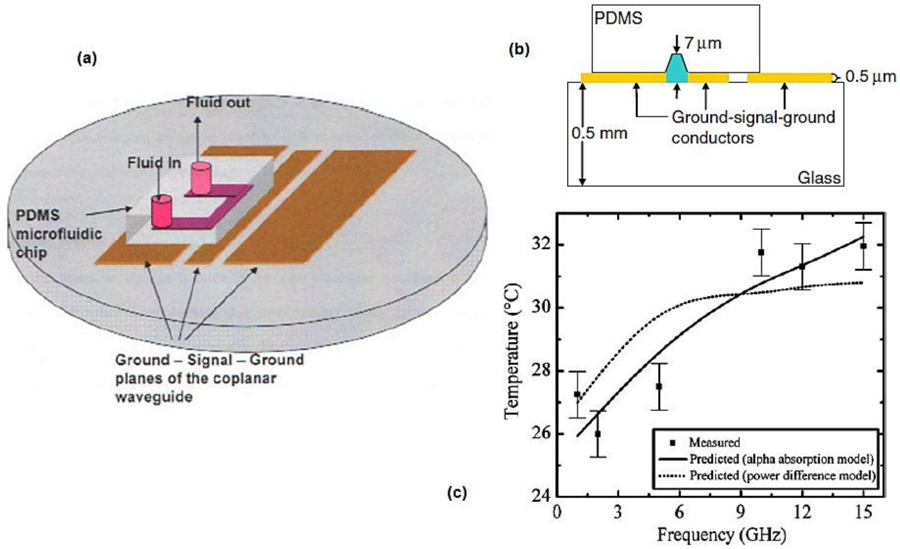

Figure 2.24. a) Schematic of coplanar waveguide coupled with the microchannel structure, (b) Typical dimensions, (c) Measured and predicted temperatures of an aqueous solution as a function of frequency[249],[255].

Shaw et al.[258] carried out a study on a microwave heating system in combination with air impingement cooling for performing PCR in a microfluidic device. The heating system with air impingement cooling provided rapid thermal cycling with heating and cooling rates of 65 ℃/s.

Within the context of droplet-based microfluidics, Issadore et al.[259] described the first experiment on microwave heating with droplets. Their design consisted of coplanar transmission lines. The metal electrodes are directly integrated into the PDMS device using a low-melt solder fill technique, which delivers microwave power, and the microfluidic device integrated a flow-focusing drop maker (Figure 2.26). The temperature change of the drops was measured by observing the temperature-dependent fluorescence of cadmium selenide nanocrystals dispersed in the drops.

Authors demonstrated characteristic heating times as 15 ms to steady-state temperature changes, and 30 ℃ above the base temperature of the microfluidic device. As a potential application of their work, the authors claim that, by setting the base temperature of the oil the device to 65 ℃, and appropriately setting the microwave power, a 30 ℃ change in temperature could cycle the temperature from 65 ℃ to 95 ℃, as required for PCR. However, in terms of microwave concept such parallel transmission line designs that the method is based on propagating wave on the transmission line, are not efficient for heating and sensing. In this scope, a newer heating sensor concept was developed by Boybay et al.[260].

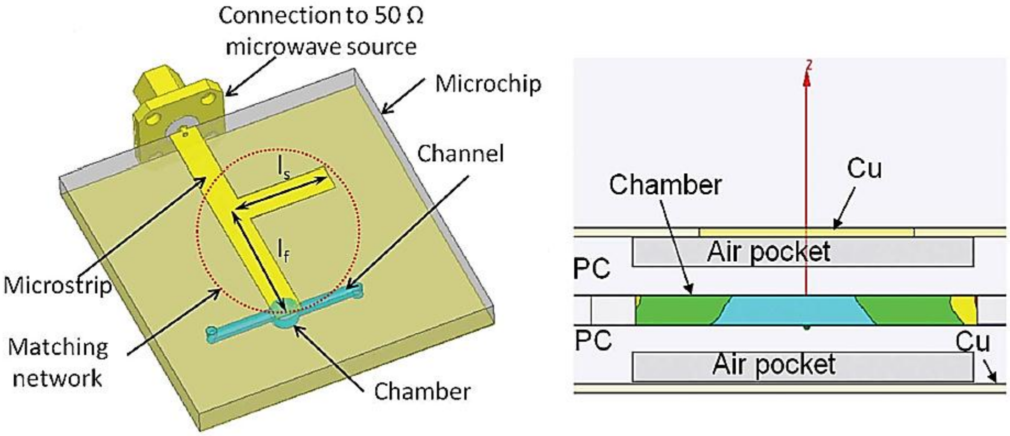

Figure 2.25. Device schematic and side view of chip with channels and air pockets [250].

In this approach, energy is stored into a resonator, and does not struggle with a propagating wave. Since there is no propagating wave, all energy is confined in a tiny capacitance region. This method is more efficient because in the Issadore et al.[259] method, depending on the transmission line length, energy is spread out.

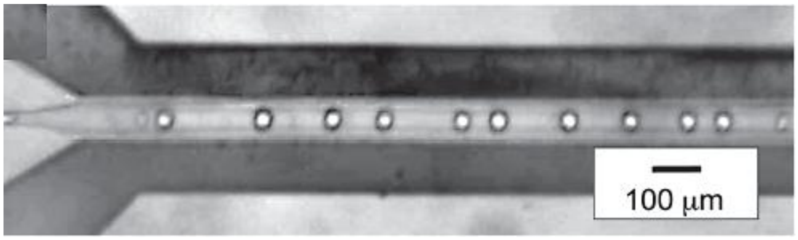

Figure 2.26. Microwave heater. The dark regions are the metal lines, and the gray region in the middle is the channel[259].

Consequently, different approaches have been attempted to perform heating tasks in microfluidics. The conventional methods are not promising for microfluidics in terms of integration with Lab-on-a-chip devices, portability and scalability. Particularly for droplet-based microfluidics, a higher throughput and efficiency are necessary functions. The inertial nature of conduction based heating methods are not compatible with droplet systems because the heating time is around 1-2s for these techniques and, even when the power is off, energy transport does not end immediately, which is contrary to microwave. Additionally, microwave heating requires less power consumption. On the other hand, in the scope of droplets microfluidics, efforts on the microwave heating of microfluidics are not suited well to droplets. This is due to the fact that droplet microfluidics would require selective and localized heating to heat up individual droplets, and would need to also integrate with other functionalities of Lab-on-a-chip tasks.

2.8 SUMMARY

This literature review has briefly discussed Lab-on-a-chip applications in the biomedical, chemical, pharmaceutical and medical fields. Then the fundamentals of two-phase flows in regards to droplet microfluidics were reviewed, followed by a discussion on droplet generation and droplet manipulation methods through active and passive means. Later, essential principles, applications and state-of-the-art studies of microwave sensing and heating were summarized, and the rational need for integration of microwaves was discussed. As related discussions under various sections have emphasized the need to develop robust, low-cost, scalable and integrated Lab-on-a-chip devices is significant. Adding new functionalities to microfluidics is, however, challenging, especially for high-throughput applications where doing so is more difficult. Most available methods are bulky with off-chip equipment, operate at too low throughput, are not easy to scale down, or are too expensive and complicated to incorporate in Lab-on-a-chip platforms. As well, such methods are not suitable with droplet microfluidic systems in terms of individual droplet heating and sensing, and cannot realize multiple functions at the same time. Thus, there is a clear need for miniaturized, portable, high-throughput and sensitive platforms for droplet based microfluidics, in particular for sensing and heating.

Chapter 3

METHODOLOGY, EQUIPMENT AND FABRICATION

This section explains fabrication protocols, experimental procedures and equipment used for the projects throughout the thesis study.

3.1 EXPERIMENTAL FACILITY

Experimental facility is comprised of several equipment and systems. Generally the system is designed as a combinations of the microfluidic chip integrated with the microwave sensor, a pressure system, syringe pumps, a microscope, a high-speed camera, a microwave signal generator, a vector network analyzer and the microwave custom circuitry (Figure 3.1).

Fluids are controlled using a microfluidic pressure controller system (Fluigent MFCS-8C) and/or syringe pump (Pump33, Harvard Apparatus). Fluids are connected to the device by ETFE (ethyltrifluoroethylene) tubing (Tefzel, Upchurch Scientific). Pressure system can control up to 8 output channels at the same time with a maximum pressure of 1bar and 0.5mbar accuracy. Water in oil (fluorocarbon oil FC40, Sigma Aldrich) droplets are generated using a T-junction or flow-focusing geometry for sensing and detection experiments. Droplets are manipulated through microfluidic channel network designs and by adjusting the pressure of the inlets. They are visualized using an inverted epifluorescence microscope system (Eclipse Ti, Nikon). The system mainly consists of programmable stage in 3D (x, y, z), objective nose piece, fluorescence turret and shutters. The properties of the objectives are (NA, working distance): 10x (0.3, 16mm), 20x (0.5, 2.1mm), 40x (0.75, 0.72mm). Filter cubes are provided for Rhodamine B (500-550nm ex, 565nm em) and Fluorescein (495nm ex, 505nm em) dyes. Illumination is provided by a 100 W halogen lamp for bright field applications and phase contrast and a 100W mercury halide lamp (Intensilight C-HGFIE, Nikon) for fluorescence applications. A high speed camera (Phantom v210, Vision Research) is used to record the microscopic images and videos. At full resolution (1280x800) the camera can take images at 2190 fps, with a 12 bit digital image quality. By lowering the resolution, or cropping the field of view, the camera can easily exceed 10k fps. All videos and images captured are analyzed with the image- processing program ImageJ (National Institute of Health, MD, USA) and validated with

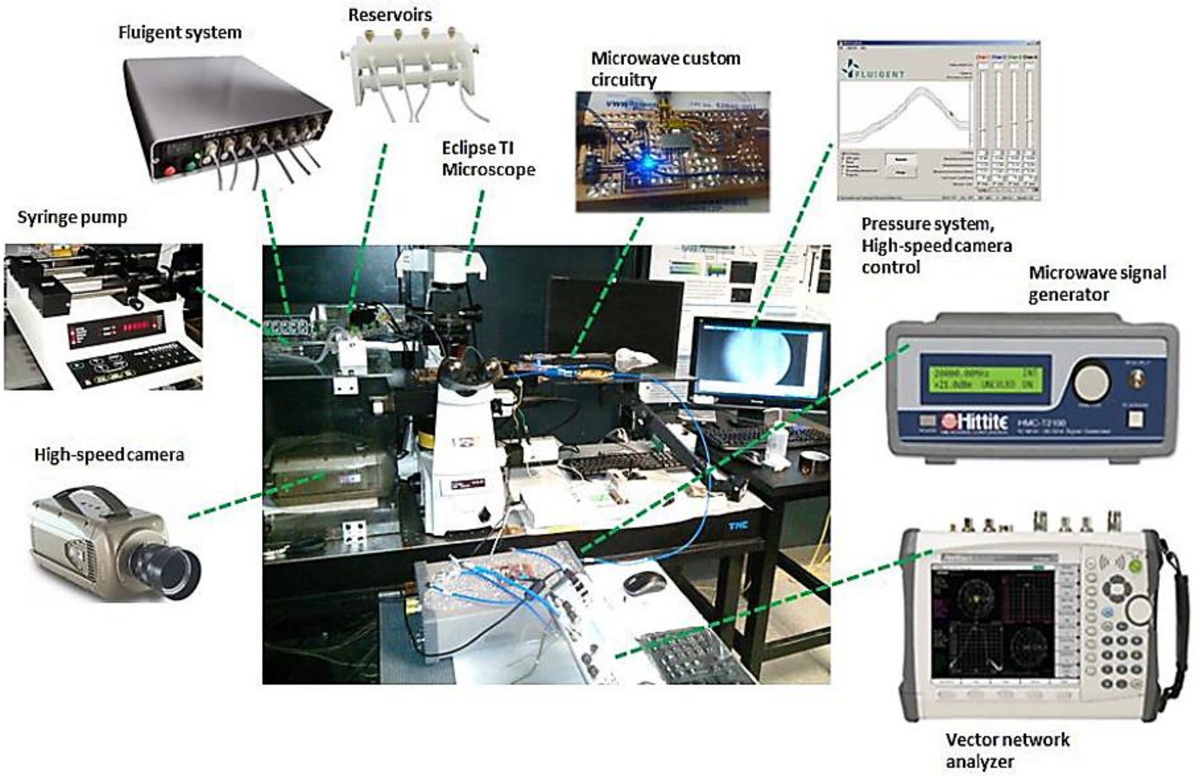

Figure 3.1 Experimental facility with components.

the results obtained by circuitry. A data acquisition device and Labview software (National Instruments) are used to control the system and create computer interface. Also, in order to measure ionic conductivity, a conductivity meter kit (Thermo Scientific, Orion 5-Star) is used after calibration of the probe with three different calibration solutions.

3.2 FLUIDS AND CHEMICALS

Generally as continuous phase FC-40 (Sigma Aldrich) oil is used, and in some occasions silicon oil with various viscosities (5 cSt, 25 cSt, 50 cSt and 100 cSt), hexadecane and mineral oil are used, too. As disperse phase ultrapure water, DI water and glycerol-water mixtures are used. However, for biological sensing and chemical synthesis experiments, bio-reagents and chemical compositions in aqueous droplets are used. These will be provided specifically in related chapters below. Span 80 and custom synthesized surfactants are employed when they are desired. And, dyes are used for the visualization purposes mixed into disperse and continuous phases when needed, such as fluorescein, ThS, ThT, Alexa Fluor 546, methylene blue, and fluorescent beads.

3.3 SOFT LITHOGRAPHY FOR MICROFLUIDIC CHIP FABRICATION

Microchannels are fabricated from PDMS using standard soft-lithography techniques. The PDMS is mixed in a 10:1 ratio of base to curing agent, degassed and molded against SU- 8/ silicon masters and then cured at 95 ^{0}C for 2 h. The molds are then cut out from the masters and fluidic access holes are made using a 500 mm biopsy punch. Both the finished microwave parts and the PDMS chip are then treated with oxygen plasma at 29.7 W, 500 mTorr for 30 s. The plasma treatment process renders the PDMS hydrophilic; however, for water in oil droplets, the PDMS channels should be hydrophobic to form droplets. For this purpose, a surface treatment process is applied that the walls of the microfluidic channels are coated with Aquapel (PPG Industries) to ensure that they are preferentially wet by the fluorocarbon oil. A microchannel with all four walls being hydrophobic, which is necessary for maintaining aqueous droplets in an oil-based continuous phase. A custom made surfactant that chemical structure is PFPE-PEG-PFPE (or Krytox-Jeffamine-Krytox, where Krytox has MW of 7500 and Jeffamine has MW of 900) is used to stabilize droplets. A descriptive process steps of the fabrication is described in Figure 3.2[32].

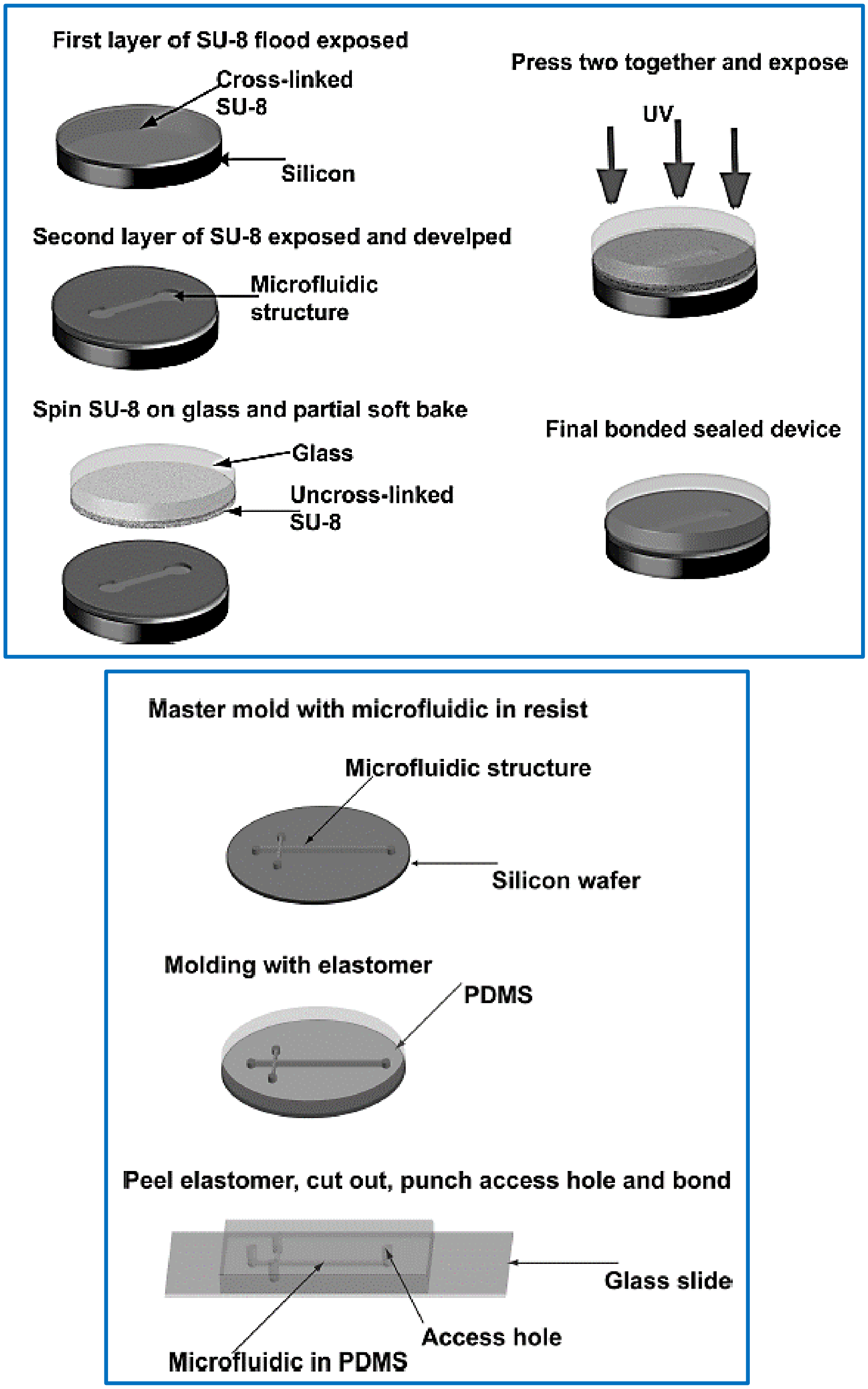

Figure 3.2 Fabrication of microfluidic networks in PDMS elastomer based on the soft-lithographic process[32].

3.4 SURFACE TREATMENT

Surface Treatment of PDMS/Glass Hybrid Microfluidic Chips for Biomaterial Droplet Generation

Objective

This report describes a general protocol for bonding of PDMS molds including microchannels inside to glass substrates, and the surface treatment of the channel walls for biomaterial droplet generation. This protocol can be implemented to generate droplets of biological content such as blood, milk, cell culture (e.g., fetal bovine serum) solutions and other related compositions.

Fabrication of Microfluidic Chips

Using standard soft-lithographic techniques Si-wafer masters and PDMS replica molds can be prepared. Adjustment of PDMS hardness can be employed by varying the curing agent ratio (e.g., 10:1, 9:1, etc.), which is acceptable by the protocol. Lower ratios such as 8:1 will create a harder PDMS while higher ratios a softer PDMS.

- After mixing PDMS and curing agent will trap bubbles in the PDMS that must be removed.
- About 30 min. in the vacuum oven, the bubbles must be removed, then PDMS should be poured on Si-master and put on 95 ºC hot plate for curing, i.e., at least 2 hours is recommended depending on PDMS mold thickness.
- Usually, 40 to 50 grams of total PDMS/curing agent mixture on aluminum tray used in the lab gives between 2.5 to 5 mm thicknesses.

Cleaning

- After PDMS mold is cured and cooled down, using a scalpel the mold should be cut in proper dimensions of the substrate to be used. Oversize of PDMS on substrate may cause weak bonding due to mechanical stresses while positioning and mounting on microscope. With the scalpel the excess PDMS should be trimmed off and cut into the desired shapes.
- Then the reservoirs must be punched with a proper biopsy punch diameter accordingly to the tubing will be used. This step will cause tiny pieces of PDMS inside the holes.
- First, use a smaller diameter of biopsy punch and check that holes are open and clean them.
- Second, blow compressed nitrogen into the holes.
- Third, spray isopropanol alcohol into punched holes and front and back side of PDMS completely, then again with compressed nitrogen dry it, and place into the plasma cleaner chamber.

- Later on, use two step cleaning with acetone and isopropanol alcohol in sequence to clean the glass substrate and dry with nitrogen and place into the plasma chamber.

Note: the channel (design) side of PDMS must be upside when it is placed into the chamber. Additionally, the whole PDMS mold cleaning with isopropanol is important that dust, particles or contaminants on it might cause inefficient bonding on the plasma and makes the chamber itself dirty over time. PDMS attracts dust and particles easily on its surface.

Bonding

- Once the substrate and PDMS are cleaned and placed into the plasma chamber, close the lid.
- Make sure that the two rotameter valves (oxygen and air) are closed.
- Turn on the pump and evacuate the chamber. Wait until the air inside is removed (e.g., until the gauge reaches 300mTorr).
- Open the oxygen valve and release oxygen approximately 16s, then slowly close the valve to adjust the pressure on the gauge about 500mTorr.
- When the pressure is stabilized, turn on the Plasma Cleaner to HIGH, and wait 2 min.
- After 2 min. turn off the plasma cleaner and the pump. And open the air valve to equalize the pressure in the chamber.
- Afterwards, quickly take the PDMS and substrate out of the chamber and put them in contact. (Please close the chamber lid again to keep inside clean all the time).
- To make the bonding strong, gently apply pressure to the hybrid glass/PDMS chip from sides and top to insure there is not any bubbles left in between glass and PDMS, and the channels are sealed.

Note: Once you are done using the plasma cleaner, make sure the two rotameter valves are closed. Then close the valve of the oxygen tank. Make sure the lid of the chamber is closed, too. In order to release the excess of oxygen inside the hose (the dark green hose), open the oxygen rotameter valve, temporarily, and release it. ***And, close the valve again.*** *The failure or forgetting this step will cause oxygen release to the room for the next person who uses the Plasma cleaner when he/she opens the oxygen tank valve.*

Surface Treatment

- Afterwards, introduce the surface treatment agent (Aquapel) into the channels. Injection is recommended through the continuous phase inlet. This can be done with a green or blue dispensing tips and a syringe.

- Do this step inside the fume hood, this is important and no exceptions, due to safety. Keep your face using the fume hood window that should be lowered down during the process.
- Count up 2 min. and later on with low pressure air, empty the channels from the chemical.
- Bake the chip for 1 min. on 95 ^{o}C.
- Then cool it down, it is recommended to come back to room temperature or at least below 30-35 ^{o}C, which makes the process efficient.
- After that introduce the chemical into channels for another 1 min., and blow air and clean the channels.
- Put on 95 ^{o}C hot plate for at least 30 min.
- Cool the chip down, inject oil and wait until the channels swollen well.
- You now have a complete microfluidic chip ready to generate droplets.

Note: After using the chemical (Aquapel) properly dispose the dispensing tip to the chemical waste container. Then, fill the rest of bottle with nitrogen and tightly close since it is sensitive to air.

3.5 MICROWAVE SENSOR FABRICATION

The electrical traces for the microwave components are fabricated using a combination of photolithography and electroplating. The positive photoresist, S1813 (Rohm-Haas), is spin coated at 1500 rpm for 60 s onto the 50 nm thick copper film (EMF Corporation) that is pre-deposited on a glass slide and then baked at 95 ^{0}C for 120 s. The resonator design is patterned into the photoresist via UV lithography and subsequently developed with the developer, MF-319 (Rohm- Haas) for 2 min. The patterned slide is then immersed in an acidic copper electroplating solution (0.2 M CuSO4, 0.1 M H3BO3, and 0.1 M H2SO4) and electroplated at 2 mA for 4 min and then 7 mA and for 20 min. as illustrated in Figure 3.3. After electroplating, the photoresist is removed with acetone leaving an electroplated copper film approximately 5 mm thick. Next, the original base layer of copper is removed by etching with dilute ferric chloride (MG Chemicals). A passivation layer of a PDMS (Sylgard 184, Dow Corning) and toluene (1:1 (w/w) PDMS/toluene) mixture was spin-coated at 4000 rpm for 60 s followed by 1hr curing at 95 ^{0}C to protect the electrical traces. A subminiature version A (SMA) connector (Tab Contact, Johnson Components) is then soldered to the electrodes of the microwave components to provide an external connection to the microwave circuitry. Completed microfluidic chip with the microwave sensor is shown in Figure 3.4.

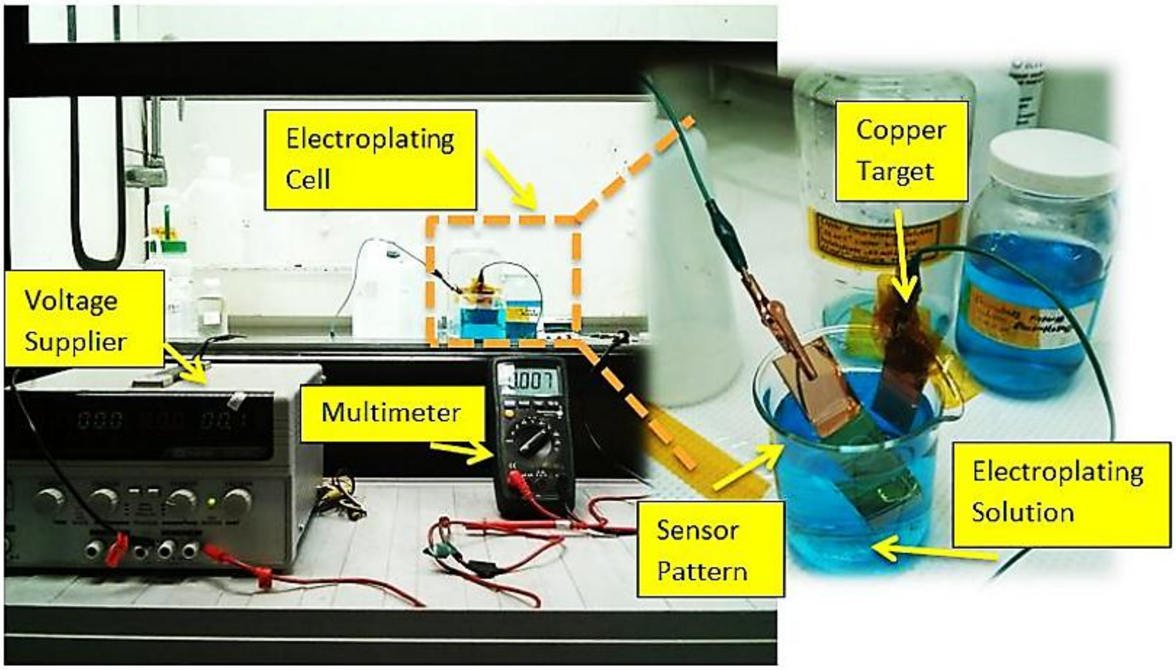

Figure 3.3 Electroplating process and resonator (sensor) fabrication.

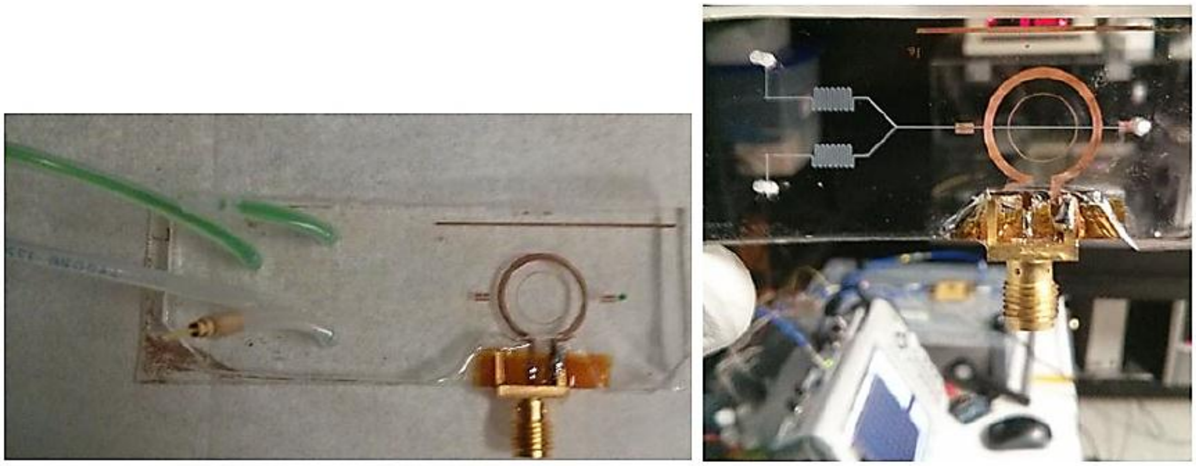

Figure 3.4 Completed microfluidic chip, microchannels with the microwave sensor.

3.6 GOLD SENSOR FABRICATION FOR DNA HYBRIDIZATION

The copper electroplating protocol is slightly changed for the fabrication of gold microwave sensors. In this case, instead of using a copper target, gold electroplating solution is used to provide the source of the deposition material, and niobium anode is used. The solution temperature is set to 60 °C, while a magnetic mixer is stirring the gold electroplating solution. Figure 3.5. shows a representative picture for gold microwave sensor fabrication, and Figure 3.6 demonstrates the steps of photoresist coating, gold and chrome etching, and the gold plating.

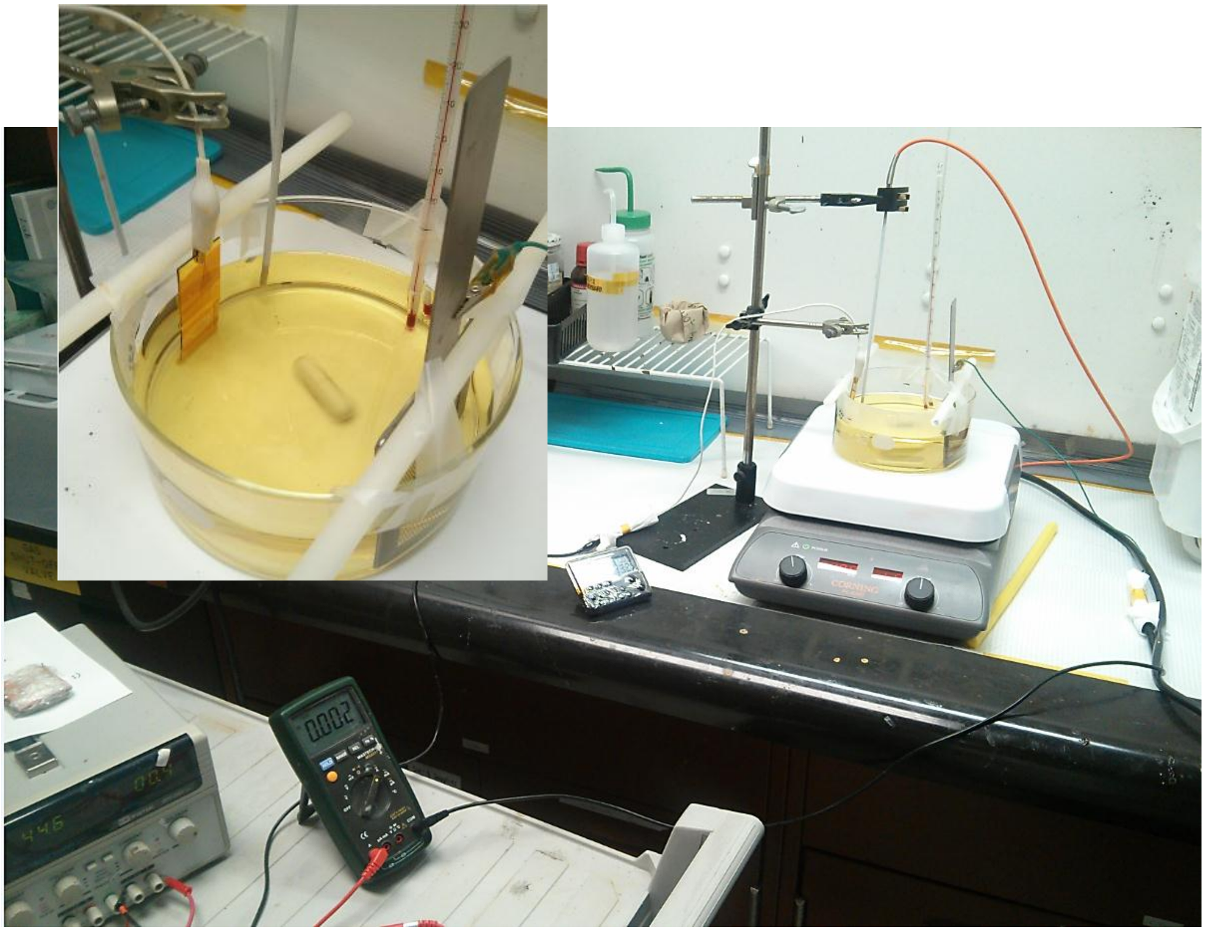

Figure 3.5 Representative picture of gold electroplating setup.

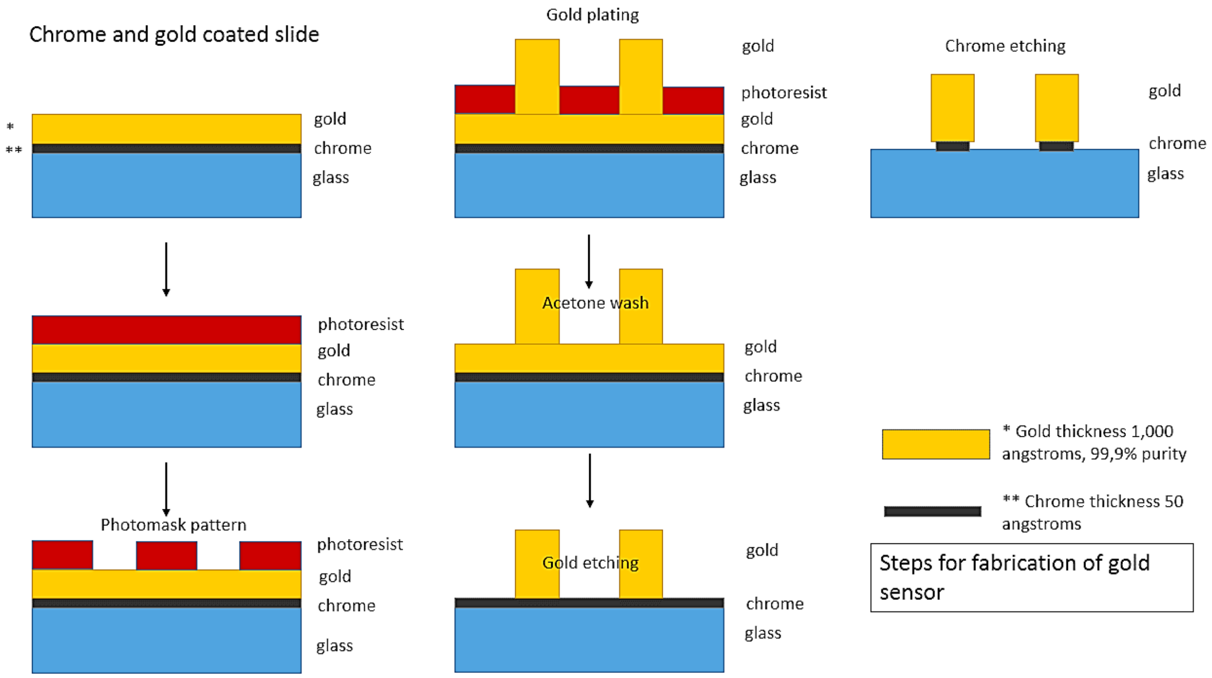

Figure 3.6 Steps for fabrication of gold sensors.

Chapter 4

LABEL-FREE, HIGH-THROUGHPUT DROPLET DETECTION AND CONTENT SENSING[1]

4.1 MOTIVATION

In recent years, there has been growing interest in droplet-based microfluidics because of its promise to facilitate a broad range of scientific research and biological/chemical processes. Potential applications can be found in many areas such as cell analysis[186,261-263] DNA hybridization[264], detection of bioassays[265], bio-reactions[266-268] drug screening[269] and diagnostics[270-271]. Major advantages of droplet-based microfluidics versus traditional bioassays include its capability to

---

[1] The contents of this chapter have been previously published in Lab on a Chip (RSC) 15, 4008–4019 (2015), by Yesiloz G., Boybay M.S. and Ren C.L., as “Label-free High-throughput Detection and Content Sensing of Individual Droplets in Microfluidic Systems”. The paper was selected as back cover of the issue. G.Y. developed the methodology, designed and executed experiments; G.Y. and M.S.B. built up the system; G.Y., M.S.B. and C.L.R. worked on the idea formation; G.Y., M.S.B. and C.L.R. contributed to the paper writing.

provide highly uniformed, well-isolated environment for reactions with orders of magnitude higher throughput (i.e. kHz). Most droplet-based microfluidic studies rely on high-speed imaging[169,272-275] to provide details of droplet generation and transport, which usually require expensive and bulky high-speed camera, and exhaustive post imaging analysis. In addition, in order to differentiate subtle differences in droplet content, fluorescent imaging is often used which, however, tends to lower down the throughput because longer residence time is needed for the droplet to stay in the field of view in order to obtain sufficiently high fluorescent intensity. Although this can be improved by using a pulse solid state laser that is synchronized with the camera, which further complicates the system due to the need for precise alignment and fluorescent labelling.

In contrast, electrical techniques allow the miniaturization of multiple sensor arrays and their integration into one single microfluidic chip with low power requirement. Of these capacitive, electrochemical and impedance based electrical detection methods are widely available. In electrochemical detection, the measurements are based on the interactions between analytes and electrodes or probes that usually occur in an electrolytic cell. They are not able to distinguish analytes that are not electroactive[170,276-277]. In addition, the detection electrodes are sensitive to variations in temperature, ionic concentration and pH that affect the shelf life of the sensor and shift electrodes' response requiring frequent calibration[276-279]. Conventional capacitive and impedance detection approaches operate at low frequencies, which causes either low signal-to-noise ratio or long response time and thus limit their applications to droplet microfluidics where droplets are generated at high frequencies. For example, the throughput achieved by a capacitive sensor[184] for droplet detection was up to 90 Hz with reasonable sensitivity and for an electrical impedance-based detection[280] around 10.

Microwave technology, as a versatile non-optical method, has the potential to address the above issues because it eliminates the need for chemical modification or physical intrusion of the sample and operates at high frequencies (i.e. GHz). It differentiates materials based on their electrical properties including electrical conductivity and/or dielectric constant. In a previous attempt it was demonstrated that a microwave sensor that can be integrated with microfluidic devices to differentiate single phase fluids in microchannels and detect the presence of droplets at a very low frequency (i.e. up to 1.25 Hz) [260]. The low detection frequency was mainly restricted by the response time of the vector network analyzer (VNA). In addition, the sensing of droplet content was not achieved because insufficient sampling of droplets did not allow the accurate determination of the time for the droplet to arrive at the capacitive gap, neither differentiation of the content changes[260]. Also, in order to get a reliable reading by the microwave sensor, the effect of droplet geometry on sensing performance must be eliminated, and the sensitivity of the microwave sensor must be sufficiently high to detect subtle variations.

In this regard, the thesis starts with designing and developing a sensitive, low-cost, portable microwave circuitry suitable for detection of droplet presence and label-free sensing of individual droplet content in microfluidic devices at high-throughput. More importantly, for future point-of-care application purposes, the choices of cost-effective off-the-shelf components for developing the circuitry is considered. The circuitry that consists of surface mount components is able to generate microwave signal and measure the response of the sensor (reflection coefficient of the sensor) in a very fast manner. It is validated that the system has a detection limit of several kilohertz (kHz) itself, and in the experiments, over 3 kHz is reached. This microfluidic-microwave system might potentially be used as a coulter counter and content analysis in many Lab-on-a-chip applications.

4.2 SYSTEM OVERVIEW

The system illustrated by the schematic description in Figure 4.1[281] (please see Figure 4.2 for the entire experimental setup and assembled module of the microwave custom circuitry) consists of a microfluidic chip integrated with a microwave sensor, a pumping unit which could be a pressure controller (Fluigent MFCS-8C) or a syringe pump (Pump33, Harvard Apparatus) depending on the particular study case, an inverted microscope (Eclipse Ti, Nikon) mounted with a high-speed camera (Phantom v210, Vision Research) and the developed microwave custom circuitry. Fluid reservoirs are connected to the microfluidic chip via ethyltrifluoroethylene (ETFE) tubing and connectors (Tefzel, Upchurch Scientific). Two slightly modified configurations (simple flow focusing and double T-junction) were used for droplet generation. For the detection of droplet presence, the simple flow focusing geometry was used while for the sensing of droplet content, the double T-junction geometry was used where droplets with different contents were alternatively generated by the two T-junctions. Droplet generation and transport were manipulated through the microfluidic channel network design by adjusting the pressures of the inlets or the pumping flow rate of the syringe pump. The high speed camera was used to record microscopic images and videos through the image processing program ImageJ (National Institute of Health, MD, USA) which were also used to validate the experimental results obtained through the developed circuitry. A data acquisition device and Labview software (National Instruments) were used to control the system and set off the computer interface.

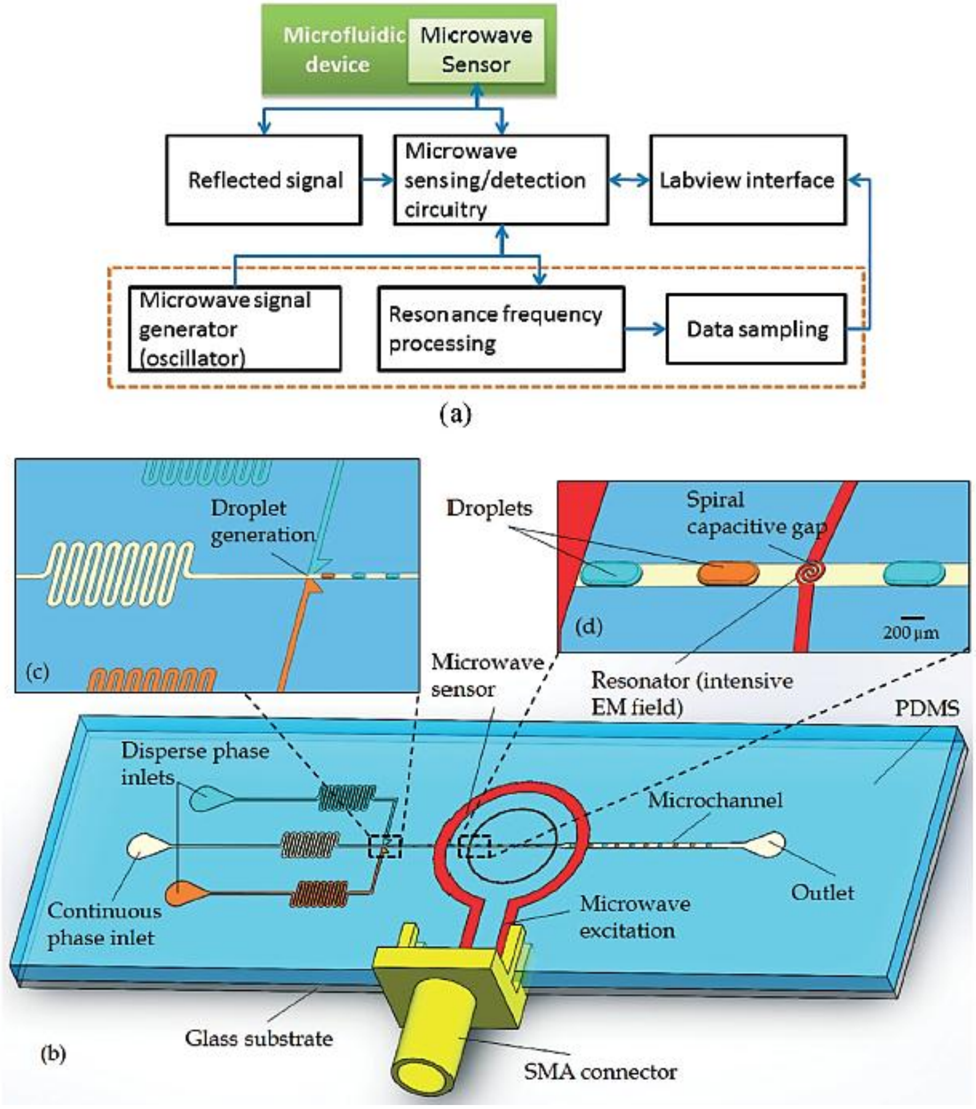

Figure 4.1 Schematic description of the microwave-microfluidics integrated device, (b) schematic of microwave sensor with a spiral resonator design and an excitation loop, (c) and (d) a closer view of droplet formation channels and spiral capacitive gap, respectively[281].

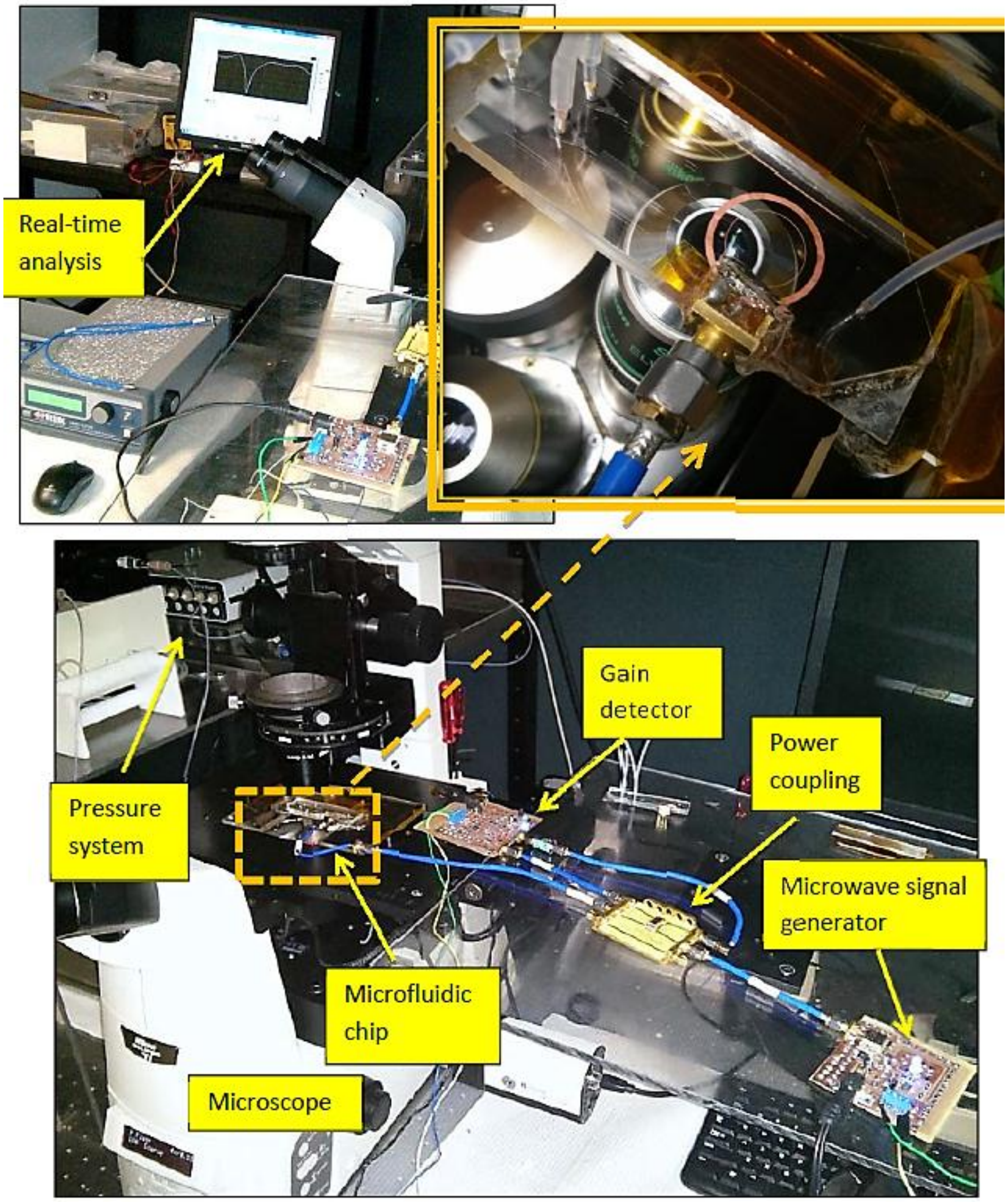

Figure 4.2 Experimental setup and assembled module of the microwave custom circuitry, which includes gain detector, power coupling and microwave signal generator units.

4.3 MATERIALS

Fluorinated oil (FC40 from Sigma-Aldrich) with a 2% custom-made surfactant are used as the continuous phase. The surfactant has a chemical structure of PFPE-PEG-PFPE (or Krytox-Jeffamine-Krytox, where Krytox has a molecular weight of 7500 and Jeffamine 900). D-(+)-Glucose (Sigma-Aldrich) and potassium chloride (EMD Millipore) solutions are prepared in ultra-pure water. Penicillin-Streptomycin-Neomycin antibiotic mixture (containing 5,000 units penicillin, 5 mg streptomycin and 10 mg neomycin/mL), Fetal Bovine Serum (FBS; Sigma-Aldrich) and milk (contains 2%MF) are used in the sensing of droplet content without further purification or dilution. For Alzheimer's disease (AD) tests tau-derived hexapeptide (AcPHF6) are obtained from Celtek Peptides, which is used to model the tau-protein aggregation related to AD. The assay is carried out with orange G, which is a known inhibitor to the tau-protein aggregation (Sigma-Aldrich). AcPHF6 is prepared in ultrapure water at a concentration of 2.5mg/ml as stock solution, and diluted to a final concentration of 0.316 mM. All other solutions are prepared in morpholinepropanesulfonic acid (MOPS) buffer with 0.01% NaN3 and adjusted to pH 7.2, and with assay grade DMSO at 1% (v/v).

4.4 THE MICROWAVE SENSOR AND WORKING PRINCIPLE

The designed microwave sensor works essentially as a resonator. The sensor structure is made of two concentric copper loops similar to the one presented previously[260]. Microwave signal is excited by the outer coplanar transmission line loop, which supplies a time-varying oscillating current circulating around the loop and a magnetic field passing through the loop. The inner loop with a small gap constructs the resonator and the microchannel where droplets are passing through is aligned on top of this gap. When materials with different electrical properties (permittivity, conductivity) pass by the gap region, the capacitance of the gap changes and the resonance frequency shifts which can be used to characterize the materials. Take water-in-oil emulsion as an example, water droplets have a much higher dielectric constant (~80) than the carrier fluid, oil (~2-3). When a water droplet passes by the resonator, the resonance frequency will be shifted which can be used to detect droplet's presence. Similarly, when droplets with different materials pass by the resonator, the magnitude of shift in the resonance frequency can be used to characterize the droplet content. The resonance frequency shift caused by a perturbation in the permittivity of the medium is described by[194].

$$\frac{\Delta f}{f} = \frac{-\int \Delta\varepsilon \vec{E}.\overrightarrow{Eo}dv}{\int(\varepsilon\vec{E}.\overrightarrow{Eo} + \overrightarrow{\mu H}.\overrightarrow{Ho})dv} \qquad (1)$$

where E_0 and E are the electric fields before and after the perturbation, H_0 and H are the magnetic fields before and after the perturbation, f is the resonance frequency before the perturbation, ε is the permittivity of the medium and μ is the permeability of the medium. In this study, a spiral-shaped capacitive region is designed for sensing purposes because it allows the system to operate at lower frequencies compared to T-shaped designs[260], which thus allows inexpensive off-the-shelf components to be chosen for the circuitry design.

4.5 FABRICATION

The microfluidic chip consists of two main components, a glass base with the microwave components and a polydimethylsiloxane (PDMS) mold with the designed microchannels for droplet generation and transport, which are fabricated separately and then bonded together. Thus, the device fabrication consists of two stages: microchannel and microwave component fabrication. Details of the fabrication protocols can be found in Chapter 3.

4.6 MICROWAVE CUSTOM CIRCUITRY

Vector Network Analyzers (VNAs) are widespread tools for microwave characterization due to their accuracy and user-friendly interface. However, VNAs are expensive normally which has driven the development of inexpensive alternatives[282],[283],[284]. Regular VNAs have limitations on the data sampling rate and thus throughput which only allowed a very low throughput (i.e. up to 1.25 Hz for droplet detection). Another major disadvantage of such bulky benchtop setups is their size which makes it difficult to be widely applied for point-of-care applications. In this regard, it is necessary to develop portable yet affordable microwave circuitries that have comparable accuracy and sensitivity as commercially available VNAs. In this study, such a microwave circuitry for label-free detection and content sensing of droplets in microfluidic devices is developed. Considering the microwave structure used in detecting and sensing droplets, a microwave circuit that measures the reflection coefficient from a one port network is designed since the change in the resonance frequency can be monitored in the reflection coefficient. The microwave circuitry is mainly composed of three sub-systems: i) signal generator, ii) power coupling unit, and iii) gain detector as shown in Figure 4.3.

4.6.1 MICROWAVE SIGNAL GENERATOR

This subsystem consists of a voltage controlled oscillator (VCO) (Mini-Circuits, ROS-2350-519+), a voltage regulator (Rohm Semiconductor, BA17805FP-E2), a data acquisition system (DAQ) (National Instruments), an op-amp (Texas Instruments, LM358DR), and a power supply (24V battery) that supplies voltage to the op-amp and voltage regulator. The VCO provides the required microwave frequency by converting the input analog voltage, which consists of two components: one voltage source provided by the 24V power supply but regulated by the voltage regulator to the maximum of 5V and the other by the DAQ (0 - 10V) for tuning purposes. Tuning voltages are amplified by the op-amp with a gain factor of 2. The total amplified voltage ranging between 0 to 20V controls the tuning voltage of the VCO which is measured by the DAQ and LabView program and characterized by a spectrum analyzer (Agilent, E4440A). Serial capacitors are used in order to reduce the parasitic effects and filter the signal for the op-amp and VCO input. The microwave signal generator subsystem facilitates the sweeping over the desired frequency range (1.9 GHz to 2.6 GHz). We designed the sensor operating below 3 GHz at which the corresponding microwave components are widely available and inexpensive that allow the total cost of the electronic components below $200. Wider frequency ranges can be achieved by adjusting the tuning voltage of the VCO.

4.6.2 POWER COUPLING

The primary function of the power coupling unit is to provide proper microwave signals to the sensor and the gain detector which would require careful isolation of signals without sacrificing the useful power. The high operating frequency at the GHz range brings in more challenges in the design and fabrication of the microwave components. First, the impedance of the transmission lines in the printed circuit board must match to the characteristic impedance of 50 Ω because any mismatch between the transmission line traces causes reflections and reduces the performance[282]. For this purpose, 0.79 mm thick FR-4 PCB material (ε=4.34) is used and microstrip impedances are carefully calculated

Considering the trace width, thickness and substrate height. The copper ground (at the bottom of the PCB) and ground planes (on the top of the PCB) are connected with vias closer to 1/20th λ where λ is the wavelength of the signal flowing through it to reduce noise[285]. In order to minimize parasitic coupling to the transmission lines, separations between the ground planes and all other traces are designed to be at least three times larger than the substrate thickness. Second, reflections between different components must be controlled well which include the reflection from the attenuator, VCO, and directional coupler, to the microwave sensor which is connected to the circuitry through coaxial

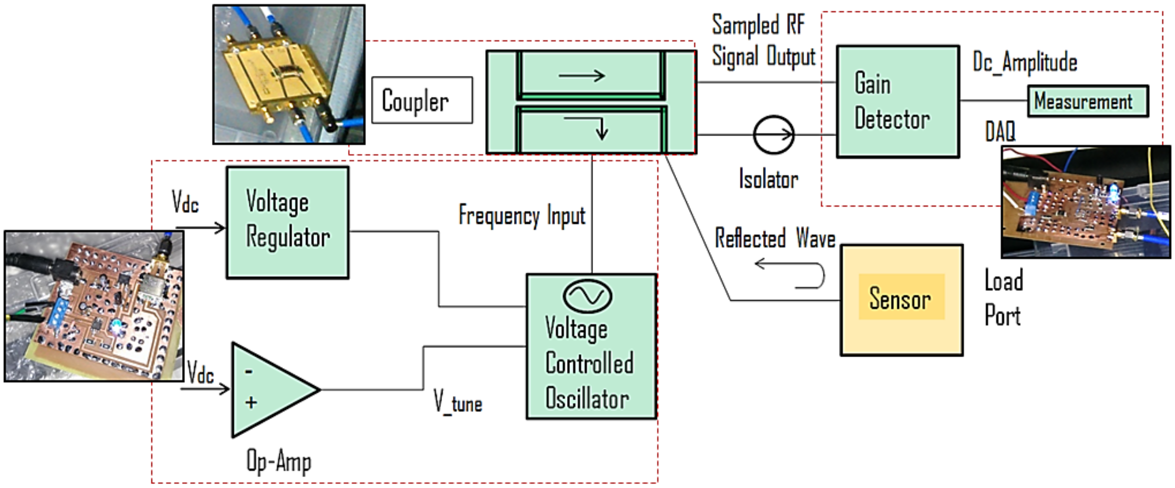

Figure 4.3 Schematic description of the microwave circuitry.

cables, and that from the microwave sensor back to the VCO which have disturbing effects on robust frequency generation. The above concerns are taken into consideration in the design of the power coupling and isolator subsystem. Specifically, a high directivity bi- directional coupler (Mini-Circuits, SYBD-16-272HP+) with 16 dB coupling is used to regulate microwave power to the resonator. Additionally, a 20 dB resistive attenuator is used as an isolator network which is chosen to isolate the reflected signal because of the mismatch of the sensor while not reducing the useful power significantly.

4.6.3 GAIN DETECTOR

An integrated circuit (Analog Devices, AD8302) is employed in the gain detection subsystem, which communicates with the microwave sensor and the power-coupling unit. The signal traveling from the signal generator is coupled by the bi-directional coupler to the gain detector as a reference signal and to the resonator, which is aligned with microchannel. Then the gain detector enables the amplitude and phase difference between the signal reflected from the sensor and the reference signal to be measured which is described by the reflection coefficient.

$$RL = \frac{Reflected\ Voltage}{Incident\ Voltage} = \frac{(Z_R - Z_0)}{(Z_R + Z_0)} \qquad (2)$$

where Z_R is the frequency dependent input impedance of the device presented in Figure 4.1(b) that includes the resonator and the excitation structure and Z_0 is the characteristic impedance of the transmission line used for feeding the structure. The gain detector converts the microwave signals to

DC signal, and this magnitude ratio of electronic signal is post-processed and used to relate nanoliter-sized droplet detection and sensing of its content. For example, if different materials pass by the sensor, the reflected signal would be different even though the incident voltage would be the same which can be used for detection and sensing of materials. The system is able to detect ac-coupled input signals from -60 dBm to 0 dBm. The output reflection coefficient range can be accurately measured between -30 dB to +30 dB which is scaled to 30mV/dB. The system is also able to measure the phase over a range of 0 °–180 °. The minimum and maximum levels of the detection limits are characterized by the limit that each individual log amp can detect as well as the finite directivity of the coupler.

The LabVIEW program is used as an interface to collect and convert the measurement data, and control the system real time. Meanwhile, a calibration algorithm is used to correlate the measured data readings of the gain detector to the reflection coefficient of the microwave sensor which carry the information of the physical droplet system.

4.7 EXPERIMENTAL RESULTS AND DISCUSSION

4.7.1 CHARACTERIZATION OF MICROWAVE CIRCUITRY

Prior to the droplet detection and sensing using the developed microwave circuitry, its sensitivity and accuracy is first evaluated by comparing its measurement results with that obtained using a commercial VNA (MS2028C, Anritsu). Table 1 below shows the comparison of the measured resonance frequencies for FC-40 (ε=1.9), air (ε=1), and water (ε=78.54) between the custom-made circuitry and VNA. The developed microwave circuitry has very similar performance to the commercial VNA with the maximum difference of 1.283% found for water.

Table 4.1 Comparison of the resonance frequencies between custom microwave design and the VNA.

Material (Liquid)	**f@S_{11} min using VNA (MHz)**	**f@S_{11} min using Custom Design (MHz)**	**Variation Percentage (%)**
Air	2588	2580	0.309
FC-40	2582	2573	0.349
Water	2417	2386	1.283

Then the detection and counting function of the developed circuitry was thoroughly evaluated by measuring the reflection coefficient of the resonator for various fluids in microchannels as a function of frequency. In order to prevent potential contamination caused by the residual of the previous sample; the microchannels were primed with the solution to be tested for at least 15 min prior to each test, and flushed with oil for 10 min. The tubing was cleaned twice before measurements by purging air and then with isopropanol.

As shown in Figure 4.4, the circuitry is able to differentiate between fluids with permittivity effects dominant (Figure 4.4a) and conductivity effects dominant (Figure 4.4b). Different concentrations of D-(+)-Glucose and potassium chloride solutions (KCl) were prepared with ultra-pure water. The minimum assessed concentration is 0.001 g/ml for KCl and 0.01 g/ml for glucose. The frequency step size was 0.1 MHz in the analysis. The lower detection limit was achieved for the KCl solutions because of the combined effects of permittivity and ionic conductivity (dominant effect). For example, the conductivity of potassium chloride increase from 17.84 mS/cm to 60.8 mS/cm when its concentration increases from 0.01g/ml to 0.05 g/ml, which were experimentally measured using a conductivity meter kit (Thermo Scientific, Orion 5-Star) after calibration of the probe with three different calibration solutions. While increasing KCl concentration causes a decrease in the resonance frequency, increase in the glucose concentration results in higher resonance frequencies. As well, concentration changes cause sharp decline in the reflection coefficient (S_{11}) so that the change in resonance frequency can be monitored in the reflection coefficient. The differentiation of fluids with small differences in electrical properties validated the dynamic performance of the customized microwave circuitry along with the microwave sensor integrated with the microchannels.

4.7.2 HIGH-THROUGHPUT DROPLET DETECTION

The performance of the microwave circuitry for droplet detection and counting is performed using a flow focusing generator as shown in Figure 4.5. The channel height is 50 µm and assumed to be uniform across the entire chip. The channel width smoothly narrows down from 300 µm to 80 µm at the intersection which is the same as that of the dispersed phase for generating droplet stably. The wider channels were designed to lower down the hydrodynamic resistance for easy pumping while the uniform channel widths near the generator is the most stable design for droplet generation[71]. Initially, the droplet generation and transport were visualized and characterized with the optical microscope (Eclipse Ti, Nikon) integrated with a high speed camera which captured images at a frame rate of 9000 fps. Figure 4.5 (a) shows the image of the generator and generated droplets which

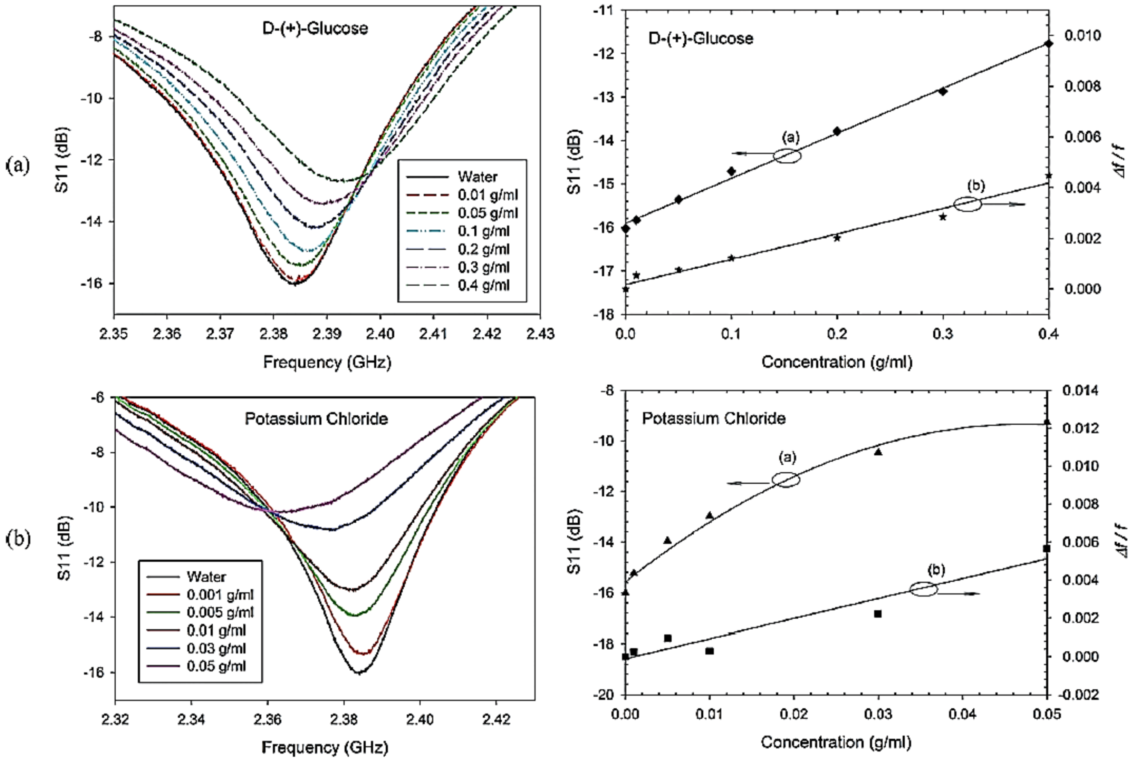

Figure 4.4 Reflection coefficient of the resonator for a series of glucose–water (a) and KCl–water (b) mixtures for testing the circuitry.

are around 1nl considering the droplets are fully confined by the channel (50um high, 80um wide) with a length varying from 1~3 channel widths (80um ~ 240um). Figure 4.5 (b) compares the droplet generation frequencies measured by the optical imaging and microwave sensor. When a droplet passes the capacitive region (gap) of the resonator, the electromagnetic field is disturbed by the presence of the droplet and the dielectric change (from the oil phase to the aqueous droplet phase) causes a peak in the collected signal. The perturbation in the EM field can be used to determine the droplet generation frequency by counting the number of the perturbations over a specific time period. As shown in Figure 4.5 (c), the signal peaks correspond to droplet presence while the valleys correspond to the carrier fluid (oil). The resonator was operated at 2.59 GHz which was the resonance frequency for FC40 oil, and at this frequency the signal change in reflection coefficient is used to determine the droplet presence. It is worthy to mention that the sinusoidal look of peaks at very high droplet formation frequencies is caused by shorter and unstable droplet spacing which are likely due to the use of syringe pump which cause unpredictable uncertainties[71]. Due to the limitation of the maximum pressure that the pressure controller can provide which limits the throughput of droplet generation, a syringe pump was used in order to evaluate the detection performance of the microwave system. With carefully cleaning and preparation of microfluidic chips we reached as high flow rates as 4000 µl/hr for water and 4750 µl/hr for the continuous phase (i.e. oil). Correspondingly, we were able to generate droplets at the maximum rate of 3.33 kHz which can be detected with the microwave system successfully. Further high frequencies can be achieved by increasing the flow rate, which however tends to break chip made of PDMS[286].

Ideally, in order to detect a droplet, at least one signal level needs to be sampled from carrier fluid and one from dispersed (droplet) phase. This will result to give a minimum and a maximum value, and maximum detection limit can be estimated to be the half of the signal generation rate provided that the data sampling rate of the system is equal or larger than signal generation rate. In our system, since the signal generation frequency is at microwave range (i.e., GHz), which is extremely higher than data sampling that the data sampling rate basically determines the maximum detectable limit. However, since the droplet spacing is low in our very high droplet generation frequencies because of the droplet generation limitations explained above, the collected data gives a sinusoidal look. For a clearly resolved droplet detection data for very high-throughput scenarios, the droplet spacing should be at least one droplet length or higher. Here, with a data sampling rate of 10 µs and well-spaced droplets, the theoretical droplet detection limit of the developed microwave system is 50 kHz.

Over a period of ten minutes, two million droplets were counted without missing any droplet. In order to assess the minimum sensible dielectric variation for detectable droplets, it is important to evaluate the resolution of the circuitry. An RMS noise level of 0.78 mV has been calculated over an interrogation time of 20 s. With this noise level, a resolution threshold of 0.026 dB in reflection coefficient was obtained. Since a resonant microwave sensor is designed and used in the study, electromagnetic energy into small region is accumulated, which is extremely sensitive to small changes. Likewise, utilizing the characteristic feature of microwaves, i.e., operation at GHz frequencies, allows working at shorter time scales. This gives a great opportunity and advantages over other detection techniques such as capacitive and electrochemical which operate at lower frequencies.

4.7.3 DROPLET CONTENT SENSING

4.7.3.1 DROPLET SYNCHRONIZATION AND BIOMATERIAL CONTENT SENSING

Microwave sensing of droplet content was also carried out with the spiral resonator design. The spiral resonator was placed 8 mm away from the generator intersection. The microfluidic channel network

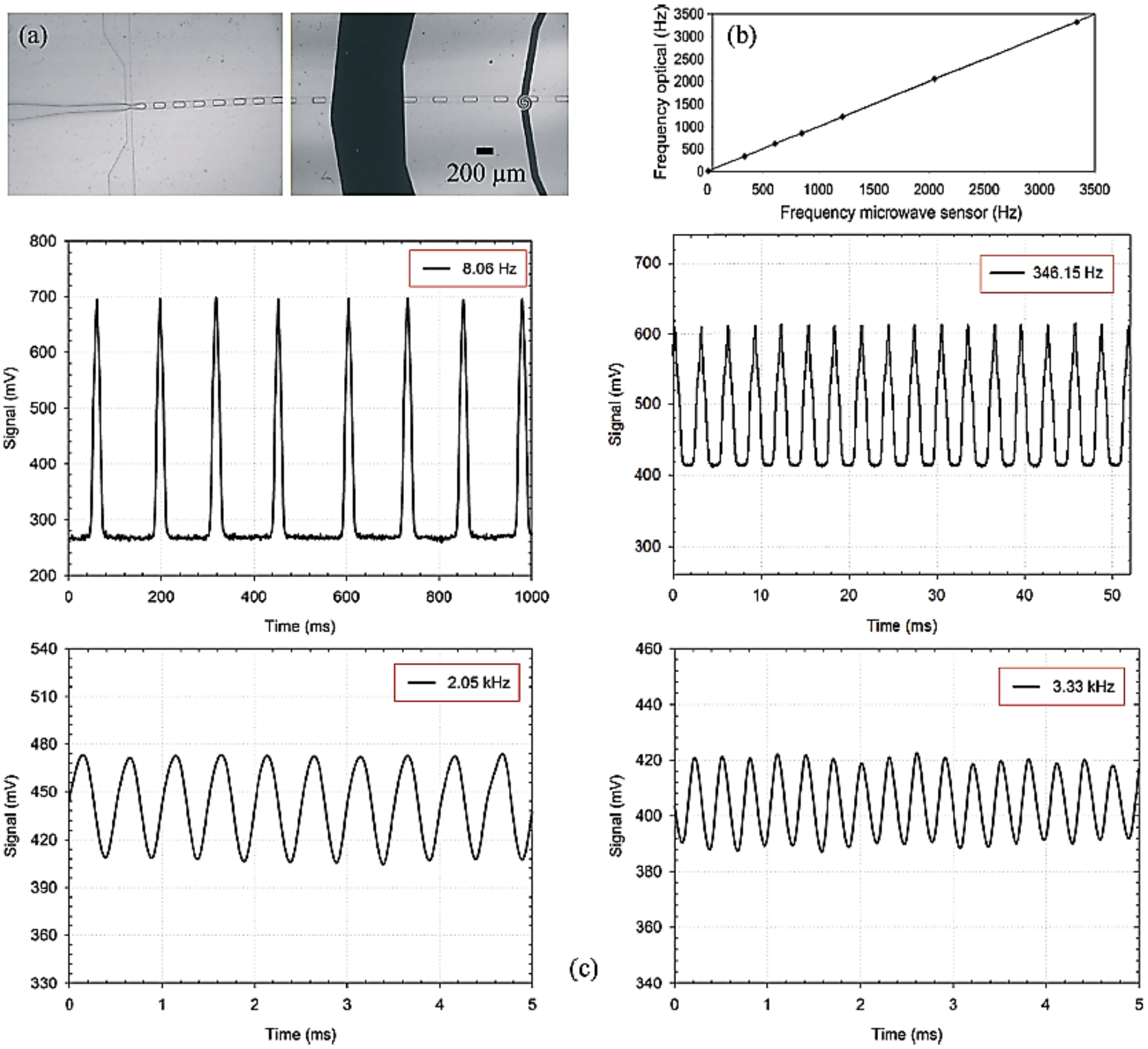

Figure 4.5 (a) Image of the generator and generated droplets, (b) comparison of the droplet generation frequencies; optical imaging vs. microwave sensor, (c) high-throughput droplet detection.

and droplet generators are shown in Figure 4.6 (a). Fluid pumping and droplet generation were controlled using a microfluidic pressure controller system (Fluigent MFCS-8C) which can provide more stable droplet generation[71]. For this set of experiments, a double T-junction generator was used to alternatively generate droplet pairs with different materials encapsulated[105] such as type A and type B. The alternating generation works as follows. When one droplet (i.e. with content type A) is being generated in one of the T-junctions, it obstructs the main channel as it is growing and thus restricts the flow of the continuous phase, which causes a dramatic increase in the pressure upstream of the T-junction intersection. When the pressure increases to a critical value, it drives the continuous phase to neck and then pinch off the droplet[68],[122],[287]. After pinch off the remaining interface recoils back to the T-junction inlet. While this process is taking place, the other T-junction generator repeats similar droplet (type B) formation process. By well-tuned applied pressures, two alternating droplets can be formed sequentially (see video appendix-C). During the formation of droplets, although two pairs come to close proximity, they do not coalesce or cross-contaminate at certain operating regimes[105]. This configuration has advantages over a simple Y-channel design in terms of operation of the two droplet generators and robustness. In addition, with this configuration there is no need to add a dilution stream in order to increase droplet spacing.

To demonstrate the sensitivity of the sensor and its potential to be applied in the area of biosensing with appealing features of no chemical and physical intrusion to the sample, some materials were strategically chosen. In particular, aqueous based solutions with slight differences in their concentration such as the potassium chloride solutions and glucose solutions used here, which result in similar dielectric constant and/or electric conductivity values, were chosen to demonstrate the sensitivity of the sensor. Two biochemical materials, fetal bovine serum that is a widely used serum-supplement for in vitro cell culture of eukaryotic cells and penicillin-streptomycin-neomycin antibiotic mixture (contain 5,000 units penicillin, 5 mg streptomycin and 10 mg neomycin/mL), that is widely used to prevent bacterial contamination of cell cultures due to their effective combined action against gram-positive and gram-negative bacteria, were chosen to demonstrate its potential for biosensing. Thawing fetal bovine serum and penicillin solution started in the fridge at 8 ^{0}C, then completed at room temperature while the bottles was swirled gently to mix the solution during the thawing process. D-(+)-Glucose and potassium chloride solutions were prepared in ultra-distilled water, and 2% fat content of milk was used. The reflection coefficient versus frequency characterization is demonstrated in Figure 4.7 below.

In order to ensure that the microwave system can differentiate droplets with small difference in dielectric properties, the experiments were carefully designed to eliminate the droplet size effect. As can be seen in Eq. (1), the frequency shift is a function of permittivity difference and the relative size of the droplet over the resonator. Considering that the electromagnetic field is accumulated in the sensing region, and the droplet width and height is confined with the channel, droplet size has no effect on the reflection coefficient as long as its length is longer than the sensor region. This

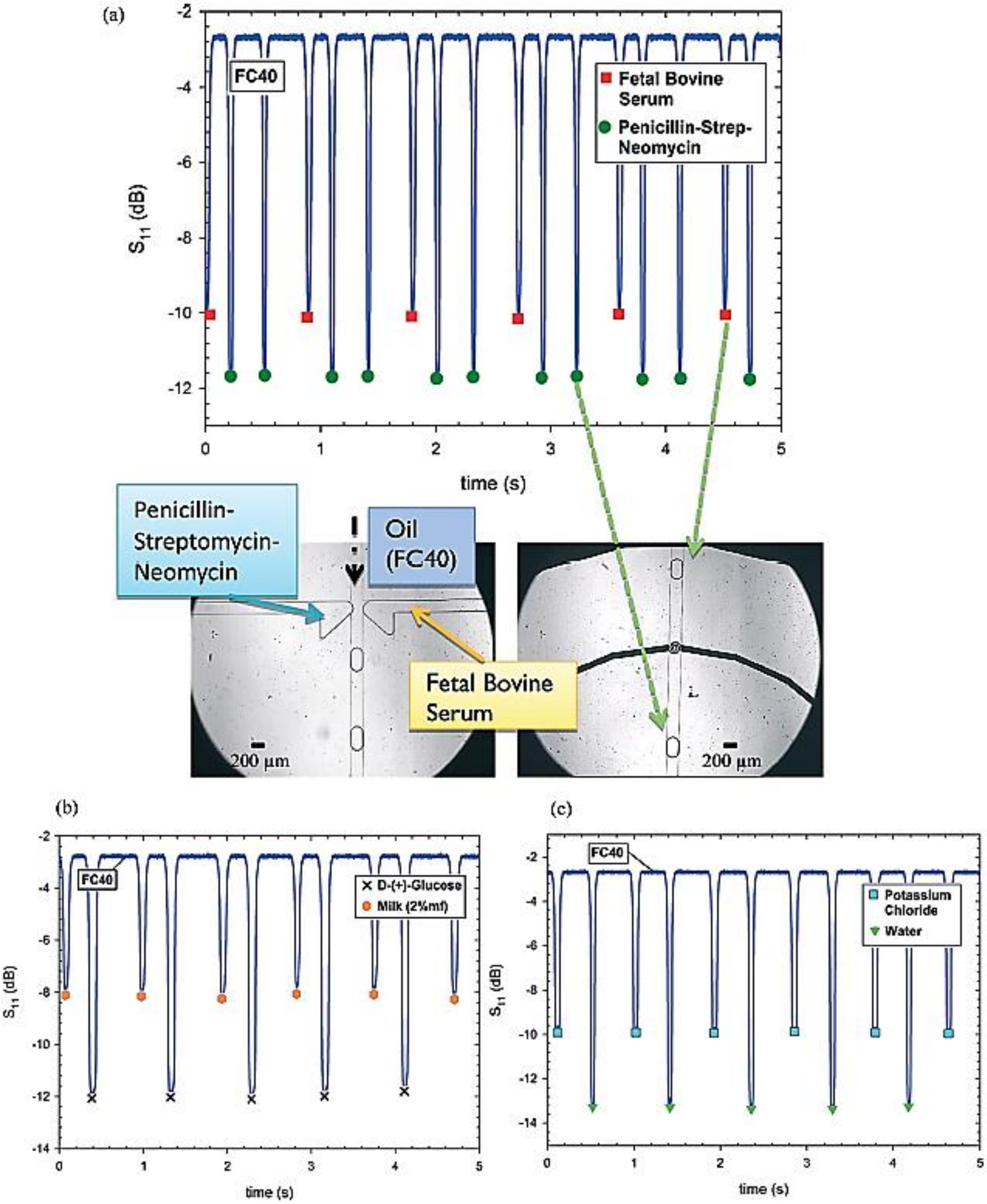

Figure 4.6 Label-free content sensing of individual droplets. (a) FBS–penicillin, (b) glucose (0.2 g ml^{-1})–milk, (c) water–potassium chloride (0.03 g ml^{-1}) droplets.

consideration ensures that the response of the sensor to different droplets is caused by dielectric property variation, namely by the specific droplet content.

In order to verify the sensing performance of the microwave system, ultra-pure water droplets were generated from both T-junction generators with FC40 oil as the continuous phase. The same sized droplets and different sized droplets were sensed with the same signal magnitude and the longer droplets resulted in wider signals due to their longer residence time in the sensing region (see Figures 4.8-4.9). Subsequently, a set of droplet pairs of the same size were sensed which include a pair of Fetal bovine serum and penicillin-strep.-neomycin, a pair of D-(+)-glucose(0.2g/ml) and milk(2%mf), and a pair of potassium chloride(0.03 g/ml) and water droplets. Figure 4.6 (a) shows the coordinated optical imaging and microwave sensing results while Figure 4.6 (b) and (c) shows the microwave sensing results.

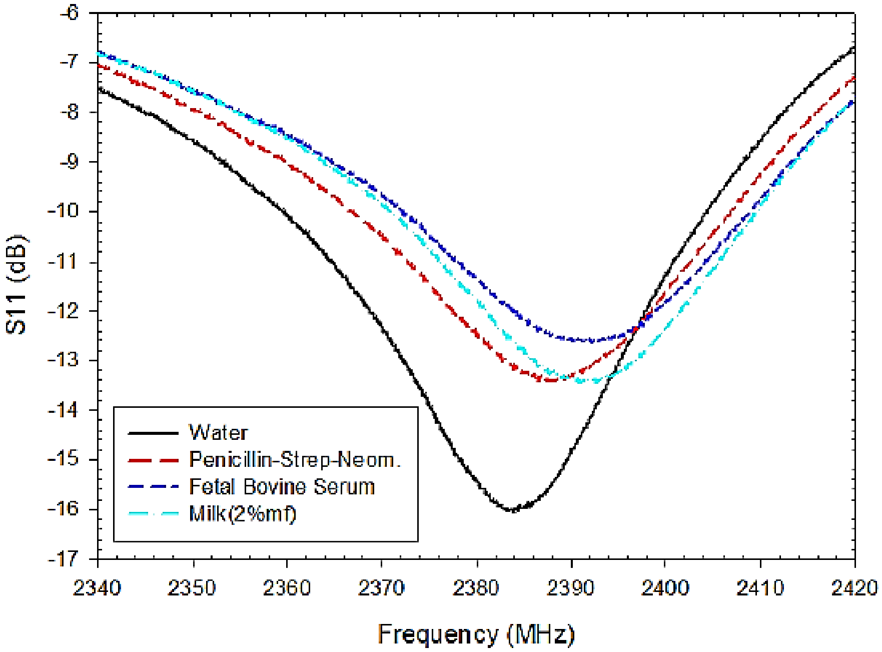

Figure 4.7 S-parameter vs. frequency behaviour of biomaterials used in the droplet content sensing experiments.

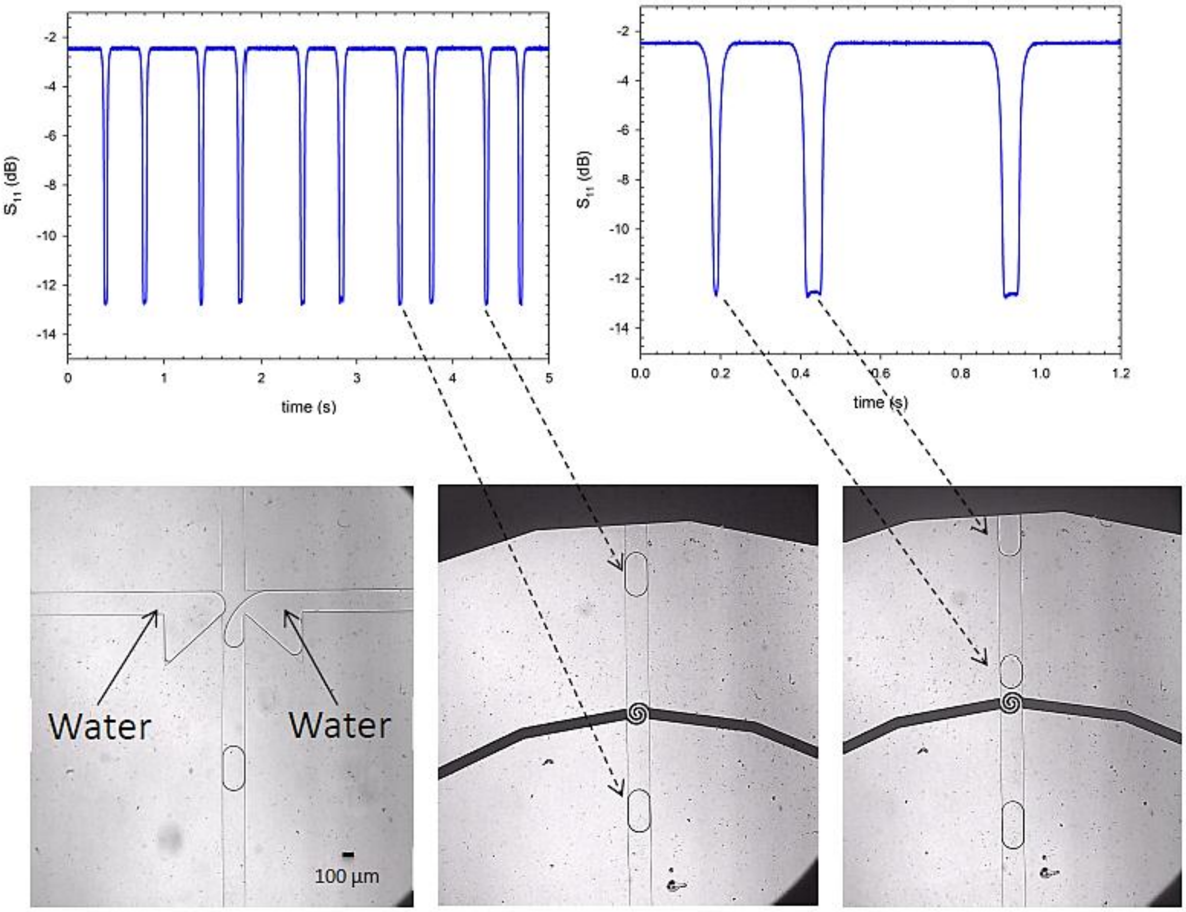

Figure 4.8 Water-Water Droplet Pair. Alternating droplet pair generator using an opposing two T-junction configuration. Ultra-pure water droplets were employed in both droplet generators; as expected same peak was obtained for both water droplets (top left). Longer and shorter water droplet pair was formed. Again, same signal amplitude was monitored that droplet length has no effect on reflection coefficient (top right). In other words, the response of the resonator is not caused by droplet geometry. Considering that the electromagnetic field is accumulated in the sensing region, and the droplet width and height is confined with the channel, droplet size has no effect on the reflection coefficient as long as its length is longer than the sensor region. These backward experiments ensure that the sensor is sensitive to dielectric property variation only.

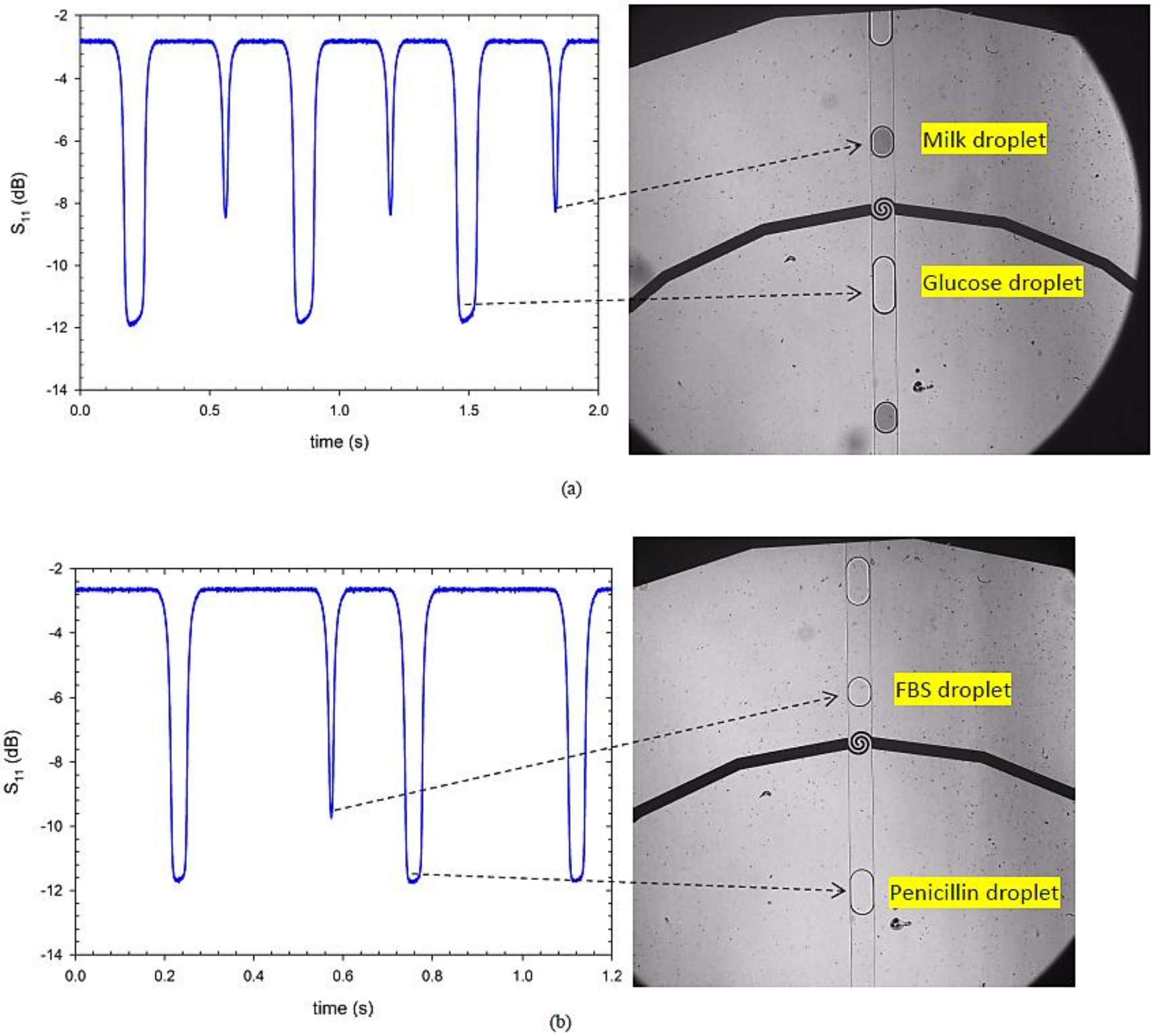

Figure 4.9 Longer-Shorter Droplet Pairs. All droplet content sensing experiments were repeated as pairs of longer and shorter droplets in order to provide backward control. There is no amplitude change in S-parameter, and only wider signal is obtained for the longer droplet which is coherent that droplet residence time on sensing region is longer. The content of droplets was distinguished very sensitively: Milk-Glucose droplets (a), FBS-Penicillin droplets (b).

The reflection coefficient difference between the fetal bovine serum droplets and penicillin droplets is -1.61 dB, which is 1.16 times lower, while -9.01 dB difference with the baseline of carrier oil FC40. As well, the difference between glucose and milk droplets is -4.02 dB, and between KCl and water droplets -3.45 dB. It is worthwhile that very low (-5 dBm) output excitation power was used in order to avoid any heating effect on droplets. These results show that our microwave module is very sensitive to nanoliter droplet permittivity contrast and can easily distinguish various droplet contents. Very high reproducibility is accomplished. This microwave system can also be used with other bio-materials for content analysis or for synthesis and reaction monitoring. It should be noted that the demonstrated throughput of sensing is not high; however, it is limited by the throughput of droplet generation for the particular scenarios considered here rather the sensor which has been demonstrated for high throughput sensing as shown in Figure 4.5.

4.7.3.2 ALZHEIMER'S DISEASE DRUG ASSAY AND INHIBITORS

To demonstrate that this platform has the potential to be used as a tool for pharmaceutical applications, it is applied to perform a similar assay developed to screen inhibitors for tau-aggregation that is linked with neurodegenerative disorders such as the Alzheimer's disease (AD)[288],[289]. The tau-derived hexapeptide (AcPHF6) which is normally considered as a model for tau-protein aggregation in many assays was used as the peptide and orange G which is one of the common inhibitors used in the traditional assay was chosen for this preliminary testing.

Figure 4.10 shows that the microwave sensor is able to differentiate the droplets with and without the mixture of peptide and inhibitor and the droplets with different concentrations of the inhibitor (orange G), which are 0.665 mM and 0.332 mM respectively (inhibitor I and II respectively in the figure). The peptide concentration was kept at 0.316 mM and all droplets contain Thioflavin S (0.05 mg ml^{-1}), which is a fluorescent indicator dye normally used in tau-aggregation assays. Figure 4.11 demonstrates the fluorescent imaging results of the effect of inhibitor. Since different concentrations of inhibitor reacts with the peptide at different ratios, this effects the emission of the fluorescent dye due aggregation rate. Fluorescent observation is used herein as the validation of the drug assay is working correctly. The samples were prepared in 4-morpholinepropanesulfonic acid (MOPS) buffer of 20 mM with a pH of 7.2. There is only one set of droplets containing no mixture of orange G and AcPHF6, which is used as a base similar to the negative control in the traditional assay[288]. It should be noted that the sensing shown in Figure 4.10 only demonstrates that the developed microwave and microfluidic platform has the potential to serve as a tool for drug discovery or pharmaceutical applications. These results are not a quantitative measure of the effects of the inhibitor on tau-aggregation because it is difficult to judge whether the signal difference is caused by the concentration of the inhibitor or the degree of peptide aggregation induced by the different inhibitor concentrations. To perform such an assay to quantitatively compare with the traditional assay would

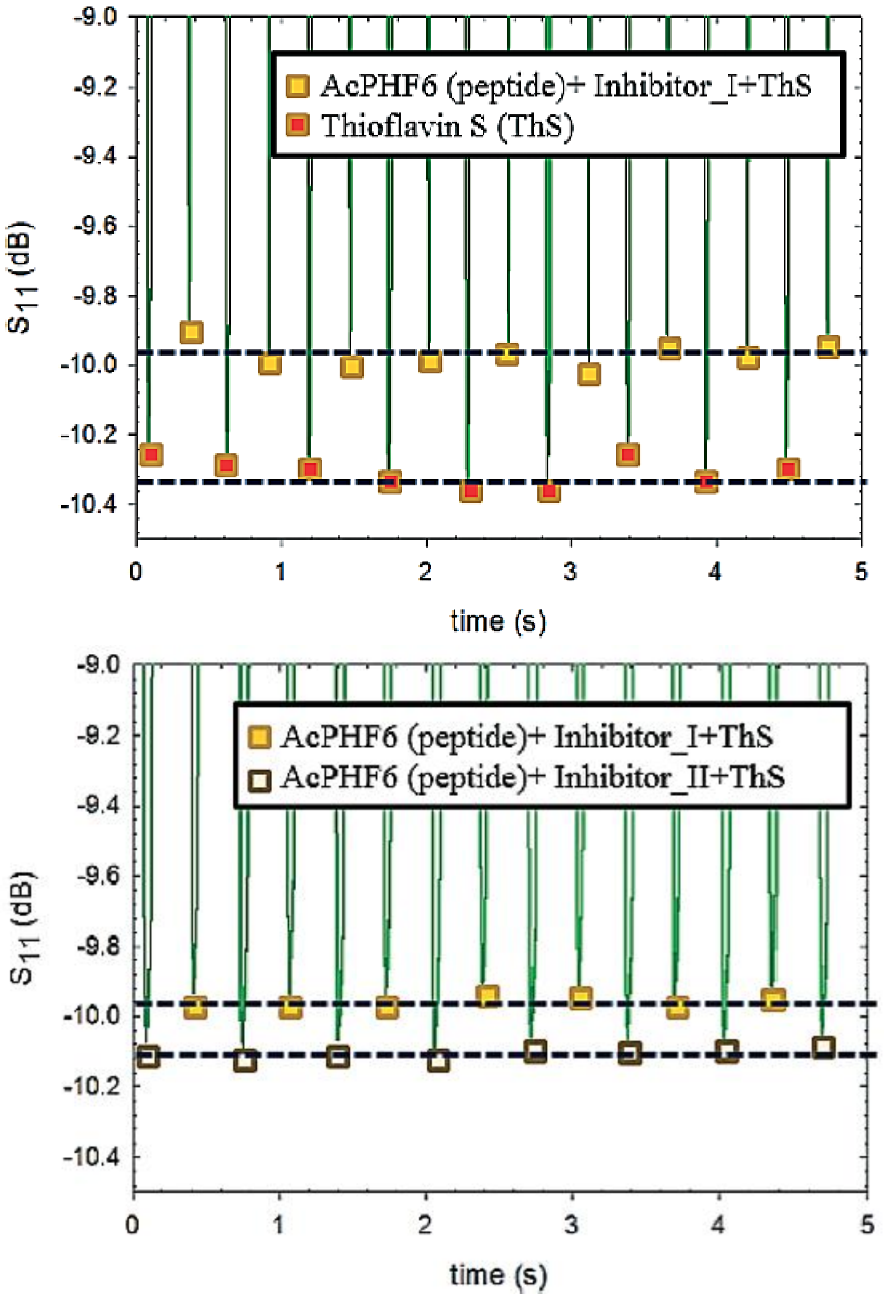

Figure 4.10 Demonstration of sensing of droplets involving AcPHF6 and orange G which are the model peptide and inhibitor respectively used in traditional tau-aggregation assays that is linked to neurodegenerative disorders such as the Alzheimer's disease.

require systematic design of the microfluidic chip and microwave sensor and require further improvements on the sensor fabrication protocol as well to improve its sensitivity, which is beyond the scope of this study. However, with a calibration process of drug assays, the platform developed herein presents promising and insightful results for Alzheimer's disease drug screening assays.

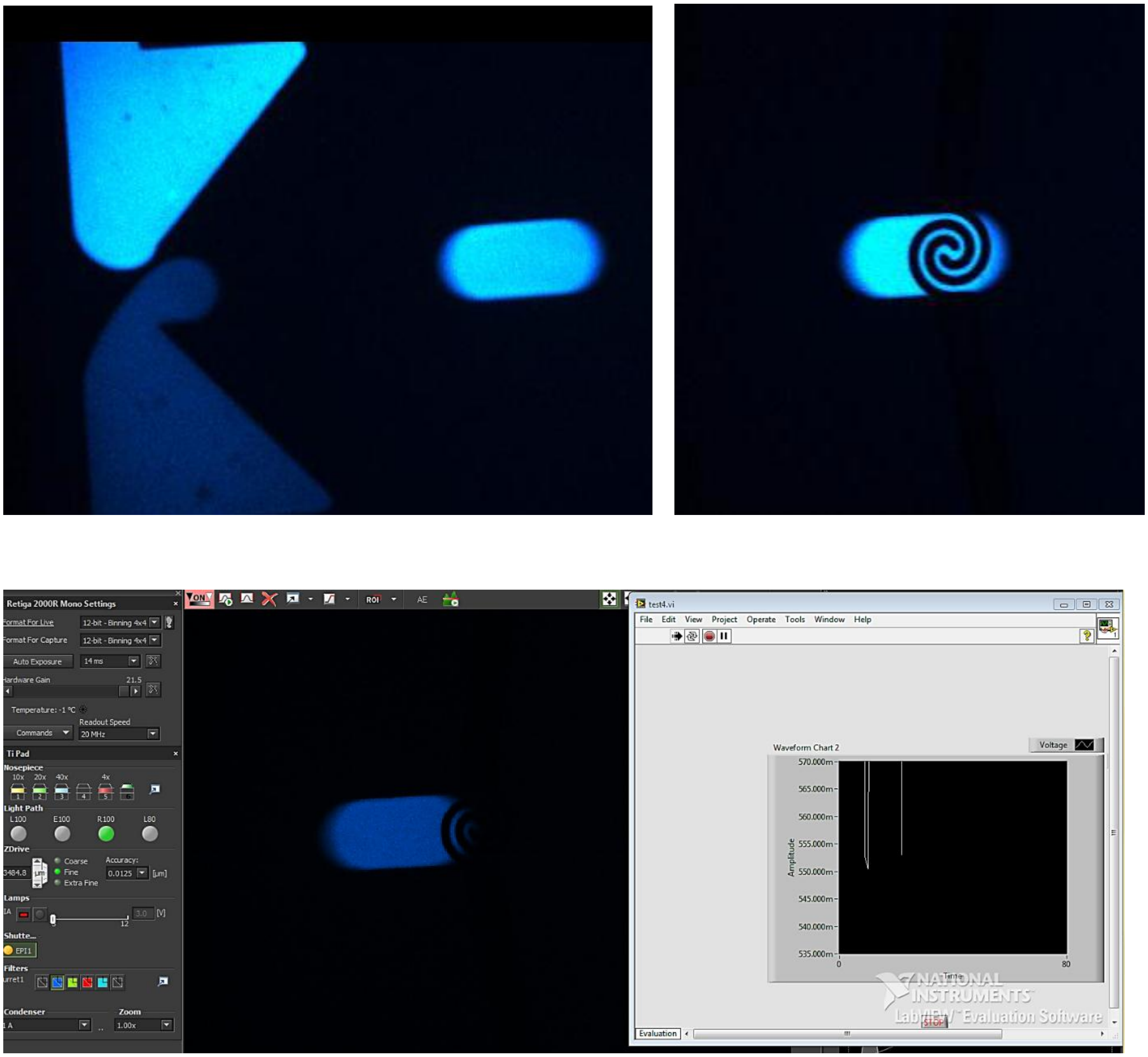

Retiga 2000R Mono Settings

ormat For Live: 12-bit - Binning 4x4

ormat For Capture: 12-bit - Binning 4x4

Auto Exposure: 14 ms

ardware Gain: 21.5

Temperature: -1 °C

Readout Speed: 20 MHz

Ti Pad

Nosepiece: 10x 20x 40x 4x

Light Path: L100 E100 R100 L80

ZDrive: 3484.8 µm, Fine, Accuracy: 0.0125 [µm]

Lamps: 3.0 [V]

Shutte...: EPI1

Condenser: 1 A

Zoom: 1.00x

Figure 4.11 Fluorescent imaging of peptide aggregation at different inhibitor concentrations. Top image shows the droplet generation and when droplet is passing over the sensor. Bottom image demonstrates the snapshot of the real-time optical and microwave detection system together.

4.8 CONCLUSIONS

In this chapter of the thesis, a platform is demonstrated, which consists of a custom microwave circuitry and microwave sensor integrated with microfluidic channel networks for label-free detection and content sensing of individual droplets. High-throughput and label-free droplet detection at kHz range are realized as an alternative to optical methods while many other non-optical techniques mostly fail at kHz rates. As well, without any chemical or physical intrusion individual droplet contents have been distinguished successfully in real-time operation. Biomaterial sensing and Alzheimer's disease drug assay screening are also experimentally implemented to present the capability of the platform. This system has significant advantages over optical detection systems for droplet microfluidics in terms of its infrastructure and operation cost, ease of use and portability for Lab-on-a-Chip applications. It also presents significant improvements compared to most electrical-based droplet detection systems in terms of its sensitivity and throughput. Therefore, it potentially facilitates the application of droplet microfluidics in point-of-care settings.

Chapter 5

COMBINATORIAL ANALYSIS OF PARAMETERS EFFECTING MICROWAVE HEATING/SENSING PERFORMANCE ON INTEGRATED DROPLET MICROFLUIDIC PLATFORMS[2]

5.1 MOTIVATION AND OBJECTIVES

Microwave heating and sensing have several advantages over traditional heating and sensing methods. Microwave heating has the unique benefit of its selectivity since only the medium with a high dielectric loss or, as with resonator designs, only the desired medium (e.g., liquid) heats up

---

[2] The contents of this chapter have been incorporated within a paper, which is being prepared for submission, by Yesiloz G., Boybay M.S. and Ren C.L. "A Parametrical Study on the Analysis of Microwave Heating/Sensing Performance on Integrated Droplet Microfluidic Platforms". G.Y. conducted simulations, collected and analyzed data; the idea formation was developed by M.S.B., G.Y. and C.L.R.; G.Y., M.S.B. and C.L.R. contribute to the paper writing.

significantly. Microwave heating occurs in a short time scale, and it is on the order of the relaxation time of the molecules. This implies that the heating rate is limited by the power absorption efficiency and the excitation power source[290]. Contactless and inertialess nature of the heating are other advantages of the microwave heating. Additionally, microwave sensing shows great benefit of high sensitivity for fast detection, which is operating at high frequencies. Miniaturized microwave sensors are easy to incorporate into microfluidics for a low-cost, and potentially without the need of large equipment.

Although there are relatively few studies exist, the combination of the microwave sensor and heater units with microfluidics have been studied, and limited number of research has been reported for droplet based systems. However, studies for the combinatorial analysis of microwave sensing and heating performances of the droplet based microfluidics, under different effecting parameters, need to be investigated comprehensively, for which more research is required in this field. The materials and the sizes of the microfluidic channel and the droplet, the microwave resonator features, and the dielectric properties of the microfluidic chip components have influence on both heating and sensing efficiency. Besides, absorbed power distribution in different components, passivation layer effect, resonance frequency behavior and internal electric field inside droplet are also important parameters. As undesirable designs may cause sharp performance damping, it is important to precisely control the operational parameters to improve the capability of the device. Thus, a thorough understanding is necessary to control the heating and sensing properties of the microwave resonator incorporated with droplet microfluidics. For instance, a passivation layer is a necessary technique to isolate electrodes and biological samples from contamination, and it has an important effect on device operation efficiency as well. In a recent work, Samiei et al. (2017) [291] states that the use of a material with a high dielectric constant and smaller thickness as the insulating layer could potentially decrease the required voltage/frequency for the mixing of stationary droplets in their study. They identified that a thorough study investigating the effects of the dielectric properties is necessary. Another example is that precise management of heating for temperature induced cell lysing or DNA amplification which are critically depend on accurate oversight of heating rate, which requires the knowledge of the system’s capabilities. Furthermore, for microfluidic chip fabrication, currently polydimethylsiloxane (PDMS) is a widely accepted material used with standard soft-lithographic techniques to make microfluidic chips, and planar electrodes can simply be added to the device with this process. Nevertheless, in the case of other materials to be used as microfluidic chip components with different permittivity values, the heating and sensing response of the device will be altered[292]. Indeed, using a microwave low loss or high dielectric constant material will affect the selectivity of heating and the detection limit[290]; thus the effects of the permittivity of the chip components are needed to be analyzed. For these necessities, this chapter is dedicated to provide a comprehensive numerical investigation on the parameters which influence the microfluidic device’s heating and sensing performance. It should be noted that including both microwave and microfluidics parameters, this is a complicated and a coupled multi-physics problem. Experimentation for analyzing the influencing parameters are too expensive or impossible either due to the nature of the problem (e.g., calculation and monitoring the E-field or absorbed power inside the droplet) or due to the limitations with the available fabrication techniques and proper materials. Hence, this research demonstrates a guidance and understanding in order to design droplet microfluidic and microwave integrated systems.

5.2 COMBINED MICROFLUIDIC AND MICROWAVE PLATFORM OVERVIEW

The integrated microwave and microfluidics device is subsequently composed of a microwave sensor (resonator), which includes an excitation (outer) loop, a split ring (inner loop) and a spiral design of capacitive discontinuity; and a microfluidic chip that the chip consists of a polymeric mold that houses the microchannel, a glass substrate, a passivation layer between the microwave electrodes and the substrate, and an aqueous droplet as described in Figure 5.1. For easy and compact integration with the microfluidics, the microwave sensor is designed as a co-planar configuration, which makes the fabrication cost-effective and enables further investigation of Lab-on-a-chip platforms through, for example, a microscope since it does not require a ground plane of a conductor. In Figure 5.1a, the overview of the system components are shown. In order to achieve an authentic numerical model, the exact components of the Lab on a chip platform are incorporated in the numerical model despite the fact that this increases the computational time-cost and effort. However, it provides more realistic model with including the actual device components. In this perspective, the coaxial microwave feeding and the SMA connector are placed into the solution to excite the outer loop as well as the PDMS chip mold. In Figure 5.1b, the cross section view at yz-plane which intersects the middle half of the droplet is shown in order to provide a closer look for identifying the places of the substrate, the passivation layer, the droplet and the PDMS mold with the microchannel. The microwave electrodes are placed at the interface of the passivation layer and the substrate. Droplet is placed in the microchannel, which is separated from the substrate and electrodes with the passivation layer. In Figure 5.1c, a closer snapshot of the droplet and the spiral capacitive region are illustrated along with the microchannel. The microchannel is aligned with the spiral gap and the droplet is positioned on it.

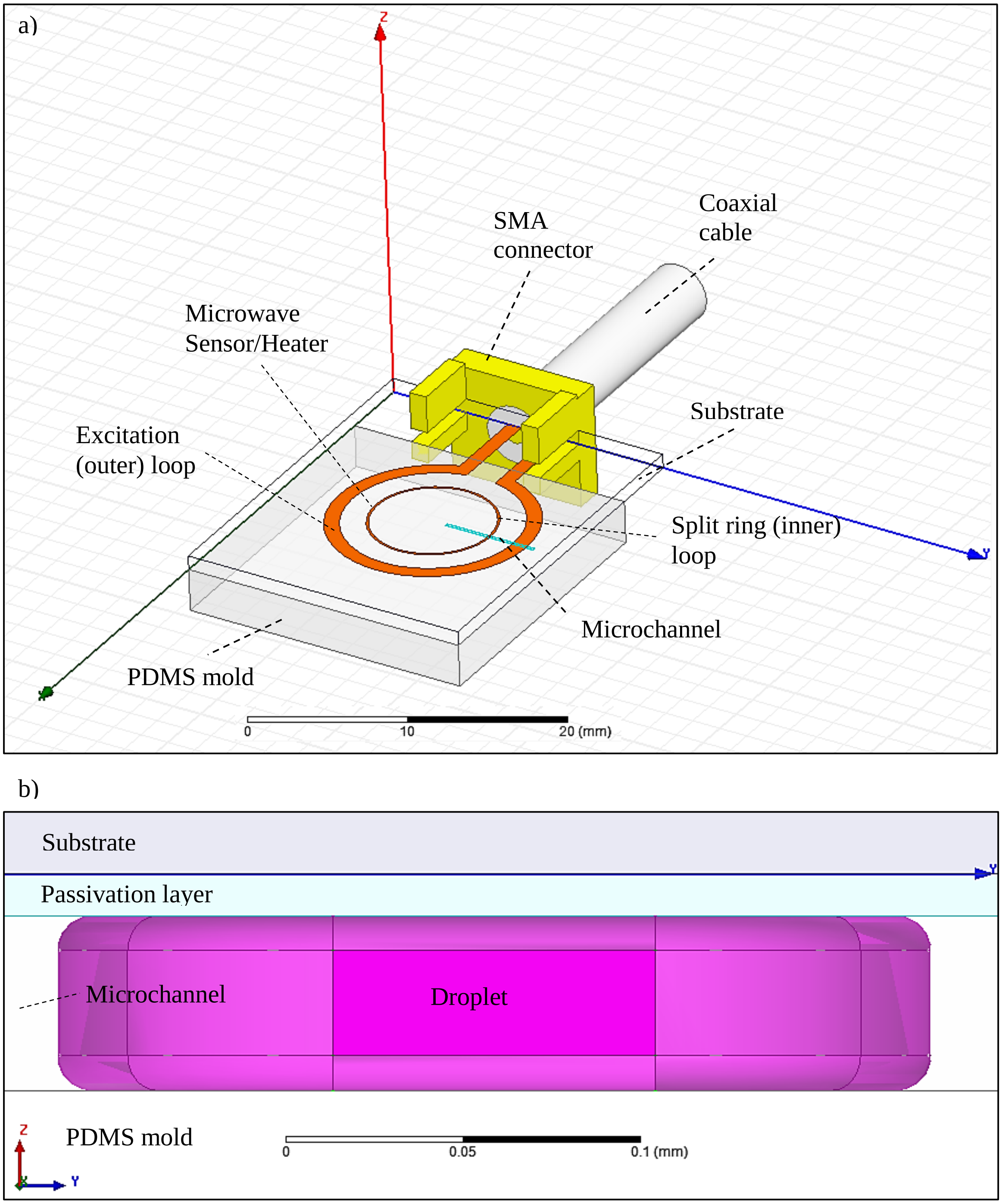

Figure 5.1 Continued.

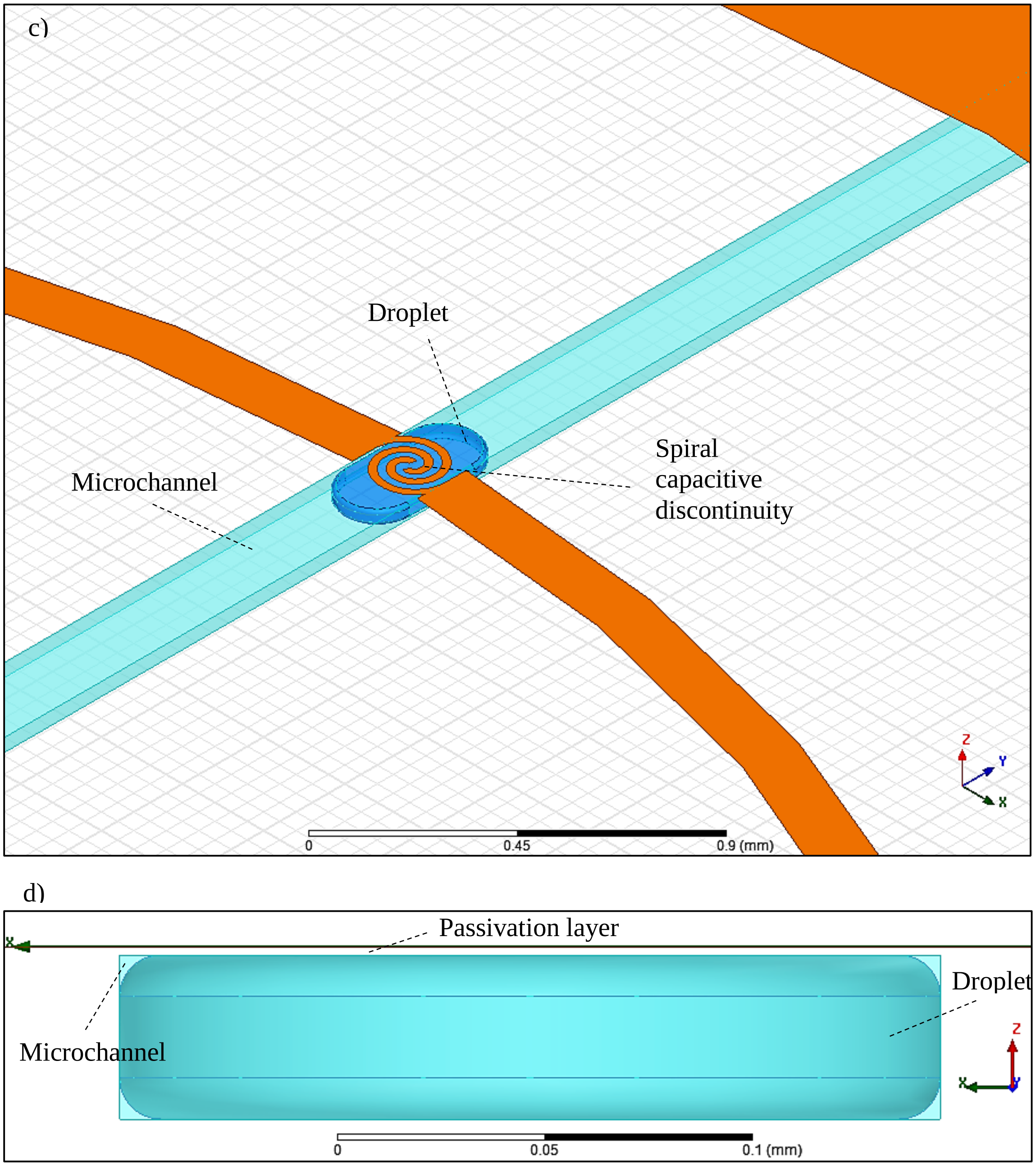

Figure 5.1 Combined microfluidic and microwave components which are modeled in numerical simulations.

Additionally, in two-phase droplet flows in microchannels as explained in Chapter 2, due to the interfacial tension between oil and aqueous (droplet) phase a curvature occurs at the corners of the channel, which is called as gutter region. For this reality, the geometric model of the droplet is designed considering the actual shape of the droplet from the experiments using an external solid design software (SolidWorks Inc.), and imported to the system. As can be seen from Figure 5.1d, which shows the cross-section view of the microchannel at zx-plane that intersects the middle half of the droplet, the droplet and the channel include the gutter region. All of the structure (platform) components are modeled in order to have a complete physical system according to experimental conditions.

5.3 DIMENSIONS OF THE RESONATOR STRUCTURE

Resonator dimensions and the spiral structure are shown in Figure 5.2.

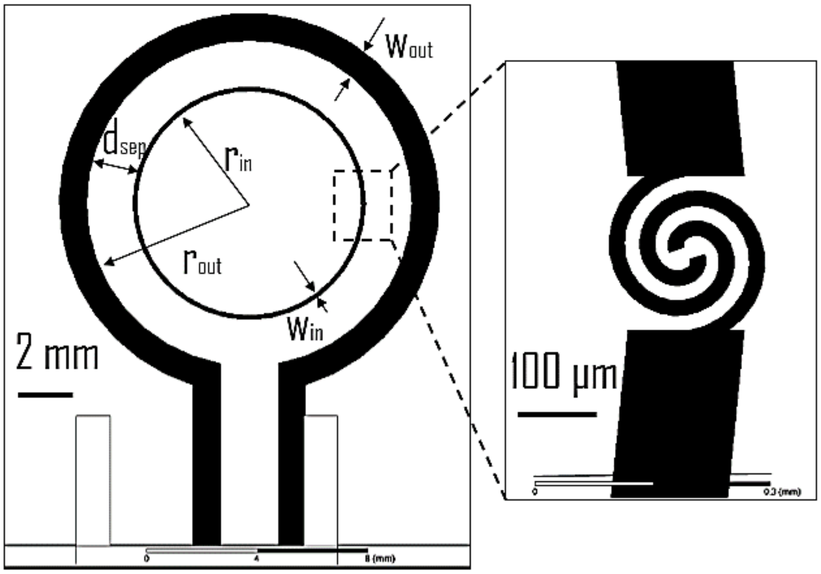

Figure 5.2 Resonator structure and dimensions.

Table 5.1. Sensor dimensions (in mm)

r_{in}	r_{out}	d_{sep}	W_{in}	W_{out}
4.25	6.1	1.7	0.15	1

5.4 NUMERICAL MODEL AND THE PARAMETRICAL STUDY WITH ANSYS HFSS

5.4.1 PROBLEM DEFINITION

The working principle of the microwave resonator is explained in Chapter 4.4. In this section a numerical model is set up considering the actual physical device components and operation parameters. The full wave simulations are conducted using a commercial software, Ansys HFSS. Microwave signal feeds the excitation (outer) loop through a coplanar transmission line which is connected to the SMA connector and the coaxial cable as shown in Figure 5.1. The split-ring (inner) loop with the spiral capacitive design confines the microwave energy in the gap (capacitive discontinuity) region. A microchannel is aligned on top the spiral gap where a droplet is also positioned. The whole device is bounded in a radiation boundary to run the simulations. In such a structure energy dissipation occurs in three mechanisms which are conductive, dielectric and radiative losses. Dielectric properties of the microfluidic chip components (e.g., permittivity of chip material and substrate material), passivation layer thickness, droplet presence, microchannel geometry effects, and mutual coupling of the resonator structure are analyzed through the resonance frequency shift and the power absorption inside the droplet. Reflection coefficient of the sensor is evaluated for optimum conditions. The microwave resonator structure has a versatile feature that it can work as a heater and a sensor. In order to have an efficient heater, electric field must be accumulated inside the droplet by means of the spiral capacitive gap, and the source power, which is set to 1W by default, must be transferred to the droplet as far as possible. Conductive and other dielectric losses should be kept minimum. Radiation loss is also important to be considered due to that the sensor dimensions are close to the wavelength which is around 8-10 cm regarding the operation frequency range of the sensor. Likewise, for a sensor with high sensitivity, a large resonance frequency shift must be obtained in order to detect subtle changes by means of the droplet presence and the droplet content.

5.4.2 SOLUTION PROCESS

The entire electromagnetic phenomena and the solution boundary, including capacitance and inductance effects, are described in by Maxwell's equations. Electromagnetic phenomena express the electric field ($\vec{\boldsymbol{E}}$) to the magnetic field $\vec{\boldsymbol{H}}$ in the presence of materials described by electric permittivity (ε), conductivity (σ) and magnetic permeability (μ). In differential the frequency-domain form, Maxwell's equations are

$$\nabla\vec{\boldsymbol{E}} = -j\omega\mu\vec{\boldsymbol{H}} \qquad (1)$$

$$\nabla\vec{\boldsymbol{H}} = (\sigma + j\omega\varepsilon)\vec{\boldsymbol{E}} \qquad (2)$$

$$\nabla.\,\varepsilon\vec{\boldsymbol{E}} = \rho \qquad (3)$$

$$\nabla.\,\mu\vec{\boldsymbol{H}} = 0 \qquad (4)$$

where ρ represents the density of free charges, j is the imaginary unit, and $\omega=2\pi f$ is the angular frequency. As Maxwell's equations certainly show that electric and magnetic fields are coupled: electric fields can act as sources for magnetic fields, and vice versa. This coupling is two-way, and causes to various effects (radiation, wave propagation, phase delays, etc.)[293].

5.4.3 BOUNDARY CONDITIONS

Boundary conditions specify the field behavior at the edges of the problem region and object interfaces. Boundaries in HFSS are used for two main reasons: i) to construct an open or a closed electromagnetic model, ii) to simplify the electromagnetic or geometric complexity of the electromagnetic model[293]. In a closed model energy cannot escape except through the applied port, whereas in an open system electromagnetic energy can radiate away, which is used in this study. The following boundary conditions are assigned in the numerical model for the microwave and microfluidics hybrid platform in this work.

5.4.3.1 RADIATION BOUNDARY CONDITION

Radiation boundary condition represents an open and absorbing boundary which absorbs the outgoing waves and allows waves to radiate far into space. All of the microfluidic chip and microwave sensor components are enclosed by a radiation boundary region. As a common approach, the boundary region should be located at least λ/4 (λ represents the wavelength) away in all directions from the radiation source, which is the microwave resonator structure herein. The physical meaning of the radiation boundary is that the boundary is not supposed to generate any unphysical reflection. Thus, the numerical solution truncates the calculation appropriately at the radiation boundary domain for the radiating and scattering structures from the device. In order words, the outgoing waves are not allowed to come back to effect the solution that they are absorbed at the boundary.

5.4.3.2 FINITE CONDUCTIVITY

Finite conductivity boundaries represent imperfect conductors. At such boundaries, the following conditions exists:

$$\boldsymbol{E}_{tan} = Z(\hat{n}x\boldsymbol{H}_{tan}) \qquad (5)$$

where $\mathbf{E}_{\mathrm{tan}}$ is the tangential component of the electric field component, $\mathbf{H}_{\mathrm{tan}}$ is the tangential component of the magnetic field component, Z is the surface impedance of the boundary. Also, this boundary condition is valid when the skin depth of the microwave sensor electrodes are high enough

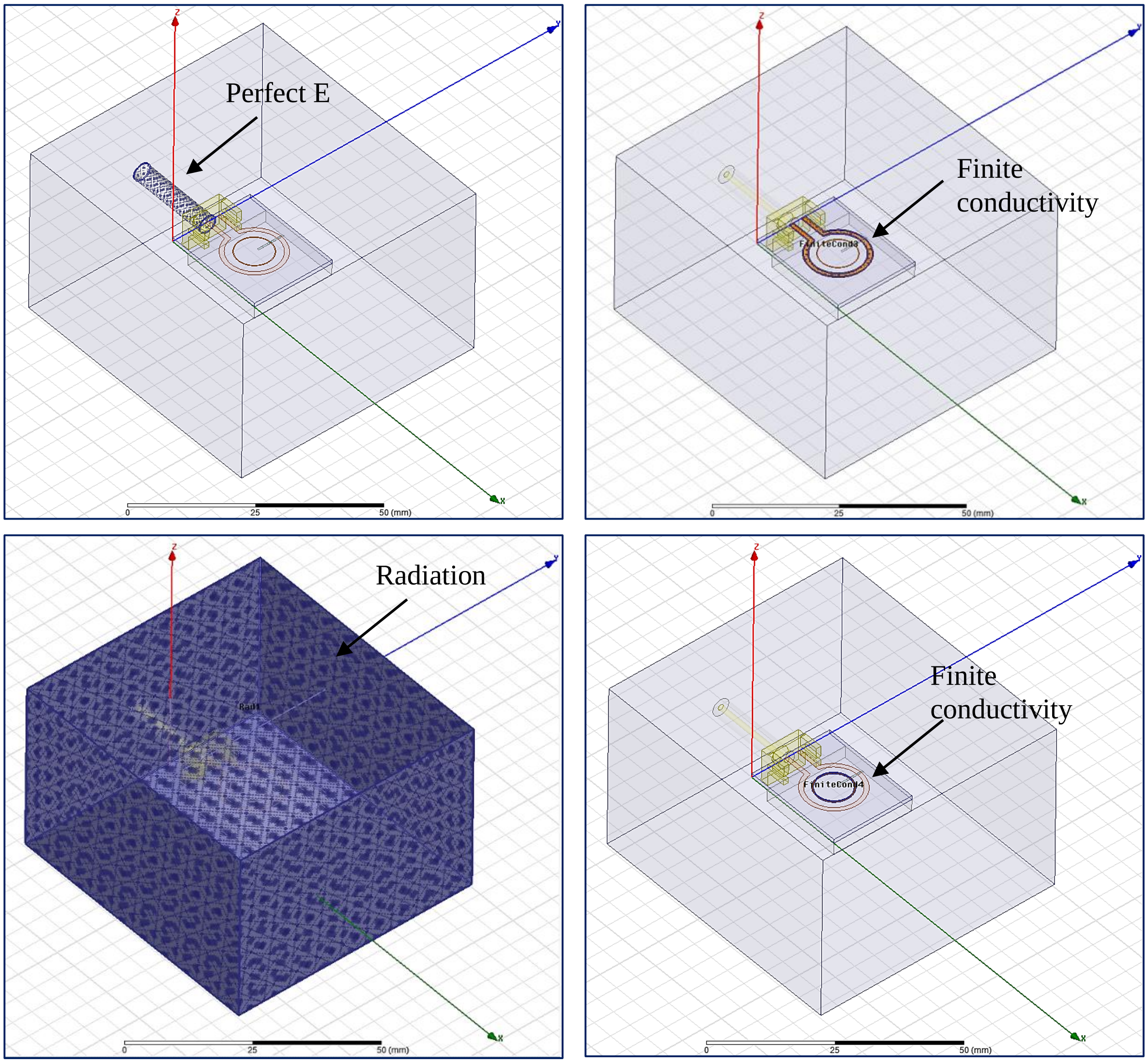

Figure 5.3. Boundary conditions.

at the operating frequency band. Surface roughness model can also be used for the conductive electrodes, which is not considered in this study. Since electric field has tangential component at the surface, the numerical solution in HFSS uses an approach to calculate fields at the surface, and not in the conductor. The outer excitation loop and the inner (split-ring) loop are assigned as finite conductivity boundary conditions in the solutions.

5.4.3.3 PERFECT E

A perfect E boundary condition represents a perfectly conducting surface in the structure. Also, any structure that is defined as perfectly conducting material is considered as perfect E boundary. The microwave excitation through the SMA connector and coaxial cable is assigned as perfect E boundary condition. All of the assigned boundary conditions can be seen in Figure 5.3 below.

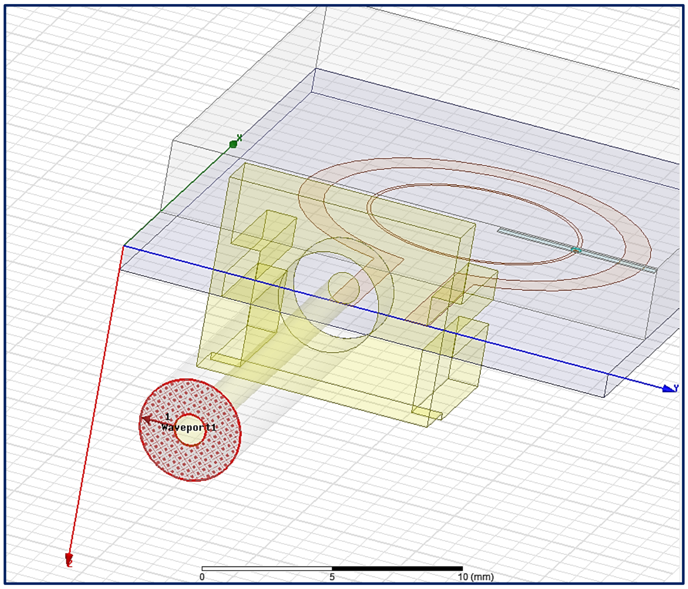

Figure 5.4. Wave port excitation.

5.4.4 EXCITATIONS

Excitations provide the sources of electromagnetic fields into the structure, where the incident fields have interaction with the device components. There are several types of excitations that can be applied such as wave port, lumped port, terminal, incident wave, voltage source, current source, etc. For the structure used here, a wave port excitation is assigned, and it represents an external surface at which the microwave signal access into the system. Transmission lines and waveguide structures can be implemented by wave ports. The cross section surface of the coaxial cable is assigned as the excitation port, and since the port size is defined by the inner and outer radius of the shield, there is no need to define a port size. The excitation port assigned in the design is shown in Figure 5.4.

The defined wave ports calculate the characteristic impedance, complex propagation constant, and generalized S-Parameters by solving Maxwell's equations. The excitation field pattern that is solved is valid only at a single frequency and if there is a frequency sweep each frequency point is calculated for different excitation field patterns. A source power of 1W is applied in all cases in the simulations.

5.4.5 MESH GENERATION AND OPERATIONS

The geometric model is automatically divided into tetrahedral mesh elements in Ansys HFSS, and these tetrahedral elements generate the general mesh structure. Maxwell's Equations, which govern the electromagnetic problem, and are valid in three-dimensional space in the problem region are discretized with a mathematical model, then the partial differential equations are solved using the finite element formulation. In HFSS, a mesh is discretized into small three-dimensional tetrahedral and two-dimensional triangular elements. The reason is that a tetrahedron (a solid with four triangular faces) forms a simplex for R3 space which means that any 3-dimensional (3D) arbitrary domain can be decomposed into tetrahedral elements. Therefore, by stretching or pulling the tetrahedral mesh elements, the 3D geometric model can be filled and decomposed by these meshes which enables an advantage for mesh control. Figure 5.5 demonstrates different types of tetrahedral elements used in meshing.

Another aspect that is worthwhile to mention is that the adaptive mesh refinement is an essential part of the solution. Adaptive meshing technique is a specialty for this tool compared to other electromagnetic simulators. Typically, after defining boundary conditions, excitations and materials for example, the geometry is decomposed by adaptive meshing for sequential iterations. In this technique, an initial mesh is generated and solved to estimate the error in the solution. Then the higher-error regions are implemented by finer meshes, and another solution is generated and the error is re-computed. This process continues until the convergence is obtained. Hereafter, each step of adaptive meshing process will be called an 'adaptive pass'. Adaptive mesh refinement ensures that strong electromagnetic field regions have finer meshes, while the remaining areas have coarser meshes. This is useful for efficient calculations.

An optional but important mesh refinement operation is called seeding mesh, which enables to guide critical mesh construction on important regions that the precise calculation of electromagnetic field is crucial with an engineering knowledge on the problem. This operation can be done before the adaptive passes start to solve the process which gives an initial guidance to the solver. Providing such as engineering guidance to the solver prior to beginning the adaptive analysis can tremendously reduce the number of passes required for the convergence, and the total number of tetrahedral mesh elements as well. This leads to more accurate results, and it provides less computation effort. Without the seeding mesh operation, the adaptive pass analysis still can converge and find the critical fields to refine the mesh, however, seeding mesh helps to find the critical electromagnetic fields after the first a couple of the passes are solved.

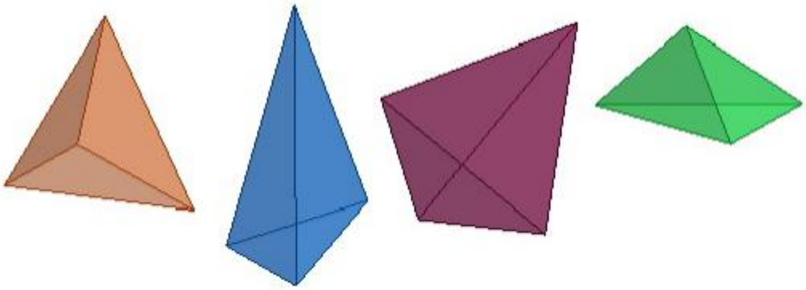

Figure 5.5. Different types of tetrahedral meshing elements[293].

Again, this is due to prior knowledge of the critical points and behavior of the problem field, and due to the provided engineering guidance. For instance, the same problem may need to calculate 25 adaptive passes with a total number of 400,000 tetrahedral elements which is costly in terms of time and computation effort. On the other hand, the same problem can be solved with only 10 adaptive passes and around 100,000 tetrahedral meshes, with more accuracy and a shorter time, when using a seeding mesh operation at the beginning. For the current problem in this study, since it includes microwave sensor and microfluidic components, and especially the heating and sensing performance is analyzed on droplets which is at nanoscale volume, also the spiral resonator design is electrically and physically very small with strong electromagnetic field confinement, the seeding operation is always used in this work. For example, the spiral resonant structure along with the inner ring, droplet because it is load on capacitive gap and excitation loop, etc. are structured with seeding mesh refinement before the adaptive analysis. The seeding mesh is done through length-based mesh refinement. As a rule of thumb in this study, a gradual mesh size decrease of 20% of the maximum mesh element length in three steps are implemented upon the default initial solver tetrahedral mesh size.

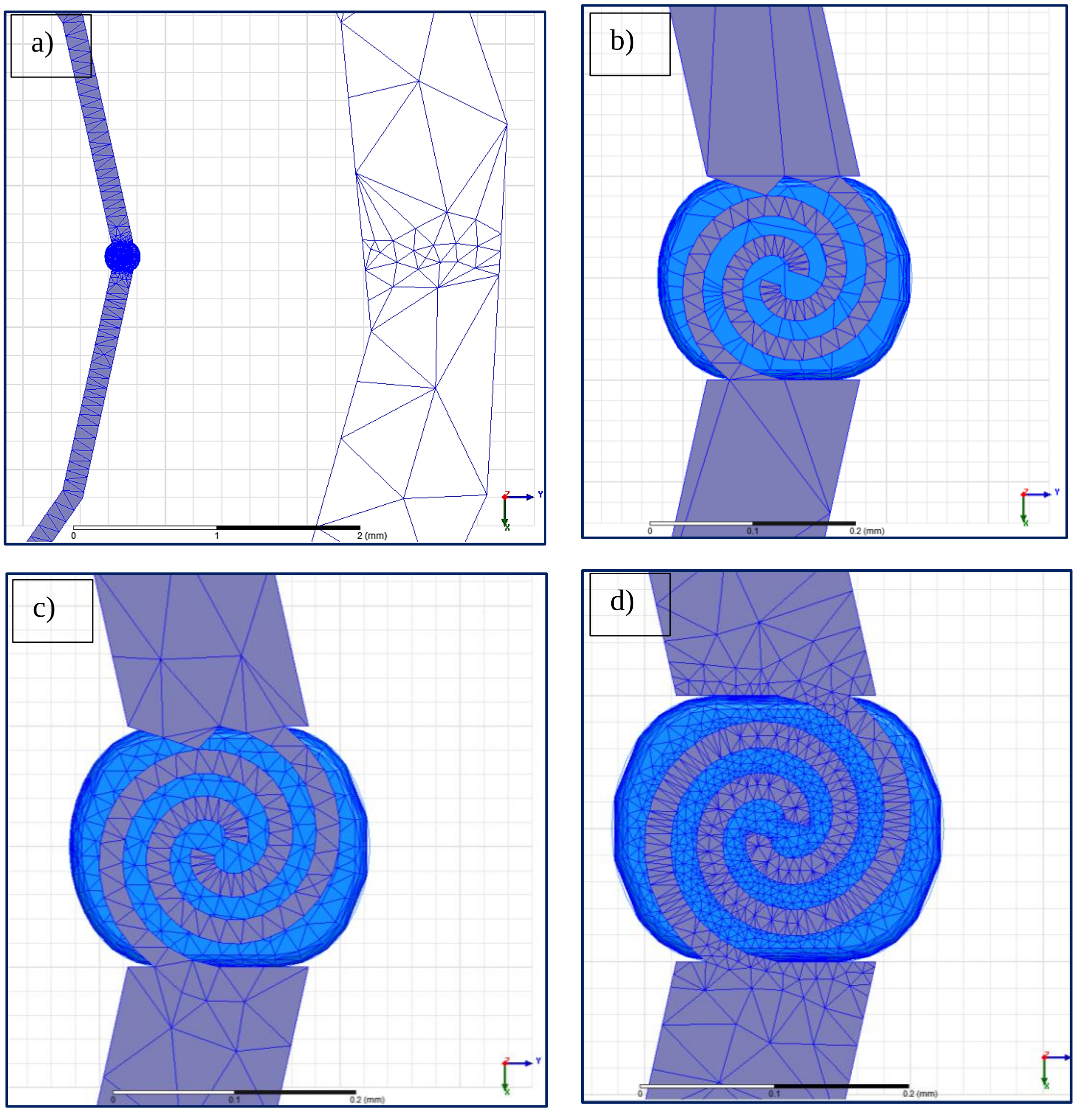

Figure 5.6 (a) Coarse and finer meshes at the outer (excitation) and inner (split) loop by adaptive meshing. (b) Initial adaptive pass at spiral region and droplet without seeding mesh operation. The droplet and the inner split loop have coarse mesh elements. (c) Initial adaptive pass at spiral region and the droplet with seeding mesh operation prior to adaptive process. Initially, droplet and spiral gap have finer elements. (d) A later adaptive pass in comparison to the mesh structure in (c) with seeding mesh that strong electric fields are assigned even finer meshes intelligently to help convergence and reduce the error.

In Figure 5.6a, an example of structured meshes for outer (excitation) and inner loops are depicted. Since a weaker electric field occurs at the outer loop, the coarse meshes are structured. Also, since the inner split loop consists of the droplet and spiral capacitive gap, a strong electric field happens there, and the finer meshes are structured. Additionally, a close view of the meshing at the droplet and spiral region is shown in Figure 5.6b for regular adaptive meshing. And, in Figure 5.6c and Figure 5.6d, an initial and a later adaptive pass are shown with seeding mesh operation, respectively. As can be seen from comparing Figure 5.6b and Figure 5.6c, without a seeding mesh, as is used in Figure 5.6b, the droplet and spiral capacitive region have a very coarse mesh assigned. On the other hand, in Figure 5.6c, with a prior seeding mesh operation, tetrahedral meshing on the droplet and spiral gap starts with finer elements. Furthermore, as mentioned, the solution in Figure 5.6c is conducted by the seeding mesh. With this, the error is calculated, and strong electric field regions are identified. Then, for the next adaptive pass, these regions are intelligently assigned even finer meshes, as in Figure 5.6d.

5.4.6 ADAPTIVE SOLUTIONS, CONVERGENCE AND MESH INDEPENDENCE STUDY

Adaptive solutions are carried out with the initial mesh generated either with or without seeding for optimal efficiency, accuracy, size and density of the tetrahedral elements. Then, the adaptive passes are repeated and the error is calculated from one adaptive pass to the next. When the provided convergence criterion is met, the solver stops the calculation. The flow of the adaptive solution algorithm is demonstrated in Figure 5.7.

The convergence criterion, delta S, is the magnitude of the change of the S-parameters between two consecutive passes. When a maximum delta S is reached, the solution has converged, and delta S defines the relative change of consecutive iterations in terms of the magnitude of all the S-parameters in the solution matrix. Namely, $\mathrm{Max}_{ij}[\mathrm{mag}(S^{N}_{ij} - S^{(N-1)})_{ij})]$, where i and j cover all matrix entries, and N represents the pass number. Now, two ways can be used to stop the calculation. First, the maximum delta S value can be met as the convergence criterion or, second, the number of adaptive solution cycles can be controlled as a stopping criterion for the adaptive solutions. In the second case, even if the convergence criteria has not been met, whenever the maximum number of adaptive passes are completed, the analysis stops. If a large number of adaptive passes have been defined, the analysis will continue until the convergence criteria is satisfied. However, it should be noted that each adaptive pass is guaranteed to use a larger total number of tetrahedral elements, and this is not always feasible due to computer capacity. In order to obtain an accurate and efficient result, in these regards, adaptive mesh refinement, adaptive solutions/passes and convergence criteria are important parameters. Mesh independent analysis should also be completed so as to get results which are not dependent on mesh. However, it has been noticed that controlling only the maximum delta S value as a convergence criterion does not always provide accurate results, and usually the results become still mesh dependent. The reason is that, as mentioned before, each adaptive pass is guaranteed to use a higher number of mesh elements than the previous one. It assigns them into strong electromagnetic field regions, but the mesh number increase rate in each adaptive pass is not controlled. Also, the critical electric field distribution is a function of the material and geometrical properties (e.g., the permittivity of chip material, passivation layer thickness, droplet shape, etc.) and, for different cases, the convergence criteria can be met with different meshing structures or numbers, and at different adaptive pass cycles, which may not be consistent all the time. Consecutive adaptive passes might cause fluctuations in the maximum delta S value that determines the convergence that use of large number of meshes can end up with high convergence criteria (maximum delta S) that is expected to be opposite way. Increasing the mesh number does not mean decreasing the maximum delta S.

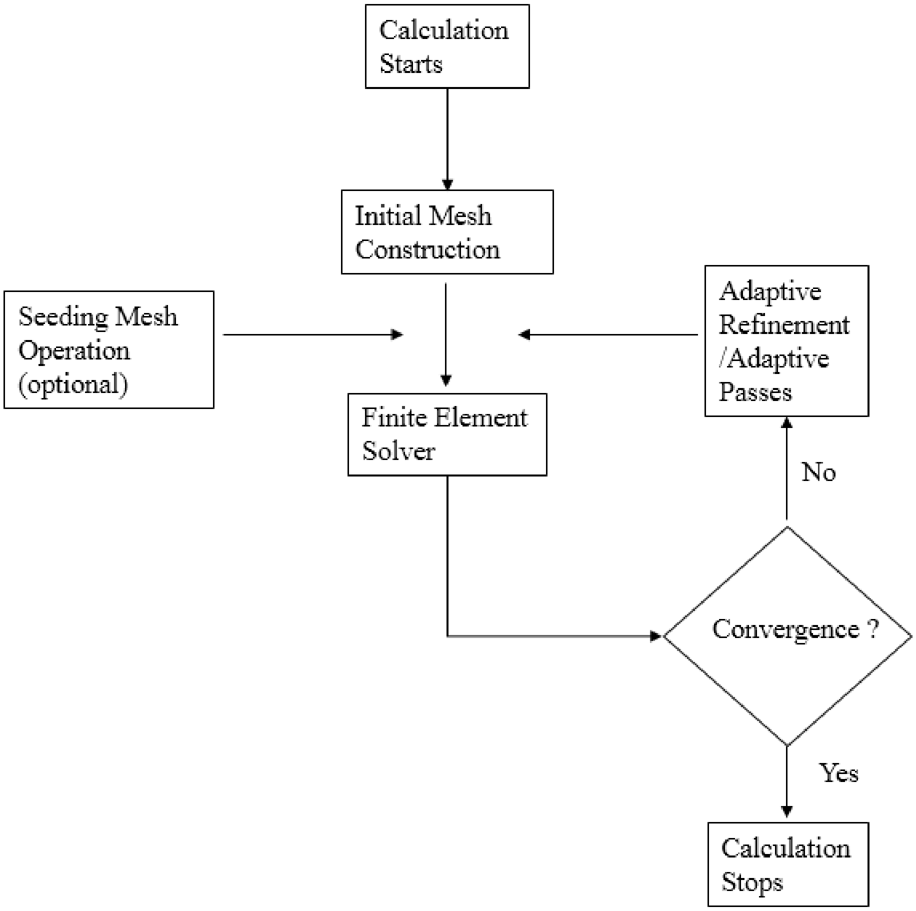

Figure 5.7 Adaptive solution process.

To solve that problem, a hybrid approach is accepted in this study. First, a very low maximum delta S value is defined (e.g., 1x10^-5), and the adaptive solutions are controlled by the number of passes cycles. As well, it is important to note that a maximum refinement and refinement rate per pass for mesh structuring are adopted. For instance, a 100% refinement rate per pass, and a 10,000 maximum refinement, controls the number of mesh increments to be 10,000 for consecutive adaptive passes. This method satisfies consistent mesh refinement and, more importantly, the maximum delta S

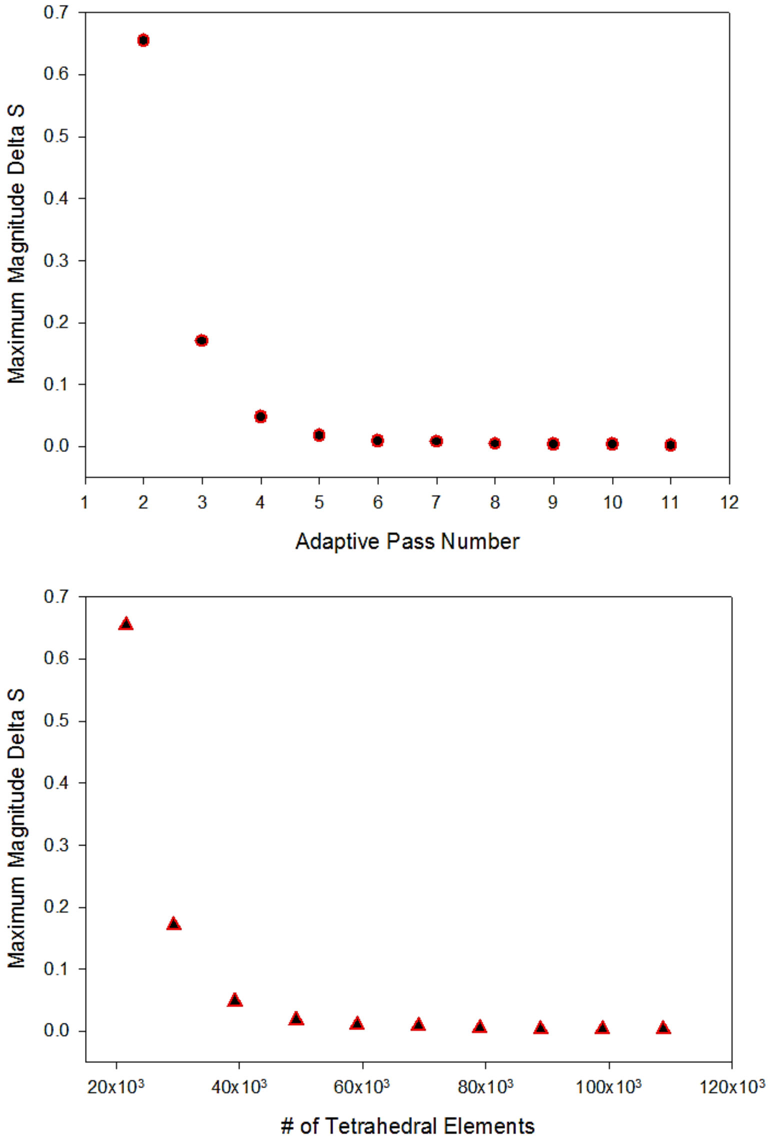

Figure 5.8. Maximum magnitude delta S versus number of adaptive passes and tetrahedral elements.

convergence criteria. Through this hybrid approach, accurate and efficient results are obtained for different cases. In Figure 5.8 mesh independent results are demonstrated. As can be seen from Figure 5.8, for ΔS_{max}=0.003 (0.3% error), consistent results are achieved with mesh independent convergence.

5.4.7 SWEEP ALGORITHM

After a converged mesh occurs, or an end to the adaptive pass solutions, the response of the system to different frequencies can be obtained through a frequency sweep computation. Frequency sweep can be performed by different algorithms such as fast sweep, discrete sweep and interpolating sweep. The discrete sweep gives an accurate solution, however, it calculates a full solution to the frequency band given at every frequency separately using the last (or converged) mesh, and that increases the solution time and limits the number of frequency steps to scan the full desired frequency range. On the other side, a fast sweep can be performed, which uses an Adaptive Lanczos-Pade Sweep (ALPS) based solver that extrapolates the entire bandwidth solution from the center frequency[293]. As soon as the center frequency is computed, and the frequency band is extrapolated, a high number of frequency points can be assigned and calculated without a penalty.

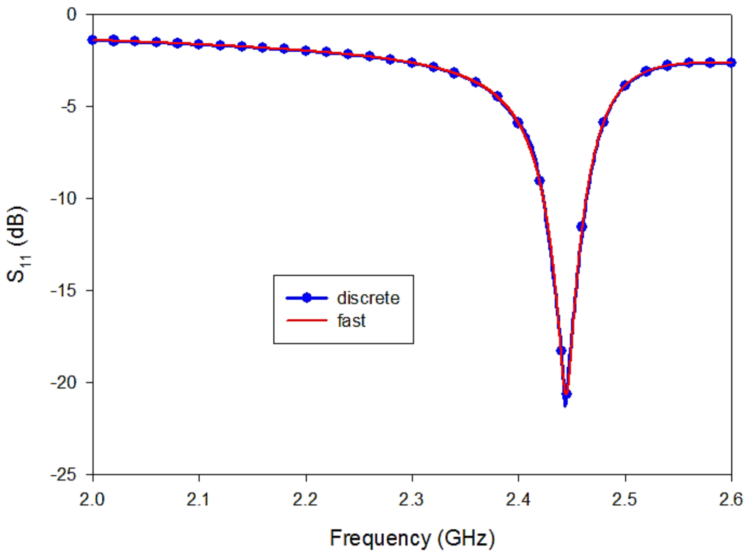

Figure 5.9. Fast and discrete frequency sweep solutions.

And, as a rule-of-thumb in this study, up to a 4 GHz frequency band is suggested to sweep the frequency with high efficiency. As another alternative for frequency sweep, interpolating can be performed, which solves at discrete frequency points that are fit by interpolating. The solver determines the frequency solution based on the error in the interpolation between consecutive passes.

In Figure 5.9, for a given frequency band, fast and discrete sweep algorithms are compared, and a good solution accuracy is obtained for both types. Since a large frequency range is observed to be calculated in a shorter time, with a large number of frequency steps, the fast sweep is used in the simulations.

5.5 EQUIVALENT CIRCUIT MODEL

The structure can be modeled as lumped element circuitry as depicted in Figure 5.10. Z_{in} shows the input impedance due to the excitation (outer loop) transmission line. R_{outer} and L_{outer} represent the losses of the excitation loop by means of conduction and radiation, and the inductance of the outer loop, respectively. For the inner loop which has the split, similarly, due to current circulation, it has inductance as represented by L_{SRR}. R_{cu} and R_r denote the conductive losses and radiated losses on the inner loop, respectively; while R_d shows the dielectric loss caused by the droplet on top of spiral capacitive region which has a capacitance of C_{SRR}. If a change happens in the dielectric constant of the fluid, this will be reflected by a change at C_{SRR}, while a change in the imaginary part of the fluid's permittivity will be revealed through R_d, where the power dissipation in R_d is converted to heat.

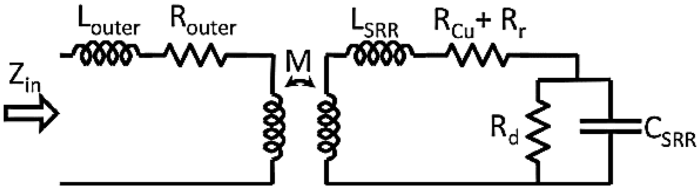

Figure 5.10. Equivalent circuit model of microwave heating/sensing structure [292].

The input impedance can be defined as [292],

$$Z_{in} = R_{outer} + j\omega L_{outer} + \frac{\omega^2 M^2}{Z_r} \tag{6}$$

and

$$Z_r = R_{Cu} + R_r + j\omega L_{SRR} + \frac{R_d}{1 + j\omega C_{SRR} R_d} \tag{7}$$

where M shows the mutual inductance and Z_r is the impedance at the inner loop.

5.6 ANALYSIS OF PASSIVATION LAYER EFFECT

It is clear that the dielectric properties of microfluidic chip components effect the sensing and heating performance of the system. However, the passivation layer used between the microwave transmission lines and the droplet also has a dominant effect. The passivation layer is used in many applications of electrode-liquid based fluidic systems in order to prevent contamination, to make all the channel walls same material, and to prevent short circuits from occurring if capacitive electrodes are in use. The electromagnetic interaction between the droplet and the electric field, generated by the microwave resonator, is also a function of the distance between them. In Figure 5.11 and Figure 5.12 below, the effect of passivation layer thickness (γ_p) on the resonance frequency (f_{res}) and absorbed power inside droplet ($P_{d,abs}$) are shown for case 1 listed in Table 5.2. Otherwise stated throughout the chapter, channel height (H_D), channel width (W_D) and droplet length (L_D) are kept at 40 µm, 200 µm and 400 µm, respectively. As passivation layer thickness increases, the absorbed power decreases dramatically. For thicker γ_p the absorbed power in the droplet does not change too much. This is due to that the droplet is far away from the capacitive region and further increase of γ_p has less impact. Similarly, resonance frequency of the sensor is effected by γ_p significantly at lower passivation layer thicknesses, however, it saturates and shows an asymptotic behavior at higher γ_p. Thus, the

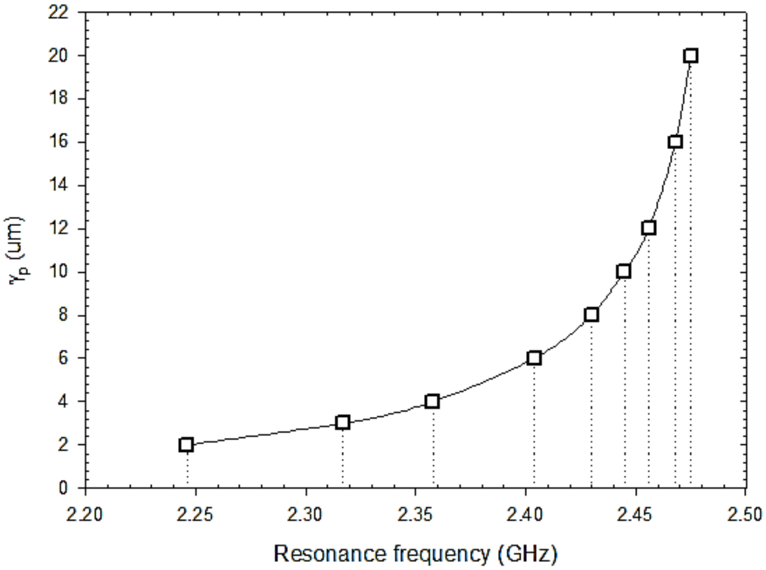

Figure 5.11 Resonance frequency vs passivation layer thickness.

passivation layer thickness is always under investigation in this study.

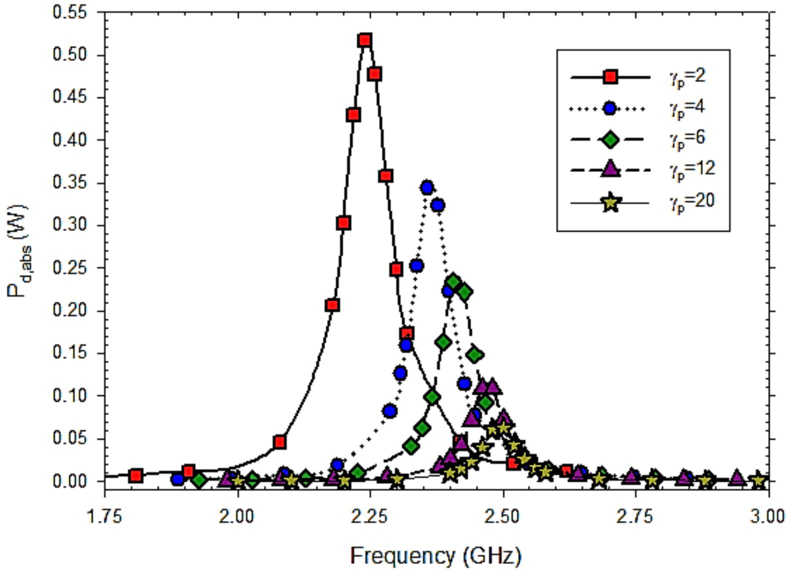

Figure 5.12 Effect of passivation layer on absorbed power inside droplet.

5.7 EFFECT OF LOSS TANGENT OF THE SUBSTRATE

In order to evaluate the effects of the loss tangent and permittivity of the substrate and the chip material, combinations of the parameters listed in Table 5.2 are investigated. These parameters reflect the materials used for a generic microfluidic system. For typical glass, polydimethylsiloxane (PDMS), polycarbonate (PC) and polymethylmethacrylate (PMMA) that are used for microfluidic chip fabrication permittivity falls in the range of ε=2.5-5, and loss tangent has a range of $\tan\delta$=0.005-0.06. And the combinations are used for the numerical analysis of these effects on heating and sensing efficiency.

Figure 5.13 shows the effect of loss tangent of the substrate on absorbed power in droplet for different passivation layer thicknesses. The effect of $\tan\delta_{subs}$ can be analyzed in comparison to lossless case. The cases 1 to 5 from Table 5.2 can be observed for this analysis. Although increasing $\tan\delta_{subs}$ decreases the heat generation inside the droplet, the reduction rate is not the same for different γ_p values. At γ_p=2 um, a 17.9% decrease in heating occurs when $\tan\delta_{subs}$ is 0.01 compared to lossless condition. When $\tan\delta_{subs}$ is further increased to 0.02 (which is doubled), the power absorption inside droplet is not doubled, however, reduces 32.17% further. On the other hand, for thicker passivation layer thicknesses, the decrease in absorbed power is almost constant. This is due to the fact that the droplet is far enough from the heater, which means the effect of distance is almost eliminated, and the reduction in heat is mainly due to the increase in $\tan\delta_{subs}$.

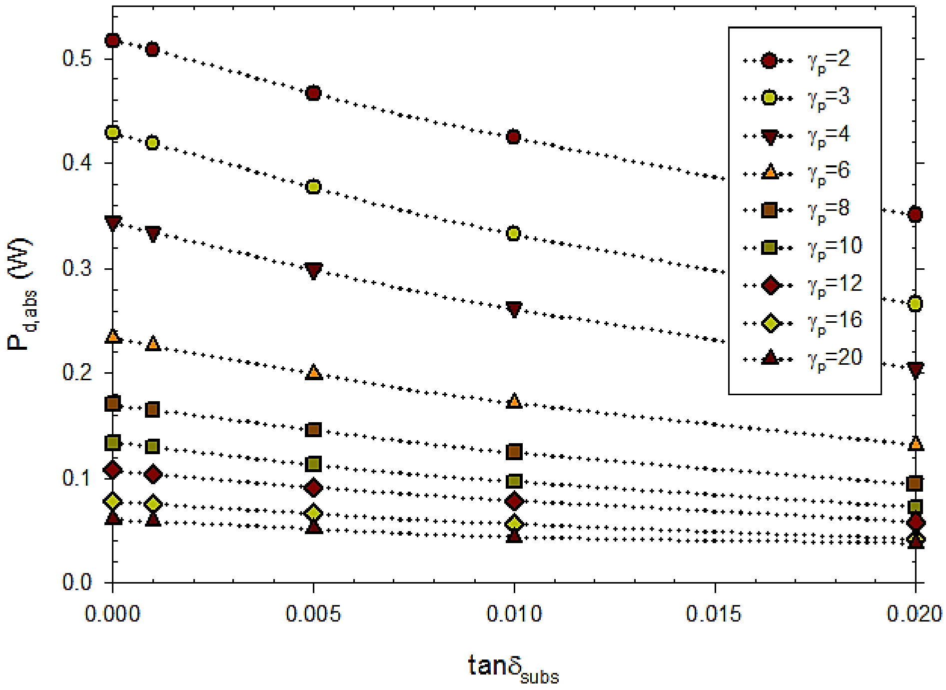

Figure 5.13. Loss tangent of substrate versus absorbed power.

Although $\tan\delta_{subs}$ has an effect on the heating efficiency, it does not dramatically reduce the efficiency. At lower γ_p values (e.g., γ_p=2) with high loss ($\tan\delta_{subs}$=0.02) still over 35% of the excitation power can be confined inside the droplet. However, for critical heating applications and better efficiency, low-loss substrate material should be used. Additionally, $\tan\delta_{subs}$ did not show any significant impact on the resonance frequency.

Table 5.2. Various combinations of chip and substrate material dielectric properties.

Case	ε_{subs}	$\tan\delta_{subs}$	ε_{chip}	$\tan\delta_{chip}$
1	**5.5**	**0**	**3**	**0**
2	**5.5**	**0.001**	**3**	**0**
3	**5.5**	**0.005**	**3**	**0**
4	**5.5**	**0.01**	**3**	**0**

5	5.5	0.02	3	0
6	3	0	3	0
7	7	0	3	0
8	10	0	3	0
9	5.5	0.01	1.5	0
10	5.5	0.01	2.5	0
11	5.5	0.01	4	0
12	5.5	0.01	5.5	0
13	5.5	0.01	8	0
14	5.5	0.01	10	0
15	5.5	0.01	15	0
16	5.5	0.01	20	0
17	5.5	0.01	25	0
18	5.5	0.01	3	0.015
19	5.5	0.01	3	0.03
20	5.5	0.01	3	0.06

5.8 EFFECT OF PERMITTIVITY OF THE SUBSTRATE

Figure 5.14 reveals that increasing ε_{subs} causes a decline in the resonance frequency. This indicates a link between ε_{subs} and C_{SRR}. As described in the section of the Chapter 5.5, due to the spiral gap, a combined split-ring capacitance occurs which is a combination of the parallel capacitances of the substrate, the chip, the passivation and the droplet ($C_{SRR}=C_{subs} + C_{chip} + C_{passv} + C_{drop}$). A higher permittivity for the substrate material allows it concentrate more electric field within it, which increases the capacitance component of C_{subs}, and the overall C_{SRR}. According to the relation between resonance and capacitance change as described by the following equation,

$$f = \frac{1}{2\pi\sqrt{LC}} \qquad (8)$$

the resonance frequency decreases. Furthermore, for $\varepsilon_{subs}=3$, a resonance frequency shift of 332 MHz occurs when γ_p is increased from 2 to 20, which means that the droplet is moved away from the substrate and the resonator. However, a 148 MHz of frequency shift occurs for $\varepsilon_{subs}=10$ for the same γ_p range. This result can be attributed to the fact that since higher permittivity of the substrate suppresses more electric flux within the substrate, this reduces the disturbance effect of the droplet, which causes less sensitivity (frequency shift). On the other hand, another notable result is that absorbed power inside droplet ($P_{d,abs}$) appears to be unaffected by the permittivity of the substrate material, and the only significant change of absorbed power is seen through the passivation layer thickness (γ_p) variation. This is due to that permittivity of the substrate has an impact on C_{SRR} and it effects the resonance frequency but not the R_d.

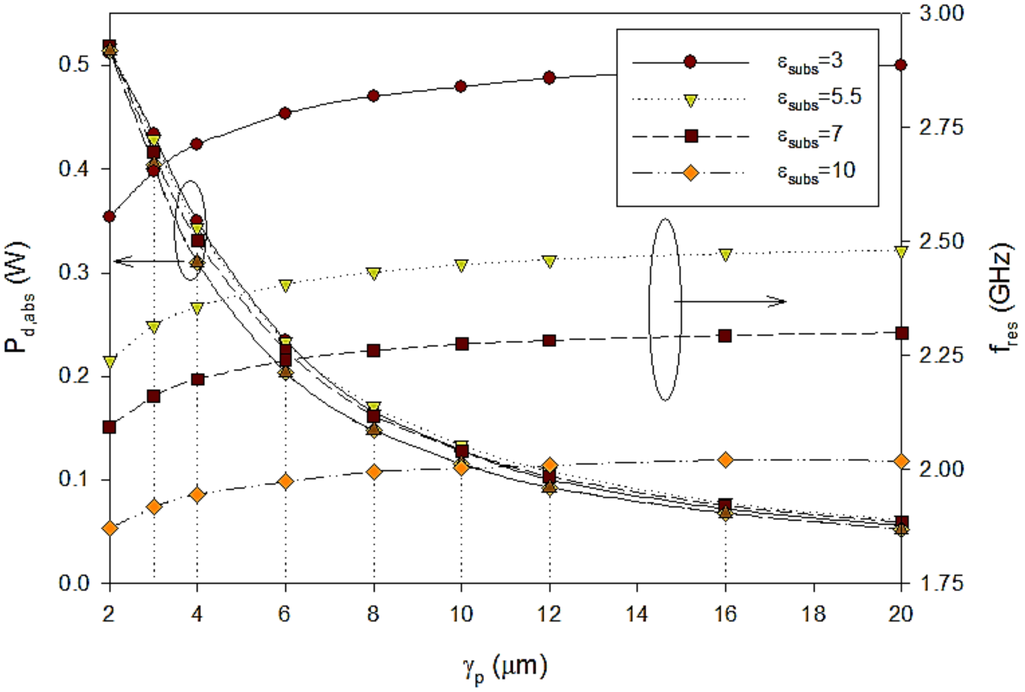

Figure 5.14. Effect of permittivity of substrate on resonance frequency and absorbed power inside droplet.

5.9 EFFECT OF PERMITTIVITY OF THE MICROFLUIDIC CHIP MATERIAL

Similar to permittivity effect of the substrate, discussed above, permittivity of the microfluidic chip material plays a critical role in C_{SRR}. However, the main difference in this situation is that, since the droplet is encapsulated in the chip material, the permittivity of the chip material is expected to have more impact on the absorbed power through the droplet and the resonance behavior. In other words, increasing permittivity of the substrate material concentrates the E-field inside the substrate, which is in the direction opposite to the droplet; the E-field concentration is towards the droplet location and, when permittivity of the chip material increases, this provides more interaction between the droplet and the electrical energy. Figure 5.15 demonstrates the resonance frequency shift behavior at different ε_{chip} values between droplet presence and absence on the resonator for different γ_p. For lower ε_{chip} values, frequency shift increases by increasing ε_{chip}, which increases the sensitivity of the sensor. However, after observing a maximum frequency shift around ε_{chip}=5, further increases of ε_{chip} decreases the shift. This result is attributed to a decrease in the permittivity contrast between the droplet and the chip material. Higher values of ε_{chip} get closer to the droplet permittivity (ε_{drop}=81) which decreases the contrast, in regards to equation (9) before and after disturbance in the E-field;

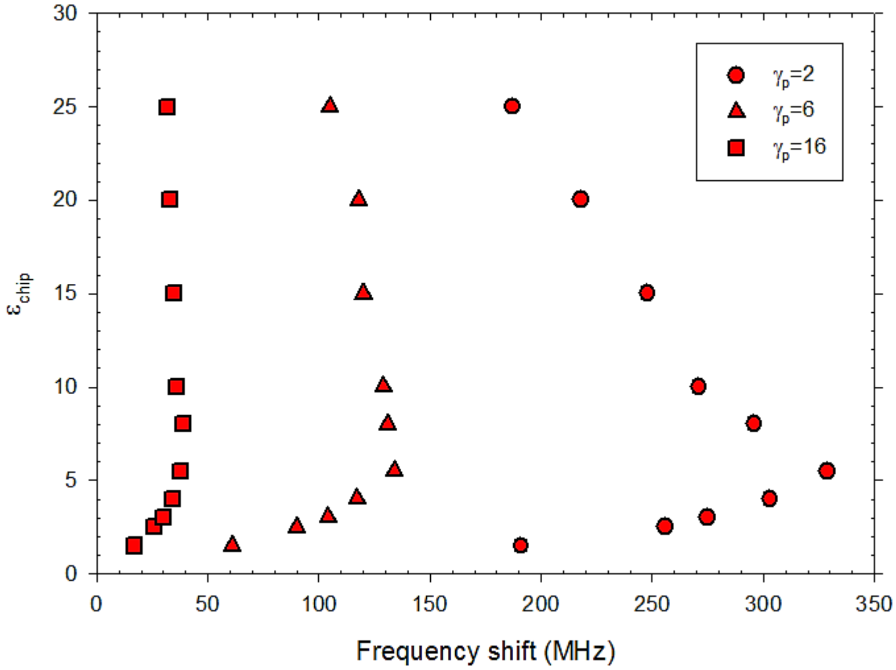

Figure 5.15. ε_{chip} versus frequency shift.

$$\frac{f_{res,1} - f_{res,2}}{f_{res,1}} = \frac{-\int (\Delta\varepsilon \vec{E}.\overrightarrow{Eo})dv}{\int (\varepsilon\vec{E}.\overrightarrow{Eo} + \overrightarrow{\mu H}.\overrightarrow{Ho})dv} \qquad (9)$$

where E_0 and E are the electric fields before and after the perturbation, H_0 and H are the magnetic fields before and after the perturbation, $f_{res,1}$ and $f_{res,2}$ is the resonance frequency before and after the perturbation, ε is the permittivity of the medium and μ is the permeability of the medium.

Ultimately, when ε_{chip} reaches the same value as the ε_{drop}, the frequency shift is expected to be zero since there is no disturbance happening in the E-field due to the droplet. In addition, the combined effect of the passivation layer and ε_{chip} is illustrated in Figure 5.16. As expected a thicker passivation layer increases the resonance frequency since the capacitance of the resonator decreases. At lower ε_{chip} values, the resonance frequency saturates at around γ_p=12 to 16 so that the passivation layer thickness does not change the resonance frequency significantly. This saturation effect is seen at even thinner γ_p values with increasing ε_{chip}. This observation can be accounted for the compensated capacitance difference by C_{chip}. When the passivation layer thickness increases, this causes lowering of the C_{SRR}, yet increase in ε_{chip} raises C_{SRR}, and this compensates for the effect of γ_p at higher ε_{chip} values. Another noticeable result is that a higher ε_{chip} dramatically reduces the resonance frequency; while f_{res} is around 2.6 GHz for ε_{chip}=1.5 at γ_p=2, it goes down to 1.2 GHz at ε_{chip}=25, which is due to its effect on capacitance, as explained previously.

In the meantime, the effect of ε_{chip} on the heating efficiency can be followed from Figure 5.17 by comparing Cases 9-17 in Table 5.2. Figure 5.17 reveals that permittivity of the chip material has a strong influence on the heating performance, and higher ε_{chip} values increases the heating. For values of ε_{chip} =5 and below, a steep fall occurs in heating as passivation layer thickness increases. At thicker γ_p values (γ_p >16) and small ε_{chip} values of 2.5 and less, the heating efficiency almost levels off. However, for higher values of ε_{chip} =~5 and above, heating keeps rising up to a maximum, then gradually decreases with increasing γ_p. Especially, for ε_{chip}=8 and above a sharp rise in heating performance occurs at the beginning until an optimum value, in parallel with γ_p, is reached. It is rather clear that a higher permittivity of the chip material confines more E-field and electrical energy inside the droplet and the chip itself, instead of in the substrate, and this helps with the dissipation of the energy within the droplet. Besides, higher ε_{chip} values alleviates the decay constant of evanescent waves [292],[294],[295].

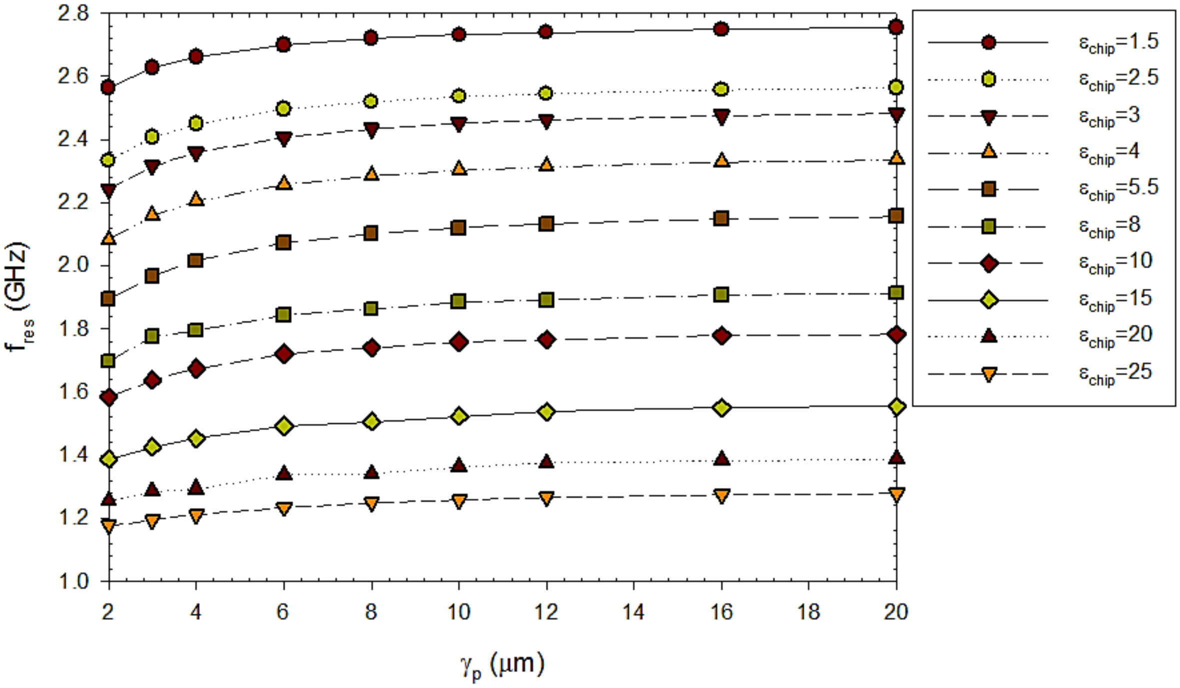

Figure 5.16. Combined effect of passivation layer and ε_{chip} on resonance frequency.

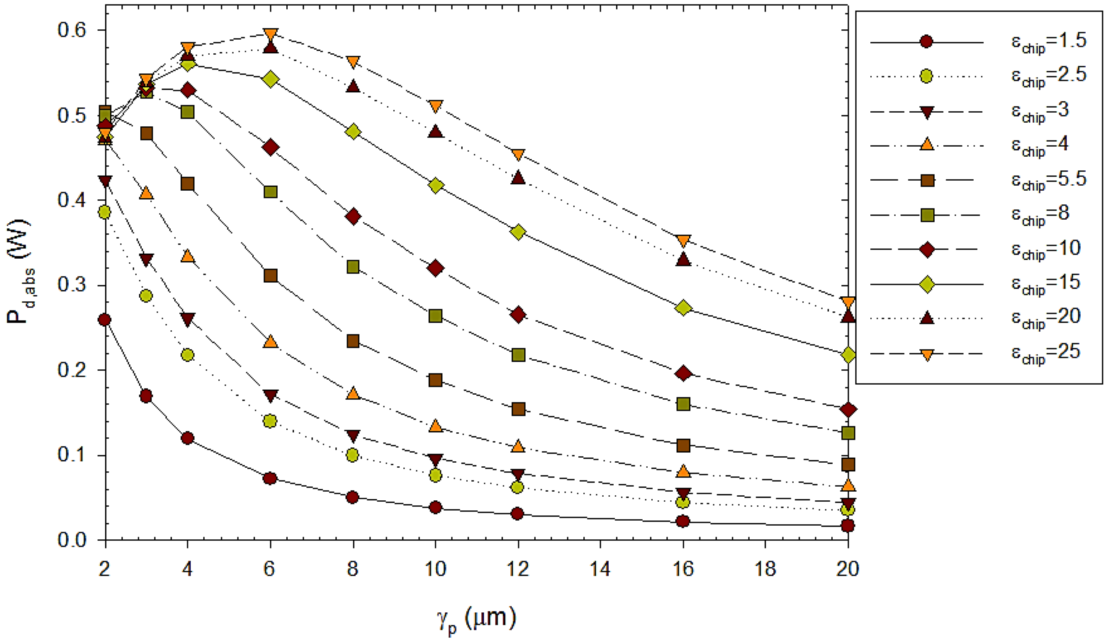

Figure 5.17. Effect of ε_{chip} on absorbed power ($P_{d,abs}$) along with γ_p.

Evanescent waves (or evanescent fields) do not propagate as an electromagnetic wave but they oscillate and concentrate close vicinity of the surface. Evanescent waves from the surface die off exponentially in normal circumstances. However, these results claim that increasing permittivity values of the chip material concentrates the E-field within the chip, which extends the penetration of evanescent fields[292]. It is also worthy to discuss the behavior of the maximum heating with increasing γ_p in detail considering evanescent fields. First, the stepped decrease in droplet heating as the passivation layer thickness increases, is expected due to the fact that the droplet gets far away from the microwave electrode, while the evanescent fields decreases. This phenomena is well observed for low ε_{chip}, as shown in Figure 5.17. Secondly, as the droplet moves away from surface (capacitor), the resistance on the capacitor decreases, which makes the capacitor work more ideally, that increases the quality factor of the resonator. The opposite is also true that when droplet is closer to the capacitor, the reflection of the sensor increases due to the decrease in the quality factor. However, a high quality factor *does not always* mean a higher heating efficiency [292]. The reason behind this is that, while the quality factor is high, the majority of the E-field may not be concentrated inside the droplet at high γ_p. On the other hand, the quality factor may be low due to the droplet being closer to the capacitor.

When it is closer to the capacitor, the droplet can absorb and accumulate more E-field inside it while the quality factor is low, compared to a high quality factor situation. This behavior is a consequence of the coupled relationship among the E-field, γ_p, and quality factor. Therefore, at higher ε_{chip} values, increasing γ_p could cause a higher power absorption by the droplet because of this coupled relation. The relation of the reflection and γ_p is shown in Figure 5.18 for high permittivity case (ε_{chip}=20, case 16 in Table 5.2).

5.10 EFFECT OF LOSS TANGENT OF THE MICROFLUIDIC CHIP MATERIAL

The influences of loss tangent of the chip material on the heating and sensing characteristics of the device are investigated for different passivation layer thicknesses in comparison to the lossless case. Droplet power absorption and the resonance frequency behavior are presented in Figure 5.19 as a function of γ_p, for cases 18-20, compared to case 4 in Table 5.2. PDMS is the most common material used in microfluidic chip fabrication, and it is set at $\tan\delta_{chip}$=0.015 in this study. In order to cover other materials to be used in chip fabrication, and analyze the effect of loss tangent, the combinations of material properties are shown in Table 5.2.

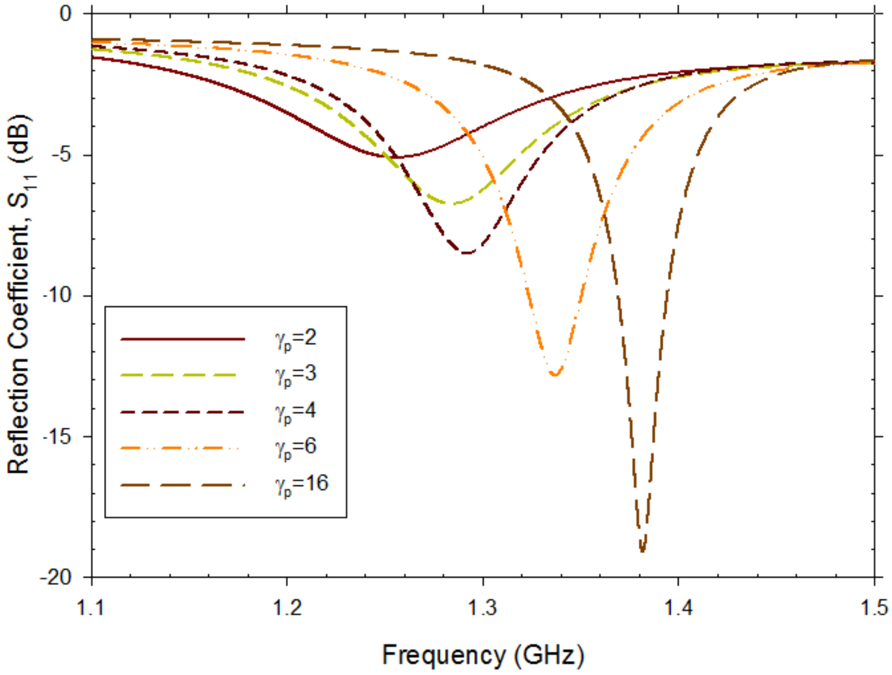

Figure 5.18. Reflection coefficient versus frequency behavior for different γ_p at ε_{chip}=20. Higher γ_p increases the quality factor.

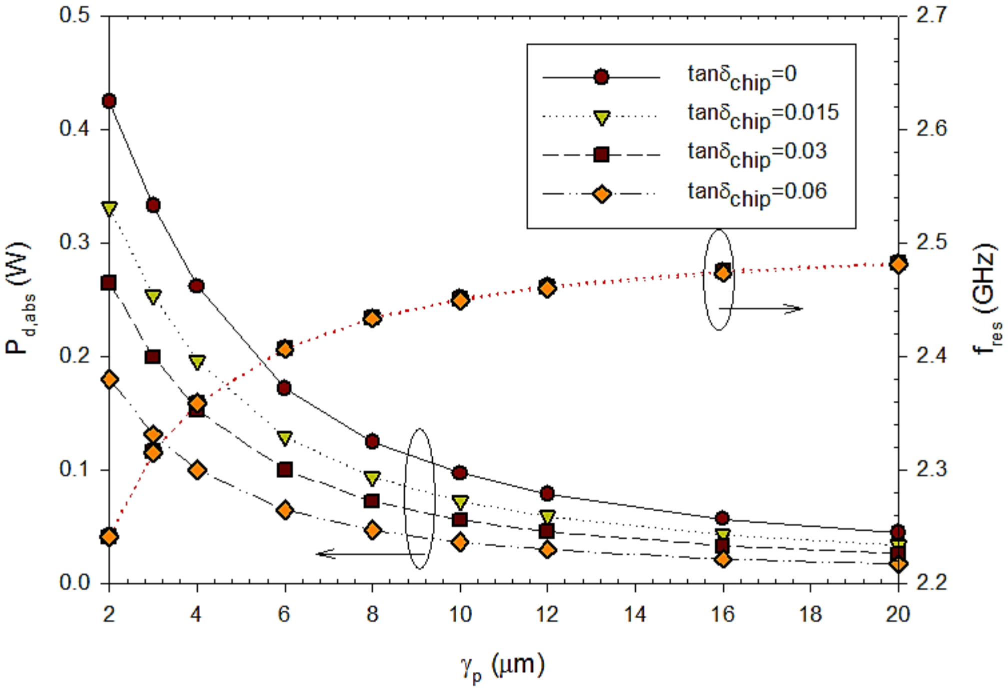

Figure 5.19. Effect of $\tan\delta_{chip}$ on heating efficiency of droplet as a function of γ_p.

As can be followed from Figure 5.19, increasing $\tan\delta_{chip}$ decreases the absorbed power inside the droplet. This is accounted for since, with increasing $\tan\delta_{chip}$, the energy dissipation ability of the chip material increases. The portion of the excited power (feeding power to the system) is absorbed by the chip itself, which causes a reduction in the heat dissipation within droplet. Conversely, the resonance frequency stays the same for varying $\tan\delta_{chip}$ due to that $\tan\delta_{chip}$ does not have an impact on C_{SRR}. Instead, it has the major effect on R_d. At γ_p=2 µm, $\tan\delta_{chip}$=0.015 causes a 22% decrease in the absorbed power, compared to the lossless case. Meanwhile, $\tan\delta_{chip}$=0.03 and $\tan\delta_{chip}$=0.06 causes a 20% and 45.6% decrease in the absorbed power compared to $\tan\delta_{chip}$=0.015, respectively. For thicker passivation layer conditions, the decrease in the heating efficiency is mainly due to γ_p, the effect of $\tan\delta_{chip}$ becomes less important and is masked by γ_p. Table 5.3 lists distribution of the absorbed power in the structure from different sources for the case 4 and cases 18-20 at γ_p=2. Evaluation of the absorbed power distribution shows interesting findings on the strong coupling between the effecting parameters. As expected increasing $\tan\delta_{chip}$ decreases the absorbed power through the substrate ($P_{subs,abs}$), as well, besides $P_{d,abs}$. However, increasing $\tan\delta_{chip}$ decreases the conductive loss on the inner ($R_{cond,inner}$) and outer ($R_{cond,outer}$) loop, while radiated power (P_{rad}) is increased.

Table 5.3 Distribution of the absorbed power in the integrated structure.

Loss (W)		Dielectric			Conductive		Radiated
		$P_{d,abs}$	$P_{subs,abs}$	$P_{chip,abs}$	$R_{cond,inner}$	$R_{cond,outer}$	P_{rad}
γ_p=2	Case 4	0.4241	0.1195	0	0.2326	0.0089	0.1624
	Case 18	0.3306	0.0948	0.1258	0.1817	0.0074	0.1737
	Case 19	0.2646	0.0776	0.2040	0.1464	0.0066	0.1821
	Case 20	0.1799	0.0555	0.2859	0.1008	0.0055	0.1965

These results propose that, as long as there are available fabrication techniques to make microfluidic chips, choosing a low loss chip material is a better option for microfluidics/droplet heating purposes.

5.11 EFFECT OF W_D, L_D AND H_D

Dielectric properties of the chip materials and their combinations have great importance on the heating and sensing characteristics, as presented above. In addition, the disturbance and concentration of the E-field that is in close vicinity to the microwave resonator is also another aspect that effects the device performance. This is caused, in droplet microfluidics/Lab-on-a-chip platforms, through the channel geometry, droplet size, aspect ratio and the passivation layer thickness. In this study, the droplet regime is taken as operating within the squeezing regime, where droplet fills the entire microchannel. Thus, the droplet or channel width (W_D) and height (H_D) represent the same geometrical parameters. Moreover, the length of the droplet (L_D) should be considered. In this regard, the effect of channel height and width as well as droplet length are investigated on the resonance frequency and the heating behavior.

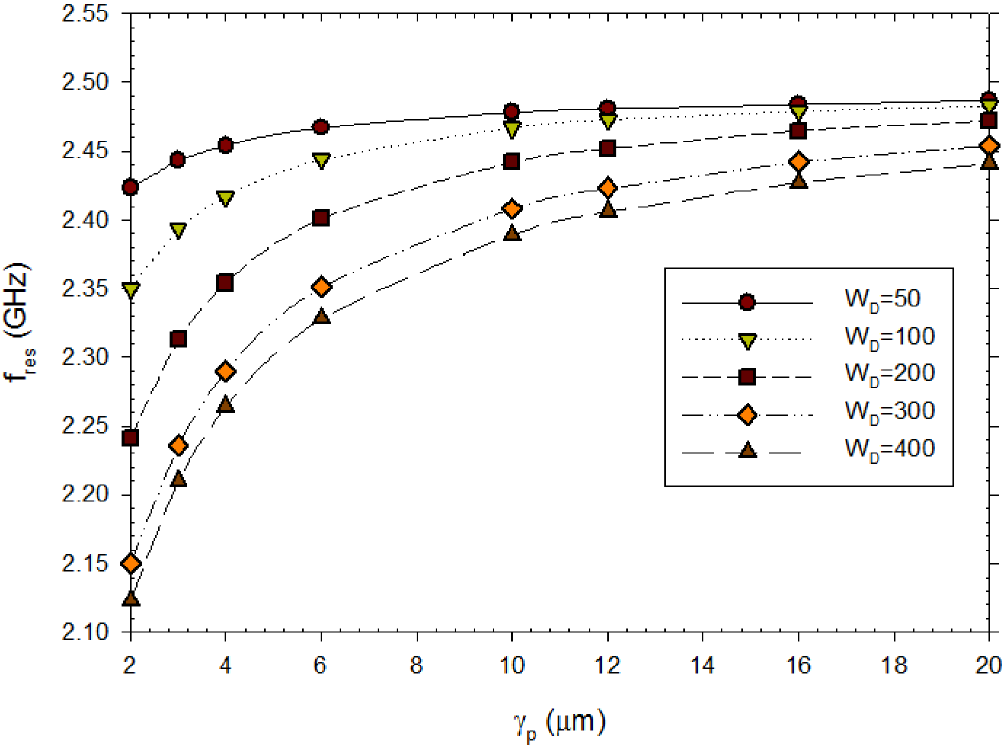

Figure 5.20. Effect of channel width on resonance frequency along with γ_p.

Figure 5.20 shows the effect of the channel width on the resonance frequency and γ_p. Increasing the channel width effects the resonance frequency significantly. For instance, the resonance frequency shifts 318 MHz from γ_p=2 to 20 at W_D=400 µm, while it shifts only 64 MHz for the same γ_p range and at W_D=50 µm. Although, the majority of the capacitance happens between the legs of the spiral design, the junction region which connects the spiral design to the inner (split) inner has capacitance as well. This is the reason that increasing W_D increases C_{SRR}, which reduces f_r. On the other hand narrower channel width only disturbs small portion of the spiral capacitive discontinuity that causes less effect on C_{SRR}, and this almost eliminates the effect of γp on f_r for narrower channel width case (e.g., W_D=50 µm).

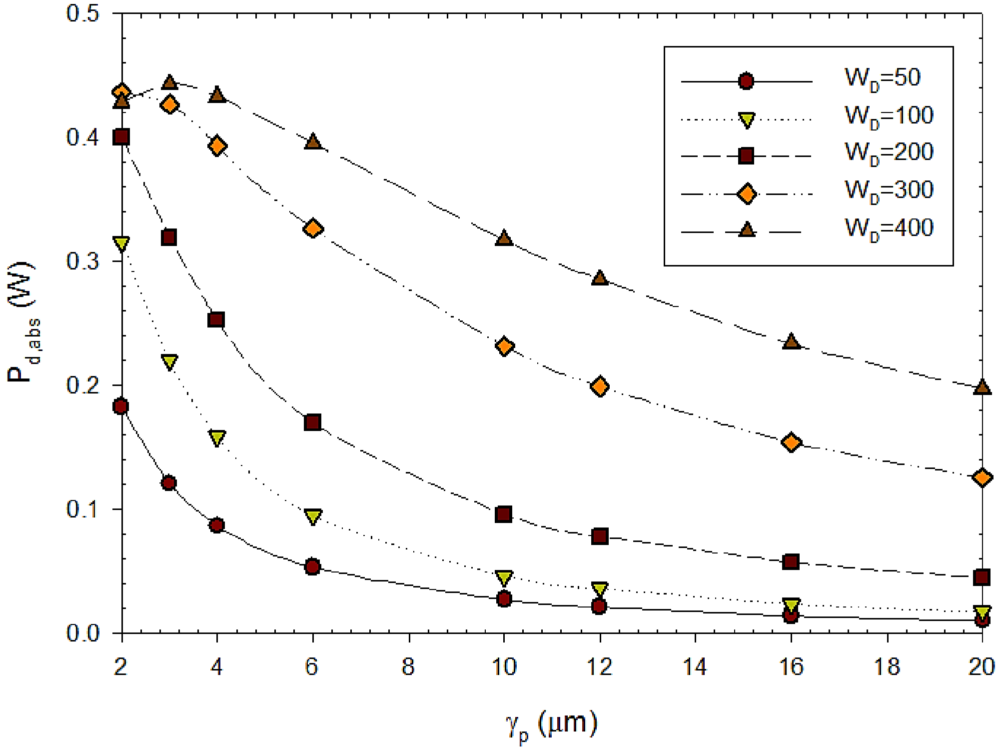

Figure 5.21. Absorbed power within droplet versus W_D and γ_p.

For the heating characteristics, the effect of W_D presents an interesting behavior (see Figure 5.21). A W_D value wider than the resonator size, demonstrates a similar impact as the higher ε_{chip} effect does, as was analyzed above (Figure 5.17). A constant decrease is expected in the absorbed power within the droplet as γ_p increases due to that droplet moves away from the resonator. However, while this is true up to W_D and the resonator sizes (spiral gap) are the same, for larger values of W_D than that of the spiral gap, as γp increases initially $P_{d,abs}$ increases. Then after a maximum is reached, it starts decreasing, but the decrease is not sharp compared to the case that W_D is smaller than the spiral gap. This result suggests that, at relatively higher γ_p values, better heating performances can be obtained.

As can be seen from Figure 5.22, droplet length has negligible influence on the absorbed power and the resonance frequency. This result suggests that as long as L_D is larger than the size of the spiral gap, f_{res} and $P_{d,abs}$ keep the same sensing and heating performance. However, since the absorbed power is the same for different L_D, and longer droplet length means higher volume of the droplet, the temperature of the droplets will be different.

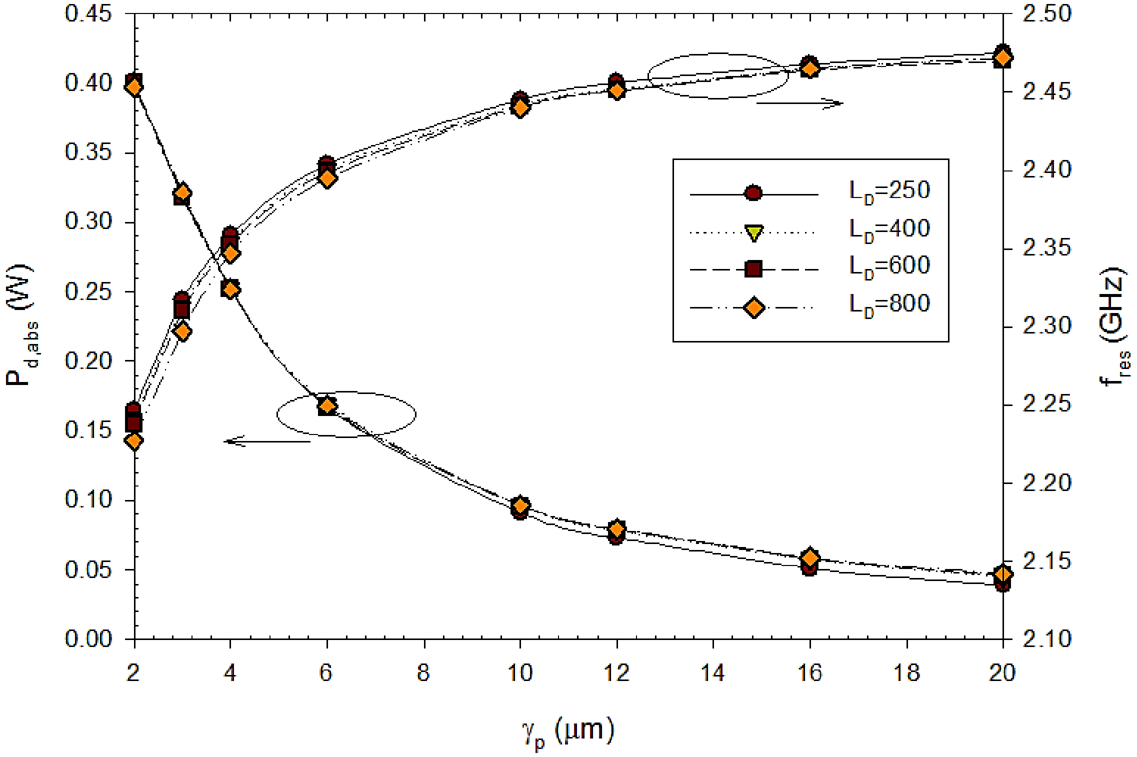

Figure 5.22. Effect of L_D on f_{res} and $P_{d,abs}$.

Interestingly, a similar results are observed for the effect of the channel height, H_D. For a range of H_D between 20 and 100 μm, channel height has negligible impact on the absorbed power by the droplet and the resonance frequency behavior (see Figure 5.23). However, as mentioned above, due to that droplet volume varies with H_D, temperature of the droplets at different channel height values will be different.

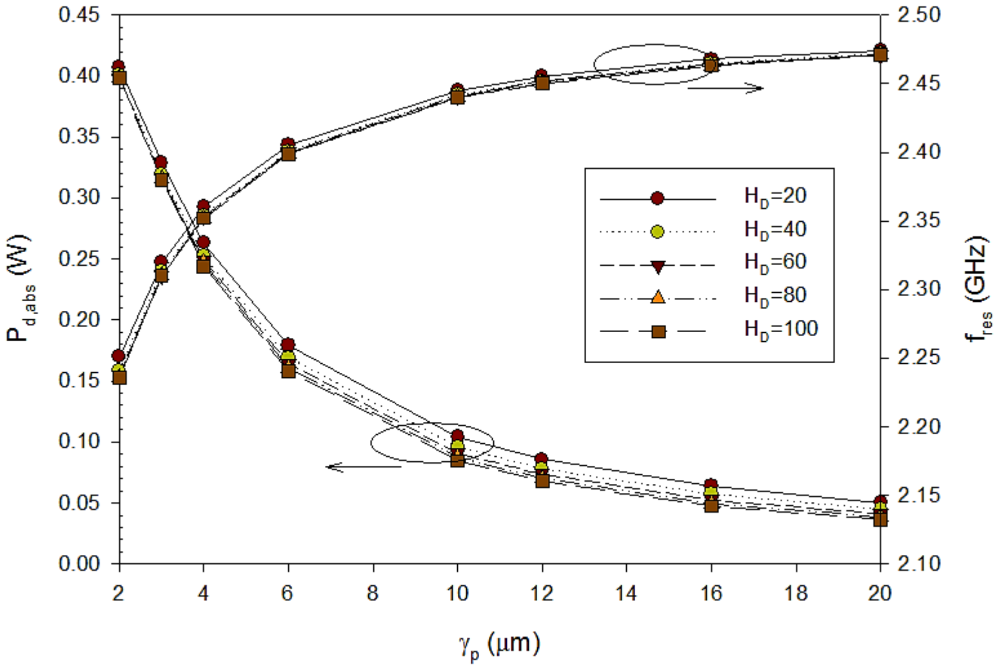

Figure 5.23. Effect of H_D on f_{res} and $P_{d,abs}$.

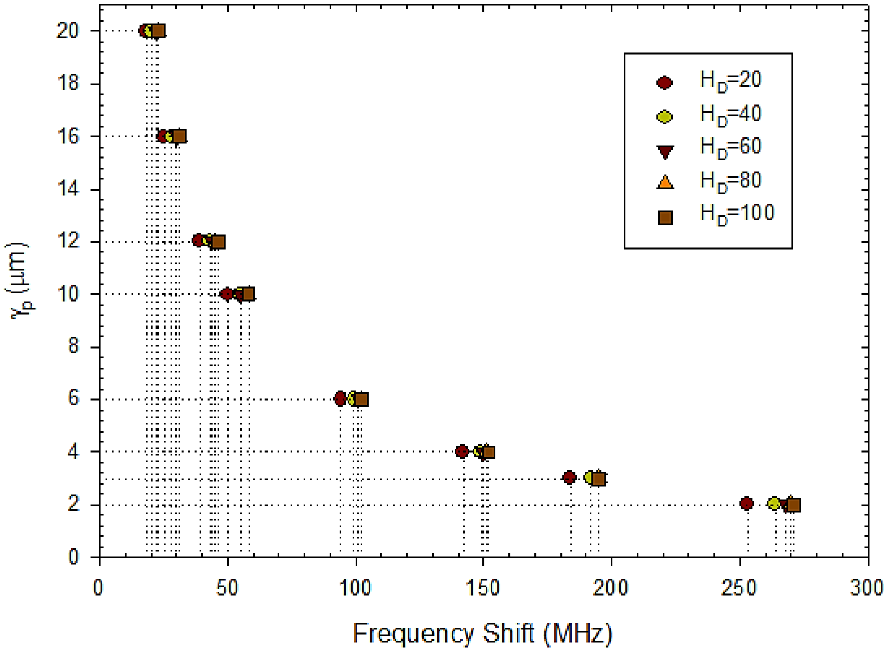

Figure 5.24. Effect of H_D on frequency shift.

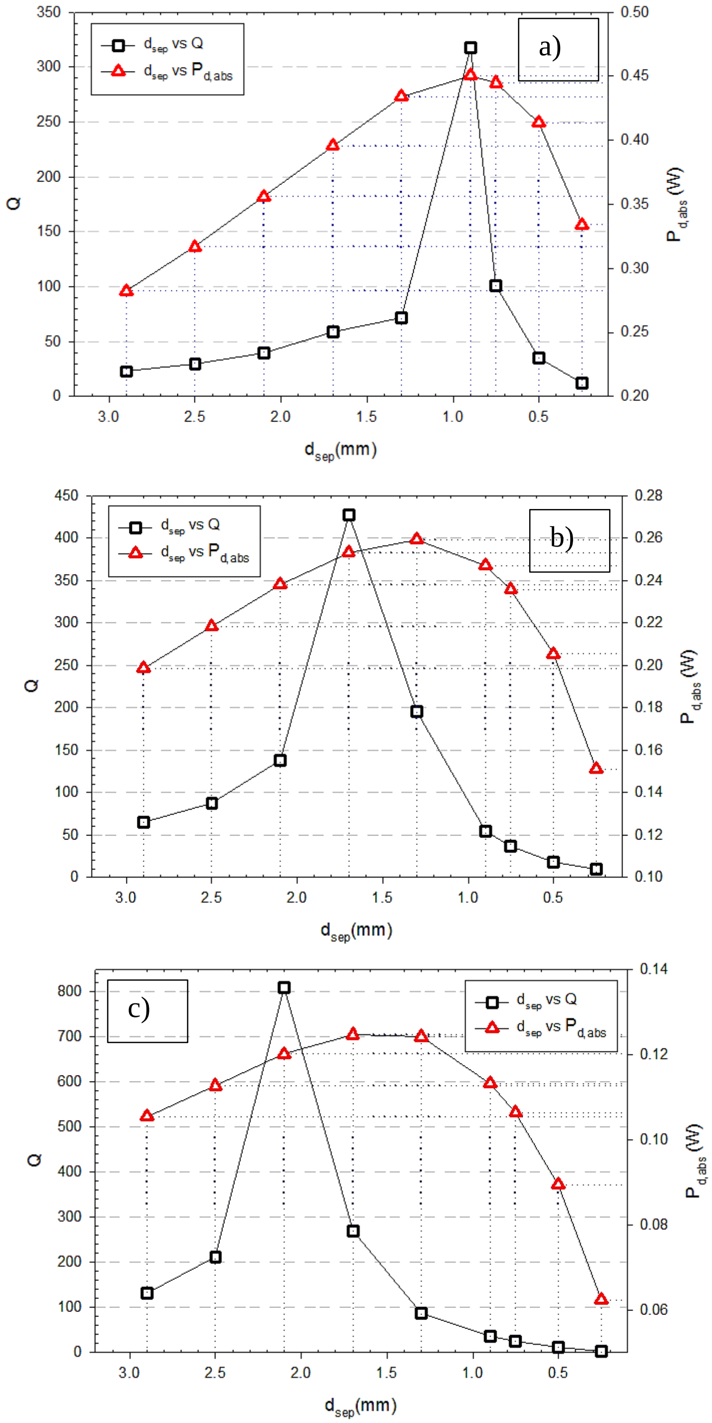

Figure 5.25. Mutual coupling effect on quality factor and $P_{d,abs}$ for a) γ_p=2, b) γ_p=4 and c) γ_p=8.

Additionally, the effect of H_D on the resonance frequency shift is investigated for the presence and absence of the droplet over the microwave resonator. This case simulates the resonator sensitivity for a permittivity change between 81 (droplet permittivity) and 2.1 (oil permittivity). A noticeable frequency shift is observed between different H_D values when γ_p is lower than 6 μm. Increasing channel height causes a larger frequency shift for this range of γ_p. At $\gamma_p=2$ and $H_D=100$, droplet presence over the resonator causes a 271 MHz frequency shift (see Figure 5.24).

5.12 MUTUAL COUPLING EFFECT

Subsequently, mutual coupling effect between the excitation (outer) and split (inner) loop is analyzed through the variation of separation distance (d_{sep}) between the two loops. Figure 5.25 demonstrates the effect of d_{sep} on the quality factor of the resonator and the absorbed power through the droplet at different γ_p. Results indicate that as γ_p increases the optimum d_{sep} switches to larger separation distances. For example, at $\gamma_p=2$, while the quality factor is around 50 for $d_{sep}=1.7$, it increases beyond 300 for $d_{sep}=0.9$ at the same γ_p. Likewise, the absorbed power increases by 13% with the change of the distance from $d_{sep}=1.7$ to $d_{sep}=0.9$. For optimum heating and sensing performance, it necessary to consider the separation distance between the loops corresponding to the passivation layer thickness used.

5.13 CONCLUSIONS

A numeric and parametrical analysis in order to understand better the performance of the integrated platform, the microwave resonator structure and the behavior of the dielectric properties of the microfluidic chip components on sensing and heating efficiency are investigated. Since the sensor is operating at high frequencies, the design of the system is very sensitive to these parameters such that any improper design may cause sharp performance damping than the actual capability of the device. In order to control the microwave sensing and heating functionalities for an appropriate Lab-on-a-chip platform development, findings in this study can be used as a guidance.

Nomenclature

PDMS	Polydimethylsiloxane
E	Electric field
H	Magnetic field

Z	Impedance
ΔS_{max}	Maximum change in consecutive S-parameter calculation
L	Inductance
C	Capacitance
L_{SRR}	Inductance on inner (split) loop
L_{outer}	Inductance on outer (excitation) loop
C_{SRR}	Capacitance due to the spiral gap
C_{subs}	Capacitance due to the substrate
C_{chip}	Capacitance due to the chip mold
C_{passv}	Capacitance due to the passivation layer
C_{drop}	Capacitance due to the droplet
Z_{in}	Input impedance
Z_r	Impedance at the inner loop
M	Mutual capacitance
R_{cu}	Resistance due to conductive losses
R_r	Resistance due to radiation
R_d	Resistance due to dielectric loss within the spiral capacitor
F	Frequency (GHz)
f_{res}	Resonance frequency (GHz)
Δf	Frequency shift (MHz)
$P_{d,abs}$	Absorbed power through the droplet (W)
$P_{subs,abs}$	Absorbed power through the substrate (W)
$P_{chip,abs}$	Absorbed power through the chip (W)
P_{rad}	Radiated power (W)
$R_{cond,inner}$	Conductive loss in the inner loop (W)
$R_{cond,outer}$	Conductive loss in the outer loop (W)
W_D	Microchannel and droplet width (µm)
L_D	Droplet length (µm)
H_D	Droplet and channel height (µm)
d_{sep}	Separation distance between the inner and outer loops (µm)
Q	Quality factor

Symbols

ε	permittivity
σ	conductivity
μ	permeability
ω	angular frequency
λ	wavelength
γ_p	passivation layer thickness (µm)
ε_{chip}	permittivity of chip material
ε_{subs}	permittivity of substrate material
$\tan\delta_{chip}$	loss tangent of chip material
$\tan\delta_{subs}$	loss tangent of substrate material

Chapter 6

EFFECTIVE THERMO-CAPILLARY MIXING IN DROPLET MICROFLUIDICS INTEGRATED WITH MICROWAVE HEATER[3]

6.1 MOTIVATION

In many microfluidic applications rapid, on-demand mixing is crucial because of the need of homogenization of multiple reagents in bio-chemical reactions, drug delivery and synthesis of nucleic acids, as well as dissolving enzymes and proteins in liquids where analysis take place[296,297]. However, mixing in microfluidics is challenging due to its laminar flow nature and is often dominated

---

[3] The contents of this chapter have been previously published in Analytical Chemistry (ACS) 89, 1978-1984 (2017), by Yesiloz G., Boybay M.S. and Ren C.L., as "Effective Thermo-Capillary Mixing in Droplet Microfluidics Integrated with a Microwave Heater". G.Y. launched the idea and methodology, designed and executed experiments; G.Y. and C.L.R. worked on evaluation of the results, fostered by M.S.B.; G.Y and C.L.R. contributed to the paper writing.

by molecular diffusion. For this reason, many strategies have been reported[298-300] to enhance mixing using different methods as outlined in recent review articles[301-302].

In general, microfluidic mixing mechanisms can be classified as active and passive methods, while active techniques utilize external forces to perturb the fluid flow, passive techniques rely on particular microchannel designs to increase con-tact time or area between different reagents[50,302]. Most passive mixing methods employ one or a combination of several of the following techniques: splitting-and-recombination, chaotic advection, serial and parallel lamination, serpentine channels, injection and droplets[303-304]. Although passive methods operate without the need for additional external components, they have limitations such as long mixing lengths (> a few centimeters) which may result in unmixed regions and low efficiency for mixing highly viscous fluids[304-305]. In addition, fabrication of such mixers likely experience higher risks for failure due to their complex channel configurations. In contrast, active methods have the potential to overcome these limitations with the cost of incorporating active control components to induce external disturbance to the flow. Common active methods for microfluidic mixing include dielectrophoresis[306],[307], electro-kinetics[308-310], magneto-hydrodynamics[311-314], thermal[315-316], pressure[317-318] and acoustics[319-323]. Despite the success of various active mixing methods, there are still challenges for achieving rapid mixing, usually limited by the actuation and response time of the system[305]. Effective mixing of highly viscous fluids often requires increasing the magnitude of the external source and thus power consumption[305]. Integration of active control components with a single microfluidic chip also remains a challenge as well due to relatively large system footprints.

It is well known that rapid mixing can be achieved in droplet microfluidics because of the three-dimensional (3D) flow occurring within them. However, 3D flow only occurs within each half of the droplet[324-326] if they are travelling through straight channels and mass transfer in the transversal direction still relies on molecular diffusion as shown by the measured flow pattern in droplets using PIV techniques[324]. Boybay et al. [260] attempted to employ microwave heating to mix two halves of a droplet, one half filled with fluorescent dye and the other pure water, but failed unfortunately. Mixing of the reagents within the entire droplet is usually realized by pumping it through serpentine channels[327], which induces 3D flow within the entire droplet or by agitating it using active means such as laser or acoustic wave. With the promising potential of droplet microfluidics as enabling tools for high throughput analysis, developing methods to achieve rapid mixing within droplets without the need for long or serpentine channels is important.

For this reason, in this study, a microwave based thermocapillary microfluidic mixer that enables almost instantaneous mixing, requires simple integration with microfluidic devices, and consumes less than 0.5W of power is presented. It is demonstrated that it has excellent performance in mixing highly viscous fluids within nanoliter-sized droplets. More importantly, this microwave mixer can also trigger and initiate reactions at the same time of mixing using the microwave energy. To the best of my knowledge, thermo-capillary mixing of droplets via an integrated microwave source is the first time to be successfully achieved. This work demonstrates a very unique approach of utilizing microwave sensor technology to facilitate in microfluidics mixing.

6.2 METHODOLOGY

6.2.1 MATERIALS AND EXPERIMENTAL METHODS

The experimental setup consists of a microfluidic chip integrated with a microwave resonator, which is the heater as well, a microwave signal generator (HMC-T2100, Hittite), a vector network analyzer (VNA) (MS2028C, Anritsu), a fluid pumping unit (Fluigent MFCS-8C) and an inverted microscope (Eclipse Ti, Nikon) equipped with a CCD camera (Q-imaging). The schematic description of the integrated mixer unit is demonstrated in Figure 6.1, where the microwave heater is a concentric ring structure with the outer ring excited at a desired operating frequency and provided with power through the signal generator and the inner ring resonating accordingly. The signal generator was controlled via a computer and the VNA was used to characterize the microwave resonator. Droplets were generated using a flow focusing generator where the continuous phase is a fluorinated oil, FC-40 (Sigma-Aldrich) and the dispersed phase consists of an aqueous solution and the same solution seeded with fluorescent dye that were flowing side by side before reaching the generator. The aqueous solution was varied from pure water to a highly viscous liquid, 75% (w/w) glycerol solution, with a viscosity of 35.5 mPas at 20 ºC. A Y-channel design was used to generate the side by side dispersed flow streams. Fluorescent dye, Thioflavin S (ThS) (Sigma-Aldrich) was used to seed one of the flow streams and the mixing performance was evaluated using the fluorescent images obtained through the microscope and CCD camera. The acquired images were processed using ImageJ (National Institute of Health, MD, USA).

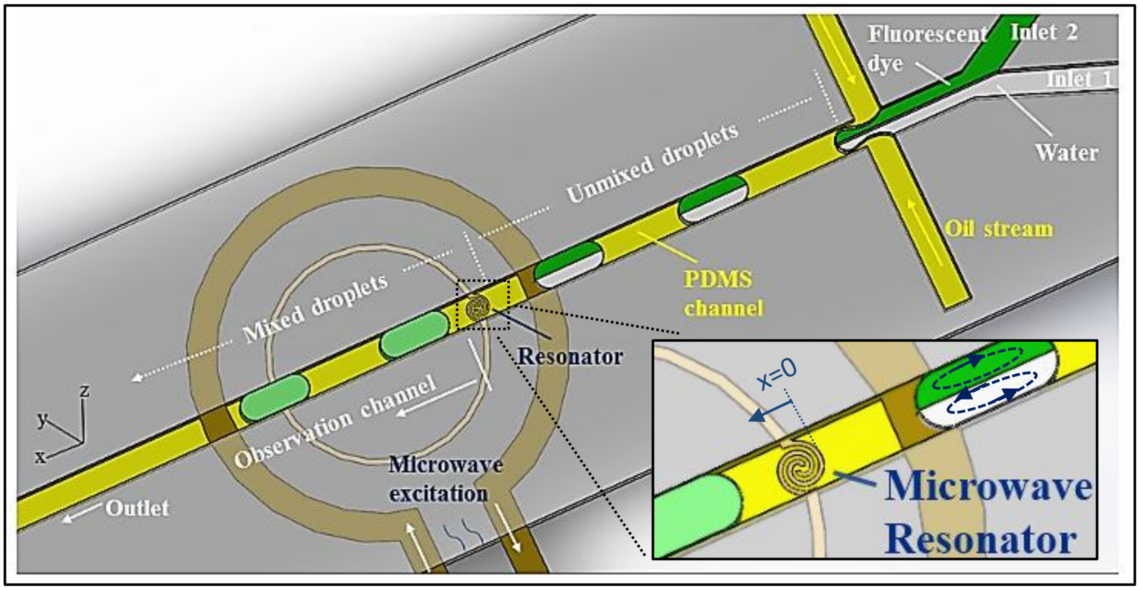

Figure 6.1 Schematic description of the microfluidic mixer.

6.2.2 DEVICE FABRICATION

The mixing device consists of a PDMS mold with the designed microchannels for droplet generation and transport and a microwave sensor; a glass base with the microwave components. On top of the microwave sensor is a thin layer of SiO2, which was coated on the sensor using magnetron sputtering (AJA Orion 5) techniques. This layer was designed to prevent direct contact between the working fluids and metal-made sensor to avoid any contamination. Its thickness is around 500 nm, which is estimated using the protocol of the sputtering system. The electrical traces for the microwave components were fabricated using a combination of photolithography and electroplating.

Briefly, the positive photoresist, S1813 (Rohm-Haas), was spin-coated at 1500 rpm for 60 s onto a 50 nm thick copper film (EMF Corporation) that had been predeposited on a glass slide and then baked at 95 ℃ for 120 s. The design was patterned into the photoresist via UV lithography and subsequently developed with MF-319 (Rohm-Haas) for 2 min. The patterned slide is then immersed in an acidic copper electroplating solution (0.2 M CuSO4, 0.1 M H3BO3, and 0.1 M H2SO4) and electroplated at 2 mA for 5 min and 4 mA for 10 min. After electroplating, the photoresist was removed with acetone leaving an electroplated copper film approximately 2 μm thick. Next, the base layer of predeposited copper was removed by etching with dilute ferric chloride (5%) (MG Chemicals). SiO2 was deposited on top of it. A subminiature version A (SMA) connector (Tab Contact, Johnson Components) was then soldered to the electrodes of the microwave components to provide an external connection to the microwave signal generator. For the fabrication of microfluidic chips, SU-8 masters were fabricated on silicon wafers using the same soft-lithography technique developed previously. In order to make PDMS replica molds, PDMS prepolymer was mixed at a 10:1 ratio of base to curing agent, degassed, and molded against the SU-8/ silicon master and then cured at 95 °C for 2 h. The molds were then peeled off from the master, and fluidic access holes were made using a 1.5 mm biopsy punch. Both the finished microwave components and the PDMS mold were then treated with oxygen plasma at 29.7 W, 500 mTorr for 30 s. The plasma treatment process renders PDMS hydrophilic; however, for generating water in oil droplets stably, the PDMS channels need to be hydrophobic which was realized by coating Aquapel (PPG Industries) onto the channel surface.

6.3 MIXING MECHANISM AND DEVICE WORKING PRINCIPLE

The working principle of the microwave-microfluidic mixing device is shown in Figure 6.1. Droplets are transported through a straight microchannel and when there is not any disturbance, two symmetric counter-rotating recirculation zones are formed in each half of the droplet, which creates a barrier limiting the mixing between the two halves through diffusion. The flow topology and internal dynamics inside droplets were studied in detail elsewhere[325],[326] using μ-PIV techniques. A complete mixing happens when these two halves are agitated in the cross-stream direction. The essential element and main trigger of the mixing, herein, is the localized microwave heater, which works as a microwave resonator fundamentally.

The resonator structure is made of two concentric copper loops similar to the one presented previously[281],[328]. Microwave signal is excited via the outer coplanar transmission line loop, which supplies a time-varying oscillating current circulating around the loop and a magnetic field passing through the loop. The inner loop with a small gap constructs the resonator and the microchannel where droplets are passing through is aligned on top of this gap perpendicularly. Microwave energy is inductively coupled to the resonator by the excitation loop and there is no physical contact between the two loops. In this microwave structure, the electric field energy is stored within the capacitor of the resonator (the spiral region) and the magnetic field energy is stored in the inductor of the resonator. When there is a perturbation in the permittivity of the medium, the resonance frequency of the microwave structure shifts. For example, when a droplet with aqueous solutions enters the resonator region, it causes a shift in the operating frequency because of its different electrical properties from those of the continuous oil phase. This shift could be used to sense the droplet content and heat the droplet if power is supplied to the resonator only at the shifted frequency associated with the droplet content. After the droplet completely leaves the resonator region, the operating frequency shifts back to that associated with the oil and no energy is received. Therefore, the microwave heating is self-triggered, remote and selective.

The electrical field in the resonator region is three-dimensionally nonuniform as shown in Figure 6.2[329], which is a numerical prediction using a commercial software, Ansys HFSS. It can be seen that the spiral region has a high and intense E field and the rest of the structure holds very weak E field, which is negligible in comparison to the spiral. This confined electric energy is transferred to droplets with the relation be-tween the volumetric power and the electric field intensity by the following equation

$$P = \frac{1}{2}\omega\varepsilon_0\varepsilon^{"}|E|^2 \qquad (1)$$

where ω is the angular frequency, ε_0 the permittivity of free space, ε'' the imaginary part of the relative permittivity and E the electric field intensity. For further analysis, the distribution of volume loss density inside droplet and the electric field at different magnitudes can be found in Figure 6.2 and Figure 6.3, respectively.

The nonuniform energy distribution within droplets results in nonuniform temperature distribution which induces spatial variation in fluid properties such as density, viscosity, diffusion coefficient and interfacial tension. The temperature-dependent fluid properties induce cross-stream flow enhancing 3D mixing within droplets. In general, when a droplet is passing through a straight channel without any external disturbance, the mixing is governed by symmetries in the flow that brings invariant surfaces which causes suppressed mixing[299],[330]. Grigoriev et al.[299] presented a theoretical analysis on the existence of invariant surfaces inside droplets and reported that the presence of chaotic advection *does not guarantee* a full mixing, which requires a mechanism to destroy the symmetry (flow invariant). The microwave induced spatially non-uniform temperature distribution over the entire droplet over-comes symmetries resulting in 3D mixing. Moreover, the motion of droplet dynamically influence the electrical field which further enhances the chaotic motion and thus mixing within the droplet.

The mixing mechanism is a complex phenomenon involving the understanding of nonuniform electrical field, non-uniform energy distribution within droplets and their strong dynamic coupling, which is beyond the scope of this study. In order to shed light on the mixing mechanism, magnitude analysis on the influencing parameters is performed using the Buckingham Pi theorem[331],[332],[333], which is presented below.

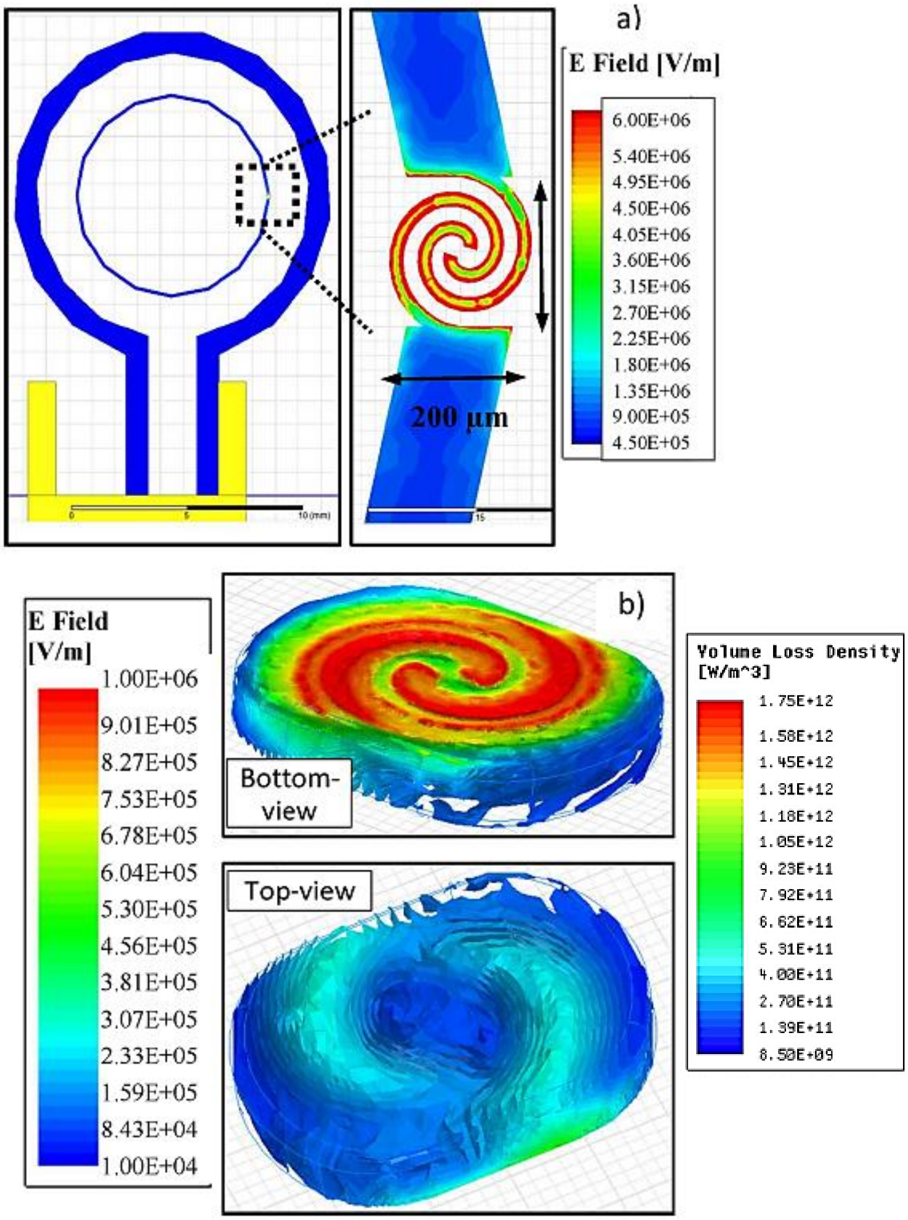

Figure 6.2 Operating mechanism of the microfluidic mixer, nonuniform electrical field and volume loss density distribution inside droplet[329].

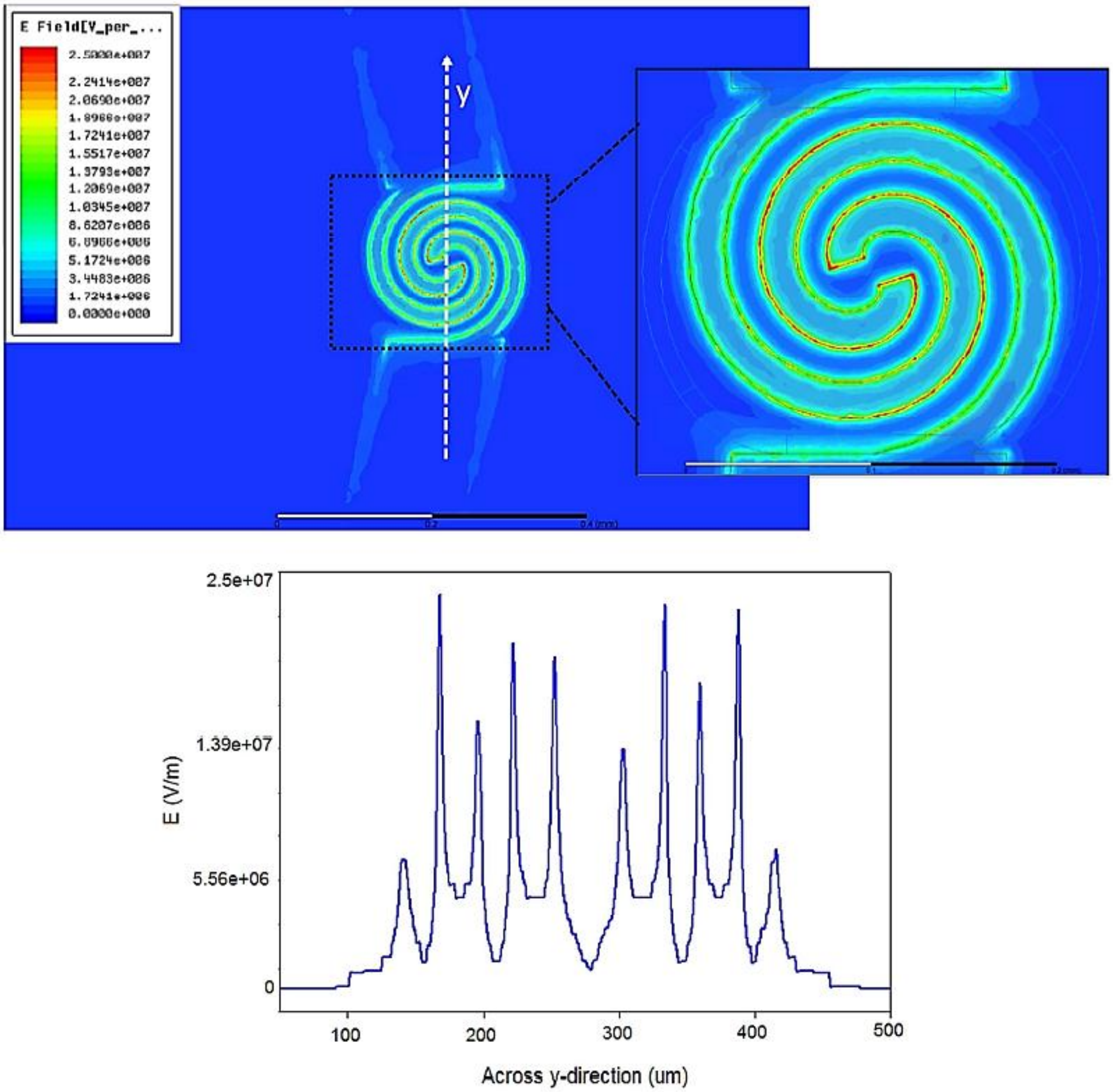

Figure 6.3 Along the y-direction, which is across the droplet (channel) width, high electrical field peaks occur at the edges of the spiral legs, which results in non-uniform heat dissipation inside the droplet.

6.4 BUCKINGHAM PI THEOREM FOR ANALYSIS OF COMPETING FORCES

Mixing index (MI) that indicates the mixing efficiency is influenced by both the fluid properties and operating conditions, which can generally be described as,

$$MI = f\left(P_{exc}, \gamma, U_d, \mu, \rho, \alpha, D_{dif}, L_d, L_{cw}, L_h, L_{dis}\right) \qquad (2)$$

where P_{exc} [W] denotes the microwave excitation power, γ [N/m] the interfacial tension, U_d [m/s] the droplet velocity, μ [mPa.s], ρ [kg/m^3], and α [m^2/s] the dynamic viscosity, density, and thermal diffusivity of the droplet material respectively, D_{dif} [m^2/s] the diffusion coefficient of the fluorescent dye, L_d [m], L_{cw} [m] and L_h [m] the droplet length, width and height respectively, and L_{dis} [m] the distance that a droplet needs to travel to achieve homogenization. In this study droplet generation was in the squeezing regime[287] where droplets are filled almost the entire cross-section of the channel leaving a very thin film (~ 2% of channel width) of the continuous phase between the droplets and channel walls. Therefore, the droplet width and height are also representing channel width and height. Detailed derivations of the dimensionless groups are presented below.

There are 12 (n=12) variables and the dimensions of each variable are defined as follows in Table 6.1:

Table 6.1. Pi theorem variables and dimensions.

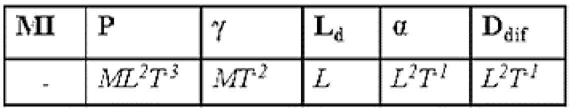

MI	**P**	γ	L_d	α	D_{dif}
-	ML^2T^{-3}	MT^{-2}	L	L^2T^{-1}	L^2T^{-1}

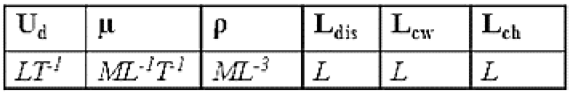

U_d	μ	ρ	L_{dis}	L_{cw}	L_{ch}
LT^{-1}	$ML^{-1}T^{-1}$	ML^{-3}	L	L	L

Three dimensions {M,L,T} which are mass, length and time, respectively are involved in this problem. By choosing the same number of repeating variables as the number of the dimensions such as j=3, the parameters can be nondimensionalized which will help further understand the key influencing parameters. In this study, μ, D_{dif} and L_{cw} are chosen as the repeating variables, which will result in 9 independent Π groups, such as k=n-j=9, described as below;

$$\Pi_1 = (\mu)^a.(D_{dif})^b.(L_{cw})^c.P_{exc} = M^0L^0T^0$$

$$\Pi_1 = \frac{P_{exc}.L_{cw}}{\mu.D_{dif}{}^2}$$

for convenience,

$$\Pi_{1,\text{mod}} = (\Pi_1).10^{-17} = P^*_{exc}$$

and similarly,

$$\Pi_2 = (\mu)^a.(D_{dif})^b.(L_{cw})^c.U_d = M^0L^0T^0$$

$$\Pi_2 = U_dL_{cw} / D_{dif} = Pe$$

$$\Pi_3 = (\mu)^a.(D_{dif})^b.(L_{cw})^c.\rho = M^0L^0T^0$$

$$\Pi_3 = \frac{\rho.D_{dif}}{\mu}$$

modifying Π_3 as

$$\Pi_{3,\text{mod}} = 1/\Pi_3 = \frac{\mu}{\rho.D_{dif}} = Sc$$

groups the Schmidt number. Likewise,

$$\Pi_4 = (\mu)^a.(D_{dif})^b.(L_{cw})^c.\gamma = \frac{\gamma.L_{cw}}{\mu.D_{dif}}$$

$$\Pi_5 = (\mu)^a.(D_{dif})^b.(L_{cw})^c.\alpha = \frac{\alpha}{D_{dif}} = Le$$

where Le denotes the Lewis number. And, to produce Π_4 into a better established Π, Π_4 can be performed as[331]

$$\Pi_{4,\mathrm{mod}} = (\Pi_4 / \Pi_5) = \frac{\gamma.L_{cw}}{\mu.D_{dif}}.\frac{D_{dif}}{\alpha} = \frac{\gamma.L_{cw}}{\mu.\alpha}$$

considering the Marangoni number,

$$Ma = -\frac{d\gamma}{dT}\frac{L\Delta T}{\mu\alpha}$$

where ΔT denotes temperature difference, and assuming the average change in interfacial tension as (γ-γ_0) before and after heating, respectively

$$\Pi_{4,\mathrm{mod}} = \frac{(\gamma-\gamma_0).L_{cw}}{\mu.\alpha} = \gamma^*$$

which groups non-dimensional γ^* as the effect of interfacial tension on mixing with the competition of viscous forces in a similar way. In addition, other Π groups form as,

$$\Pi_6 = \frac{L_{dis}}{L_{cw}} = L^*_{dis}$$

$$\Pi_7 = \frac{L_h}{L_{cw}} = L^*_c$$

$$\Pi_8 = \frac{L_d}{L_{cw}} = L^*_{dl}$$

$$\Pi_9 = \boldsymbol{MI}$$

Hence, the mixing index can be stated as a function of

$$MI = f(P^*_{exc}, \gamma^*, \mathrm{Sc}, Pe, Le, L^*_c, L^*_d, L^*_{dis}) \qquad (3)$$

where, in summary,

$$P_{exc}^{*} = \frac{P_{exc}.L_{cw}}{\mu.D_{dif}{}^{2}}$$

$$\gamma^{*} = \frac{(\gamma-\gamma_0).L_{cw}}{\mu.\alpha} \quad , \quad Pe = \frac{U_d L_{cw}}{D_{dif}} \quad , \quad Sc = \frac{\mu}{\rho.D_{dif}} \quad , \quad Le = \frac{\alpha}{D_{dif}} \quad ,$$

$$L^{*}_{dl} = \frac{L_d}{L_{cw}}, \qquad L^{*}_{c} = \frac{L_{ch}}{L_{cw}}, \qquad L^{*}_{dis} = \frac{L_{dis}}{L_{cw}}$$

Herein, Pe, Sc, and Le stand for Peclet number, Schmidt number, and Lewis number, respectively. For a given set of geometric and flow conditions, droplet size can be considered uniform. The main focus would then be evaluating the relative importance of different driving forces for mixing. Considering the ThS dye with a nominal radius of 0.4nm in the glycerol solution (75% w/w) with a dynamic viscosity of 22.7 [mPas], its diffusion coefficient can be estimated as 2.27 x 10^{-11} [m^2/s] at 22 ^{o}C [334], which could increase to 2.06 x 10^{-10} [m^2/s] when temperature is increased to 87^{o}C. For the power used in this study ranging from 24 - 27dbm (0.25 to 0.50 watts), the measured temperature change ranged from 47^{o}C to 65 ^{o}C above room temperature (see Figure 6.4) which results in the highest temperature of 87^{o}C. Based on this temperature range, the Sc number which indicates the competition between viscous and mass diffusivity ranged from 7.93x10^5 to 1.49x10^4 meaning that viscous diffusivity is more important. Similarly, the Pe number which indicates the competition between convection and mass diffusion ranged from 2196 to 251 suggests convection is more dominant than mass diffusion, the Lewis number that indicates the relative importance between thermal and mass diffusion ranged from 3805 to 358 suggesting that thermal diffusion is dominant over mass diffusion. Comparing these three numbers, viscous diffusion is relatively more dominant than the others. By examining the dimensionless interfacial tension which indicates the competition between interfacial tension and viscous and thermal diffusivities, it is found that it varies from almost zero when no heating to ~4500 with the maximum heating. It suggests that when temperature increases, interfacial tension force is mainly dominant over all the other driving forces. The thermally induced interfacial tension gradient results in strong Marangoni effect over the droplet interface in a massive, 3D manner[298],[335]. As a result, 3D flow is induced within the droplet which leads to almost instantaneous mixing as shown in Figure 6.5.

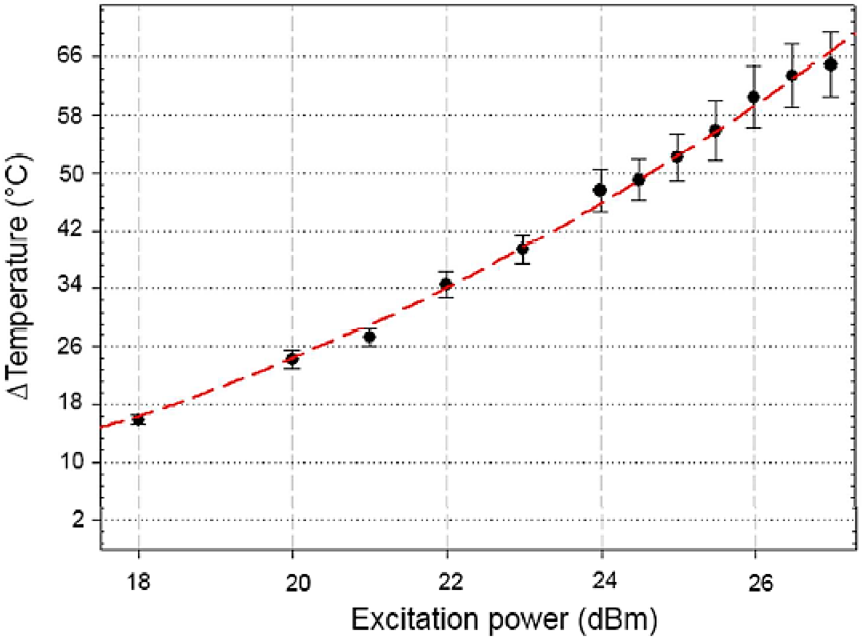

Figure 6.4 Estimation of temperature change with respect to applied excitation power using fluorescence thermometry technique.

6.5 EXPERIMENTAL RESULTS

To demonstrate the mixing efficiency of the microwave based microfluidic mixer, droplets with half doped with ThS dye are generated in a straight microchannel, where the channel width and height are fixed to be 200 um and 50 um, respectively. As illustrated in Figure 6.1, a combination of Y-channel and flow focusing design was used to form the droplets where the two fluid inlets from the Y-channel form the dispersed phase and a perpendicular oil stream serving as the continuous phase pinches off droplets. In the experiments, fluids were pumped through a pressure system. In order to demonstrate its mixing performance on regular and highly viscous aqueous solutions, both water and 75% (w/w) glycerol solutions were used as the continuous phase. Figure 6.6 shows the mixing of droplets with the glycerol solution when they are passing by the microwave resonator at different time lapses under the on/off scenarios of the microwave. Cross-stream mixing between the two halves of droplets is negligible when the microwave resonator is off while mixing is almost instantaneous when the microwave resonator is on.

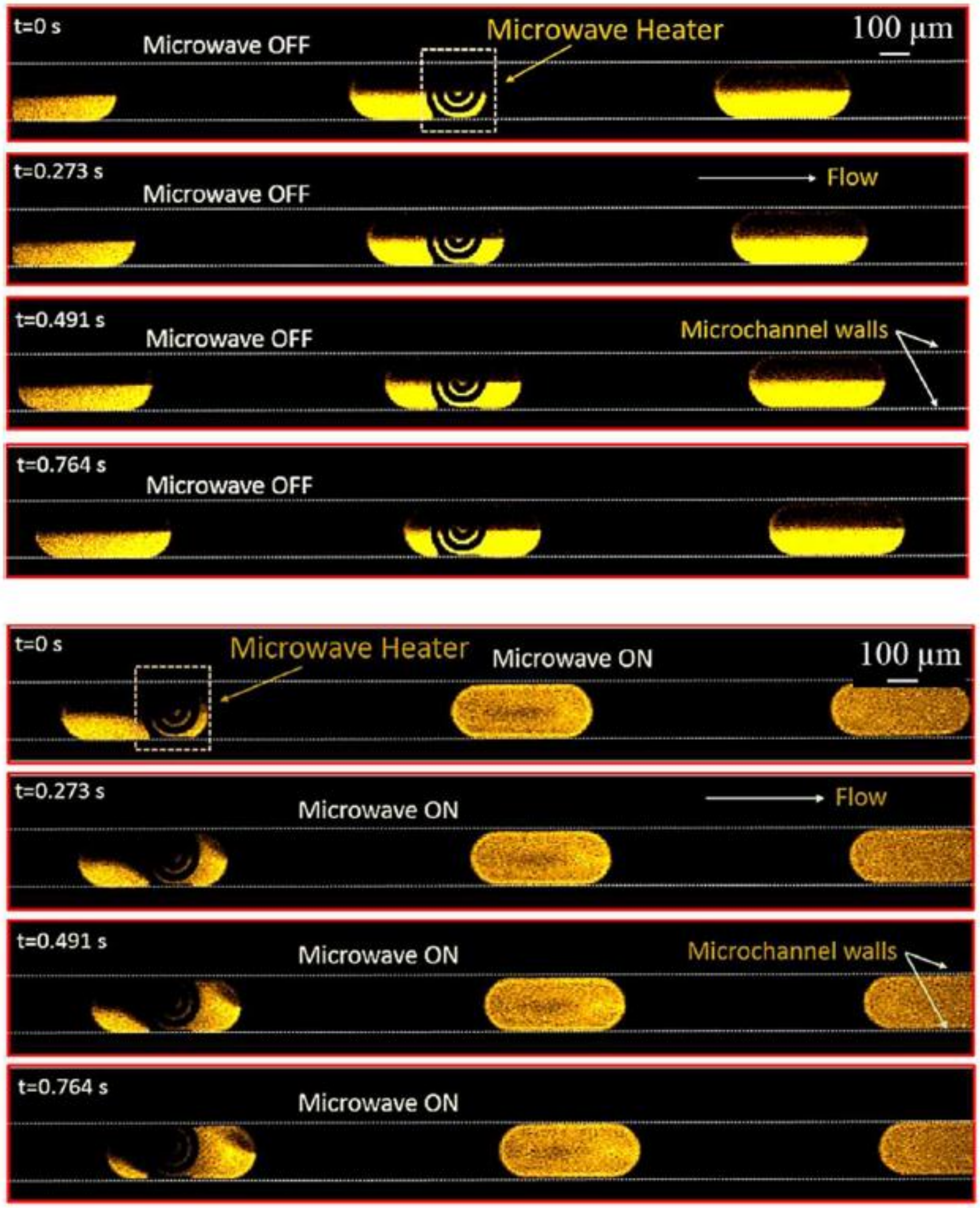

Figure 6.5 Droplets are moving and passing over the microwave heater. Microwave heating initiates mixing between the two halves and agitates flow pattern inside the droplet, which helps stirring the two halves of the droplet.

As discussed by Muradoglu and Stone[297], and Wiggins and Ottino[336], the required condition to produce chaotic advection is to have time-dependent cross-stream flow motion. As seen in Figure 6.5, while the droplet enters the resonator region and starts receiving heating, the dye in the front region is pulled cross the flow stream towards the upper half of the droplet by following the resonator shape. This stirring phenomena should occur in the height direction as well as suggested by the non-uniform electrical field in this direction shown in Figure 6.2. It is also noted that while mixing is happening in the front region, the back of the droplet is almost unaffected since it is not being heated yet. As droplet keeps sweeping through the resonator region, the time-varying Marangoni effect induces 3D motion over the entire droplets resulting in chaotic mixing. A video showing the microwave agitation event with the comparison of the resonator being on and off can be found in video appendix-D and V3). Quantitative analysis of mixing was also done by measuring the fluorescent intensity profiles of the images. In Figure 6.6, the intensity profiles across the droplet width before and after mixing cases are denoted. The image showing complete mixing is taken from the third droplet in Figure 6.5. It is clearly seen that the fluorescent intensity is relatively homogeneous across the entire droplet width.

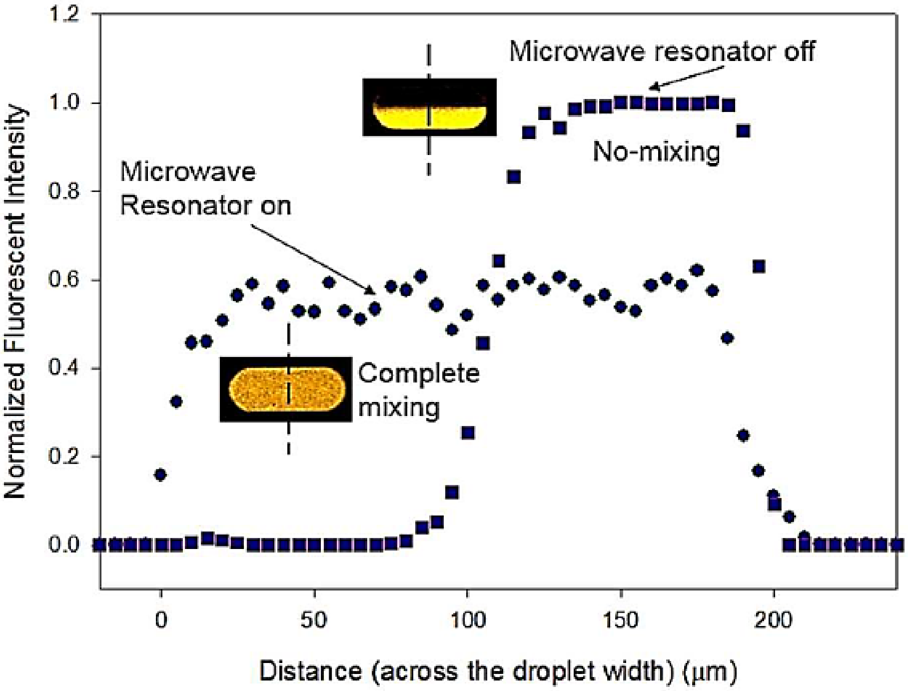

Figure 6.6 Mixing in the absence and presence of microwaves.

It should be noted that rapid mixing is difficult to obtain in microfluidics, which could take a significantly longer time than the microwave-assisted mixer presented here. For example, the mixing time driven by pure diffusion can be estimated by $t_D \approx l^2/D$, where t_D is the time elapsed since diffusion starts, l the characteristic length which could be considered as the channel width in this study as diffusion occurs between two halves of the droplets that are aligned side-by-side in the width direction, and D the diffusion coefficient of the fluorescent dye, ThS. Then the time scale to reach full mixing is estimated as 1762 s considering l = 200 μm and D = 2.27×10^{-11} m^2/s, which is 3 orders of magnitude longer than the mixing time achieved here (i.e., less than 1 s). Although mixing occurs almost instantaneously when a droplet enters the resonator region, thorough mixing is achieved after the droplet travels a few hundred micrometers away from the resonator, as shown in Figure 6.5. When temperature increases which can be achieved by increasing the input power to the resonator, the Marangoni effect is stronger which should result in faster mixing. In other words, thorough mixing could occur within a shorter distance when the input power is higher. In order to quantitatively investigate the effect of the input power on mixing, mixing index is calculated based on the following equation[296]:

$$MI = 1 - \frac{\sqrt{\left(\frac{1}{n}\right)\sum(I_i - I_{av})^2}}{I_{av}} \qquad (4)$$

where I_i is the fluorescent intensity of each point, I_{av} the average intensity and n the total number of the pixels. An in-house written Matlab code was used to calculate the mixing index by scanning the fluorescent intensity values over the entire droplet. The mesh of the droplet can be seen in Figure 6.7.

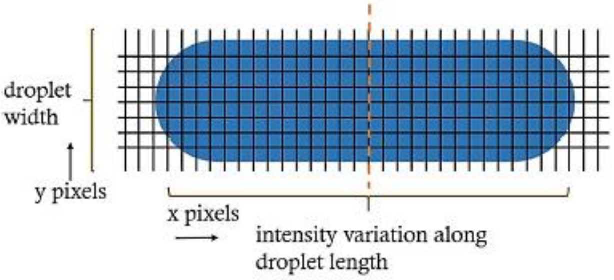

Figure 6.7 Mixing index calculation.

in the calculation of the mixing index for a droplet, fluorescent intensity values were scanned using the Matlab code along the droplet length for a corresponding y-pixel line and averaged to reduce a single value. Then, a matrix of *Ii = [Iiy] (1) x (y-pixels)* along the droplet width is obtained and using eq. (4) the mixing index was calculated. *Iav* was the average of *Ii*.

Figure 6.8 shows the effect of the input power on the mixing index where x-axis is the distance that the droplet travelled after completely leaving the resonator region (the edge of the resonator is marked as x=0 in Figure 6.1), which is scaled by the droplet width. It can be seen that the mixing index increases with the input power for the same distance that the droplet travelled. In addition, thorough mixing represented by a mixing index of 0.97 can be achieved after the droplet travelled about two droplet widths when the input power is as high as 27 dBm while it takes the droplet to travel more than three droplet widths to achieve full mixing when the input power is reduced to 24 dBm. It is also noted that when the input power is above 26 dBm, no significant benefits by further increasing the input power.

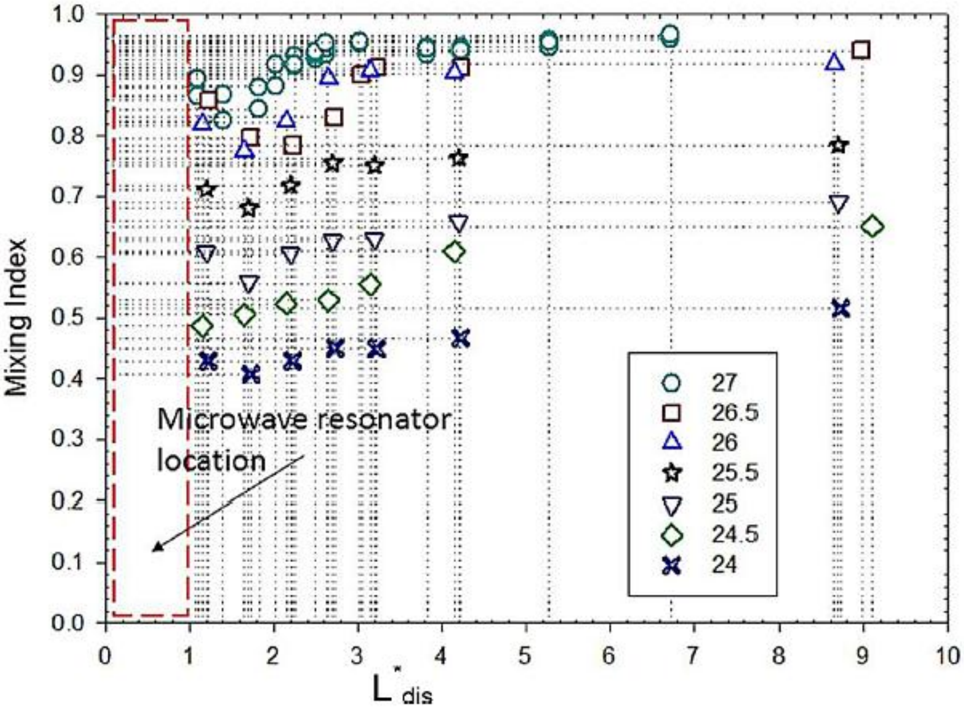

Figure 6.8 Effect of excitation power (dBm) and L^*_{dis} on mixing efficiency.

Considering the dominant role of Marangoni effect in microwave mixing, it is beneficial to obtain a correlation between the mixing index and dimensionless interfacial tension, which could be used for design guidance. Figure 6.9 shows that the mixing index increases with the dimensionless interfacial tension which is expected as the higher influence from the interfacial tension, the faster and stronger mixing. A qualitatively critical interfacial tension is observed, γ^*=3500, at which the mixing reaches 90%. We obtained an experimental correlation as below,

$$MI = [1 - \exp(-1.226 * 10^{-3}.\gamma^{*}]^{7.654} \qquad (5)$$

As mentioned earlier, most active mixing methods are based on hydrodynamic disturbance of flow which is not very effective for mixing highly viscous fluids such as the situation considered in this study[337],[304]. Therefore, in order to demonstrate the mixing performance of the microwave resonator, only the images for mixing of highly viscous solution, 75% (w/w) glycerol solution, were shown. To further examine our microwave based microfluidic mixer, mixing within larger droplets (meaning longer droplets as they are confined by the channel width) was also studied. Figure 6.10 shows effective mixing occurring within droplets of 750 μm long.

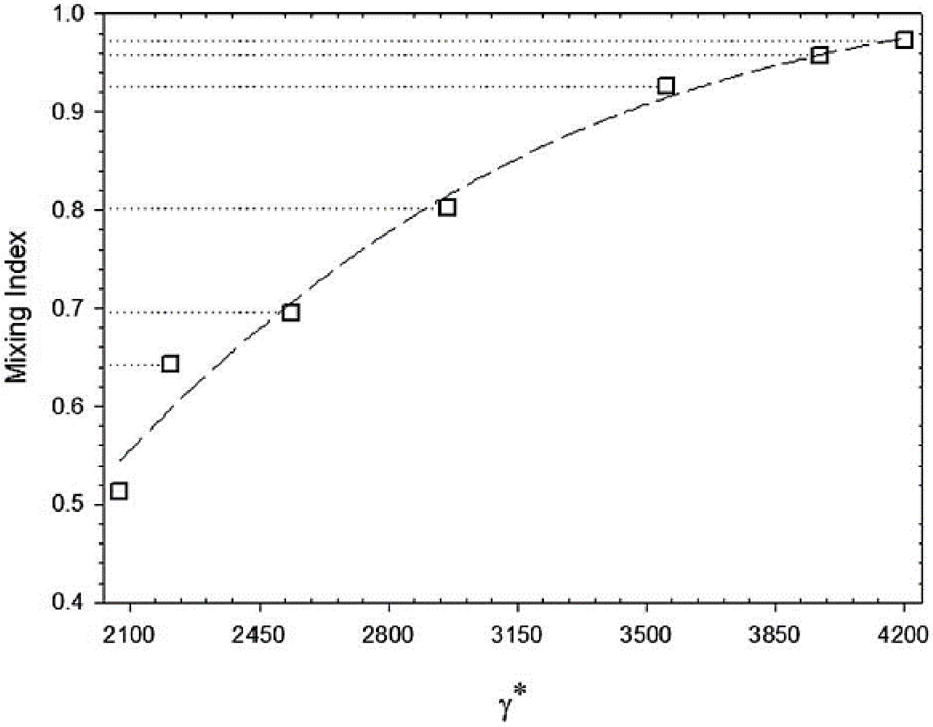

Figure 6.9 Influence of γ* on mixing index.

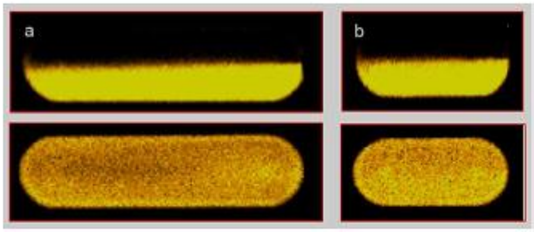

Figure 6.10 Longer droplets are generated and analyzed for the mixing behavior. a) Droplets for L*d = 3.75, MI=0.9671, and b) L*d = 2.18, MI=0.9739 at Pexc=27 dBm. Droplets are shown when microwave heater is off and on, respectively.

6.6 CONCLUSIONS

In this study, the concept of mixing with microwaves in microfluidic devices, the mechanism of agitation and mixing, effects of excitation power, relative influence of different forces using Pi theorem and droplet length were investigated. The mixing platform demonstrated here is simple to integrate with microfluidics, easy to operate, and provides great potential for mixing in many Lab-on-a-chip applications that requires rapid and effective mixing. This new mixer may open a new window for mixing bio-chemical assays. The mixer can trigger and initiate reactions at the same time of mixing phenomena happening using the microwave energy while many other mixers can do the mixing function only. This unique approach of utilizing microwave sensor technology to facilitate in microfluidics mixing is expected to find wide applications in the field of biochemical synthesis and click-chemistry.

Chapter 7

MICROWAVE TEMPERATURE MEASUREMENT IN DROPLET AND SINGLE PHASE MICROFLUIDIC DEVICES[4]

7.1 MOTIVATION AND OBJECTIVES

The motivation of this study is that although there are various techniques exist for macroscale temperature measurement, many of those are not applicable to temperature measurement in microfluidics. In addition, the currently available techniques for microfluidic temperature measurement still have their own disadvantages and limitations. And, on the other hand, temperature measurement of droplets in Lab-on-a-Chip/microfluidics applications is even a harder task than that of single phase microfluidics due to that droplets flow as segmented and isolated pieces in the channel

---

[4] The contents of this chapter have been previously published in Lab on a Chip (RSC) 16, 2192–2197 (2016), by Wong D., Yesiloz G., Boybay M.S. and Ren C.L., as “Microwave Temperature Measurement in Microfluidic Devices”. This work was carried out in collaboration with David Wong, a MSc student. G.Y., M.S.B. and C.L.R. developed the idea; G.Y. and D.W. designed the methodology; D.W. executed experiments; G.Y. supervised and assisted with the experiments; D.W., G.Y. and C.L.R. contributed to the paper writing.

and usually they move fast which requires high response time for the temperature sensor to give feedback. Another, yet the most important challenge is that, for the measurement of individual droplet temperature, the temperature measurement tools must be selective and specific to the temperature of the droplet only not to be effected by the other side temperature variations such as the chip material or the substrate.

In this regard, considering the challenging task of droplet temperature measurement in microfluidics and lack of the variety of available techniques for this task, the objective of this study is leveraging a microwave thermometry technique to measure droplet and single phase temperature, which is selective only to the fluid in the channel to be measured and the droplets, utilizing and implementing the advantages of the microwave sensor used in this thesis work.

7.2 INTRODUCTION

Temperature measurement and control is a critical effort in many Lab-on-a-Chip applications that require precise thermal management as part of device operation[328]. For instance, polymerase chain reaction requires DNA sample mixtures to be continuously supplied at three different temperature steps such that 95 ºC for denaturing DNA molecules, 72 ºC for annealing and 60 ºC for extension. The sensitive control of temperature is essential for DNA replication and long-term chip performance[338]. In heat transfer control as in isoelectric focusing with thermally generated pH gradients[339-340] and temperature gradient focusing[341-342] techniques are particularly important for the analysis[338]. In chemical reactions such as the Reimer-Tiemann reaction, boiling and thermal runaway issues can be avoided through a quick feedback control that is possible only with presence of instantaneous temperature measurement. On other circumstances such as quantum dot synthesis, temperature must be controlled during crystallization in order to attain the desired photoluminescence peak and full width at half maximum[52], which also requires accurate and precise temperature measurement for a controlled process. Hence, an immediate and reliable temperature measurement technique is necessary for on-chip analysis and process control.

Many techniques have been reported for measuring temperature profiles in microfluidic chips[343-347]. However, precise temperature measurement on the micro-scale is still a difficult task because of the rapid thermal diffusion and short dissipation timescales or due to complications in micro-fabrication or size of the probe. Of these, a common technique is the use of a resistance temperature detector (RTD), which is a simple solution that requires minimal external equipment. The most important property of an RTD is its temperature coefficient of resistance (TCR) usually denoted by α. The TCR is defined as the relative change in resistance per unit change in temperature as described in [348],

$$\alpha(T) \equiv \frac{1}{R}\frac{dR}{dT} \tag{1}$$

where R is the resistance and T is the temperature. There are several methods for the measurement of the resistance of an RTD sensing unit as illustrated in Figure 7.1.

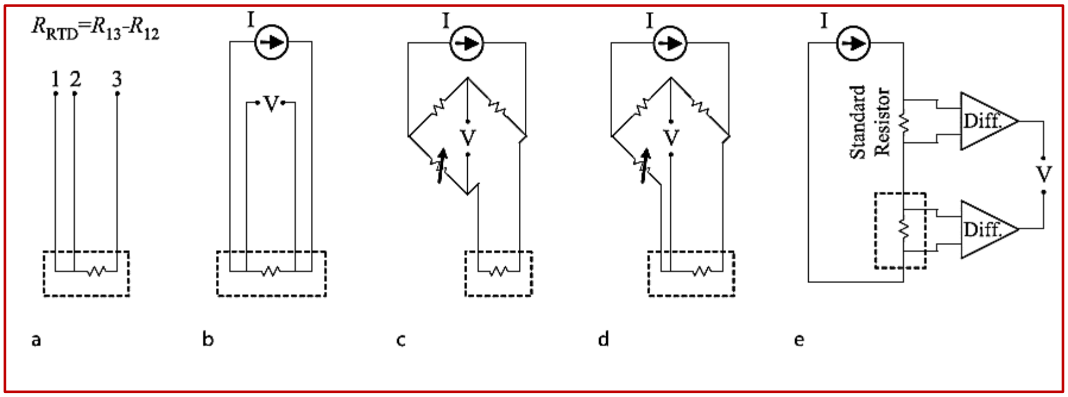

Figure 7.1. Several methods for measuring the resistance of an RTD sensing element. (a) The 3-wire connection which is most widely used in commercial RTDs. (b) A 4-wire arrangement for use with a digital multimeter or lock-in amplifier. (c) 2-wire arrangement in a classical Wheatstone bridge, which is subject to errors due to the lead resistances. (d) An improved bridge using the Siemens arrangement. (e) A half-bridge with two differential amplifiers[348].

RTDs are relatively easier to fabricate and suitable for steady state temperature monitoring but the response time of RTD is slow due to the heat transfer between the sample fluid and the sensor. Moreover, segmented droplets are often smaller than the sensor footprint required for RTD operation, resulting in a significant error.

To measure the temperature of the microfluidic sample in situ, methods based on fluorescence intensity ratio (FIR) are often used. The quantum yield of some fluorescent dyes such as Rhodamine B is temperature dependent, which allows spatial temperature distribution to be measured with less than 3.5 ℃ uncertainty[349],[350]. To improve accuracy, fluorescent systems with an ultralow temperature coefficient are required[343]. In addition, this method works well with glass-based materials but is not compatible with porous chip materials such as polydimethylsiloxane (PDMS) because dye particles tend to diffuse into and adsorb on channel walls, creating artificial fluorescence intensities. Driven by the popular use of PDMS for microfluidic chip fabrication and the high spatial resolution of temperature measurements enabled by Rhodamine B, several techniques have been

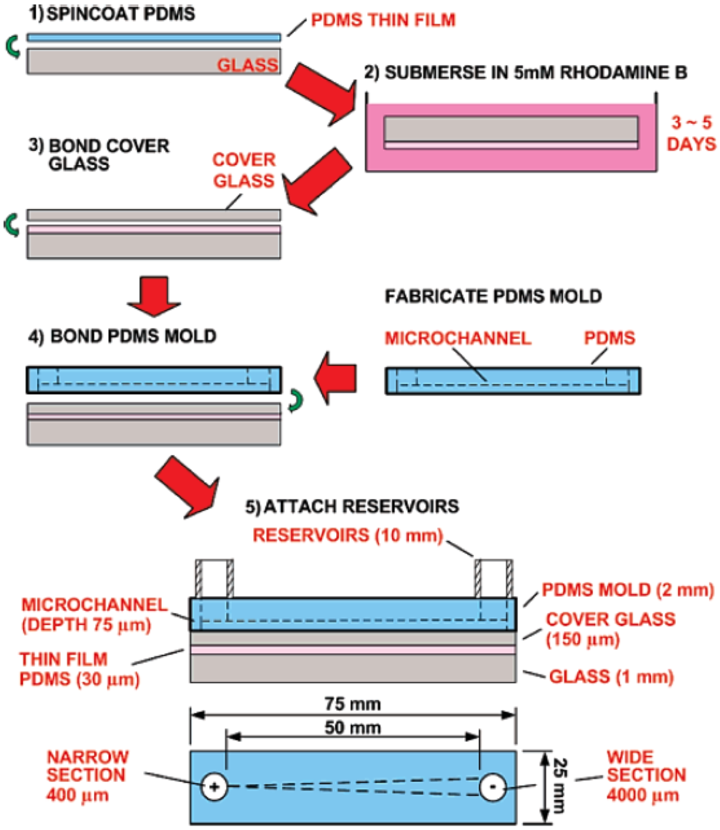

Figure 7.2. Thin film PDMS/Rhodamine B fabrication process proposed by Samy et al.[338] to overcome adsorption and absorption of Rhodamine B into PDMS.

developed to overcome such challenges[338],[351]. For example, Samy et al.[338] proposed a thin-film PDMS technique to eliminate dye absorption problem. In this method, they used a PDMS thin film which is dissolved by Rhodmaine B dye and it is sandwiched between two glass substrates (a thin glass ~150 µm), then bonded to a microchannel molded in PDMS as well (see Figure 7.2). Since the dye is sandwiched and segregated by from the fluid channel, the method prevents diffusion of the dye, and allows whole chip temperature measurement. However, this method does not eliminate photobleaching and due to the thin film a direct measurement of the fluid is not measured which causes error. Also, droplet temperature measurement is not possible through this method. In a later study, Schreiter et al.[346] demonstrated a robust thin-film thermometry technique using N,N-bis(2,5-

di-tertbutylphenyl)-3,4,9,10-perylenedi carboximide (BTBP) dye, as an additional improvement since this dye-embedded thin-film does not uses a glass cover and directly bonded to microchannels molded in PDMS. Nevertheless, BTBP thim film preparation is a long process (requires >24 hr) and still the methods allows to measure the temperature of the thin film rather than temperature in the channel yet provides a whole chip temperature mapping.

Other molecular probes, such as fluorescein, have no direct temperature dependence on their fluorescence intensity but have a temperature dependent pH change which could be used to measure temperature if a pH– temperature sensitive buffer is available for use. As a general temperature probe, the (CdSe)ZnS quantum dot is superior since its emission and absorption spectra can be tuned during growth, but synthesis and fabrication into a usable form such as coated beads remain costly[352]. For instance, Issadore et al.[259] mixed carboxyl coated CdSe nanocrystals inside droplets to measure droplet temperature in microchannels. Although quantum-dots possess photobleaching effects, the use of quantum dots in various solvents and instability in different environments limit their use. Additionally, they may cause toxic effects which restricts their application in biological systems[353]. The major sources of error for all FIR based methods are the non-uniform local probe concentration and fluctuation in excitation intensity. By employing two different dyes with separate emission spectra and two simultaneously operating cameras, temperature can be related to the ratio between the two emission spectra, unaffected by concentration and source fluctuation[354],[355]. If picosecond photo counting equipment is available, fluorescence lifetime (FL) can be used to measure temperature instead. This method is not affected by concentration and excitation source and can attain 3D temperature distribution of ±1 ℃ accuracy[356-357].

As another approach, cholesteric liquid crystals (TLC) are used to measure temperature at ±0.1 ℃ accuracy at the expense of a narrow operating range[358-360]. Its high accuracy results from a drastic hue change within a range of 1–2 ℃. Despite its high accuracy, the high viscosity and large bead size after necessary encapsulation have limited the use of TLC in microfluidic devices. Other sensing methods exist, such as through observing Brownian motion of particles by using micro PIV. Temperature can be correlated to ±3 ℃ accuracy with this method[361]. Raman spectroscopy can detect temperature based on stretching modes of a hydrogen bond but suffers from a long acquisition time of up to 16.5 s due to Raman scattering's inherent weak intensity[362]. Temperature can also be measured based on acoustic time of flight[363], from changes in refractive index using interferometry[364], as well as using nuclear magnetic resonance spectroscopy[365].

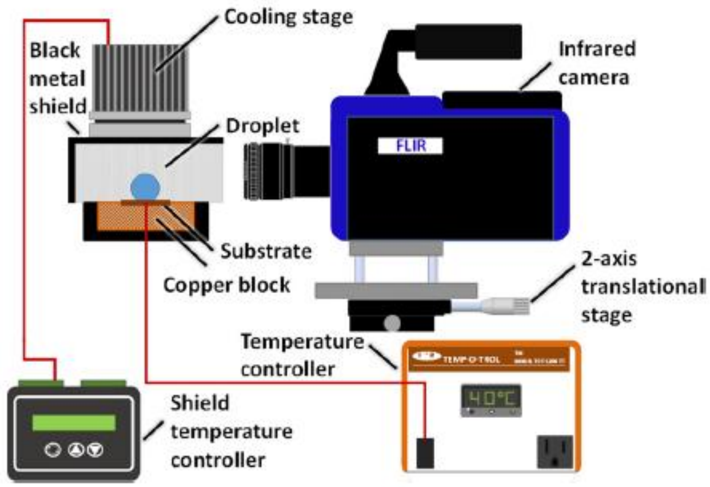

Figure 7.3. Schematic description of infrared camera temperature measurement setup[366].

Furthermore, Chandramohan et al. (2017) used a spatiotemporal infrared thermography to measure spatially resolved interface temperatures of droplets [366]. Even though this study showed a high-spatial resolution temperature fields and being non-invasive, also requires relatively less equipment comparing digital holographic interferometry, the technique needs a bulky infrared camera which is not proper for portable Lab-on-a-Chip platforms for fast temperature measurement (Figure 7.3). Lastly, in a recent study, Senapati and Nanda (2017) demonstrated a high sensitivity ratiometric optical temperature sensor using Eu:ZnO nanorods as the sensing material with sub bandgap excitation[353]. However, as mentioned previously, synthesis of these materials are costly and mixing them in biological environments for temperature measurements may not be always appropriate.

In this study, a microwave based method is proposed that can measure individual droplet temperature with accuracy comparable to FIR methods without the need for sample preparation and requires only a single commercially available device. As demonstrated previously, this device is also capable of selectively heating individual droplets and content sensing in microfluidic chips[260],[281].

7.3 THE PRINCIPLE OF THE MICROWAVE TEMPERATURE MEASUREMENT TECHNIQUE

The idea relies on that the permittivity of materials vary by temperature and frequency that can be calibrated and using this feature temperature can be measured. The complex permittivity of the polar liquids varies significantly with temperature due to the influence of heat on orientational polarization[367-368].

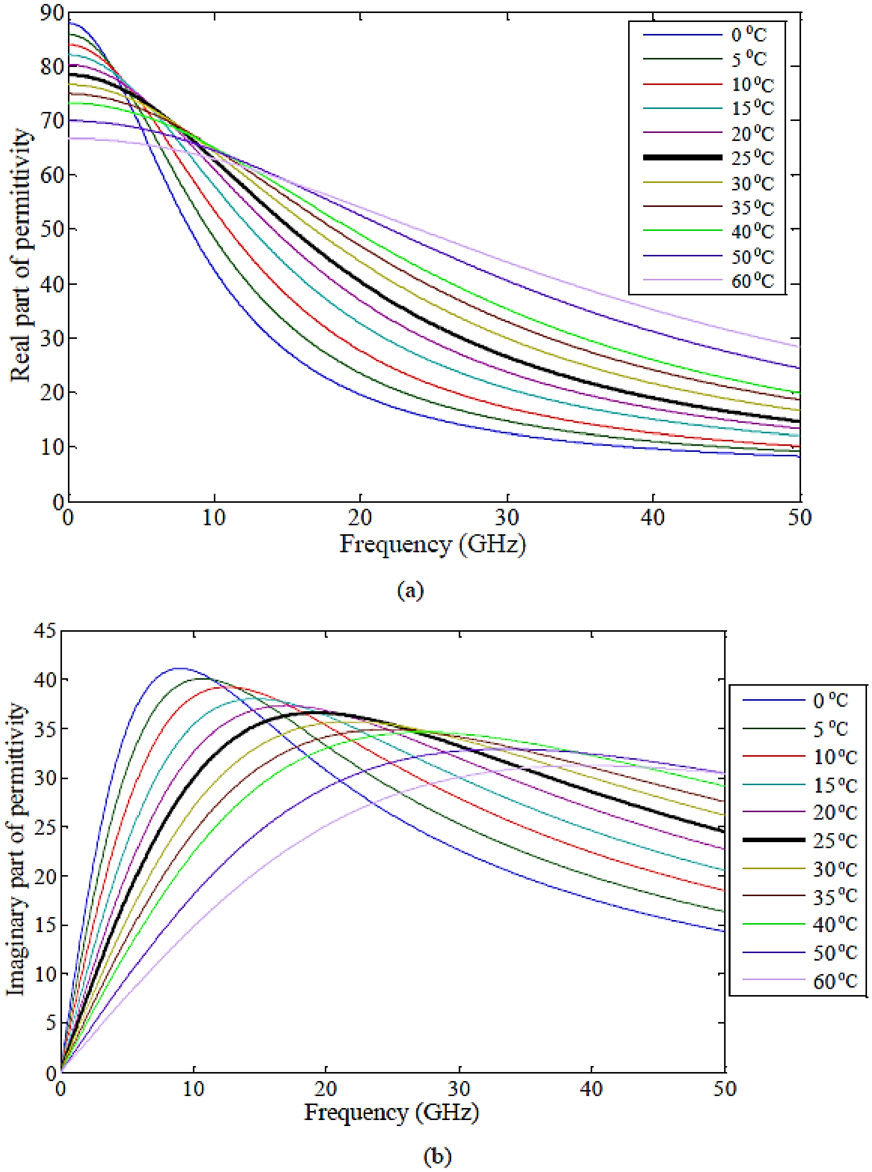

Figure 7.4. The complex relative permittivity of water as a function of frequency, with variation of the temperature from 0^0C to 60^0C and frequencies from DC up to 50 GHz. a- Real part, b- Imaginary part[368].

The behavior of permittivity change of water as a function of frequency at different temperatures are presented in Figure 7.4 and Figure 7.5.

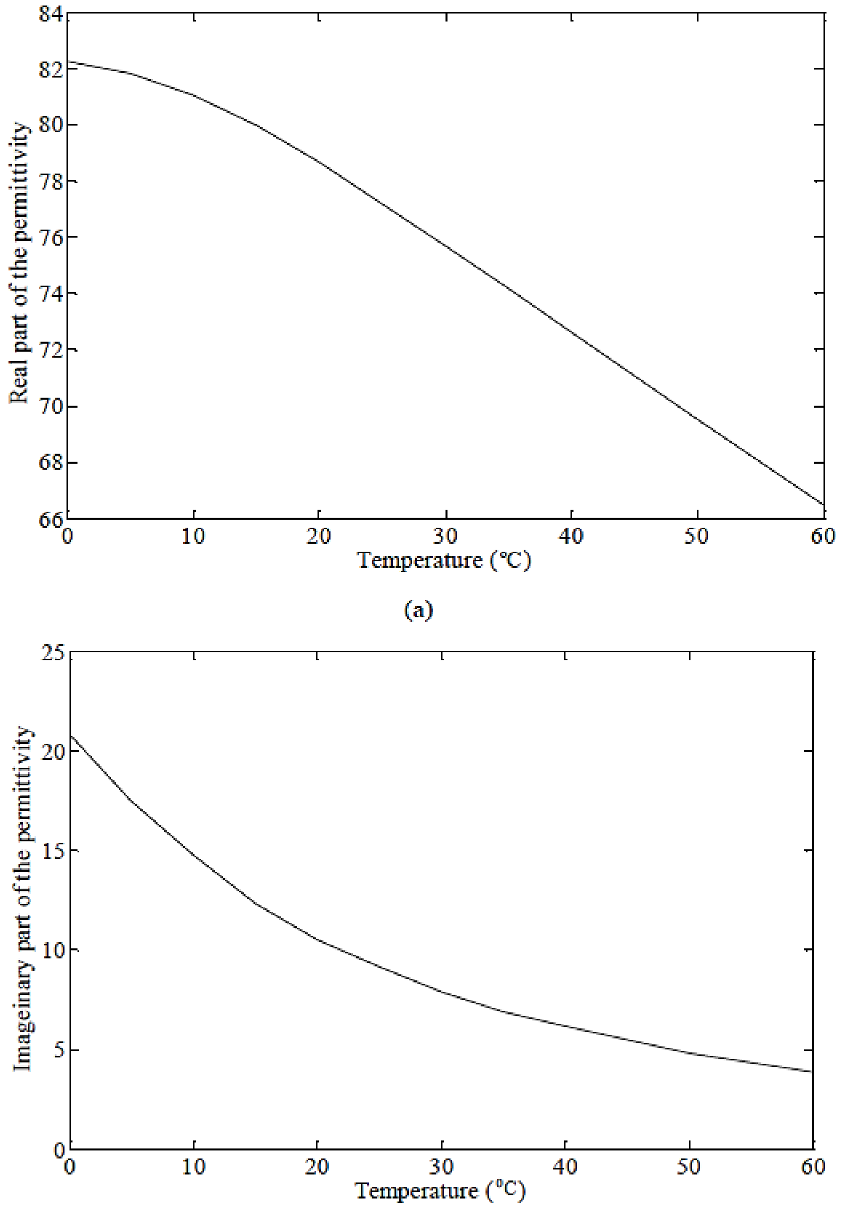

(a)

(b)

Figure 7.5. The complex relative permittivity of water as a function of temperature at 2.45 GHz. a- Real part, b- Imaginary part[368].

7.4 METHODOLOGY AND EXPERIMENTAL

The microwave sensor is composed of two planar concentric ring-shaped electrodes with spiral capacitive design as demonstrated above. Briefly, the outer ring is connected to a microwave source via a coaxial cable; the inner ring is electromagnetically coupled to the outer ring. The inner ring has a capacitive discontinuity that lies over the fluid channel. By detecting the change in the fluid permittivity, its temperature can be measured. This permittivity change is represented by the sensor's change in its resonance frequency. Based on the transmission line theory, the sensor can be treated as a load with complex impedance and temperature can be correlated to the reflective coefficient or single port scattering parameter (S_{11}) of the sensor as well, which is defined as the ratio between the incident voltage and the reflected voltage. A spectral measurement of the scattering parameter allows the extraction of the resonance frequency and quality factor, which in this case indicates the selectivity at which the microwaves are being absorbed by the working fluid. The resonance frequency, quality factor, and reflection magnitude are used to establish a relationship with temperature. The sensor is tested multiple times to demonstrate repeatability and then used to measure droplet temperature.

The microwave sensor is fabricated from copper coated glass slides (EMF Corporation). The details of the fabrication protocol can be found in Chapter 3. The glass slide is first patterned with an S1813 positive photoresist (Rohm-Haas), then electroplated (0.2 M CuSO4, 0.1 M H3BO3 and 0.1 M H2SO4) and etched with ferric chloride to achieve a thickness of around 5 μm. It is then covered with a thin layer of Sylgard 184 PDMS (Dow Corning) to isolate the electrodes from the working fluid. In order to prevent evaporation at high temperature, experiments are run at relatively high pressures which still result in deformation in PDMS channels and inconsistent measurements. The problem was overcome by adding a hard PDMS layer that contains all the channels. The sandwiched PDMS chip is fabricated using a standard soft lithography protocol. The channel design consists of a T-junction droplet generator and serpentines to achieve a residence time beyond 80 s, such that during calibration, the working fluid is heated to steady state temperature before reaching the microwave sensor. The chip is assembled using plasma bonding followed by Aquapel surface treatment (PPG Industries) in order to obtain a hydrophobic surface. A SMA connector (Cinch Connectivity Solutions Johnson) is soldered on as the last step.

The experimental setup, shown in Figure 7.6[328], consists of a fan for enhanced cooling and a hotplate (PH-121S, MSA Factory) for measuring and controlling the surface temperature. The hotplate has been recently calibrated and rated for ±0.05 ℃ accuracy and is mounted in an inverted position to allow microscope observation. The chip is pressed onto the hotplate by spring clips, separated by glass slides with a total thickness of 4.3 mm. The glass slides are necessary for electrical insulation. Thermopaste (OT-201, Omega) is applied on all contact surfaces to reduce thermal resistance. Throughout the experiments, Fluorinert FC-40 with a 2% custom-made surfactant (chemical structure of PFPE–PEG–PFPE) is used as the continuous phase and ultra-pure water as the dispersed phase. The microscope is used merely for observation and is not involved in the measurement. For microwave measurement, a vector network analyzer (VNA) (MS2028C, Anritsu) is used. The VNA has a frequency resolution of 0.05 MHz and a magnitude resolution of 0.07 dB.

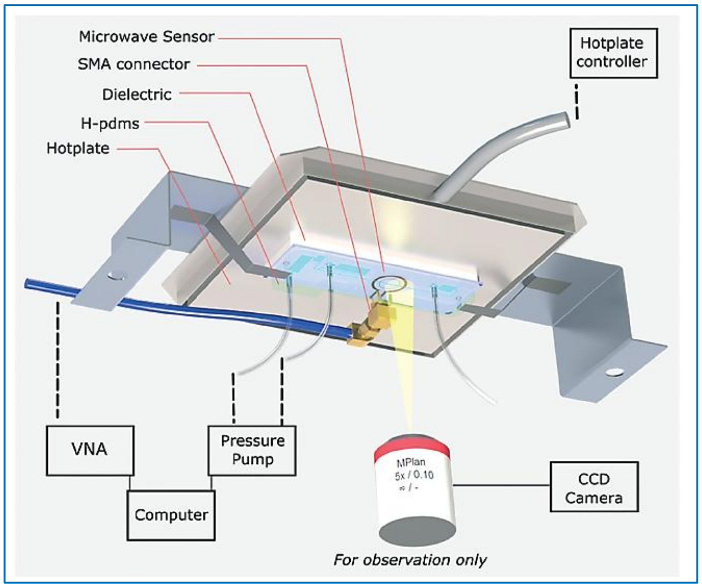

Figure 7.6 Schematic of the experimental setup. The microfluidic chip with an embedded microwave sensor is attached to the hotplate. The whole unit is mounted onto the microscope for visualization purposes[328].

7.5 RESULTS AND DISCUSSION

7.5.1 SINGLE PHASE TEMPERATURE MEASUREMENT

At first, the sensor is tested on single phase water. The continuous flow provides enough time to sweep through a large frequency range, allowing the resonance frequency and quality factor to be identified. Figure 7.7a demonstrates the resonance frequency response of the microwave sensor to the different temperature increments. It can be seen that higher temperature values cause an increase in the resonance frequency. The inset shows the behavior of the frequency sweep and reflection (S_{11}) corresponding to temperatures of 22.7 ℃, 38.5 ℃ and 56.4 ℃, respectively. Over the course of three hours, the surface temperature of the hotplate is increased in steps from room temperature to 60 ℃ and then decreased back to room temperature before new experiments are conducted. A fan is turned on when necessary to enhance cooling. For each temperature set point, the frequency sweep data are collected at 0.5 min intervals, each containing 4000 data points in S_{11} measurements. The resonance frequency for each set of measurements is identified by locating where the maximum absorption happens. The quality factor is calculated using equation (1), where BW is the half-power fractional bandwidth, Q is the quality factor and f denotes the resonance frequency of the microwave sensor. To exclude the thermal transient effects of the hotplate, only the data set attained in the last 5 minutes at each temperature step is used for further processing.

$$Q = \frac{f_{resonance}}{BW_{half-power}} \qquad (1)$$

Since the channel is separated from the hotplate surface by glass slides, a correction is added to correlate the fluid temperature to the hotplate surface temperature. The correction function is obtained by inserting a thermo-couple into the channel of a dummy chip with a PDMS thickness that is equal to the actual chip used (see Figure 7.8 and 7.9). The dummy chip is mounted in the inverted hotplate setup; the temperature difference is measured repeatedly and used to create the correction function. In lieu of this correction method, an attempt was made to measure channel temperature directly using a RTD sensor, but fabrication of both microwave and RTD sensors on the same chip was difficult. Fluorescence thermometry was also performed using fluorescein with Tris-HCl buffer. The results were later rejected since typical FIR based methods induce larger errors than that of the hotplate correction method (see appendix A for further information).

The aforementioned single phase frequency sweep test was repeated in the following two days to evaluate the sensor's repeatability, and a curve fit was performed using linear regression including all three sets of data. While Figure 7.7b shows a linear relationship between the resonance frequency and temperature that is unchanged from test to test, Figure 7.7c shows that the quality factor trend varies day by day between tests. The relationship between resonance frequency and temperature is provided in Table 7.1. It is observed that setup differences such as cable routing have a significant influence on the resonance peak shape, and such an influence is quantified by the half-power bandwidth, eventually affecting the quality factor. The contrasting behavior between the quality factor and

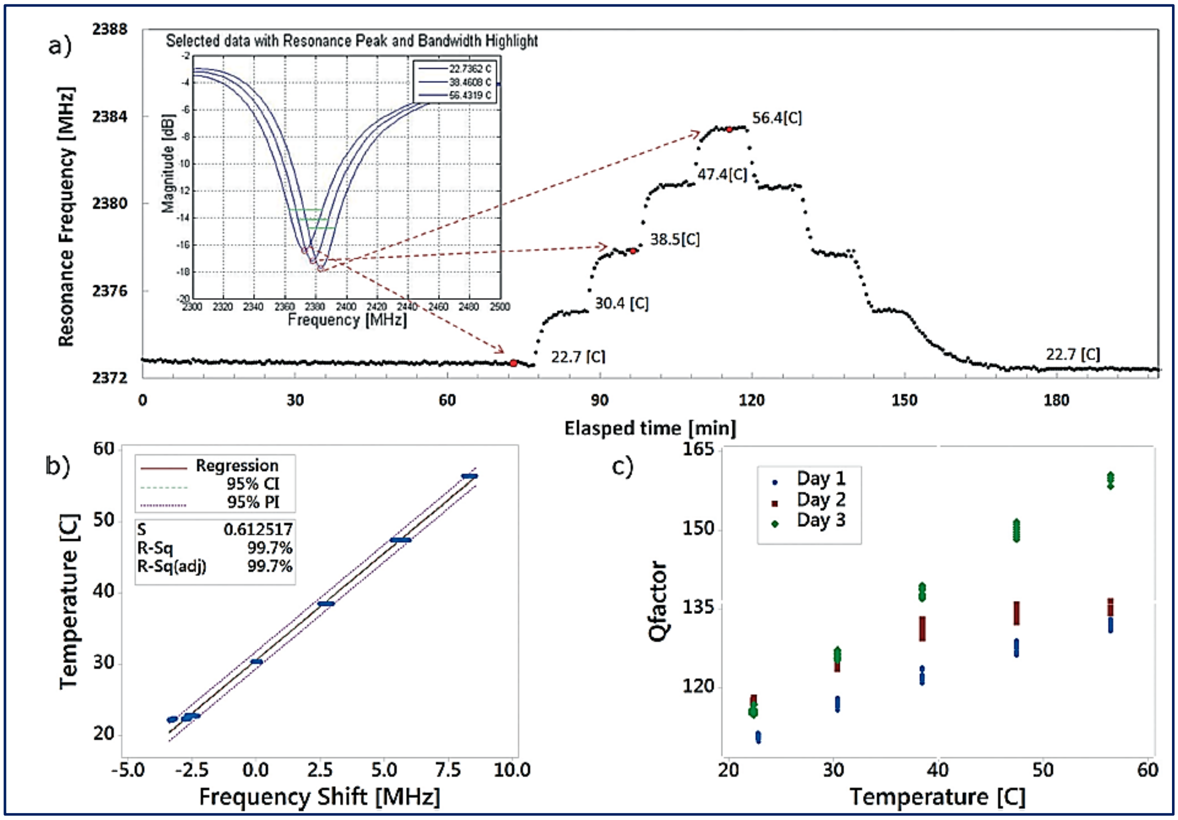

Figure 7.7. a) Resonance frequency vs. time, as temperature is increased and then decreased. The subplot shows the raw data (spectral measurement) at three temperature set points. The resonance peak is marked with a red circle, while the half-power bandwidth is shown in green. b) Temperature vs. resonance frequency shift calibration, all data from three separate tests are plotted, and 95% confidence and prediction intervals are shown. c) Quality factor vs. temperature, relationship varies from test to test, suggesting that quality factor is easily affected by setup change.

frequency shift suggests that the latter is a good temperature indicator uncompromised by external set-up changes. Based on the curve fit data, the temperature sensitivity on the resonance frequency is 0.33 MHz $℃^{-1}$. Given that the VNA is accurate up to 0.05 MHz, the temperature measurement resolution is 0.15 ℃. Prediction intervals are used to estimate that temperature measurement will have an accuracy of ±1.2 ℃.

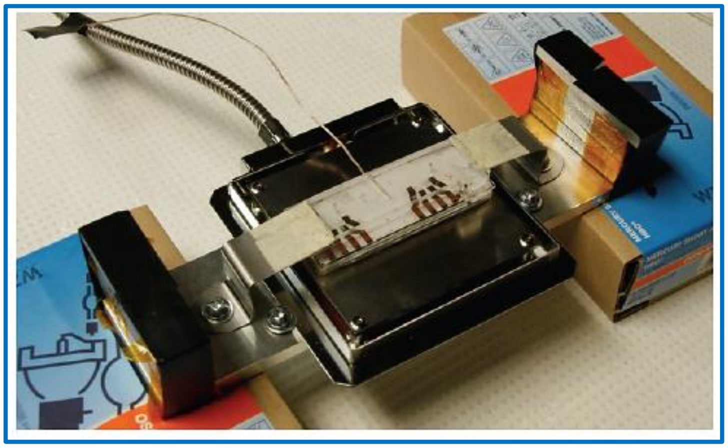

Figure 7.8 Hotplate correction and inverted hotplate setup, currently flipped over for taking the picture. Because of the need to account for the temperature difference between hotplate surface, which is accurately measured to ±0.05℃, and the working fluid, a thermal couple is inserted into a dummy chip with PDMS thickness equals to that of the actual test chip, in order to measure the channel temperature while being oriented in the inverted hotplate setup, as shown in Figure 7.6. The resulted correction function is plotted in Figure 7.9, and is subtracted from the hotplate surface temperature during experiment, in order to obtain the fluid temperature.

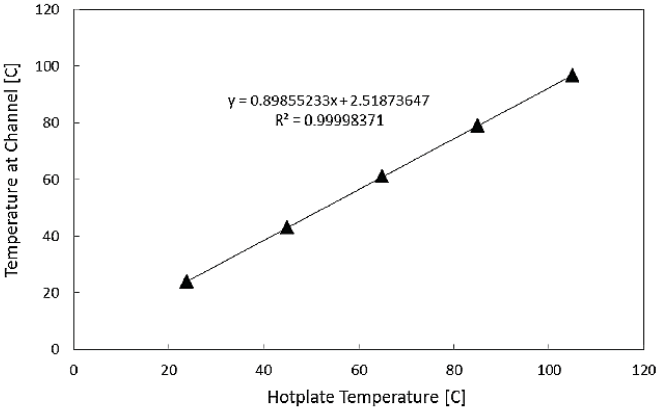

Figure 7.9 Correction function of hotplate calibration.

7.5.2 DROPLET TEMPERATURE MEASUREMENT

Compared with the single phase flow, fast moving droplets reduce the available time interval when the sample passes through the microwave sensor. If applied directly, the spectral approach described above will impose a speed limit that strikes a trade-off between droplet speed and temperature resolution. Consequently, a single frequency temperature measurement method is proposed in this study. For the droplet temperature measurement, the change of reflection coefficient at a fixed frequency to calibrate its temperature dependence is utilized. This method relies on the large difference in dielectric constant between water (80.1 at 25 ℃) and oil (2.7 for silicone oil, 1.9 for FC-40, and 2.0 for hexadecane), such that practically all microwave energy is absorbed by the aqueous droplets instead of by the continuous oil phase. While changing droplet material or composition will require a separate temperature calibration, the effects of different oil compositions or varying oil temperature are negligible. Figure 7.10a shows an excerpt of the single frequency data at 2317 MHz: the crests correspond to the continuous oil phase and the troughs correspond to water droplets at two different temperatures. During experiments, cable routing is fixed in space to eliminate errors induced by setup changes, and the hotplate temperature is varied between room temperature and 70 ℃. Notice that the water-to-oil volume ratio increases with temperature, which is caused by viscosity temperature dependence, resulting in a changing capillary number which affects droplet generation. As explained below, the increase in droplet length has no effect on temperature measurement.

A cut-off magnitude is used to discard the measurements from the continuous oil phase and isolate the data for each droplet. For each droplet, the minimum magnitude is calculated and used as a temperature indicator. The calibration is different at other frequencies, and the temperature dependence increases when moving closer towards the resonance peak, as shown in Figure 7.10b. In this test, 2317 MHz is chosen to be reasonably close to the resonance peak, resulting in a sensitivity of 0.27 dB $℃^{-1}$, which corresponds to a 0.26 ℃ resolution based on the VNA's ability to resolve S_{11} magnitude. Figure 7.10c shows the curve fit over 163 data points; residuals from the linear regression suggests that a 3rd degree polynomial provides a good description of the relationship between absorption magnitude and temperature.

Droplet temperature measurement using this method has an accuracy of ±1.17 ℃. The relationship between S_{11} magnitude at 2317 MHz and temperature is listed in Table 7.1. Varying the size of the droplet will have no effects on temperature measurement, as long as droplet length, l, is larger than the microwave sensor diameter l_0 (200 μm)[281]. During experiments, it was observed that single phase water upstream of droplet generation would evaporate, while water droplets downstream would remain in the liquid phase at even higher temperature. This suggests a higher local pressure within the droplet contributed by the interfacial surface tension, as described in equation (2). Since the

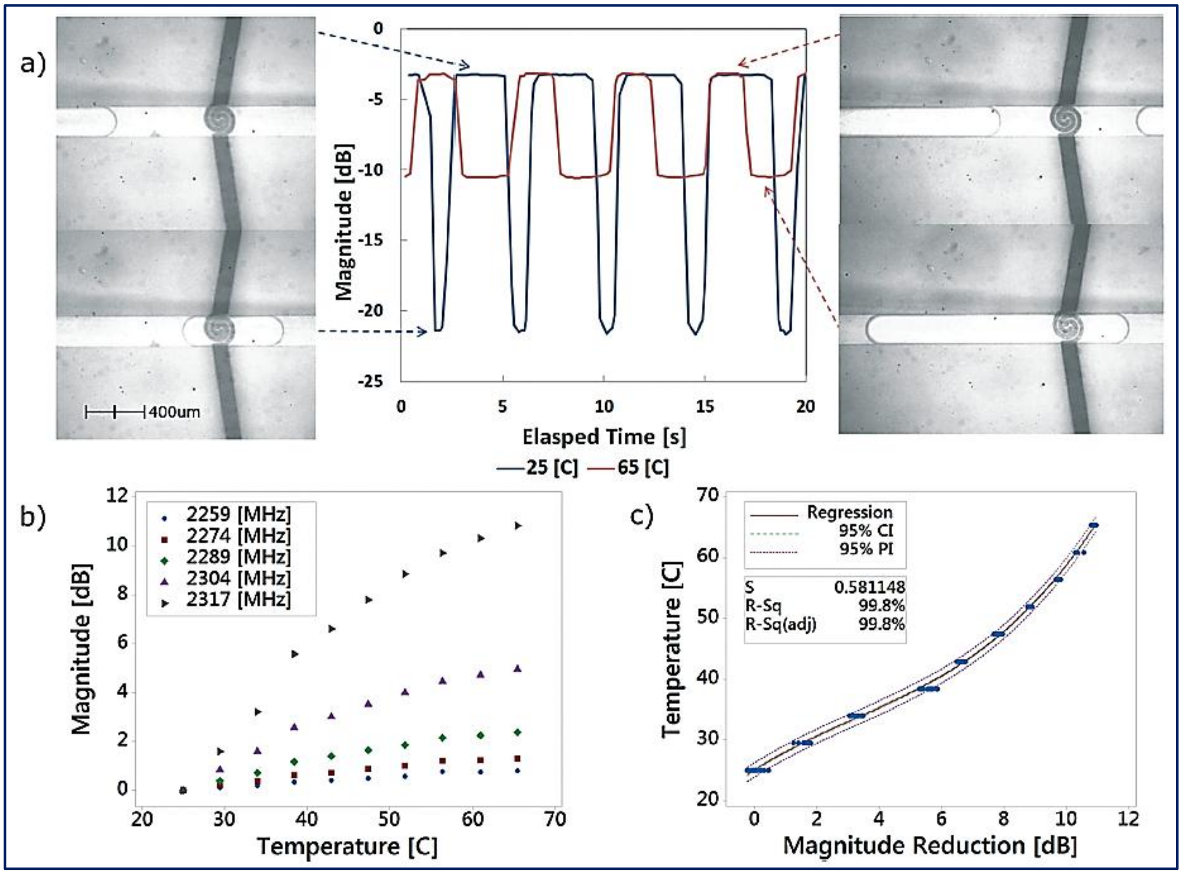

Figure 7.10 a) Single frequency S_{11} measurement magnitude vs. time. The pictures on the left show the droplet crossing the sensor at room temperature and corresponds to the blue trace. The pictures on the right show the droplet crossing the sensor at elevated temperature and corresponds to the red trace. b) S_{11} magnitude vs. temperature at various frequencies, sensitivity increases as test frequency moves towards resonance frequency. c) Temperature vs. S_{11} magnitude reduction calibrated at 2317 MHz. A 3rd order polynomial is used for calibration fit, with 95% confidence and prediction intervals shown.

microwave sensor is a local heating and sensing device, the Laplace pressure could be exploited to achieve stable operation at elevated temperature.

$$P_{droplet} - P_{continuous} = \frac{2\gamma}{R_{interface}} \qquad (2)$$

Table 7.1 Microwave temperature measurement method.

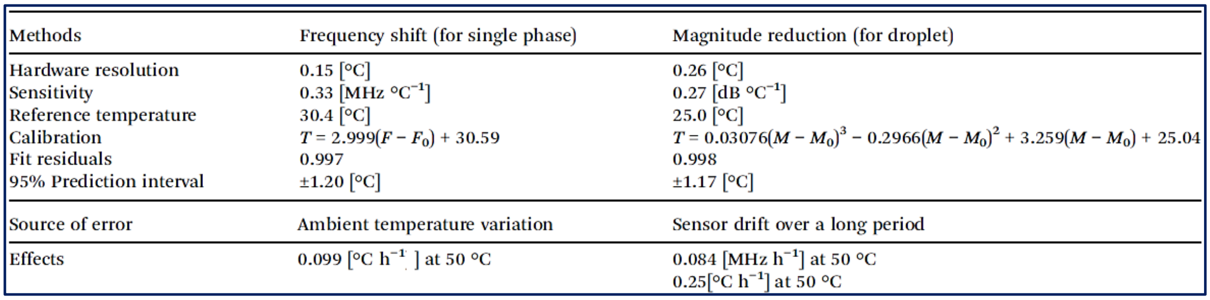

Methods	Frequency shift (for single phase)	Magnitude reduction (for droplet)
Hardware resolution	0.15 [°C]	0.26 [°C]
Sensitivity	0.33 [MHz $°C^{-1}$]	0.27 [dB $°C^{-1}$]
Reference temperature	30.4 [°C]	25.0 [°C]
Calibration	$T = 2.999(F - F_0) + 30.59$	$T = 0.03076(M - M_0)^3 - 0.2966(M - M_0)^2 + 3.259(M - M_0) + 25.04$
Fit residuals	0.997	0.998
95% Prediction interval	±1.20 [°C]	±1.17 [°C]
Source of error	Ambient temperature variation	Sensor drift over a long period
Effects	0.099 [°C h^{-1}] at 50 °C	0.084 [MHz h^{-1}] at 50 °C 0.25[°C h^{-1}] at 50 °C

7.6 CONCLUSIONS

In conclusion, the microwave sensor is a viable temperature measuring device. It has comparable or better accuracy than common fluorescence-based methods but does not require the use of intrusive fluorescent dyes and can measure individual droplet temperature without exposure time limitations imposed by optical equipment. The relationships and performance of frequency shift calibration and magnitude reduction calibration are summarized in Table 7.1. It should be noted that the listed accuracies and resolution values are preliminary in nature and contain many areas for improvement. For example, the microwave sensor on the single phase chip is observed to exhibit a slight drift over time at elevated temperature, which is quantified at 0.25 ℃ h^{-1}. Such a drift is accounted for in the calibration process and have no effect on the sensor's day to day repeatability, as demonstrated in the three repeating tests. However, it does contribute to an error within the 3 hour calibration period. The drift likely resulted from the continuous absorption of water into PDMS and could be eliminated by changing the substrate material. As for the droplet calibration method, further explorations in the sensor design can make it less susceptible to setup changes and attain potentially much higher accuracy. Lastly, the tested temperature range is by no means the operation limit of the sensor. Experiments are limited to temperatures above which evaporation occurs. Attempts to suppress evaporation by applying higher pressure often lead to irreversible damage to the bonding between the glass and PDMS. With a stronger chip, the microwave sensor will remain sensitive at much higher temperatures.

Chapter 8

MICROWAVE/MICROFLUIDICS INTEGRATED PLATFORMS FOR BIOMEDICAL AND PHARMACEUTICAL APPLICATIONS

The aim of this chapter is to extend the developed and integrated platform technology to biomedical and pharmaceutical applications such as disease diagnosis and drug delivery. The chapter includes two sections. The first section studies polymerization in microfluidics particularly copolymer hydrogel synthesis in droplets. The swelling capacity, and the effects of the monomer concentrations and the initiator are examined in microreactors (droplets). The study has been carried out via UV-polymerization, and microwave-assisted synthesis is also offered as a new controllable reaction source due its controllable mixing, heating and temperature, as discussed previously. In the second part, preliminary DNA hybridization sensing is attempted through the microwave sensor used in this thesis work, with promising results.

8.1 POLY (ACRYLAMIDE-CO-SODIUM ACRYLATE) COPOLYMER HYDROGEL PARTICLE SYNTHESIS FOR DRUG DELIVERY AND BIOMEDICAL APPLICATIONS[5]

8.1.1 INTRODUCTION

Hydrogels, in a general definition, are cross-linked three-dimensional polymeric structures that can swell and retain a significant amount of water within their structures, while they are insoluble in water[369]. Nanogels (typically 20-250 nm) and microgels (typically 1-350 μm), as a class of hydrogels, are cross-linked spherical hydrogels particles with excellent biocompatibility, a microporous structure with tunable porosities and pore sizes, and dimensions spanning from human organs, cell to viruses have been realized a viable tool for targeted drug delivery, protein release and tissue engineering[370-376]. These intelligent materials are considered to be promising carriers for drug delivery because of their abilities to response the environment specific changes that when the environment factors alter the morphological structure is stimulated to give spontaneous reflex[377-379]. For example, hydrogel particles can sustain abrupt changes in response to physical variation such as temperature[380-383], light[384], electric[385] and magnetic fields[386], or biochemical variation such as ionic strength[387-378] , pH[382-383] or chemical agents[389-390]. Such a response might be as swelling, shrinking or degradation of hydrogels. To manufacture hydrogel materials, methods and processes traditionally used are reported in a recent review study[369], however, synthetic hydrogels, due to their higher water absorbent capacity and mechanical strength and longer shelf-life, have found more research and industrial applicability than natural hydrogels over the past two decades. Examples of common natural hydrogels include fibrin, agarose and alginate, and likewise, common synthetic polymers can be formed as hydrogels include polyacrylamide, polystyrene, poly (ethylene glycol) and poly (vinyl alcohol)[391]. However, polyacrylamide- and acrylamide-related copolymers constitute one of the major base materials for super absorbance hydrogels.

---

[5] The contents of this chapter have been incorporated within a paper, which is being prepared for submission, by Tong D.*, Yesiloz G.*, Ren C.L. and Madhuranthakam C.M.R., as “Controlled Synthesis of Poly (Acrylamide-co-Sodium Acrylate) Copolymer Hydrogel Micro-particles in a Droplet Microfluidic Device for Enhanced Properties”. *Authors have equal contribution. This work was conducted in collaboration with Dizhu Tong, a MSc student, and Dr. Mouli Madhuranthakam, an assistant professor of UW’s Chemical Engineering Department. G.Y. contributed to the system design, implementation and experimentation; G.Y. and D.T. executed experiments and analyzed the results; C.M.R.M. and C.L.R. assisted in analyzing the results; D.T., G.Y., C.L.R. and C.M.R.M. contributed to the paper.

Due to that the chemical and mechanical properties of hydrogels can be controlled and engineered by various synthesis techniques, hydrogels are very suitable to solve problems in medicine and biology. For instance, since many people die because of organ failure every year, hydrogels can be employed as tissue construct. Or, in order to decrease the toxic effects of high drug doses, the drug doses can be released in a controllable manner by means of hydrogel particles[391]. This also shows the importance of controlled synthesis of hydrogel particles in terms of controlled porosity and cross-linking density. In Figure 8.1.1, schematic description of drug release mechanism of hydrogel particles are demonstrated, and potential pharmaceutical and biomedical applications of hydrogel particles are depicted in Figure 8.1.2.

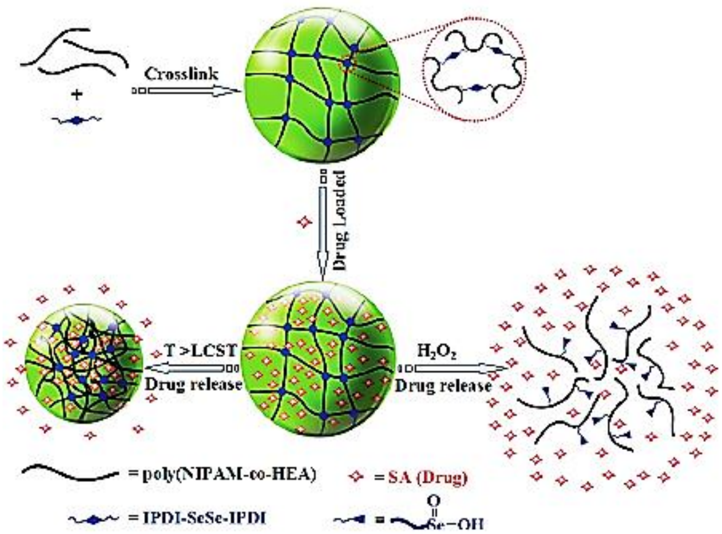

Figure 8.1.1 Thermo-and-oxidation responsive morphology change of hydrogel particles[377]

Bulk polymerization, emulsion polymerization, solution polymerization and micro-emulsion polymerization are some examples of conventional hydrogel synthesis methods. However, these polymerization techniques need either complex mixing units in reactors or large amount of surfactant and stabilizers that increase the cost. Besides, cross-linking density, molecular weight and copolymer composition are critical parameters to be controlled which are related to reaction temperature since most of polymerization reactions are exothermic. In this perspective, droplet microfluidics enables a promising tool and platform technology for polymerization for better process control that increases characteristic features of hydrogels particles. This is mainly due to that droplet microfluidics allows

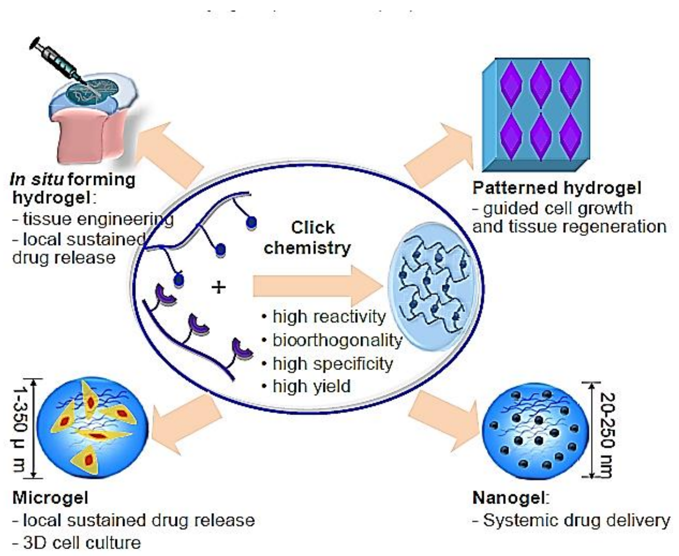

Figure 8.1.2 Preparation and potential pharmaceutical and biomedical applications of hydrogel particles[370].

highly monodispersed nano-liter sized droplets to be generated at kHz rates in microchannel networks[143,281,392-393], and that allows advantages for polymer synthesis in droplets such as precise control of reaction conditions, control over size, morphology and composition as well as advantages like fast heat dissipation because of high surface to volume ratio. Although single-phase microfluidics can also be used for polymerization in microchannels, the main challenge is the viscosity increase during polymerization which potentially causes to clog the microchannels. In this case, a mixer may be required which increases the complexity[394]. Droplet based systems become more efficient for this task.

Dang et al.[395] demonstrated a monodispersed PEG hydrogel microparticle preparation method using a flow-focusing microfluidic device fabricated using PDMS. By adjusting continuous and dispersed phase flow rates, they optimized the hydrogel concentration and with a UV-source the reaction was initiated (Figure 8.1.3). In another study, Haag et al.[396] designed and developed pH-sensitive microgels from PEG-dicyclooctyne and dendritic poly (glycerol azide) (dPG-azide) by combining click reaction and droplet-microfluidics (see Figure 8.1.4). Precise control of microgel degradation kinetics in a pH range of 4.5 and 7.4 was obtained. Also, NIH 3T3 cells were encapsulated into the microgels and the cells were released on demand by decrease the pH value. It is noteworthy to mention that the released cells showed over 94% viability.

It should be emphasized that the development of click hydrogels, micro and nanogels is a newly burgeoning field. Studies on biomedical and pharmaceutical applications with compatibility of hydrogels are highly important.

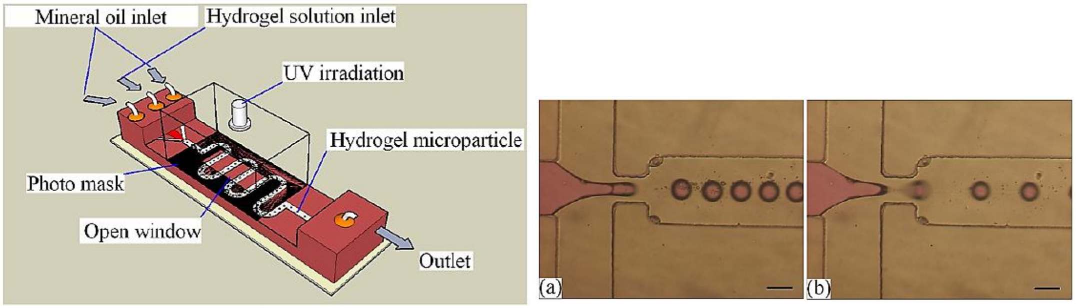

Figure 8.1.3 Schematic diagram of hydrogel droplet setup (left image). PEG hydrogel droplets formation under different flow rates (right image, 1.2 mL/h (a) and 1.8 mL/h (b))[395].

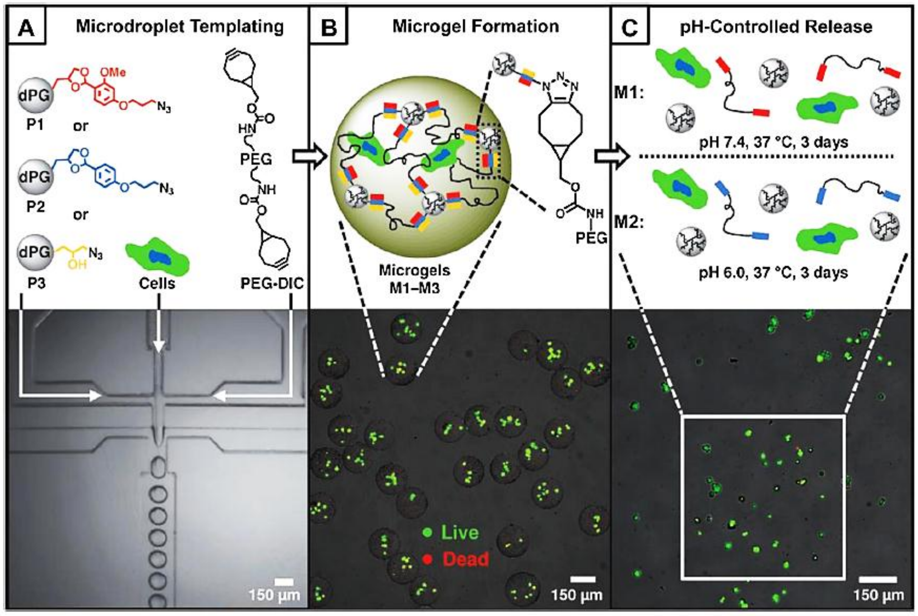

Figure 8.1.4 Click microgels with combination of droplet microfluidics showing encapsulation and releasing of living cells from microgels[396].

8.1.2 MICROWAVE-ASSISTED POLYMERIZATION

Another aspect of hydrogel particle synthesis method is microwave assisted polymerization. In recent years microwave-assisted chemical reactions have been progressively popular. Up to date, microwave energy has become an essential part in many technical applications in chemical and related industries, in particular in the food-processing, drying, and polymer industries, also range from analytical chemistry (microwave digestion, ashing, extraction), to biochemistry (protein hydrolysis, sterilization), pathology (tissue fixation), and medical treatments (diathermy)[251,397]. Even though a few research attempts were given to microwave heating to accelerate synthetically useful chemical transformations, after 1996s the number of microwave synthesis studies increased[398]. The origin of such attempts was the advantage of controlled microwave heating that considerably reduce reaction times, improve product yields and increase product purities by reducing unwanted side reactions compared to conventional synthetic methods[399-400]. Many experimental studies on microwave-assisted organic synthesis have been conducted in domestic microwave ovens, and they mostly do not allow the parameters to be controlled such as temperature and irradiation mode which is critical for chemical synthesis. And, another major drawback is that using large volumes in such systems limits the penetration depth of microwave system. The penetration depth of microwave irradiation into absorbing materials, i.e. reaction mixtures, at the common operating frequency of 2-3 GHz is usually on the order of a few centimeters depending on the dielectric properties of the medium. Namely, in a large reactor (>1 liter) only a small portion of the surface may absorb microwave power, which is not reasonable and effective. Hence, so as to overcome this physical limitation, development of *microfluidic-microwave integrated* continuous reactors, where reaction mixture passing through small microchannels is heated and penetration depth problems are avoided is extremely in urgent need. On the other hand, while there have been many studies on organic synthesis[251-253,401], the use of microwave irradiation for polymerization studies is still quite undiscovered.

As an example of using a microwave oven, a droplet-based millifluidic device is designed where aqueous droplets of monomer are used as polymerization microreactors in [402]. A tubular reactor was fixed inside the microwave cavity of a commercial instrument, and the inner diameter of the tubing is about a few millimeters that generate droplets of about 2 to 5 mm (Figure 8.1.5). Even though there was an increase in the rate of production of the polymeric material, i.e. between 30 to 40 %, the system was not efficient enough to finely control the process in terms of temperature, mixing time or heat transfer[403]. Moreover, since the tubular reactor is fixed up within the commercial microwave oven, the whole device is like an enclosed cavity; thus there is no way to observe the behavior of the droplet, neither to monitor the reaction in situ.

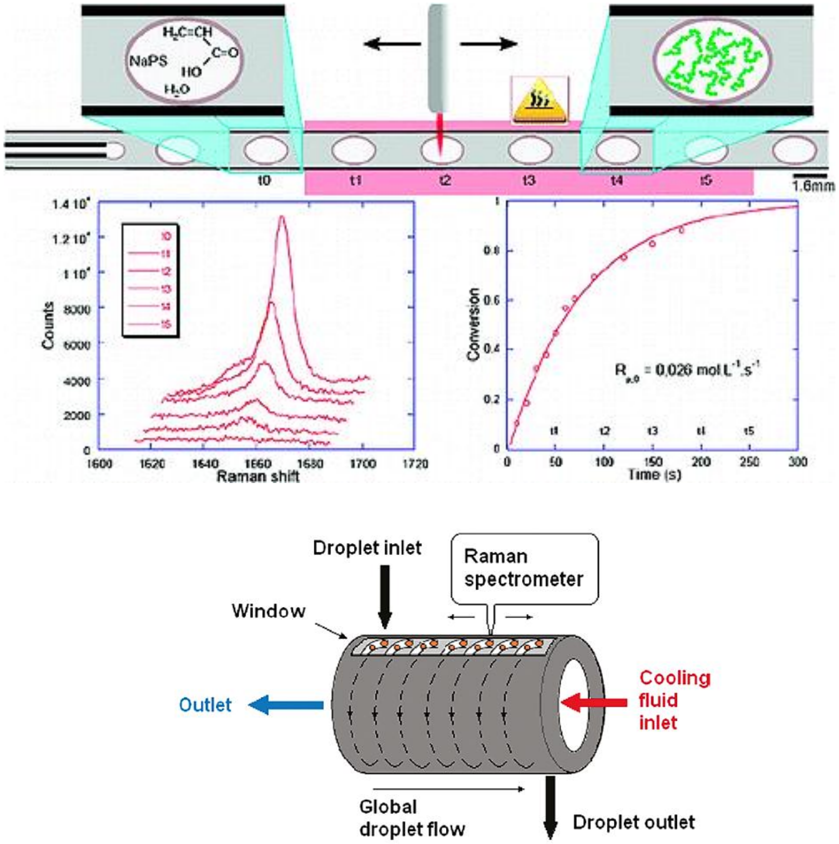

Figure 8.1.5 Schematic description of droplets with monomers and synthesis after heating (top), schematic of the millifluidic device(bottom)[402].

8.1.3 OBJECTIVES OF THE STUDY

There are two main objectives of this study.

(i) As discussed and introduced above, hydrogels are very useful tool for many pharmaceutical and biomedical applications and controlled production of them utilizing droplet microfluidics and Lab-on-a-chip technology is crucial. Thereby, the primary objective of this study is to synthesize monodispersed poly (acrylamide-co-sodium acrylate) hydrogel micro-particles with controlled compositions and overcome such limitations and propose a better design for polymer synthesis and other chemical reaction application purposes.

(ii) showing the potential of the miniaturized microwave resonator/heater integrated with droplet microfluidics device for synthesizing the hydrogel microparticles is another objective for future studies of using this platform technology. The motivation is due to that microwave-assisted synthesis dramatically reduces the reaction times and increase the product yields, and also enhances product purities by reducing unwanted side reactions. Additionally, although there are examples of organic synthesis under microwave conditions and relatively fewer for polymer science, most of them use commercially available microwave ovens. First of all, such approaches, obviously, are not applicable to droplet microfluidics that droplets need to be delivered controlled energy transfer to perform reaction properly inside the "individual droplets". Secondly, those domestic ovens do not allow to finely adjust the temperature which is critical for chemical synthesis. Penetration depth is another issue of using bulky ovens since only a small portion of the reactor surface absorbs microwave energy. Hence, the spiral design of microwave resonator used in thesis work is a good alternative to heat up individual droplets that contain proper monomer reagents to form hydrogels both utilizing the advantages of droplets (i.e., elimination of penetration problem since droplets are only around 50 um height and being isolated individual reactor for composition control) and selective heating feature of microwave resonator.

Below, free-radical polymerization, some properties of microscale hydrogels, materials and methodology used in this work are presented followed by experimental results, discussion and conclusions.

8.1.4 FREE-RADICAL POLYMERIZATION

Free radical polymerization is polymerization technique that a polymer structure is formed by addition of free radical building blocks. Acrylamide hydrogel is usually synthesized by free-radical polymerization, which typically involves four steps: initiation, propagation, chain transfer, and termination. The first step of polymerization is the initiation that the reaction starts with the decomposition of initiator and the initiation of monomer to form a monomer free radical. There are different types of initiation exists such as thermal decomposition, photolysis, ionizing radiation, etc. Once the free radical initiators are formed, monomer molecules are attracted by them to increasing the chain length, which is the step of propagation. After polymer chains are formed, a polymer chain may react with an initiator, which terminates that polymer chain, however, releases a new radical initiator. Then this initiator can begin a new polymer chain which makes the chain transfer mechanism. Chain termination happens when the reaction includes completely free of contaminants. Figure 8.1.6 shows an example process of the mechanism for preparation of microgel particles[404].

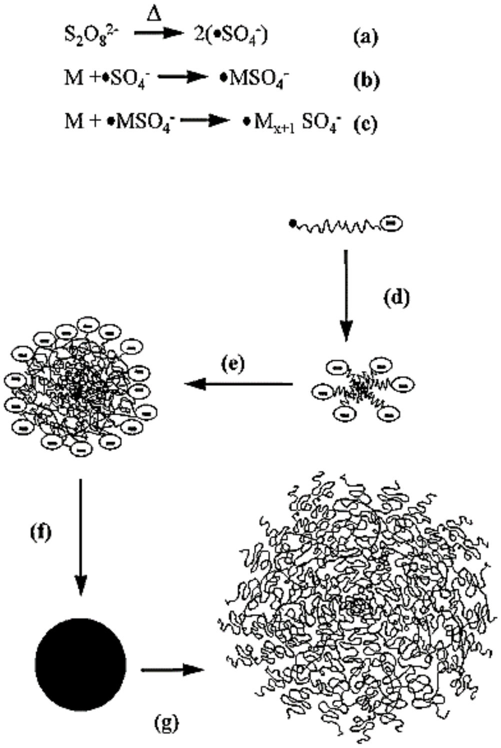

Figure 8.1.6 Mechanism for the preparation of microgel particles. The steps shown are initiator decomposition (a), initiation (b), propagation (c), particle nucleation (d), particle aggregation (e) particle growth in a poor solvent (f) and particle swelling in a good solvent (g)[404].

8.1.5 MECHANICAL PROPERTIES OF MICROSCALE HYDROGELS

8.1.5.1 CROSSLINKING, POROSITY AND SWELLING

Synthesized hydrogel particles has characteristic features such as the size of the polymer mesh, the average molecular weight, the swelling ratio and crosslinking density. These parameters affect the mechanical and chemical performance characteristics of hydrogel particles[391]. Figure 8.1.7 demonstrates weakly and highly cross-linked hydrogel structures and diagram of a microgel particle in a poor and good solvent that shows how the hydrogel particle can swell.

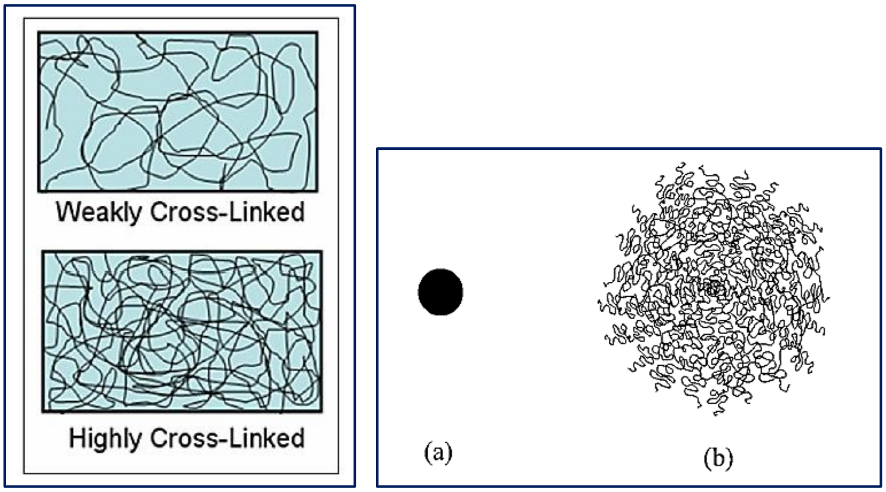

Figure 8.1.7 Highly cross-linked and weakly cross-linked hydrogels (left)[391]. Diagram depicting a microgel particle in a poor (a) and good solvent (b), respectively (right)[404].

8.1.5.2 MECHANICAL PERFORMANCE

The adaptable mechanical properties of hydrogels make them particularly use for drug delivery purposes and tissue engineering. As an example, mechanical forces effect cell viability, gene expression and cell differentiation pathways. Since human tissues have highly organized structures, synthesizing hydrogel particles with varying mechanical properties help them to be utilized better to mimic natural structures[391].

8.1.6 METHODOLOGY AND MATERIALS

8.1.6.1 MATERIALS

Monomer acrylamide (Am) and co-monomer sodium acrylate (NaA), the photo-initiator 2,2-Diethoxyacetophenone (DEAP), the cross-linker N,N′-Methylene-bisacrylamide (BIS) , and surfactant sorbitan monooleate (SPAN 80) were obtained from Sigma Aldrich Canada and used as received. The oil phase hexadecane was also purchased from the same supplier and used after filtration.

8.1.6.2 MICROFLUIDIC DEVICE

Hydrogel micro-particles were made using a flow focusing generator which enables monodispersed droplet generation in a microfluidic device made of PDMS shown in Figure 8.1.8. The microfluidic

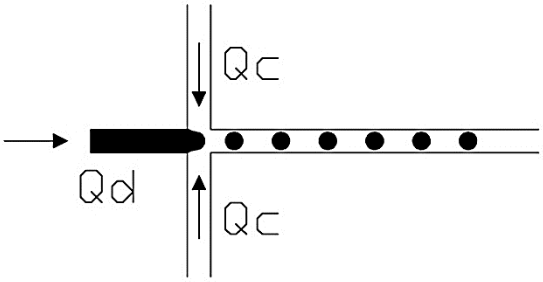

Figure 8.1.8. Schematic diagram of flow-focusing microfluidic device used to synthesize hydrogel micro-particles. Q_d represents the flow rate of dispersed phase (monomer solution) and Q_c represents the flow rate of continuous phase (oil solution).

device was fabricated using standard soft lithographic techniques that details can be found in Chapter 3. Briefly, the photoresist master was fabricated on silicon wafers using the same protocol reported in Yesiloz et al.[281]. In order to make PDMS replica molds, PDMS pre-polymer was mixed at a 10:1 ratio of base to curing agent, degassed and molded against the SU-8/ silicon master and then cured at 95 ^{0}C for 2 h. The molds were then peeled off from the master and fluidic access holes were made using a 1.5 mm biopsy punch. Both the finished components and the PDMS mold were then treated with oxygen plasma at 29.7 W, 500 mTorr for 30s. The plasma treatment process renders PDMS hydrophilic; however, for generating water in oil droplets stably, the PDMS channels need to be hydrophobic which was realized by either changing the channel property by Aquapel injection or keeping the finished microchips on a hotplate for 48 hours for microchannel wall surface treatment. In the experiments, channel width and height were fixed at 200 μm and 50 μm respectively.

Table 8.1.1. Monomer feeding compositions.

Monomer solution number	Am in feeding (%)	NaA in feeding (%)	Cross-linker weight (g)
1	100	0	0.2
2	90	10	0.1
3	90	10	0.2
4	45	55	0.1
5	45	55	0.2
6	0	100	0.2

8.1.6.3 EXPERIMENTAL PROTOCOL

In the first approach, in this study, to synthesize copolymer hydrogel micro-particles in droplet microfluidics photo-polymerization is used. The schematic diagram of the inverted chip configuration, droplet generation and UV-exposure setup is shown in Figure 8.1.9. A computer controlled pressure system (Fluigent MFCS8) is used to pump the dispersed phase fluid (monomer solution) into the center channel and the continuous phase fluid (oil) into the two side channels. The dispersed phase is an aqueous solution containing two monomers (acrylamide and sodium acrylate), a cross-linker (BIS), and an initiator (DEAP). The total monomer feeding concentration is fixed at 9.28M and its compositions are listed in Table 8.1.1. The oil phase is a mixture of hexadecane, the initiator, DEAP, and a surfactant, Span 80 (100:5:2 with respect to hexadecane: DEAP: Span80 ratio). The purpose of adding the initiator, DEAP, in the oil phase is to maintain the initiator concentration inside the monomer droplet since DEAP is miscible with both water and hexadecane.

On-chip polymerization of droplets is ideal since no external setup is needed except a UV lamp that needs to be aligned with a long channel where droplets are traveling through. However, partial or complete channel blockage often occur due to the shape and viscosity change of the droplets after polymerization. Blockage results in the change in the local resistance which slows down the coming droplets causing multiple droplets to be polymerized together forming a large polymer slug (see Appendix B-B1). In this on-chip method, the UV light is focused on the reaction channel. This method suffers from two problems. First, if the UV light intensity is too high, the UV light that is scattered horizontally through the PDMS mold due to the UV transmittance feature of PDMS initiates the monomer solution in the feeding microchannel. This issue causes early initiation of polymerization and results in clogging in the feeding channel. Second, if the UV intensity is relatively at medium or lower level, then the reaction channel is required to be extended using long serpentine design in order to increase the reaction time. However, the extension of serpentine channels can cause large pressure drop in microchannel which makes difficult to pump highly viscous droplets after polymerization. Besides, if the polymerization is not completed along the long serpentine channels, then the partially reacted polymer microparticles become as gels and coalesce each other. These merged droplets form a large and highly viscous plugs which come to a stop in the serpentine channel due to large pressure drop (see Appendix B- Figure B1.1 and Figure B1.2). The performance is improved by generating much smaller droplets than the channel width which, however, pushes the droplet generation into unstable operating regimes[99],[71],[22]. Later, a semi-on-chip polymerization approach is adopted by forming droplets containing monomer solution inside the chip

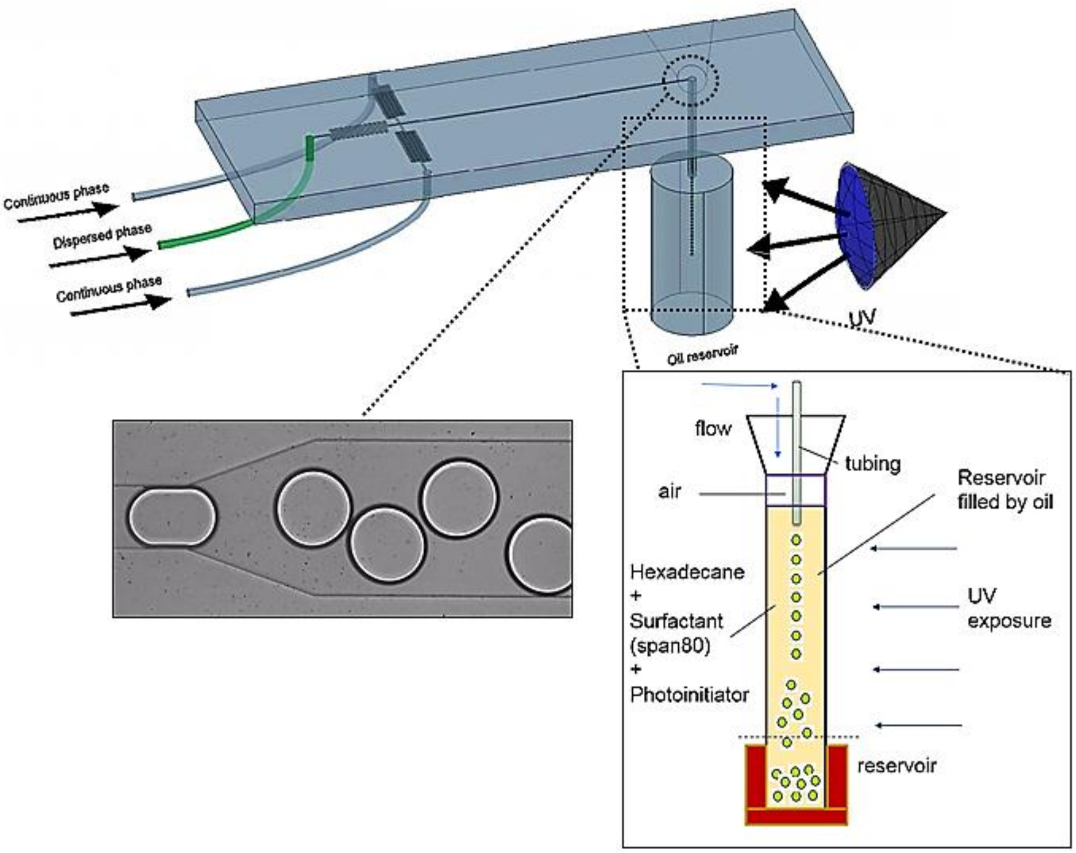

Figure 8.1.9 Schematic diagram of inverted chip method with a flow focusing microfluidic device. The green tubing indicates for dispersed phase (monomer solution) inlet and the blue tubing indicates continuous phase inlets. The serpentine before the junction is for pressure stabilization. The outlet reservoir is connected to a short tubing that transports droplets to the reaction chamber which is exposed to UV light.

and transporting them into a capillary tubing which is aligned with the UV-source to initiate the reaction. In this approach, the tubing is connected at the outlet of the microfluidic chip which is needed to be bended to be aligned with UV-source. The bending of the tubing and gravitational force on droplets cause non-uniform droplet spacing. Although larger and smaller tubing diameters than that of droplet size are used, still the droplet spacing issue results in having long polymerized slugs (see Appendix B-B2 for further information). Also, off-chip polymerization of droplets is attempted, however, after reaction droplets form a thin-film of polymer (see Appendix B-B3). Therefore a practical yet useful method is then implemented. The microfluidic chip is inverted upside down, and a short tubing is attached to the outlet of the microfluidic chip. The tubing is a straight PTFE tubing

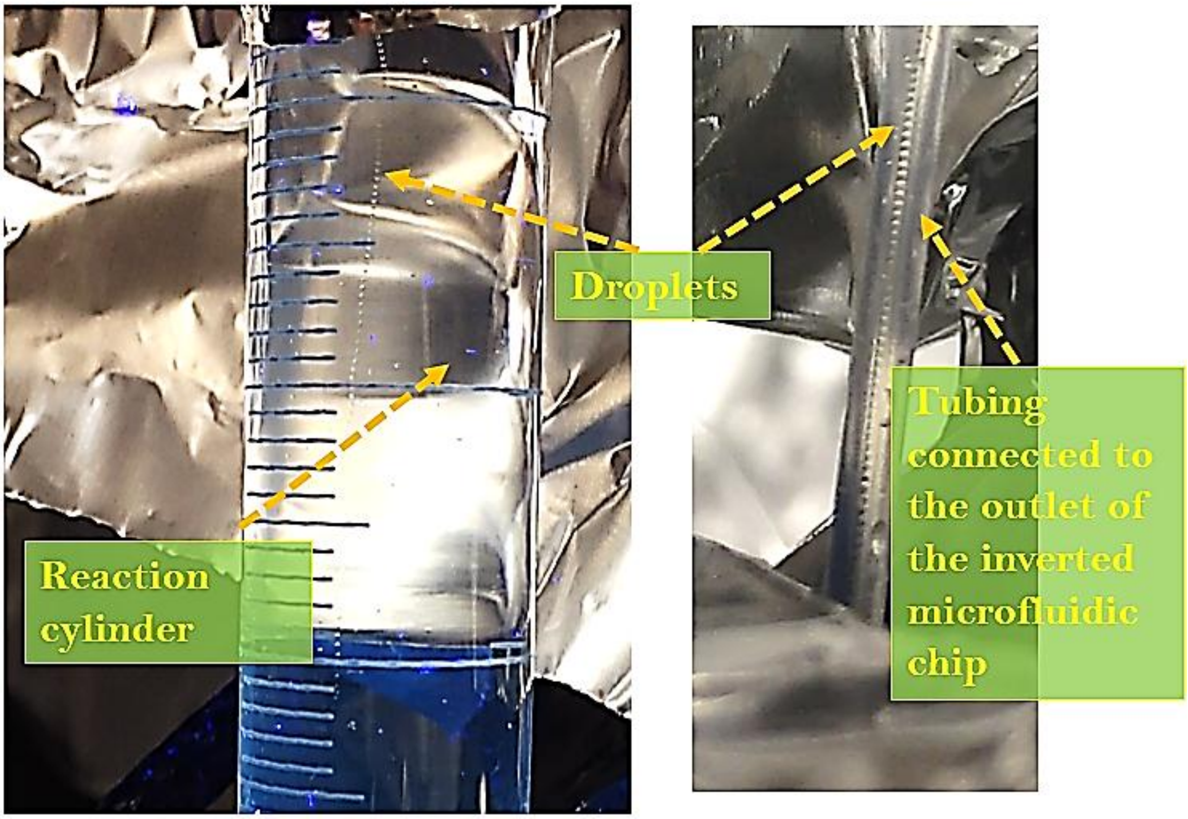

Figure 8.1.10 Images show train of droplets formed with the inverted chip approach. Left image shows droplets inside the reaction chamber and right shows inside the short capillary tubing. With this approach a well-spaced and robust droplet transport are obtained for hydrogel micro-particle synthesis which prevents droplet coalescence and aggregation.

(ID: 250 µm) which is immersed into a 10 ml graduate cylinder that serves as reaction chamber which is filled by hexadecane, surfactant (Span 80) and photo-initiator. Droplets are continuously pumped from the outlet channel to the reaction chamber with this setup. When the droplet generation is stabilized which is confirmed through an inverted microscope (Eclipse Ti, Nikon) and a high speed camera (Phantom v210, Vision Research), the microchip is removed from the microscope and inverted upside down. The generated monomer droplets flowing in the center of cylinder are polymerized via exposure to UV light (ML-3500S, 50W/cm^2, Spectroline). The microfluidic chip, outlet tubing and bottom of cylinder are covered with an aluminum foil in order to avoid undesired photo-polymerization of the droplets inside the chip and aggregation of micro-particles at the bottom of the cylinder. A train of droplets in the outlet tubing and reaction chamber can be seen from Figure

8.1.10. The reaction time is controlled by varying the length of graduate cylinder and inlet pressure. The hydrogel micro-particle is washed with isopropyl alcohol three times and centrifuged at 8000 rpm for 1 minute for three times. The washed micro-particles are dried in a vacuum oven and stored in a vacuum desiccator for further analysis.

This process can continuously produce hydrogel micro-particles without clogging issue. An advantage of this method is that it prevents the droplet from merging inside the outlet tubing and aggregation of micro-particles in the oil reservoir. In all other attempted methods, the outlet tubing points upwards, and then tubing needs to be bended to collect the samples. In those cases, the velocity of droplet changes due to the gravity. Therefore, the transport behavior of the droplets is difficult to predict. In the inverted chip method, since there is no bending on the outlet tubing and droplets travel downwards instead of upwards against gravity, the droplet velocity is not affected. As a result, the risk of merging at outlet tubing is minimized, and a well-spaced and robust droplet trains are achieved. The well-spaced droplets prevent the aggregation of micro-particles (see Figure 8.1.10).

In the second approach, preliminary hydrogel synthesis is attempted through the microwave resonator, using the same microfluidic device. However, in the microwave case, the short tubing connected to the outlet of the chip and the reaction chamber are not required. Instead, a small rectangular well is cut into the PDMS mold just after the microwave resonator, and by this means the reaction is initiated on the chip inside microchannels. The synthesized droplets leave the channel and are collected in the well. The experimental setup is demonstrated in Figure 8.1.11. In this approach to microwave polymerization, the photo-initiator (DEAP) is replaced with a thermal-initiator (Ammonium persulfate). The monomer solution is placed in an ice bath so as to control the initial temperature of the monomer solution to inhibit any potential self-reaction issues. As with the UV-polymerization process, the system needs an external UV source, and achieving a proper reaction with the droplets is challenging due to the aforementioned difficulties. Thus, microwave-assisted hydrogel particle synthesis in droplet microfluidics with an integrated microwave resonator is a promising approach, described next

8.1.6.4 CHARACTERIZATION

The size of droplets and micro-particles were observed and recorded by an inverted microscope equipped with a CCD and a high-speed camera. The size and size distribution were measured and processed by ImageJ. The Fourier Transform infrared spectra (FTIR) of dried hydrogel micro-particles is performed using potassium bromide (KBr) pellet method and recorded by Bruker (Vertex

70) FTIR (see Figure 8.1.12).

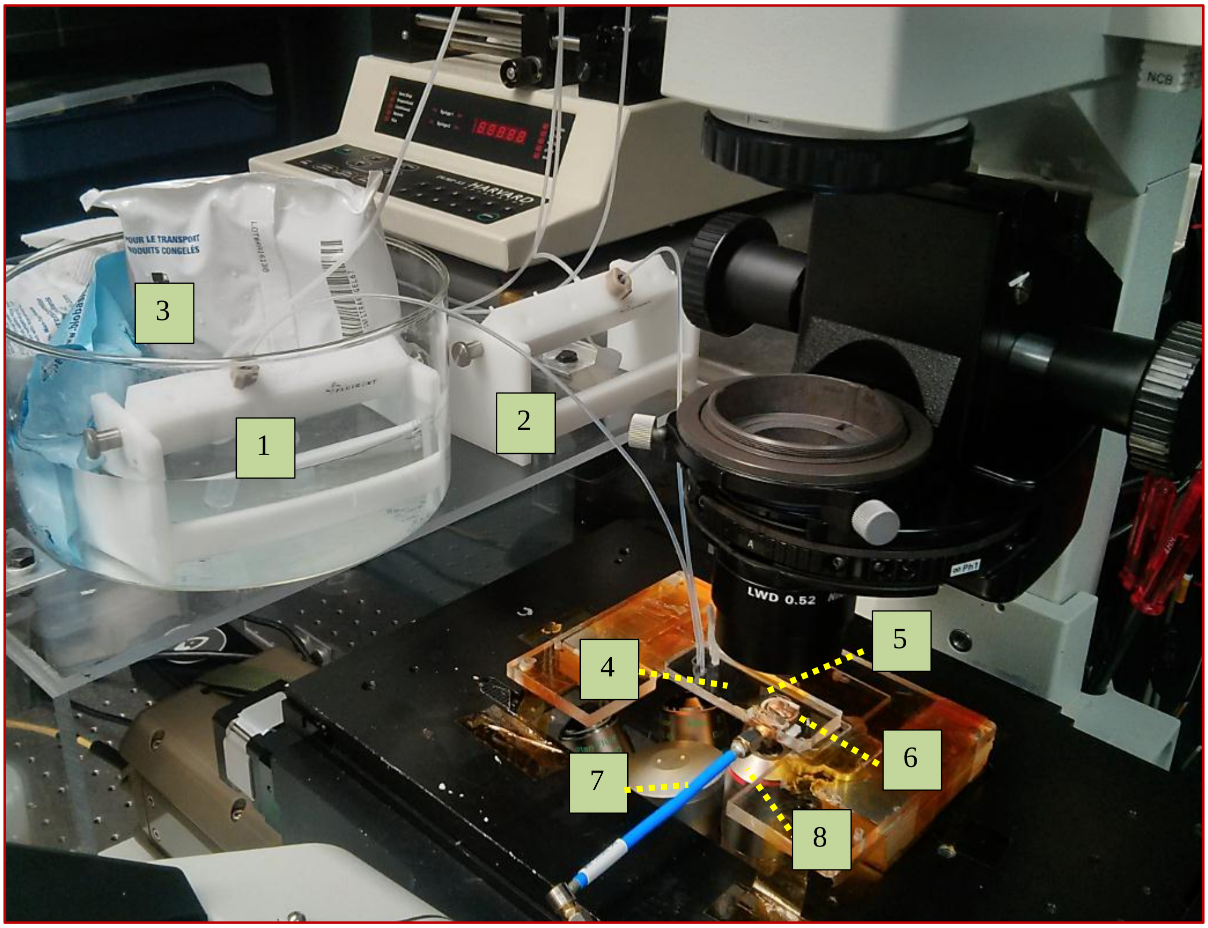

Figure 8.1.11 Microwave-assisted polymerization setup. 1-Monomer solution (disperse phase), 2-Oil (continuous phase), 3-Ice bath, 4-Microfluidic chip, 5-Microeave resonator, 6-Outlet, collection well, 7-Coaxial cable, microwave power, 8-Microscope objective for visualization.

The scan range is from 400 to 4000 cm^{-1} for 32 times. A background scan is run every time before a sample scan. The degree of swelling is evaluated by a swelling test under room temperature. The degree of crosslinking is closely related to the degree of swelling, according to the Flory-Huggins and the equilibrium swelling theories. For the micro-particle swelling test, the dried polymer micro-particles are added into a 96 well cell-culture plate, and the sizes of the dried polymer micro-particles (particle diameter) are recorded using a microscope and then analyzed with ImageJ. The analyzed dehydrated particle size is confirmed via SEM measurement as well. Then DI water at room temperature (25 ℃) is added into the corresponding well. The swelling process is recorded by using a microscope. The diameter of the swollen particle (at maximum absorbance capacity) is used to calculate the degree of swelling by the following equation,

$$Q = \frac{V}{V_o} = (\frac{D}{D_o})^3 \qquad (1)$$

where V and D are the volume and diameter of the swollen polymer micro-particle, respectively, V_0 and D_0 are the volume and diameter of the dehydrated micro-particle, respectively. Bulk polymer is synthesized in order to compare with the swelling ratio of micro-particles. The bulk polymer was synthesized by using the same monomer solution and the same UV lamp.

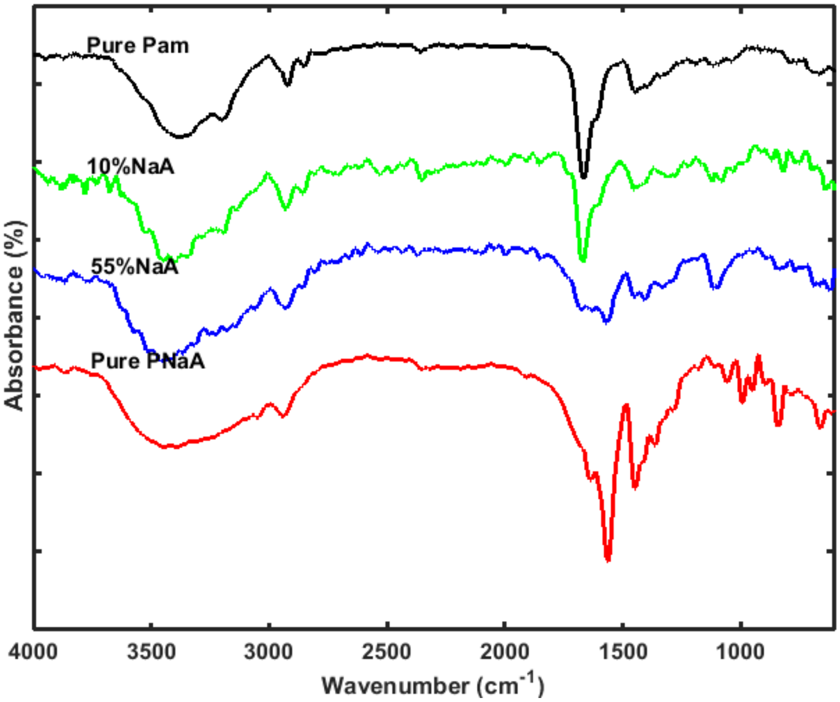

Figure 8.1.12 FTIR spectrum for the copolymer hydrogel micro-particles. From top to bottom: Pure Polyacrylamide, 10% sodium acrylate copolymer, 55% sodium acrylate copolymer and pure Sodium Polyacrylate.

8.1.7 RESULTS AND DISCUSSIONS

8.1.7.1 EFFECT OF MONOMER FEEDING ON CHEMICAL COMPOSITION OF MICRO-PARTICLES

The chemical composition of copolymer was measured and verified using FTIR spectrum as shown in Figure 8.1.12.

8.1.7.2 SWELLING RATIO

The dried polymer hydrogel microparticles with different monomer compositions are placed in the cell-culture well plate, and their original sizes are recorded using the microscope. When DI water is added, the micro-particles swell quickly and the swelling process is recorded by the camera attached to the microscope. The volume increases 4 to 39 times for different monomer compositions and different cross-linker concentrations. Figure 8.1.13 illustrates experimental results of hydrogel microparticle swelling ratio versus time for 55% NaA and 0.1 g of cross-linker concentrations, case 4 in Table 8.2.1. As can be seen from the figure particles absorb water very quickly and around 20s the swelling saturates.

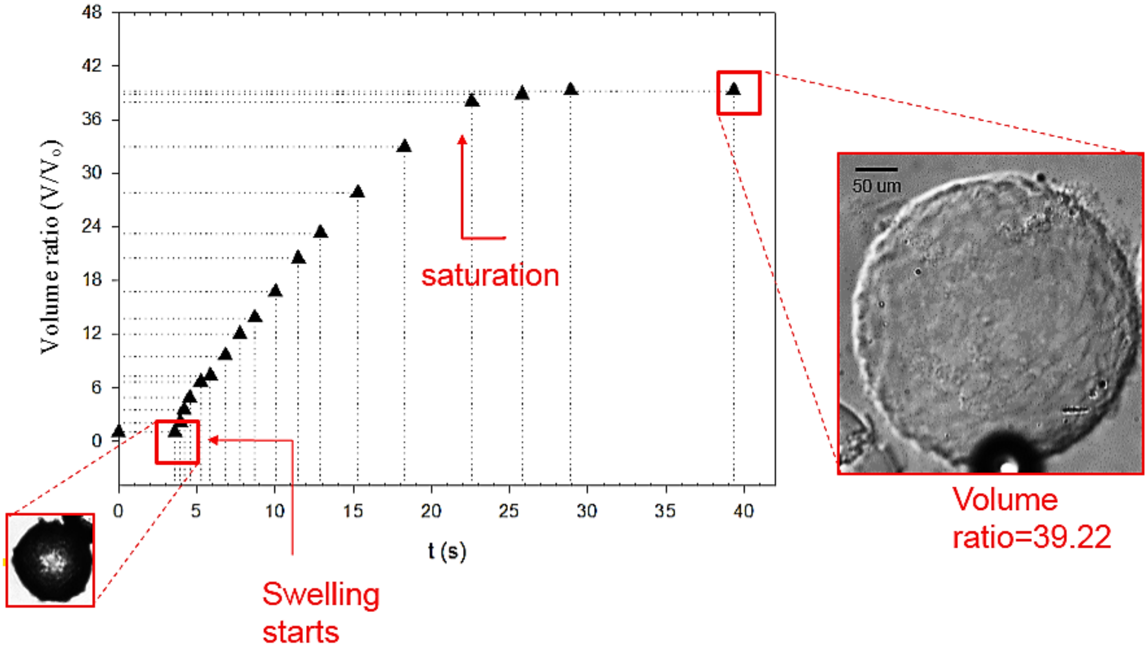

Figure 8.1.13. Hydrogel microparticles experimental swelling result for 55% NaA, case 4 in Table 8.2.1.

8.1.7.3 EFFECT OF MONOMER FEEDING AND CROSS-LINKER ON SWELLING OF MICRO-PARTICLES

After swelling, the dried micro-particles expand to almost 40 times its original size for 55% NaA copolymer. The 10% NaA copolymer has a smaller swelling ratio (~14 times). The larger swelling ratio is attributed to the higher ionic content in 55% NaA copolymer, which is in agreement with the Flory-Huggins theory (see Figure 8.1.14).

8.1.7.4 EFFECT OF CROSS-LINKER CONCENTRATION ON SWELLING OF MICRO-PARTICLES

For different monomer compositions, the effect of cross-linker concentration on the swelling of microparticles is investigated. Two different concentrations of the crosslinker (0.1g and 0.2g) are used in this study. The cross-linker concentration has an opposite effect on the swelling ratio. The higher cross-linker concentration, the higher crosslinking density and the smaller number of average molecular weight between the crosslinks; which results in less swelling.

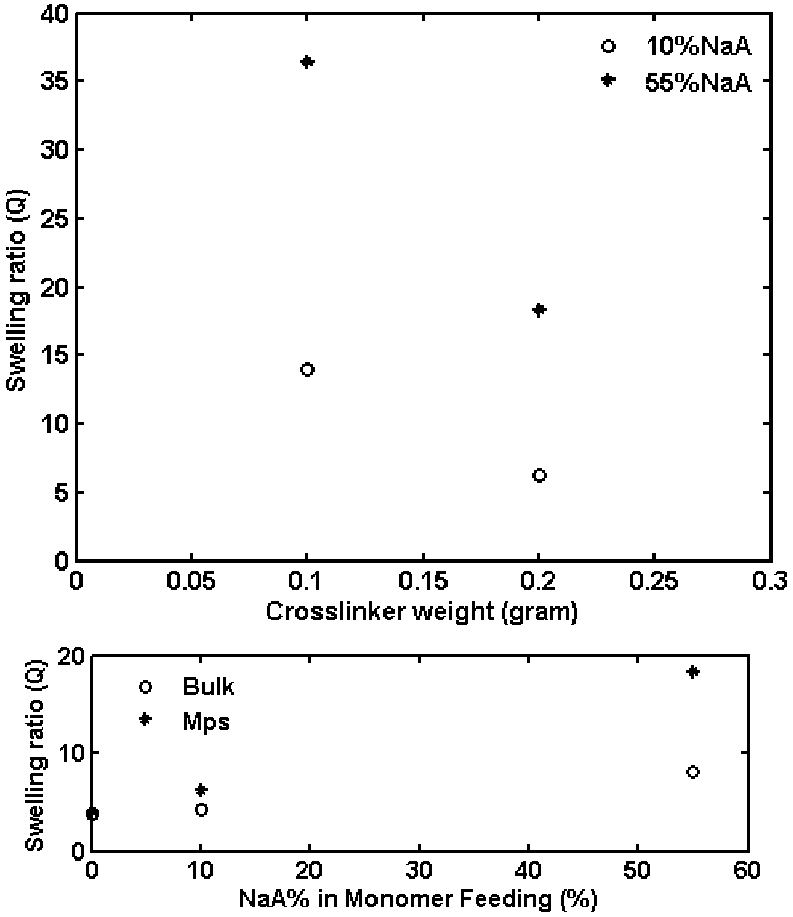

Figure 8.1.14 Hydrogel microparticles experimental swelling results for different monomer and cross-linker concentrations (top). Comparison of bulk and microparticle swelling ratio (weight of cross-linker is fixed at 0.2g) (bottom).

Compared to the bulk hydrogel, the micro-particles not only swell faster but also possess a higher swelling ratio, especially when the ionic content is at a high level. From Figure 8.1.14, the swelling ratio is the same for the polyacrylamide homopolymer obtained from the bulk and the microfluidic chip. At 10% of sodium acrylate content, the swelling ratio of the micro-particles is 47.12%, which is higher than that of the bulk. At 55% of sodium acrylate content, the swelling ratio of the micro-particles is 126.49%, which is higher than that of the bulk as well.

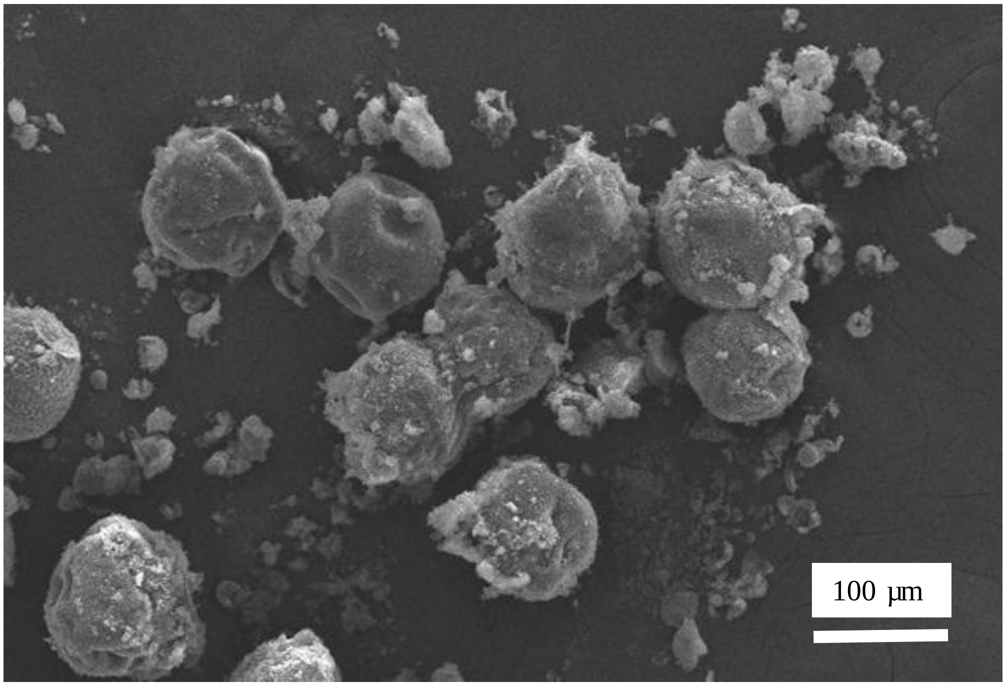

Figure 8.1.15 SEM image of dried hydrogel microparticles.

The micro-particles have a large surface-to-volume ratio compared to that of the bulk; therefore, microparticle swell much faster than that in the bulk. During polymerization, the oil phase instantaneously removes the heat released from droplet polymerization because the droplets are fully encapsulated in the oil phase. Therefore, the microparticles have a more uniform crosslink in the surface and core compared to the bulk, which allows water to penetrate to the core of micropolymer faster than in bulk. Also, SEM images of dried hydrogel microparticles can be seen in Figure 8.1.15.

8.1.7.5 MICROWAVE-ASSISTED HYDROGEL SYNTHESIS

Droplets containing the acrylamide monomer solution listed in Table 8.1.1-case1 are generated through the same flow-focusing microfluidic design used in the photo-polymerization case. Also, the microwave resonator is integrated in the microfluidic platform as described in previous chapters. In this approach, since the polymerization is initiated by thermal means, the photo-initiator is removed from the monomer solution, and ammonium persulfate is added as a thermal initiator. When droplets are passing over the microwave resonator, the power is turned on and the resonator heats the droplets, which initiates the polymerization reaction and hydrogel synthesis. It should be noted that a slightly different method is applied for the PDMS mold preparation herein. Results obtained in Chapter 5 provide a useful guideline for understanding the power absorption and heating efficiency of droplets. As per the analysis of chip material permittivity effects on power absorption (Figure 5.17), increasing the permittivity of the chip material increases the heating efficiency. Moreover, the optimum passivation layer thickness increases as chip permittivity increases. Thus, the PDMS mold is initially mixed with 3 um copper powder (5% w/w) in order to increase permittivity. Then using this mixture the chip is fabricated with the same fabrication protocol described in Chapter 3. This approach also allows the use of a thicker passivation layer, thereby an increasing heating efficiency. The modified microwave-microfluidic integrated chip is shown is Figure 8.1.16.

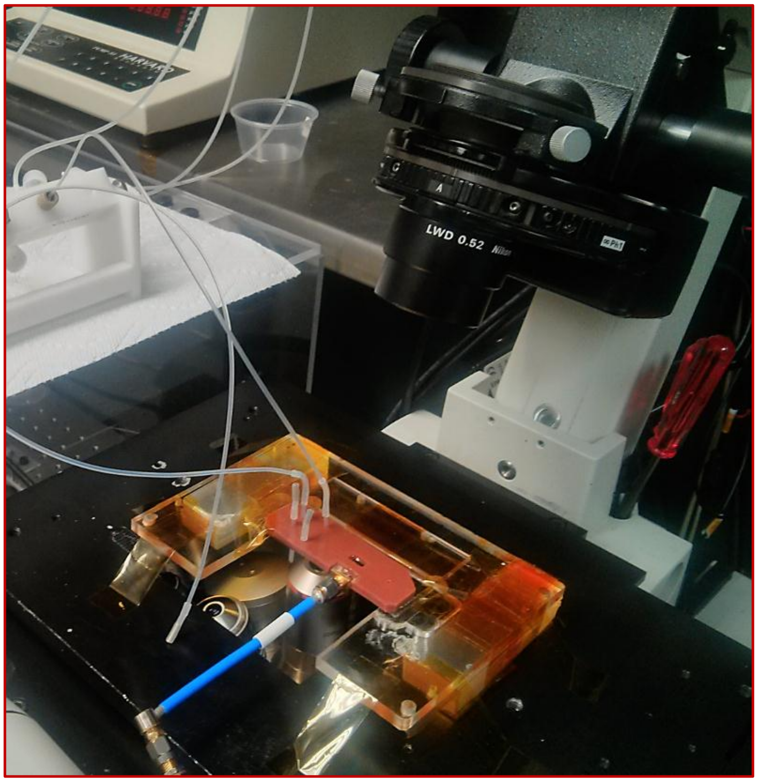

Figure 8.1.16 Modified microwave-microfluidic integrated chip.

Figure 8.1.17 demonstrates the bright field microscope images for the microwave-assisted reaction case. As can be seen from the figure, when microwave power is off, droplets containing the acrylamide monomer solution pass over the resonator without being effected (top image). As

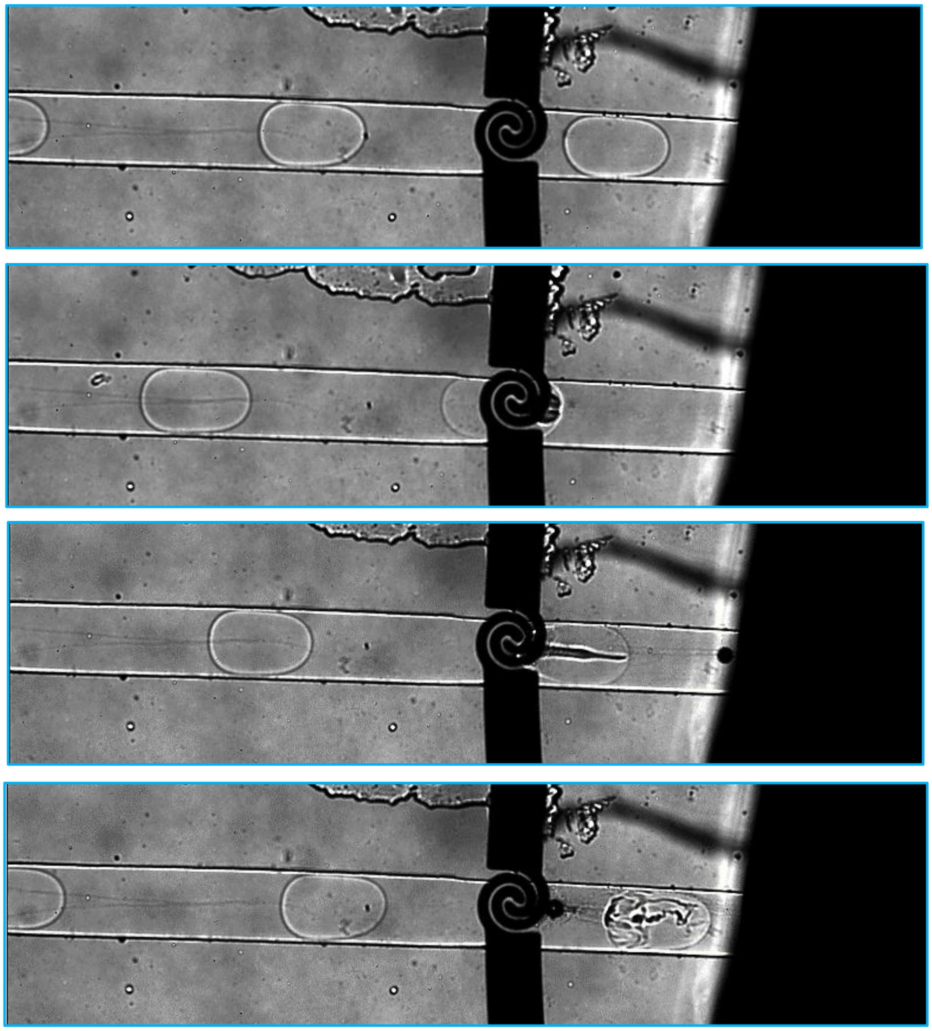

Figure 8.1.17 Microwave-assisted acrylamide hydrogel particle synthesis. Top image shows the microwave power off case. Then microwave heater is turned on and the initiation of the polymerization reaction is observed.

mentioned above, just after they pass the resonator, the droplets exit the microchannel and are collected in the well. That is, the polymerization reaction is started inside the channel, and the reacting droplets transit from the channel into the well. This transition to the well is needed prevent any potential clogging issues. When the microwave heater is on, as clearly observed, the reaction starts immediately, as captured in Figure 8.1.17. For better visualization of the hydrogel particles, a very small portion of fluorescein dye (<10uM) is added to the droplets. In Figure 8.1.18, the synthesized acrylamide hydrogel particle is seen by fluorescent imaging, which shows gradual swelling of the hydrogel. These preliminary results demonstrate that thermal initiator and microwave heater worked well to start the polymerization reaction and synthesize the hydrogel particle from droplets.

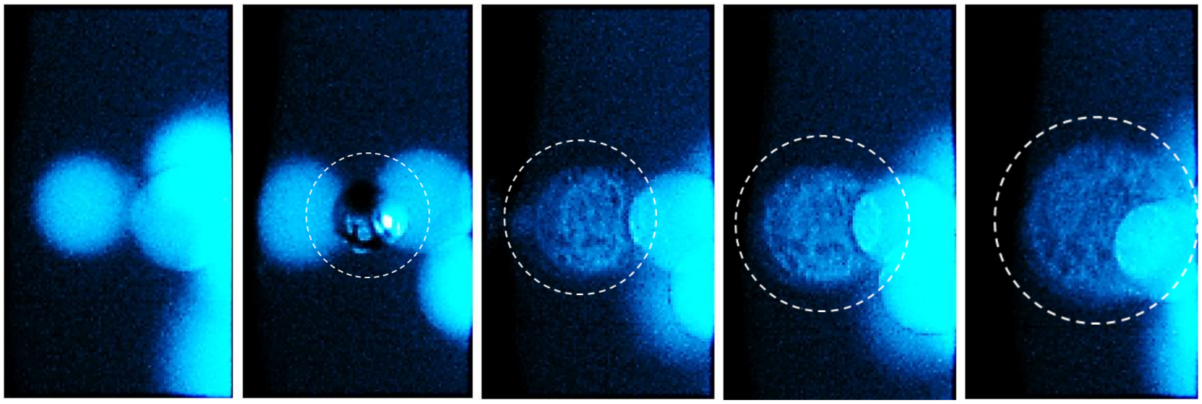

Figure 8.1.18 Swelling of microwave-assisted hydrogel particles by fluorescent imaging. The gradually expansion of particles are captured.

8.1.8 CONCLUSIONS

In this work, first, poly (acrylamide-co-sodium acrylate) hydrogel micro-particles were synthesized in an inverted microfluidic chip. This simple and robust process can continuously produce microparticles. The properties of microparticles (with various monomer compositions and cross-linker concentrations) were analyzed, such as the volume swelling ratio, composition, and size and size distribution. The swelling property was controlled by the ionic content and the cross-linker concentration. The swelling index is far higher in hydrogel microparticles that in bulk hydrogel. Second, as a preliminary work, the microwave microfluidics integrated heating platform was employed to show the microwave thermal initiation and polymerization of droplets for synthesizing hydrogel particles, suitable for use in drug delivery applications. The results show that microwave-assisted polymerization in droplet-based microfluidics has great potential, although further work is needed to enhance particle collection and test the effects of other parameters in additional cases.

8.2 DNA HYBRIDIZATION SENSING FOR DISEASE DIAGNOSIS USING MICROWAVE BASED SENSORS

8.2.1 INTRODUCTION AND OBJECTIVES

Rapid progress in identifying nucleic acid sequences has increased the importance of building high-performance detection technologies and has led to early diagnosis of many inherited diseases. The specific base sequence detection of human, viral or bacterial DNA holds crucial attention for the detection and diagnosis of many diseases. During the last decade, various detection platforms and their designs have been devoted to nano and micro length scale because the detection of infectious and inherited diseases at the molecular level would enable reliable early diagnosis[405-406]. Consequently, the determination of specific DNA sequences is a main task for various research applications and clinical analysis. Cancer, influenza, genetics, criminology, the identification of pathogenic species in medical diagnostics, detection of contaminants in the food industry are only some of these applications and show the great importance of detecting DNA[407-409]. Recently, the realization of genetically determined diseases has increased because of newly developed techniques. Currently, the detection of DNA hybridization events between two single-stranded and complementary DNA pieces by means of different sensors predominantly establish the sensitive and specific detection of DNA sequences.

Conventional diagnostic tools typically rely on combinations of radioactive labels to produce a signal due to DNA hybridization, fluorescent labelling or electrophoretic separations. Fluorescent labelling is a common technique but needs detailed sample preparation steps, and radioactive labelling requires highly trained personnel and has safety risks[406-408]. For instance, to detect fast-spreading infectious diseases using culture diagnostic techniques can take days to weeks. Moreover, for some diseases, detection might be achieved only at advanced stages because insensitive devices cannot detect the early stages[405]. Due to these time-consuming, labor-intensive and toxic effects, traditional methods should be replaced by new label-free or other techniques. Favorable and ideal detection methods are desired to provide compact, rapid, highly sensitive, selective and cost-effective solutions.

Microfluidic Lab-on-a-chip (LOC) devices provide numerous advantages in clinical diagnostics, biomedical research and environmental monitoring[410]. Such devices can sustain a controlled environment in which biomolecule binding, mixing and signal transduction can take place, using fewer reagents. However, there remains a need for platforms that integrate rapid sensing and analysis of the parallel processing of DNA hybridization events without complicated steps.

For this purpose, a microwave-based integrated LOC platform is studied preliminarily in this work. It uses a rather new technique involving nucleic acid biosensors for DNA hybridization detection and disease diagnosis. The microwave combined platform has strong potential for point-of-care molecular diagnostics as pointed out in Chapter 4 of this thesis. Furthermore, the microwave gives high possibility of multiplexing of the sensor and is a label-free approach. This section explores using the developed microwave sensor as a preliminary application of DNA hybridization detection and a potential biomolecular diagnostics tool. Before presenting the details of the DNA microwave biosensing and principles, it is useful to review background information on the structure of DNA and some of available methods.

8.2.2 THE STRUCTURE OF DNA

Deoxyribonucleic acid (DNA) is the most biologically significant target for biosensors as testing compounds. The deformation on DNA structure and binding of different molecules can be detected, and related signals can be obtained through electrical and optical techniques.

DNA is a molecule that carries genetic information used in the development, growth and reproduction of all known organisms and viruses. DNA molecules consist of two strands that forms a double helix and coils around each other. The simpler DNA strand is called the nucleotide, and each nucleotide is constructed by one of four nucleobases, namely Adenine (A), Thymine (T), Guanine (G) and Cytosine (C), as well as a phosphate group and a sugar called deoxyribose[411]. The nucleotides are linked to each other by covalent bonds, and the two strands are held to each other with hydrogen bonds, which forms the double-stranded DNA. Hydrogen bonds are theoretically ten times weaker than covalent bonds, which enables DNA denaturation and hybridization through breaking of the hydrogen bonds by means of external effects such as heating or chemical agents. Covalent bonds are not effected by heat. The double-stranded DNA structure is depicted in Figure 8.2.1.

The distance between turns of the helix structure is called a pitch and it is 3.4nm long, which consists the major and minor groove length. The two strands have opposite directions for the linking a 3’ carbon atom with a 5’ carbon atom due to natural antiparallel architecture. Also, the double helical structure of DNA is shown in Figure 8.2.2, where one pitch represents 10 nucleotides and major and minor grooves are demonstrated.

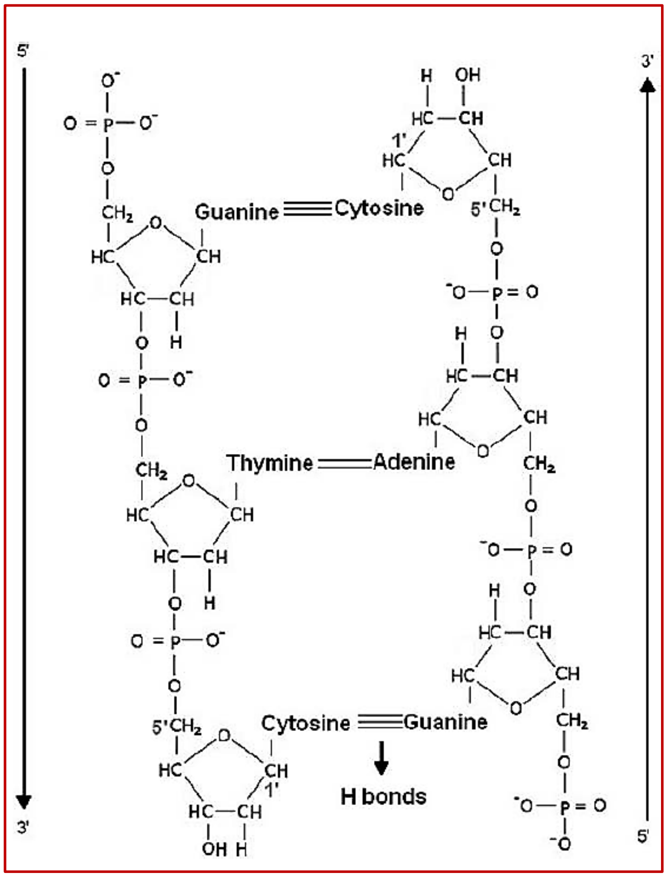

Figure 8.2.1. The double-stranded DNA structure[406].

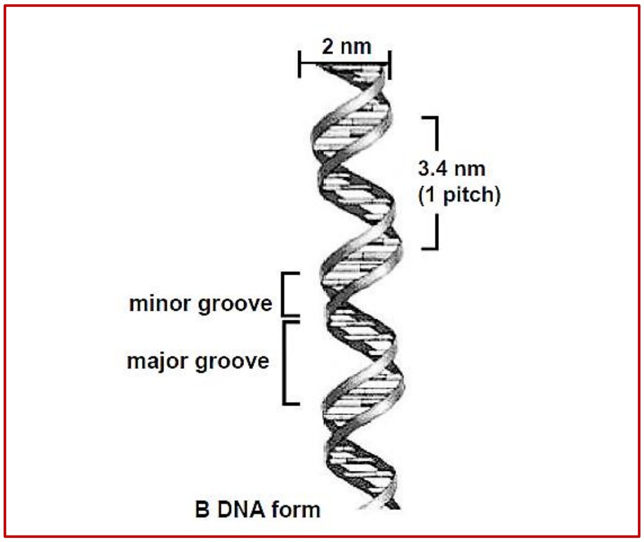

Figure 8.2.2. The double helical DNA structure[406].

8.2.3 Nucleic Acid Hybridization Biosensors

Determination of specific DNA sequences is important for many applications. A common and main approach for detection of DNA sequences is the hybridization of ss-DNA fragments. The hybridization event causes changes in some features such as surface properties, impedance etc. that are subsequently used to analyze the molecular binding phenomena. For example, quartz crystal microbalance (QCM)[412], fluorescent methods[413-414], surface plasmon resonance spectroscopy (SPR)[415] and electrochemical techniques[416-417] have been mainly applied to monitor and analyze DNA hybridization[407]. However, label-free, portable, sensitive and re-usable sensors are always desired.

Table 8.2.1. Oligomer nomenclature, modification and sequence.

Oligo #	Name	Sequence	Label	Comment
1	Prob#1	5'-/5ThioMC6-D/AC GCG TCA GGT CAT TGA CGA ATC GAT GAG T-3'	Thiol	Prob ss-DNA
2	Comp#1 (c-DNA)	5'-ACT CAT CGA TTC GTC AAT GAC CTG ACG CGT-3'	None	Target ss-DNA
3	Non-Comp#1	5'-**TCA TCA TGG GTC TAA CTA CTG GAT CTA GGT**-3'	None	Non-complimentary
4	Non-Comp#2	5'-ACT CAT CGA TTC GTC AAT GAC CTG AC**C** CGT-3'	None	One-point mismatch
5	Comp#1_60base	5'-ACT CAT CGA TTC GTC AAT GAC CTG ACG CGT ACT CAT CGA TTC GTC AAT GAC CTG ACG CGT-3'	None	Target ss-DNA

8.2.4 Reagents and Materials

Reagents and solvents were obtained from commercial sources and used as received without further purification. The probe (ss-DNA) oligo, target c-DNA and all other non-complimentary DNA oligos were obtained from Integrated DNA Technologies (IDT) Inc with standard desalting. The prob ss-DNA was added a functional thiol (-SH) group at the end (the 5'-end) of the oligo. Nuclease-free water is used for all buffer solution which was also obtained from IDT. Sequences and labels of oligonucleotides are listed in Table 8.2.1.

8.2.5 THE BIOLOGICAL PROTOCOL OF DNA HYBRIDIZATION

The preparation of buffer solutions, prob and target DNA oligomers and surface functionalization protocols used in this study are described as below:

a. *Preparation of ssDNA probe incubation solution in order to functionalize the gold surfaces.*

The solution at the end is desired to include:

- 10mM phosphate buffer,
- 100 mM NaCl (or $MgCl_2$) (if $MgCl_2$ used then the concentration should be lower)
- 10 µM Tris(2-carboxyethyl)phosphine (TCEP),
- 1 µM probe ssDNA

To prepare 1 µM probe ssDNA (for 100nmole oligo quantity), suspend oligos in 100 mL buffer in total (for aliquots 100 µM in 1 mL buffer).

1. First prepare stock phosphate buffer and stock NaCl solutions.

2. The protocol below allows to design phosphate buffered system at various pH and ionic strength.

Prepare the following stock solutions:

- 1 M Potassium Phosphate Monobasic (KH_2PO_4)
- 1 M Potassium Phosphate Dibasic (K_2HPO_4)
- 5 M Sodium Chloride (NaCl)

Note: *It's worthwhile to use Nuclease-free water (Not-DEPC treated) or Biomolecular grade water. The water being used here should not include any irrelevant mineral ions: cations and anions, as well should not include uncharged organic or inorganic compounds such as viruses or bacteria. Such impurities might affect DNA hybridization.*

3. Use the Henderson-Hasselbalch approximation to estimate the pH of the buffer solution.

$$pH = pK_a + log\frac{[A^-]}{[HA]} \qquad (1)$$

where,

pKa; acid dissociation constant,

HA; molar concentration of weak acid,

A; molar concentration of the acid's conjugate base.

pKa's of phosphoric acid are 2.15, 6.86 and 12.38. Select the pKa value that is closest to the pH of the buffer needed. For the 7.5 pH of the buffer use 6.86.

The molarity of the buffer is the sum of the molarities of the acid and conjugate base [Acid] + [Base].

For potassium phosphate buffer system, for A^- use K_2HPO_4 concentration, and for HA use KH_2PO_4 concentration:

7.5=6.86 + log(A/HA)

log(A/HA)= 0.64

A/HA=4.365

A+HA=0.05

A=0.0407 mol/L (K_2HPO_4)

HA=0.00932 mol/L (KH_2PO_4)

4. Take 40.7 ml and 9.32 ml from the each 1 M stock solutions of K_2HPO_4 and KH_2PO_4 respectively. Then combine them by mixing in a 1 liter of water in total. However, before ending up to 1 liter dilution, firstly dilute them in 0.7 liter of water.

5. Take 100 ml from 5 M stock NaCl solution and add into the solution in step 4. (Approximately, Sodium chloride lowers the pH approximately 0.01 pH unit for each 0.01 increase in molarity).

6. Then measure the pH value for the control purposes by a pH meter. Adjust the pH as necessary using Phosphoric acid (to make the buffer more acidic) or sodium hydroxide (to make the solution more basic).

7. Once the desired pH value is obtained, add water to bring the total volume of the buffer to 1 L. This is a stock solution of 0.05 M phosphate buffer with 0.5 M NaCl. Then it can be diluted to 10 mM phosphate buffer solution as needed.

8. For other pH values of phosphate buffer, use the table below. Dilute the portions of solutions in the table to 1 L with water.

Table 8.2.2. pH value adjustment of phosphate buffer solutions used for DNA hybridization.

	1 Liter of 0.05 M Phospate Buffer (25 °C)		1 Liter of 0.05 M Phospate Buffer/0.15 M NaCl (25 °C)		
pH	1 M KH_2PO_4 (P8706) (ml)	1 M K_2HPO_4 (P8584) (ml)	1 M KH_2PO_4 (P8706) (ml)	1 M K_2HPO_4 (P8584) (ml)	5 M NaCl (S6546) (ml)
6.6	32.0	18.0	26.6	23.4	30
6.7	29.8	20.2	23.7	26.3	30
6.8	26.5	23.5	20.9	29.1	30
6.9	24.0	26.0	18.1	31.9	30
7.0	21.1	28.9	15.6	34.4	30
7.1	18.4	31.6	13.2	36.8	30
7.2	16.8	34.2	11.1	38.9	30
7.3	13.4	36.6	9.2	40.8	30
7.4	11.2	38.8	7.6	42.4	30
7.5	9.4	40.6	6.3	43.7	30
7.6	7.8	42.2	5.1	44.9	30

9. Store buffers at room temperature.

10. Add 1 µM probe ssDNA into 10 mM phosphate buffer. (Note: The buffer volume must be 100 mL in total, for 100nmole ssDNA oligo). The probe comes in a dried powder form in a tube. Briefly, centrifuge the tube containing oligo in it prior to opening. This is because to help oligo to sink to bottom of the tube to prevent loss of oligo since the tiny amount is hardly visible in the tube and may stick to the side walls.

[A more concentrated DNA stock of 100uM in 1mL can be made as well. Note that for the UV-spec measurement, may need to take a sample and dilute it or the detector may be saturated. Then it can be diluted again to make the aliquots (probably not down to 1uM)].

11. Briefly, vortex the whole solution but not centrifuge.

12. Measure the exact DNA concentration by UV-spectrometer. For this the buffer solution might be prepared as 20% less amount of water since the amount of oligo shipped cannot guarantee 100 nmole precisely. Do the measurement step by step adding water to the solution. When 1 µM DNA concentration obtained, then the solution is ready to prepare aliquots. A sample calculation of concentration of DNA oligo is shown below under step 20.

13. Put the aliquots -20ºC to freeze and store them. (This requires low-binding cryogenic tubes. They must be low-binding otherwise the DNA will stick to the walls. Also need to fix the aliquot volume).

***b.** Preparation of Probe Functionalization Solutions.*

14. On the day of experiment, take enough amount from the aliquot, and thaw them. (An aliquot is to be used once and then thrown away. Each new day=new aliquot is preferred for stabile results).

15. Add 10 µM TCEP, and vortex briefly. TCEP reduces the thiol-group linked to oligo and activates oligo to covalently bond to the gold surface. Let it sit for a couple of hours at room temperature to reduce the oligo. A stock solution of TCEP is not preferred either, each day of experiment new TCEP solution is prepared and added to fresh DNA oligo aliquot.

16. Introduce the solution slowly onto the gold surface and incubate for 1 hr.

17. Rinse with PBS.

***c.** Preparation of the MCH solution.*

18. Prepare 1 mM of 6-mercapto-1-hexanol (MCH) in a buffer of 10 mM phosphate buffer, 100 mM NaCl and 1.4 mM TCEP. This is made day of gold sensor fabrication. MCH is oxidized quickly when opening the bottle, in order to minimize air exposure, fill the remainder of the bottle with nitrogen afterwards of each usage.

19. Introduce the solution and incubate for 1 hr followed by rinsing the gold surface by PBS. Then with DI water. Then with ethanol (100%). Then with DI water. Blow with nitrogen to dry. Store in vacuum desiccator cabinet under vacuum.

***d.** Prepare DNA Hybridization solution.*

20. Add 1 µM target ssDNA into 4X concentrated Saline-Sodium Citrate (SSC) buffer.

[A more concentrated DNA stock of 100uM in 1mL can be made as well. Note that for the UV-spec measurement, may need to take a sample and dilute it or the detector may be saturated. Then it can be diluted again to make the aliquots (probably not down to 1 µM)].

As explained above the buffer solution (SSC) might be prepared as 20% less amount of water since the amount of oligo shipped cannot guarantee 100 nmole precisely. Do the measurement step by step adding water to the solution. When 1 µM DNA concentration obtained (or the desired stock concentration), then the solution is ready to prepare aliquots.

The concentrations of DNA oligo and protein samples used in this work were measured by a UV-Vis spectrophotometer (NanoDrop 2000, ThermoScientific). First, to obtain a reference measurement, the blank scan of the SSC buffer was scanned and stored in the memory. Then when a measurement of the sample (target or prob DNA) is taken, the intensity of light that was transmitted through the sample is recorded. The sample intensities along with the blank and sample intensities are used to calculate the sample absorbance according to the following equation:

$$Absorbance = -log\left[\frac{Intensity_{sample}}{Intensity_{blank}}\right] \qquad (2)$$

Hence, in order to calculate the absorbance at a given wavelength, both the measured light intensities of sample and the blank are considered. The Beer-Lambert correlation is used to calculate absorbance with concentration:

$$A = \varepsilon * b * c \qquad (3)$$

where, A represents the absorbance in absorbance units (A), ε represents the wavelength dependent molar absorptivity (extinction) coefficient (L/mol-cm), b is the pathlength (cm) and c is the analyte concentration (moles/L). Here, both the blank buffer and sample solution should be at the same pH and ionic strength. For nucleic acid quantification, the Beer-Lambert equation is modified to use a factor with units of ng-cm/microliter. The modified equation for nucleic acid calculation is shown below:

$$c = (A * \varepsilon)/b \qquad (4)$$

where, c is the nucleic acid concentration in ng/microliter, A is the absorbance (A), ε is the wavelength-dependent extinction coefficient in ng-cm/microliter and b is the pathlength (cm). The extinction coefficient for nucleic acids can be taken as for Double-stranded DNA: 50 ng-cm/μL, for Single-stranded DNA: 33 ng-cm/μL and for RNA: 40 ng-cm/μL. A sample spectral measurement is shown in Figure 8.2.3. Here, concentration is calculated based on absorbance at 260 nm with the defined extinction coefficient, A260 - displays absorbance at 260 nm normalized to a 10 mm pathlength, A280 - displays absorbance at 280 nm normalized to a 10 mm pathlength and 260/280 - ratio of absorbance at 260 nm and 280 nm.

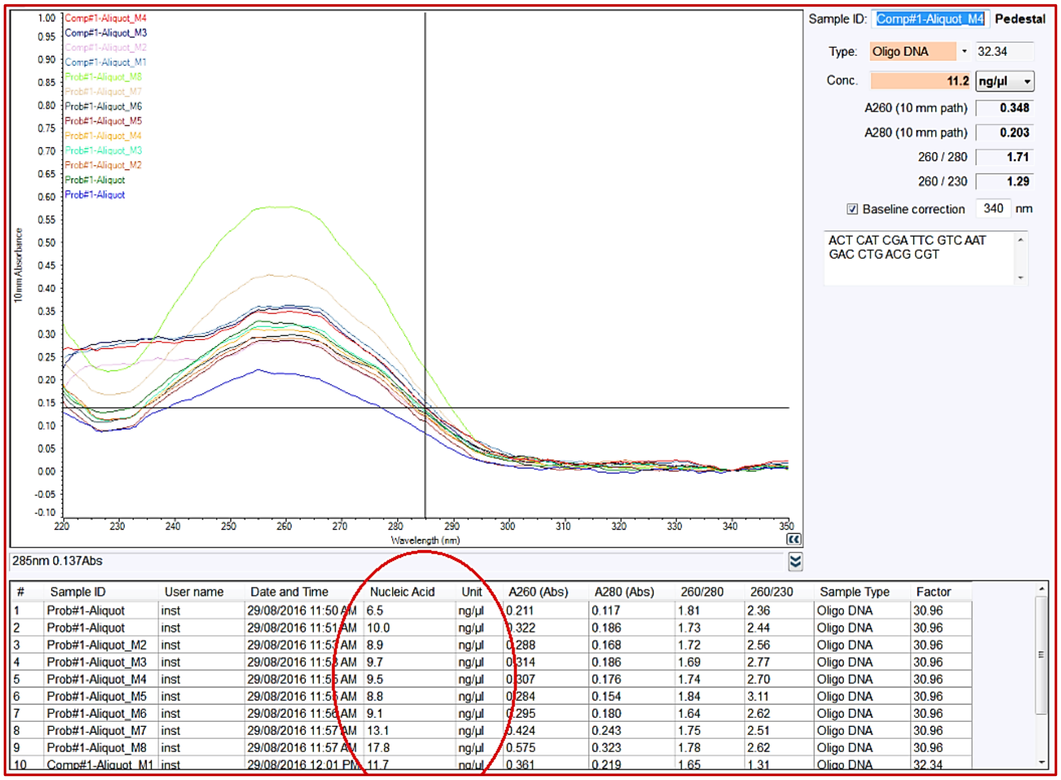

285nm 0.137Abs

Sample ID: Comp#1-Aliquot_M4 **Pedestal**

Type: Oligo DNA 32.34

Conc. **11.2** **ng/µl**

A260 (10 mm path) **0.348**

A280 (10 mm path) **0.203**

260 / 280 **1.71**

260 / 230 **1.29**

☑ Baseline correction 340 nm

ACT CAT CGA TTC GTC AAT
GAC CTG ACG CGT

#	Sample ID	User name	Date and Time	Nucleic Acid	Unit	A260 (Abs)	A280 (Abs)	260/280	260/230	Sample Type	Factor
1	Prob#1-Aliquot	inst	29/08/2016 11:50 AM	6.5	ng/µl	0.211	0.117	1.81	2.36	Oligo DNA	30.96
2	Prob#1-Aliquot	inst	29/08/2016 11:51 AM	10.0	ng/µl	0.322	0.186	1.73	2.44	Oligo DNA	30.96
3	Prob#1-Aliquot_M2	inst	29/08/2016 11:53 AM	8.9	ng/µl	0.288	0.168	1.72	2.56	Oligo DNA	30.96
4	Prob#1-Aliquot_M3	inst	29/08/2016 11:53 AM	9.7	ng/µl	0.314	0.186	1.69	2.77	Oligo DNA	30.96
5	Prob#1-Aliquot_M4	inst	29/08/2016 11:55 AM	9.5	ng/µl	0.307	0.176	1.74	2.70	Oligo DNA	30.96
6	Prob#1-Aliquot_M5	inst	29/08/2016 11:55 AM	8.8	ng/µl	0.284	0.154	1.84	3.11	Oligo DNA	30.96
7	Prob#1-Aliquot_M6	inst	29/08/2016 11:56 AM	9.1	ng/µl	0.295	0.180	1.64	2.62	Oligo DNA	30.96
8	Prob#1-Aliquot_M7	inst	29/08/2016 11:57 AM	13.1	ng/µl	0.424	0.243	1.75	2.51	Oligo DNA	30.96
9	Prob#1-Aliquot_M8	inst	29/08/2016 11:57 AM	17.8	ng/µl	0.575	0.323	1.78	2.62	Oligo DNA	30.96
10	Comp#1-Aliquot_M1	inst	29/08/2016 12:01 PM	11.7	ng/µl	0.361	0.219	1.65	1.31	Oligo DNA	32.34

Figure 8.2.3 Spectral absorbance measurement of DNA oligo.

Figure 8.2.4 shows the concentration calculation of DNA oligo for aliquot preparation. As mentioned above after centrifuging the powder form of oligo in polypropylene tube, buffer solution should be added step by step and the concentration in each step should be measured in order to obtain the desired DNA concentration for the aliquot preparation. It was observed that there is a loss in oligo quantity in the original tube that the expected 100 nmole oligo amount was found to be approximately 30% less. Thus, it is critical to measure each step until the desired concentration is obtained. Additionally, oligo calculations based on number of nucleotide bases can be made for DNA melting temperature and molecular weight determination.

21. Refer to step 12 above to make aliquots.

22. Inject onto gold surface and incubate for 20 min.

23. After incubation of target DNA, it is ready to measure the hybridization accordingly.

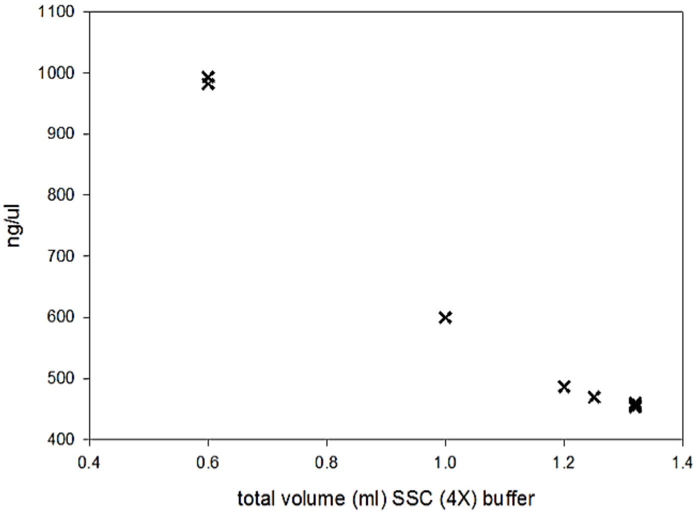

Figure 8.2.4. DNA oligo concentration for aliquot preparation and serial dilutions.

8.2.6 SIMULATION

In order to characterize the resonance modes of the sensors, prior to experiments, simulations are conducted. In this study, to increase the binding surface area on gold surface, different capacitive designs were used, such as spiral and triangular gap configurations. In Figure 8.2.5 the frequency versus S_{11} behavior of a triangular configuration is demonstrated for loaded and unloaded cases.

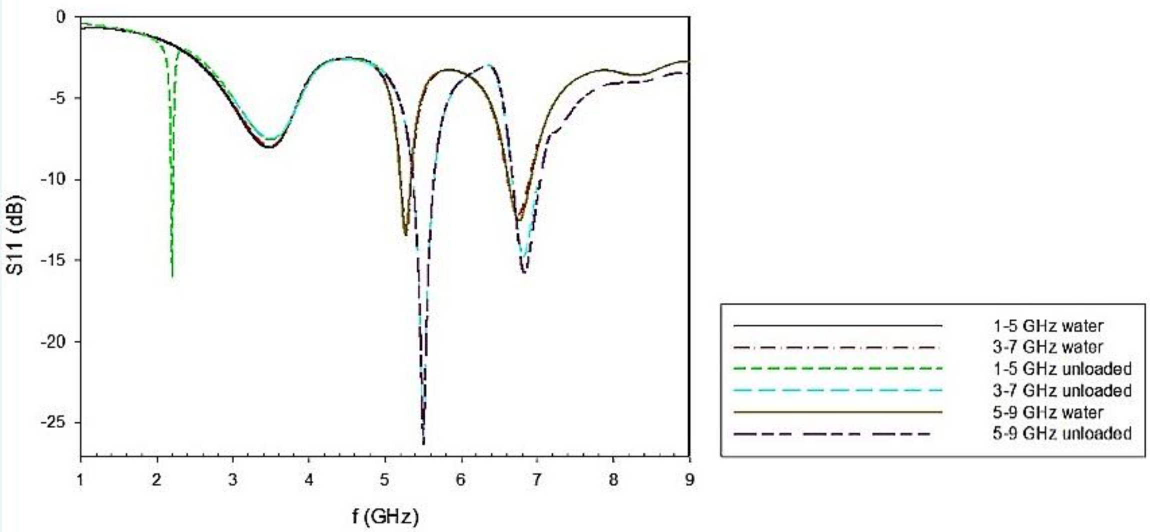

Figure 8.2.5 Frequency-S_{11} behavior of the gold microwave sensor.

8.2.7 EXPERIMENTAL PROCEDURE AND MEASUREMENTS

The fluids were driven by a high precision microfluidic pressure control system (MSFC 8C, Fluigent) and a syringe pump. Biomolecule adsorption on the gold surface was visualized using an inverted epifluorescence microscope (Eclipse Ti, Nikon) with 4× and 20×objectives and a CCD camera, with fluorescent imaging for validation purposes. First, gold sensors were fabricated as described in Chapter 3 by means of electroplating and photolithography. In each step, extra care was taken to ensure that the gold surface was very clean, which is essential for functionalization. Cleaning of the gold surface was realized in successive steps using acetone, ethanol, and isopropanol alcohol, with the help of a sonication bath. Then, positive photoresist removal was gradually carried out, also with the sonic bath. Afterwards, oxygen plasma cleaning was done to remove any other contaminants remaining on gold surface. A prob ss-DNA solution was immediately prepared according to the previously described protocol, with the gold microwave sensor either kept in a vacuum desiccator or nuclease-free water for protection of the surface. Then, the sensor is exposed to the DNA prob solution and incubated at least 1 hour. When the incubation is completed, the thiol modified prob DNA is expected to attach on gold surface, which functionalizes the surface to the target DNA. Later on, the MCH solution is also introduced to the surface for the reason of eliminating non-specific bonding of other molecules on gold surface. This is done by MCH coating on gold surface except the regions where prob DNA did not bind. Another reason is that MCH solution helps ss-DNA molecules stand up vertically. After this stage, the functionalized gold sensors are ready for exposed to the target DNA for monitoring the hybridization event. The sensors can either be stored in the desiccator which is UV-protected for future experiments or can be introduced by complimentary DNA.

For the experiments and microwave sensing, a vector network analyzer (VNA) is used. Thanks to a custom program written in Phyton, the VNA is connected to a computer (Laptop) and real time measurement with controlled frequency sweep (microwave spectra), time intervals for data recording and reflection coefficient data recording was carried out. Before each sensor and corresponding frequency range were used, the VNA was calibrated with maximum allowed data range which helps to increase the data resolution. For the hybridization and BSA experiments fluidic reservoirs, microfluidic chamber and microfluidic channels were prepared with the help of standard soft-lithography fabrication.

8.2.8 RESULTS AND DISCUSSIONS

Before starting the DNA hybridization experiments, initially Bovine Serum Albumin (BSA), which is conjugated with fluorescein and it is non-specifically attracted by gold surface, was used to monitor the surface quality and adsorption efficiency of gold microwave electrodes. This also might potentially be used for protein binding applications[418]. Figure 8.2.6 shows the optical images of BSA adsorption on gold with fluorescein tagged molecules. The optical fluorescent imaging herein in this study is used whenever possible to verify and validate the results. In Figure 8.2.6, the top image demonstrates the bare microwave sensor without any loading. As expected there is no light emission is seen. The middle image shows the Bovine serum albumin solution (1mg/ml in phosphate buffer) pumping into the microchannel that since BSA molecules are conjugated by fluorescein dye molecules, the whole solution in the channel is emitting fluorescent light. Then, the solution is left for incubation in the channel, and later BSA solution is rinsed by PBS buffer solution and the channel is cleaned. As can be observed from the bottom image in Figure 8.2.6, only the spiral capacitive gap that is exposed to BSA solution is emitting light. This proves that BSA molecules are attracted by gold surface of the microwave resonator and they bind on the gold surface.

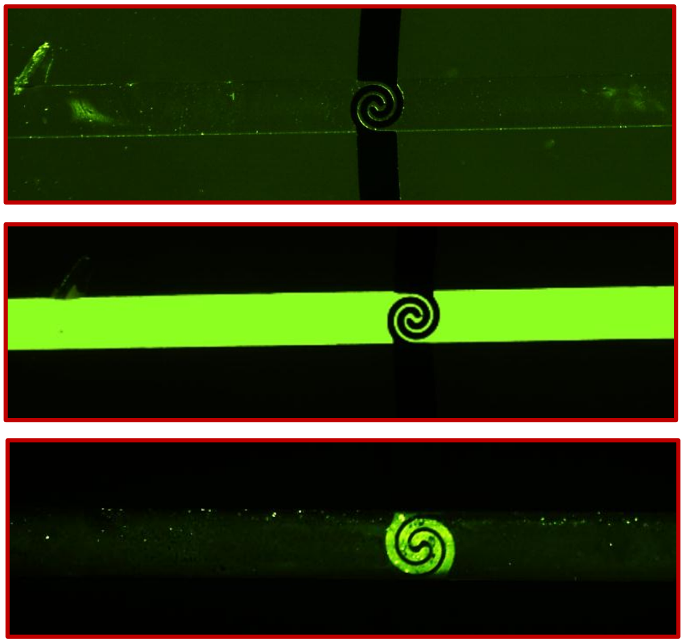

Figure 8.2.6 Bovine Serum Albumin adsorption on gold microwave sensor is visualized by fluorescent imaging. Bare microwave sensor (top image), BSA solution is introduced (middle image), after incubation and BSA solution is removed (bottom image).

Next, the DNA hybridization experiments were carried out with protocol reported above. For the hybridization event prob-solution with the sequence Prob#1 (/5ThioMC6-D/AC GCG TCA GGT CAT TGA CGA ATC GAT GAG T) and target DNA sequence Comp#1 (ACT CAT CGA TTC GTC AAT GAC CTG ACG CGT), both 1 μM in solution were used. First, the gold sensor was cleaned carefully that any potential contaminants on the surface were tried to remove. A fluidic reservoir is made for introducing the hybridization and buffer solutions on the gold microwave resonator. Enough incubation time is allowed for each step, then the solution is removed and rinsed by buffer, and the sensor was followed by the data measurement. The schematic representation of the incubation and measurement processes are depicted in Figure 8.2.7. In order to eliminate any drift in measurements and make sure the system is stable, always a drift study was performed carefully that without any loading the data recording is started and over a long time the behavior of the system was followed, then actual measurement were done.

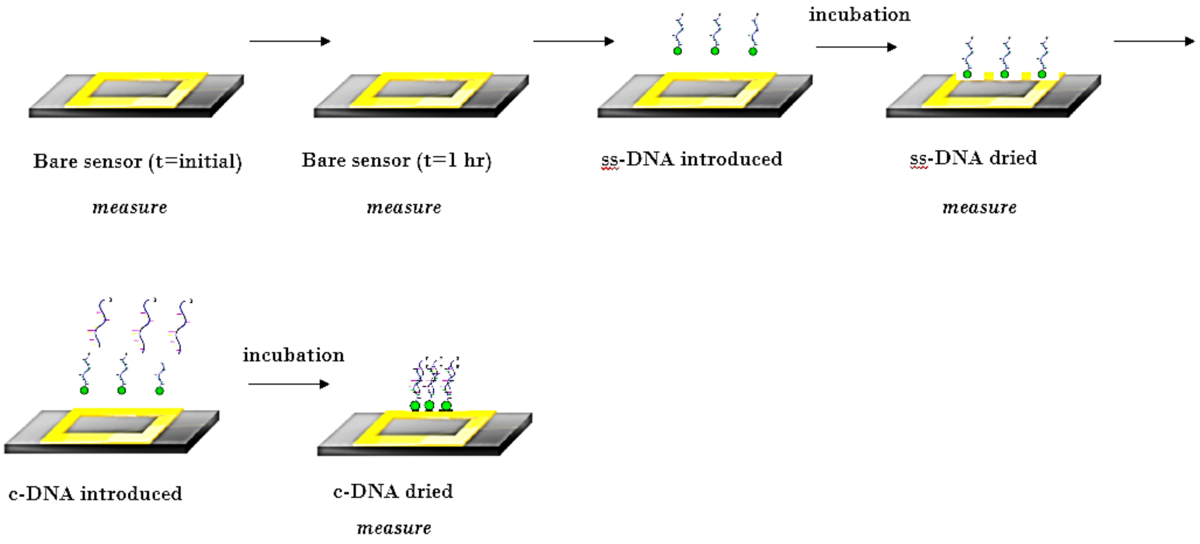

Figure 8.2.7. Schematic description of the incubation and measurement process of DNA hybridization event.

Resonance frequency shift versus reflection coefficient results of DNA hybridization is provided in Figure 8.2.8. As can be seen from the figure that bare sensor initially and after 1 hr overlaps indicating that there is not any drift in the measurement system. Binding of prob ss-DNA and the target c-DNA on gold resonator causes a shift in resonance frequency of the sensor which used to detect the hybridization event. The scanning range for the measurements was between 1800-2200

MHz with 0.1 MHz resolution. As presented in Figure 8.2.9, for the immobilization of ss-DNA a Δf=1.8 MHz frequency shift was observed relative to the bare sensor, and with the injection of c-DNA for hybridization Δf=1.2 MHz shift between ss-DNA and c-DNA was obtained. Results show that DNA hybridization event can be detected and monitored with the microwave resonator.

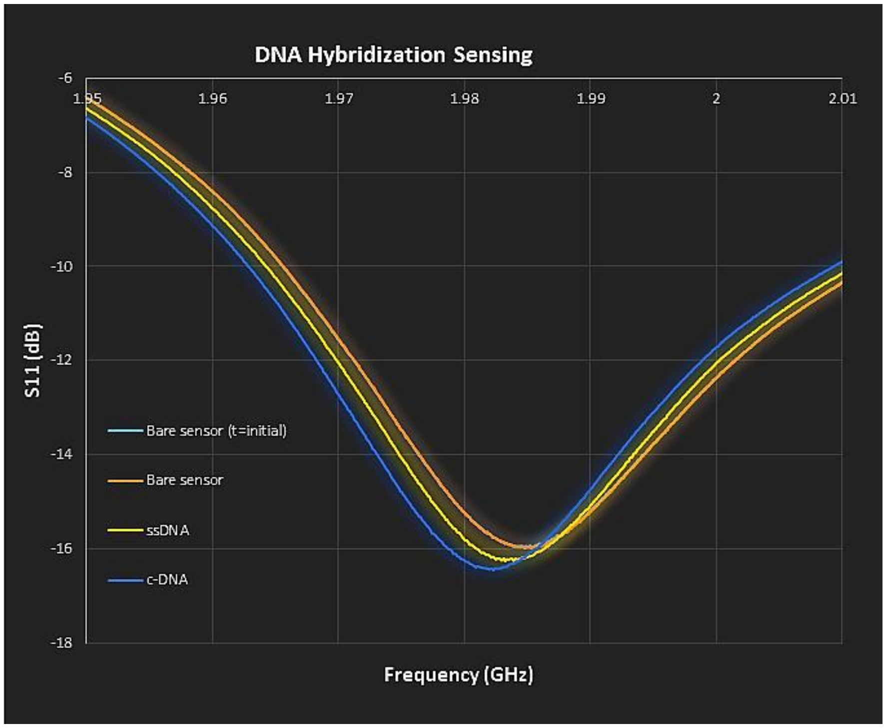

Figure 8.2.8. Frequency scan vs S_{11} for bare gold sensor, ss-DNA and c-DNA cases.

Also, in order to verify the immobilization of prob DNA on gold sensor and the event of the hybridization, an optical measurement was carried out corresponding to the microwave measurements. For this purpose a DNA intercalating dye, Rose Bengal (RB), was used. Rose Bengal does not emit light normally, however, when it is binding to DNA it starts emitting light which helps to analyze DNA. Nevertheless, while binding of Rose Bengal to complimentary DNA emits a weak light, the intensity of the fluorescent dye increases and getting brighter when the strands of DNA combines and more DNA is hybridized[264],[407]. In Figure 8.2.10 binding modes of intercalating dyes to DNA is illustrated. To validate this optical method and monitor DNA hybridization, on a microscope slide three different solution small drops were applied and optical imaging and fluorescent data recording were done. The first droplet contained only Rose Bengal (RB) (100 µM

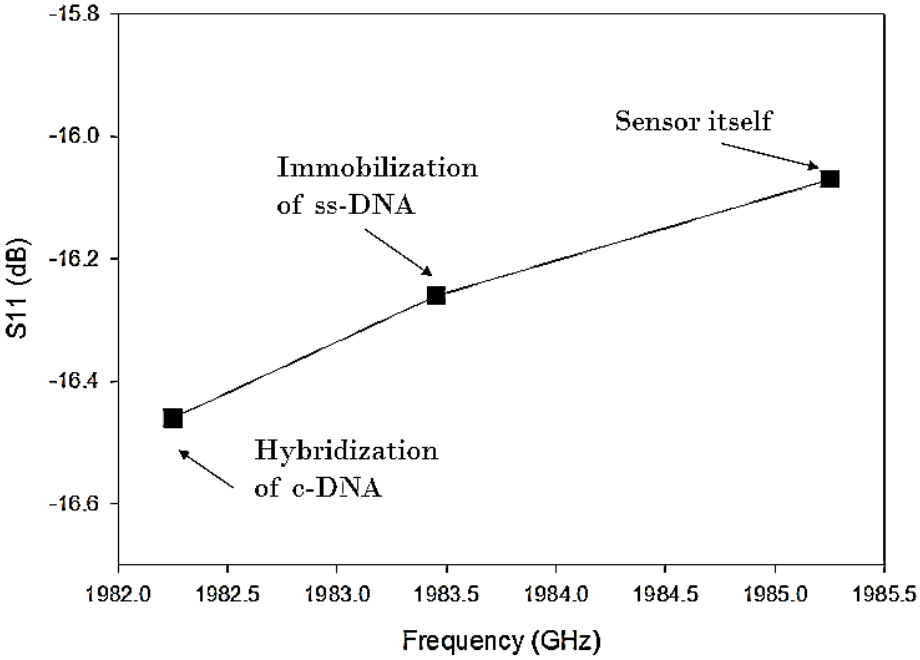

Figure 8.2.9. Change in resonance frequency and reflection coefficient for sensor itself, immobilized DNA and after hybridization.

otherwise stated) dye, the second one contained RB+ 1 μM complimentary DNA, and the third one contained RB+ 1 μM complimentary DNA+ 1 μM prob DNA. As shown in Figure 8.2.11, the intensity increases as more DNA hybridization occurs, then it saturates. This proves the hybridization of DNA and the intercalation of RB. And, Figure 8.2.12 demonstrates the fluorescent images of the DNA and RB combinations.

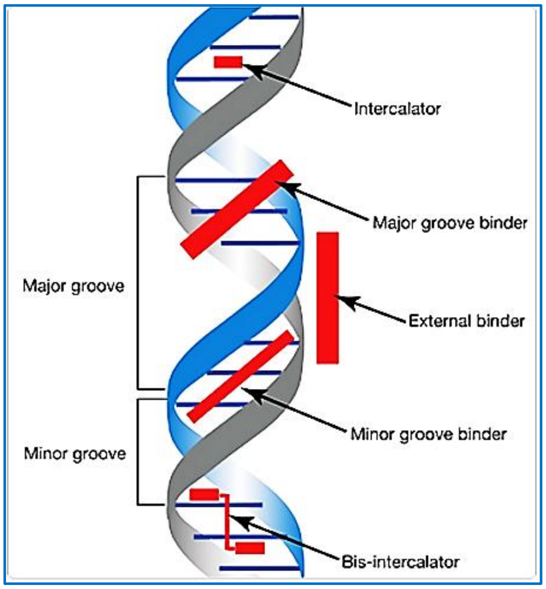

Figure 8.2.10 Schematic diagram showing different binding modes of intercalating dyes to DNA (image adapted from www.thermofisher.com/ca).

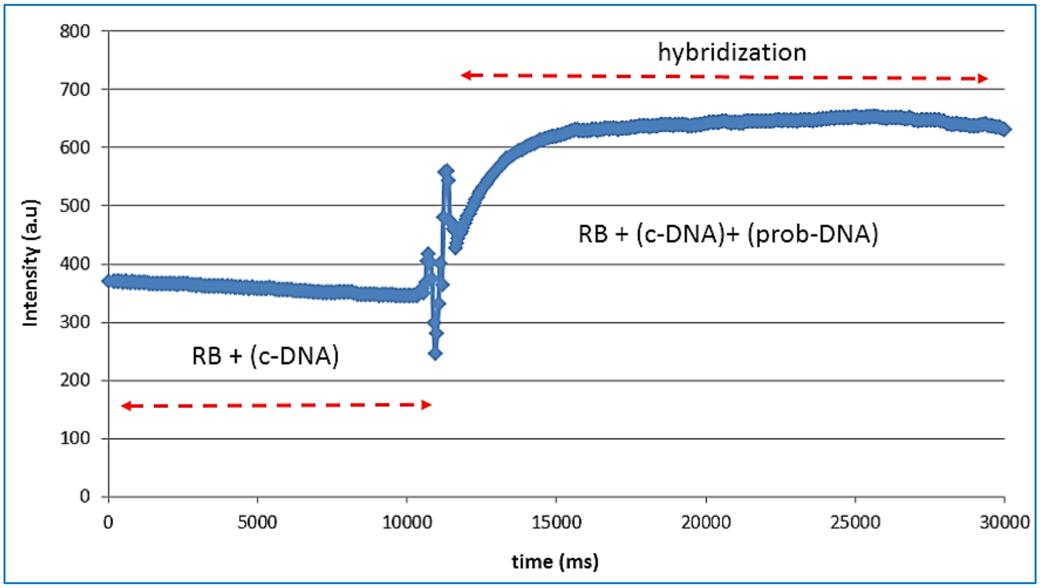

Figure 8.2.11 Intensity variation by the interaction of the intercalating dye and DNA.

After testing RB intercalation and DNA hybridization by the optical imaging, 100 μM RB was also introduced on top the microwave resonator for which hybridization result is shown above. Since the DNA hybridization happened as the last step on the microwave sensor, the surface of the resonator started emitting light in comparison to the initial condition of without RB addition (see Figure 8.2.13). This result also verifies the microwave measurement of DNA hybridization and successfully immobilization of the DNA on microwave sensor.

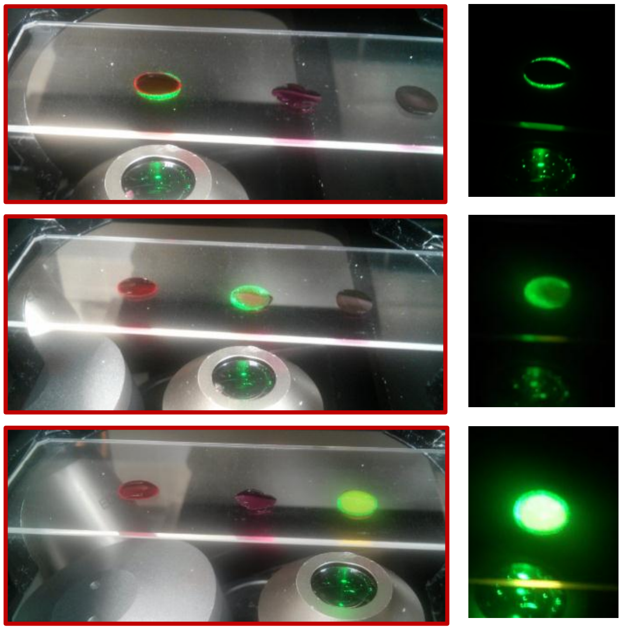

Figure 8.2.12 Three different contents of drops on microscope slide; containing RB only, c-DNA+RB, and c-DNA+prob-DNA+RB, respectively from top to bottom. Each drop excited by mercury lamp and fluorescent images were acquired with TRITC filter. Color changes due to emission at different wavelength is seen.

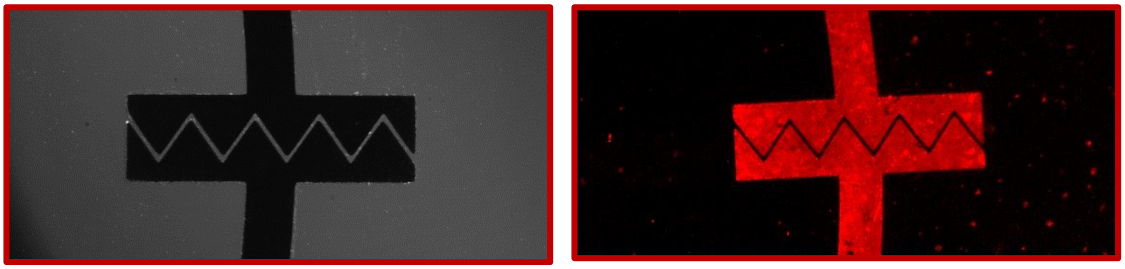

Figure 8.2.13 Microwave resonator after DNA hybridization without RB (left), and after the DNA hybridization (right) it is intercalated by RB validates that ss-DNA immobilization and hybridization event to be occurred.

8.2.9 CONCLUSIONS

In this work, the preliminary DNA hybridization sensing for disease diagnosis applications using microwave based sensor is studied experimentally. The biological protocol of DNA hybridization process was successfully developed and applied. For gold microwave resonator fabrication, a fabrication process was also implemented to obtain clean and acceptable surface properties for Thiol-modified DNA immobilization. DNA hybridization results showed that this microwave integrated platform is a promising candidate for biomolecular diagnostics purposes. Additionally, the microwave resonator has advantages such as it shows a strong potential for point-of-care and it does not need labelling. Furthermore, the microwave sensor can also be multiplexed for reducing the cost and provide portable and rapid biomolecular detection. It should be noted that the study demonstrated here is a preliminary work and shows promising future for DNA sensing. More research is planned to be conducted in this field.

Chapter 9

CONCLUSIONS

9.1 CONTRIBUTIONS OF THE THESIS

There is an increasing interest in LOC and droplet-based microfluidics because of their promise to facilitate a broad range of scientific research and biological/chemical processes. Potential applications can be found in many areas such as cell analysis, DNA hybridization, detection of bioassays, bio-reactions, drug screening and diagnostics. Major advantages of droplet-based microfluidics versus traditional bioassays include the former's capability to provide a highly monodispersed, well-isolated environment for reactions with magnitude higher throughput (i.e. kHz) than traditional high throughput systems, as well as providing low reagent consumption and eliminating cross contamination. Among the demanded functions such as droplet generation, merging, sorting, splitting, trapping, sensing, heating and storing, the sensing and heating of individual droplets is particularly challenging because the droplets' small size and high speed do not allow regular imaging techniques to be used or requires expensive equipment, or it does not allow commonly used heating methods such as resistive heating to be used because individual and selective droplet heating is lacking. This thesis addresses the above-mentioned challenges by developing microwave technology that can be integrated with droplet microfluidics for label-free sensing and rapid heating of individual droplets, which also opens up opportunities for unique applications such as single cell and controlled material synthesis.

Substantial effort has been made to structure the thesis to logically reflect the needs, challenges and applicability of the integrated LOC technology, and to suggest other potential uses for it. Thus, the thesis touches on application-driven projects, for instance, related to the pharmacology and biomedical fields, i.e., drug screening, drug carrier synthesis, biomaterial sensing and biomolecular disease diagnostics. On the other hand, it also tackles the fundamentals of the research field to improve the integrated platform. For example, the mixing phenomenon is investigated and explained (because it is crucial and challenging task at the micro/nano scale) with the microwave initiation in two-phase droplet flow; a portable and high-throughput microwave circuitry is developed for potential point-of-care sensing; and the analysis is performed for the parameters effecting droplet microfluidic and microwave integrated device performance and capabilities.

The first part of the thesis is dedicated to designing and developing a portable, high-throughput, sensitive, label-free and inexpensive custom microwave detection circuitry that can easily be incorporated in droplet microfluidics platforms. This system allows individual droplets to be detected at kHz rates as well as sensing their contents. Although many optical and electrical systems are available for sensing and detection, the key properties needed for miniaturized high-throughput analysis are portability, speed and cost. The developed microwave circuitry addresses these three criteria without compromising its sensing performance. The entire project included: i) the design proposal and optimization; ii) fabrication of microfluidic chips and microwave resonators which require soft lithography technology, traditional photolithography and electroplating techniques. Existing fabrication protocols were improved and new techniques were developed to make the integrated chip robust in performance; iii) building the microwave circuity which is not trivial, due to challenges raised by high operating frequency, which requires almost perfect connecting between different components; iv) integration of the entire system and characterization of it against droplet detection, content sensing and drug assay. The fact that a start-up company has been established around this system confirms the contribution towards the field.

The later stage of the thesis investigated combinatorial parameters affecting heating and sensing performances of the droplet microfluidics and microwave integrated system. In general, researchers in the electromagnetics community, particularly those working on RF and microwave, study the geometrical and dielectric properties of the materials, sensor structures and systems in a detailed and comprehensive manner. The microfluidics community, in contrast, is more focused on fluidic and flow manipulation tasks, as presented in Chapter 2. Integration of miniaturized microwave sensors/heaters with droplet-based LOC systems, combinatorial analysis of the sensing and heating performances and the behavior of the system parameters must be examined in detail in order to fully utilize the capability of the device. Also, sensitivity of the system is a key criterion for its deployment for different applications such as biochemical reactions or cell analysis. Because of these challenges, the combinatorial effects, such as dielectric features of the microfluidic chip material, droplet geometrical properties on internal electromagnetic field distribution, passivation layer and power absorption were examined in this project. The findings, understanding and discussion of the parameters offer a useful guide for the members of the scientific and industrial communities who work with electrical sensor components and droplet microfluidics and pursue heating and sensing tasks or wish to commercialize microfluidic platforms.

The thermocapillary droplet micromixer is another valuable development of this thesis. Many available droplet mixing techniques are either slow, require long serpentine channels, or have a mixing function only. The microwave localized heating method, on the other hand, is both novel and efficient because it enables mixing as well as the initiation of chemical reactions the same time. It relies on the non-uniform microwave energy deposition in the droplet that passes the sensor region to induce non-uniform Marangoni flow and thus enhance mixing within the entire droplet. Almost instantaneous and homogenous mixing of droplets can be achieved within milliseconds. The physical mechanism of the thermo-capillary droplet mixing is analyzed and discussed in Chapter 6, and is a useful contribution to the field since mixing is difficult and important in small scale systems due to low Reynolds number flows.

Another valuable contribution is the development of microwave thermometry for droplet temperature measurement, as it allows direct temperature measurement of droplets. Many other techniques measure temperatures of microchannels or droplets indirectly. However, using the dielectric-property-based measurement technique with the microwave resonator demonstrated in

Chapter 7, sensitive and selective temperature can be measured specific to the droplet and working fluid inside the microchannel only.

The last part of the thesis further expands on the droplet-microwave integrated device developed in this work for biomedical and pharmaceutical Lab-on-a-chip applications. First, as a drug carrier and releasing tool, hydrogel microparticles are synthesized. Second, for potential biomolecular disease diagnostics, preliminary study of DNA hybridization event is carried out using the microwave resonator. These further expansions and applications show the promising future of the integrated system that can be utilized for many purposes.

9.2 FUTURE WORK AND RECOMMENDATIONS

The topics and projects covered in this thesis, related to microwave-droplet microfluidics integrated LOC platforms for biomedical and pharmaceutical needs, demonstrate the system's wide applicability. However, as only a few studies have been done on the integration of both, the results presented here will provide guidance for the many other avenues still waiting to be investigated and explored. Among these possibilities, for instance, a numerical study could be carried out to analyze the relative importance of thermophysical properties in droplet mixing. This work is suggested because during experiments, when heating is applied, the viscosity, interfacial tension, diffusion coefficient and density change in a coupled manner because of their temperature dependence. A numerical approach would allow some parameters to be kept constant and others varied, enabling the relative importance of the competitive forces to be analyzed quantitatively. Another recommendation is that droplet generation be performed in an active manner using microwave energy. Induced energy on the liquid/liquid interface makes an imbalance, leading to instability that causes droplet breakup. Further study is needed on the microwave synthesis of hydrogels. Temperature sensitive hydrogels could also be synthesized, as a means to achieve thermo-induced slow sustained drug release.

Bibliography

[1] A. W. Chow, "Lab-on-a-chip: Opportunities for Chemical Engineering," *AIChE J.*, vol. 48, no. 8, pp. 1590–1595, 2002.

[2] K. E. Herold and A. Rasooly, Eds., *Lab on a Chip Technology, Fabrication and Microfluidics*. Caister Academic Press, 2009.

[3] D. E. Angelescu, *Highly Integrated Microfluidics Design*. Artech House Publishers, 2011.

[4] A. J. DeMello, "Control and detection of chemical reactions in microfluidic systems," *Nature*, vol. 442, pp. 394–402, 2006.

[5] E. K. Sackmann, A. L. Fulton, and D. J. Beebe, "The present and future role of microfluidics in biomedical research.," *Nature*, vol. 507, no. 7491, pp. 181–9, 2014.

[6] J. Castillo-Leon, W. E. Svendsen, and M. Dimaki, Eds., *Micro and Nano Techniques for the Handling of Biological Samples*. CRC Press, 2012.

[7] M. A. Burns, B. N. Johnson, S. N. Brahmasandra, K. Handique, J. R. Webster, M. Krishnan, T. S. Sammarco, P. M. Man, D. Jones, D. Heldsinger, C. H. Mastrangelo, and D. T. Burke, "An integrated nanoliter DNA analysis device," *Science (80-.).*, vol. 282, pp. 484–487, 1998.

[8] N. T. Nguyen and S. T. Wereley, *Fundamentals and Applications of Microfluidics*. Artech House Publishers, 2002.

[9] H. Bruss, *Theoretical Microfluidics*. New York: Oxford University Press Inc., 2008.

[10] T. M. Squires, "Microfluidics Fluid physics at the nanoliter," vol. 77, no. July, 2005.

[11] L. Shui, J. C. T. Eijkel, and A. van den Berg, "Multiphase flow in micro- and nanochannels," *Sensors Actuators, B Chem.*, vol. 121, no. 1, pp. 263–276, 2007.

[12] H. Gu, M. H. G. Duits, and F. Mugele, "Droplets formation and merging in two-phase flow microfluidics," *Int. J. Mol. Sci.*, vol. 12, no. 4, pp. 2572–2597, 2011.

[13] T. P. Lagus and J. F. Edd, "A review of the theory, methods and recent applications of high-throughput single-cell droplet microfluidics," *J. Phys. D. Appl. Phys.*, vol. 46, no. 11, p. 114005, 2013.

[14] H. A. Stone, A. D. Stroock, and A. Ajdari, "Engineering Flows in Small Devices: Microfluidics Toward a Lab-on-a-Chip," *Annu. Rev. Fluid Mech.*, vol. 36, pp. 381–411, 2004.

[15] H. Song, J. D. Tice, and R. F. Ismagilov, “A microfluidic system for controlling reaction networks in time,” *Angew. Chemie - Int. Ed.*, vol. 42, no. 7, pp. 768–772, 2003.

[16] J. Clausell-Tormos, A. D. Griffiths, and C. a Merten, “An automated two-phase microfluidic system for kinetic analyses and the screening of compound libraries.,” *Lab Chip*, vol. 10, no. 10, pp. 1302–1307, 2010.

[17] J. Sivasamy, T. N. Wong, N. T. Nguyen, and L. T. H. Kao, “An investigation on the mechanism of droplet formation in a microfluidic T-junction,” *Microfluid. Nanofluidics*, vol. 11, no. 1, pp. 1–10, 2011.

[18] D. Bardin, M. R. Kendall, P. A. Dayton, and A. P. Lee, “Parallel generation of uniform fine droplets at hundreds of kilohertz in a flow-focusing module,” *Biomicrofluidics*, vol. 7, no. 3, 2013.

[19] X. C. I. Solvas and A. DeMello, “Droplet microfluidics: recent developments and future applications,” *Chem. Commun.*, vol. 47, pp. 1936–1942, 2011.

[20] C. X. Zhao and A. P. J. Middelberg, “Two-phase microfluidic flows,” *Chem. Eng. Sci.*, vol. 66, no. 7, pp. 1394–1411, 2011.

[21] Y. Zhu and Q. Fang, “Analytical detection techniques for droplet microfluidics - a review,” *Anal. Chim. Acta*, vol. 787, pp. 24–35, 2013.

[22] P. Garstecki, M. J. Fuerstman, H. a Stone, and G. M. Whitesides, “Formation of droplets and bubbles in a microfluidic T-junction-scaling and mechanism of break-up.,” *Lab Chip*, vol. 6, no. 3, pp. 437–446, 2006.

[23] J.-C. Baret, “Surfactants in droplet-based microfluidics,” *Lab Chip*, vol. 12, no. 3, pp. 422–433, 2012.

[24] Y. Schaerli, R. C. Wootton, T. Robinson, V. Stein, C. Dunsby, M. A. A. Neil, P. M. W. French, A. J. DeMello, C. Abell, and F. Hollfelder, “Continuous-flow polymerase chain reaction of single-copy DNA in microfluidic microdroplets,” *Anal. Chem.*, vol. 81, no. 1, pp. 302–306, 2009.

[25] W. Shi, J. Qin, N. Ye, and B. Lin, “Droplet-based microfluidic system for individual Caenorhabditis elegans assay.,” *Lab Chip*, vol. 8, no. 9, pp. 1432–1435, 2008.

[26] E. M. Miller and A. R. Wheeler, “A Digital Microfluidics Approach to Homogeneous Enzyme

Assays," *Bulk Solids Handl.*, vol. 28, no. 7, pp. 1614–19, 2008.

[27] M. Shaker, L. Colella, F. Caselli, P. Bisegna, and P. Renaud, "An impedance-based flow microcytometer for single cell morphology discrimination.," *Lab Chip*, vol. 14, no. 14, pp. 2548–55, 2014.

[28] H. Hufnagel, A. Huebner, C. Gülch, K. Güse, C. Abell, and F. Hollfelder, "An integrated cell culture lab on a chip: modular microdevices for cultivation of mammalian cells and delivery into microfluidic microdroplets.," *Lab Chip*, vol. 9, no. 11, pp. 1576–1582, 2009.

[29] A. Huebner, L. F. Olguin, D. Bratton, G. Whyte, W. T. S. Huck, A. J. De Mello, J. B. Edel, C. Abell, and F. Hollfelder, "Development of quantitative cell-based enzyme assays in microdroplets," *Anal. Chem.*, vol. 80, no. 10, pp. 3890–3896, 2008.

[30] J. Riordon, M. Nash, W. Jing, and M. Godin, "Quantifying the volume of single cells continuously using a microfluidic pressure-driven trap with media exchange," *Biomicrofluidics*, vol. 8, p. 11101, 2014.

[31] J. Riordon, M. Mirzaei, and M. Godin, "Microfluidic cell volume sensor with tunable sensitivity," *Lab Chip*, vol. 12, p. 3016, 2012.

[32] C. . Kumar, Ed., *Microfluidic Devices in Nanotechnology*. John Wiley&Sons Inc., 2010.

[33] C. D. Chin, V. Linder, S. K. Sia, A. S. Daar, H. Thorsteinsdottir, and D. K. Martin, "Lab-on-a-chip devices for global health: Past studies and future opportunities," *Lab Chip*, vol. 7, no. 1, pp. 41–57, 2007.

[34] P. Yager, G. J. Domingo, and J. Gerdes, "Point-of-care diagnostics for global health.," *Annu. Rev. Biomed. Eng.*, vol. 10, no. June, pp. 107–44, 2008.

[35] W. L. Chou, P. Y. Lee, C. L. Yang, W. Y. Huang, and Y. S. Lin, "Recent advances in applications of droplet microfluidics," *Micromachines*, vol. 6, no. 9, pp. 1249–1271, 2015.

[36] O. J. Dressler, R. M. Maceiczyk, S.-I. Chang, and A. J. Demello, "Droplet-Based Microfluidics: Enabling Impact on Drug Discovery.," *J. Biomol. Screen.*, vol. 19, no. 4, pp. 483–496, 2014.

[37] G. T. Vladisavljević, N. Khalid, M. a Neves, T. Kuroiwa, M. Nakajima, K. Uemura, S. Ichikawa, and I. Kobayashi, "Industrial lab on a chip: Design, applications and scale up for drug discovery and delivery.," *Adv. Drug Deliv. Rev.*, vol. 65, pp. 1626–1663, 2013.

[38] A. M. Ganan-Calvo, J. M. Montanero, L. Martin-Banderas, and M. Flores-Mosquera, “Building functional materials for health care and pharmacy from microfluidic principles and Flow Focusing,” *Adv. Drug Deliv. Rev.*, vol. 65, pp. 1447–1469, 2013.

[39] W. Wang, M.-J. Zhang, and L.-Y. Chu, “Functional Polymeric Microparticles Engineered from Controllable Microfluidic Emulsions,” *Acc. Chem. Res.*, vol. 47, no. 2, pp. 373–384, 2013.

[40] S. Köster, F. E. Angilè, H. Duan, J. J. Agresti, A. Wintner, C. Schmitz, A. C. Rowat, C. a Merten, D. Pisignano, A. D. Griffiths, and D. a Weitz, “Drop-based microfluidic devices for encapsulation of single cells.,” *Lab Chip*, vol. 8, no. 7, pp. 1110–1115, 2008.

[41] K. Martin, T. Henkel, V. Baier, A. Grodrian, T. Schön, M. Roth, J. Michael Köhler, and J. Metze, “Generation of larger numbers of separated microbial populations by cultivation in segmented-flow microdevices.,” *Lab Chip*, vol. 3, pp. 202–207, 2003.

[42] A. M. Klein, L. Mazutis, I. Akartuna, N. Tallapragada, A. Veres, V. Li, L. Peshkin, D. A. Weitz, and M. W. Kirschner, “Droplet barcoding for single cell transcriptomics applied to embryonic stem cells HHS Public Access,” *Cell*, vol. 161, pp. 1187–1201, 2015.

[43] Q. Chen, S. Utech, D. Chen, R. M. Prodanovic, J.-M. Lin, and D. A. Weitz, “Controlled Assembly of Heterotypic cells in a Core-Shell Scaffold: Organ in a Droplet,” *Lab Chip*, vol. 16, no. 8, pp. 1346–1349, 2016.

[44] Y. Wang and J. Wang, “Mixed hydrogel bead-based tumor spheroid formation and anticancer drug testing.,” *Analyst*, vol. 139, no. 10, pp. 2449–58, 2014.

[45] A. Huebner, S. Sharma, M. Srisa-Art, F. Hollfelder, J. B. Edel, and A. J. deMello, “Microdroplets: A sea of applications?,” *Lab Chip*, vol. 8, no. 8, p. 1244, 2008.

[46] W. W. and Z.-X. L. and R. L. and S.-H. L. and A.-D. X. and Y.-J. Yang, “Droplet-based micro oscillating-flow PCR chip,” *J. Micromechanics Microengineering*, vol. 15, no. 8, p. 1369, 2005.

[47] K.-Y. Lien, S.-H. Lee, T.-J. Tsai, T.-Y. Chen, and G.-B. Lee, “A microfluidic-based system using reverse transcription polymerase chain reactions for rapid detection of aquaculture diseases,” *Microfluid. Nanofluidics*, vol. 7, no. 6, pp. 795–806, 2009.

[48] M. J. Jebrail, M. S. Bartsch, and K. D. Patel, “Digital microfluidics: a versatile tool for

applications in chemistry, biology and medicine," *Lab Chip*, vol. 12, no. 14, pp. 2452–2463, 2012.

[49] R. R. S. Sista, A. E. A. Eckhardt, V. Srinivasan, M. G. Pollack, S. Palanki, and V. K. Pamula, "Heterogeneous immunoassays using magnetic beads on a digital microfluidic platform.," *Lab Chip*, vol. 8, no. 12, pp. 2188–2196, 2008.

[50] S.-Y. Teh, R. Lin, L.-H. Hung, and A. P. Lee, "Droplet microfluidics.," *Lab Chip*, vol. 8, no. 2, pp. 198–220, 2008.

[51] S. Schachschal, H. J. Adler, A. Pich, S. Wetzel, A. Matura, and K. H. Van Pee, "Encapsulation of enzymes in microgels by polymerization/cross-linking in aqueous droplets," *Colloid Polym. Sci.*, vol. 289, no. 5–6, pp. 693–698, 2011.

[52] E. M. Chan, a P. Alivisatos, and R. a Mathies, "High-Temperature Microfluidic Synthesis of CdSe Nanocrystals in Nanoliter Droplets," *J. Am. Chem. Soc.*, vol. 127, no. 40, pp. 13854–13861, 2005.

[53] J. R. Millman, K. H. Bhatt, B. G. Prevo, and O. D. Velev, "Anisotropic particle synthesis in dielectrophoretically controlled microdroplet reactors.," *Nat. Mater.*, vol. 4, no. 1, pp. 98–102, 2005.

[54] L. Li and R. F. Ismagilov, "Protein crystallization using microfluidic technologies based on valves, droplets, and SlipChip.," *Annu. Rev. Biophys.*, vol. 39, pp. 139–158, 2010.

[55] L. Shui, J. C. T. Eijkel, and A. van den Berg, "Multiphase flow in microfluidic systems - Control and applications of droplets and interfaces," *Adv. Colloid Interface Sci.*, vol. 133, no. 1, pp. 35–49, 2007.

[56] C. N. Baroud and H. Willaime, "Multiphase flows in microfluidics," *Comptes Rendus Phys.*, vol. 5, no. 5, pp. 547–555, 2004.

[57] E. Kumacheva and P. Garstecki, *Microfluidic Reactors for Polymer Particles*. John Wiley&Sons Inc., 2011.

[58] A. S. Utada, A. Fernandez-Nieves, H. A. Stone, and D. A. Weitz, "Dripping to jetting transitions in coflowing liquid streams," *Phys. Rev. Lett.*, vol. 99, no. 9, pp. 1–4, 2007.

[59] C. C. Roberts, R. R. Rao, M. Loewenberg, C. F. Brooks, P. Galambos, A. M. Grillet, and M. B. Nemer, "Comparison of monodisperse droplet generation in flow-focusing devices with

hydrophilic and hydrophobic surfaces," *Lab Chip*, vol. 12, no. 8, p. 1540, 2012.

[60] J. Ralston, M. Popescu, and R. Sedev, "Dynamics of Wetting from an Experimental Point of View," *Annu. Rev. Mater. Res.*, vol. 38, no. 1, pp. 23–43, 2008.

[61] D. Bodas and C. Khan-Malek, "Hydrophilization and hydrophobic recovery of PDMS by oxygen plasma and chemical treatment-An SEM investigation," *Sensors Actuators, B Chem.*, vol. 123, no. 1, pp. 368–373, 2007.

[62] R. Dreyfus, P. Tabeling, and H. Willaime, "Ordered and Disordered Patterns in Two-Phase Flows in Microchannels," *Phys. Rev. Lett.*, vol. 90, no. 14, p. 144505, 2003.

[63] V. Barbier, M. Tatoulian, H. Li, F. Arefi-Khonsari, A. Ajdari, and P. Tabeling, "Stable modification of PDMS surface properties by plasma polymerization: Application to the formation of double emulsions in microfluidic systems," *Langmuir*, vol. 22, no. 12, pp. 5230–5232, 2006.

[64] P. G. Wapner and W. P. Hoffman, "Utilization of surface tension and wettability in the design and operation of microsensors," *Sensors Actuators, B Chem.*, vol. 71, no. 1–2, pp. 60–67, 2000.

[65] N. Verplanck, Y. Coffinier, V. Thomy, and R. Boukherroub, "Wettability switching techniques on superhydrophobic surfaces," *Nanoscale Res. Lett.*, vol. 2, no. 12, pp. 577–596, 2007.

[66] B. Subramanian, N. Kim, W. Lee, D. A. Spivak, D. E. Nikitopoulos, R. L. McCarley, and S. A. Soper, "Surface modification of droplet polymeric microfluidic devices for the stable and continuous generation of aqueous droplets," *Langmuir*, vol. 27, no. 12, pp. 7949–7957, 2011.

[67] R. Seemann, M. Brinkmann, T. Pfohl, and S. Herminghaus, "Droplet based microfluidics," *Rep. Prog. Phys. Rep. Prog. Phys*, vol. 75, no. 75, pp. 16601–41, 2012.

[68] C. N. Baroud, F. Gallaire, and R. Dangla, "Dynamics of microfluidic droplets," *Lab Chip*, vol. 10, no. 16, p. 2032, 2010.

[69] J. H. Xu, S. W. Li, J. Tan, Y. J. Wang, and G. S. Luo, "Controllable preparation of monodisperse O/W and W/O emulsions in the same microfluidic device," *Langmuir*, vol. 22, no. 19, pp. 7943–7946, 2006.

[70] F. Sarrazin, K. Loubiere, L. Prat, and C. Gourdon, "Experimental and Numerical Study of

Droplets Hydrodynamics in Microchannels," *AIChE J.*, vol. 52, no. 12, pp. 4061–4070, 2006.

[71] T. Glawdel and C. L. Ren, "Global network design for robust operation of microfluidic droplet generators with pressure-driven flow," *Microfluid. Nanofluidics*, vol. 13, no. 3, pp. 469–480, 2012.

[72] M. Pathak, "Numerical simulation of membrane emulsification: Effect of flow properties in the transition from dripping to jetting," *J. Memb. Sci.*, vol. 382, no. 1–2, pp. 166–176, 2011.

[73] M. C. Jullien, M. J. Tsang Mui Ching, C. Cohen, L. Menetrier, and P. Tabeling, "Droplet breakup in microfluidic T-junctions at small capillary numbers," *Phys. Fluids*, vol. 21, no. 7, 2009.

[74] T. Thorsen, R. W. Roberts, F. H. Arnold, and S. R. Quake, "Dynamic pattern formation in a vesicle-generating microfluidic device," *Phys. Rev. Lett.*, vol. 86, no. 18, pp. 4163–4166, 2001.

[75] Y. Lu, A. Sur, C. Pascente, S. R. Annapragada, P. Ruchhoeft, and D. Liu, "Dynamics of droplet motion induced by Electrowetting," vol. 106, pp. 920–931, 2017.

[76] A. Gupta and R. Kumar, "Effect of geometry on droplet formation in the squeezing regime in a microfluidic T-junction," *Microfluid. Nanofluidics*, vol. 8, no. 6, pp. 799–812, 2010.

[77] J. D. Wehking, M. Gabany, L. Chew, and R. Kumar, "Effects of viscosity, interfacial tension, and flow geometry on droplet formation in a microfluidic T-junction," *Microfluid. Nanofluidics*, vol. 16, no. 3, pp. 441–453, 2014.

[78] I. Sarig, Y. Starosvetsky, and A. D. Gat, "Interaction forces between microfluidic droplets in a Hele-Shaw cell," *J. Fluid Mech.*, vol. 800, no. 2016, pp. 264–277, 2016.

[79] Z. Z. Chong, S. H. Tan, A. M. Ganan-Calvo, S. B. Tor, N. H. Loh, and N.-T. Nguyen, "Active droplet generation in microfluidics," *Lab Chip*, vol. 16, no. 1, pp. 35–58, 2016.

[80] P. Zhu and L. Wang, "Passive and active droplet generation with microfluidics: a review," *Lab Chip*, vol. 17, no. online, pp. 34–75, 2017.

[81] N. T. Nguyen, T. H. Ting, Y. F. Yap, T. N. Wong, J. C. K. Chai, W. L. Ong, J. Zhou, S. H. Tan, and L. Yobas, "Thermally mediated droplet formation in microchannels," *Appl. Phys. Lett.*, vol. 91, no. 8, pp. 18–21, 2007.

[82] Y. F. Yap, S.-H. Tan, N.-T. Nguyen, S. M. S. Murshed, T. N. Wong, and L. Yobas, "Thermally mediated control of liquid microdroplets at a bifurcation," *J. Phys. D. Appl. Phys.*, vol. 42, no. 6, p. 65503, 2009.

[83] J. D. Tice, A. D. Lyon, and R. F. Ismagilov, "Effects of viscosity on droplet formation and mixing in microfluidic channels," *Anal. Chim. Acta*, vol. 507, no. 1, pp. 73–77, 2004.

[84] C. A. Stan, S. K. Y. Tang, and G. M. Whitesides, "Independent control of drop size and velocity in microfluidic flow-focusing generators using variable temperature and flow rate," *Anal. Chem.*, vol. 81, no. 6, pp. 2399–2402, 2009.

[85] S.-H. Tan, S. M. Sohel Murshed, N.-T. Nguyen, T. N. Wong, and L. Yobas, "Thermally controlled droplet formation in flow focusing geometry: formation regimes and effect of nanoparticle suspension," *J. Phys. D. Appl. Phys.*, vol. 41, p. 165501, 2008.

[86] S. M. S. Murshed, S. H. Tan, N. T. Nguyen, T. N. Wong, and L. Yobas, "Microdroplet formation of water and nanofluids in heat-induced microfluidic T-junction," *Microfluid. Nanofluidics*, vol. 6, no. 2, pp. 253–259, 2009.

[87] S. M. S. Murshed and et al., "Temperature dependence of interfacial properties and viscosity of nanofluids for droplet-based microfluidics," *J. Phys. D. Appl. Phys.*, vol. 41, no. 8, p. 85502, 2008.

[88] C. N. Baroud, J. P. Delville, F. Gallaire, and R. Wunenburger, "Thermocapillary valve for droplet production and sorting," *Phys. Rev. E - Stat. Nonlinear, Soft Matter Phys.*, vol. 75, no. 4, pp. 1–5, 2007.

[89] S.-Y. Park, T.-H. Wu, Y. Chen, M. A. Teitell, and P.-Y. Chiou, "High-speed droplet generation on demand driven by pulse laser-induced cavitation," *Lab Chip*, vol. 11, no. 6, p. 1010, 2011.

[90] D. R. Link, E. Grasland-Mongrain, A. Duri, F. Sarrazin, Z. Cheng, G. Cristobal, M. Marquez, and D. A. Weitz, "Electric control of droplets in microfluidic devices," *Angew. Chemie - Int. Ed.*, vol. 45, no. 16, pp. 2556–2560, 2006.

[91] S. H. Tan, B. Semin, and J.-C. Baret, "Microfluidic flow-focusing in ac electric fields.," *Lab Chip*, vol. 14, no. 6, pp. 1099–106, 2014.

[92] P. Zhu, X. Tang, Y. Tian, and L. Wang, "Pinch-off of microfluidic droplets with oscillatory

velocity of inner phase flow," *Sci. Rep.*, vol. 6, no. August, p. 31436, 2016.

[93] Y. N. Cheung and H. Qiu, "Characterization of acoustic droplet formation in a microfluidic flow-focusing device," *Phys. Rev. E - Stat. Nonlinear, Soft Matter Phys.*, vol. 84, no. 6, pp. 1–10, 2011.

[94] A. Sauret, C. Spandagos, and H. C. Shum, "Fluctuation-induced dynamics of multiphase liquid jets with ultra-low interfacial tension.," *Lab Chip*, vol. 12, no. 18, pp. 3380–6, 2012.

[95] S. Y. Jung, S. T. Retterer, and C. P. Collier, "On-demand generation of monodisperse femtolitre droplets by shape-induced shear.," *Lab Chip*, vol. 10, no. 20, pp. 2688–94, 2010.

[96] T. Franke, A. R. Abate, D. A. Weitz, and A. Wixforth, "Surface acoustic wave (SAW) directed droplet flow in microfluidics for PDMS devices," *Lab Chip*, vol. 9, no. 18, pp. 2625–2627, 2009.

[97] Y. Wu, T. Fu, Y. Ma, and H. Z. Li, "Ferrofluid droplet formation and breakup dynamics in a microfluidic flow-focusing device," *Soft Matter*, vol. 9, p. 9792, 2013.

[98] J. Liu, S. H. Tan, Y. F. Yap, M. Y. Ng, and N. T. Nguyen, "Numerical and experimental investigations of the formation process of ferrofluid droplets," *Microfluid. Nanofluidics*, vol. 11, no. 2, pp. 177–187, 2011.

[99] A. Gupta, S. M. S. Murshed, and R. Kumar, "Droplet formation and stability of flows in a microfluidic T-junction," *Appl. Phys. Lett.*, vol. 94, no. 16, pp. 16–18, 2009.

[100] G. F. Christopher, N. N. Noharuddin, J. A. Taylor, and S. L. Anna, "Experimental observations of the squeezing-to-dripping transition in T-shaped microfluidic junctions," *Phys. Rev. E - Stat. Nonlinear, Soft Matter Phys.*, vol. 78, no. 3, pp. 1–12, 2008.

[101] K. Wang, Y. C. Lu, J. Tan, B. D. Yang, and G. S. Luo, "Generating gas/liquid/liquid three-phase microdispersed systems in double T-junctions microfluidic device," *Microfluid. Nanofluidics*, vol. 8, no. 6, pp. 813–821, 2010.

[102] D. Malsch, N. Gleichmann, M. Kielpinski, G. Mayer, T. Henkel, D. Mueller, V. Van Steijn, C. R. Kleijn, and M. T. Kreutzer, "Dynamics of droplet formation at T-shaped nozzles with elastic feed lines," *Microfluid. Nanofluidics*, vol. 8, no. 4, pp. 497–507, 2010.

[103] H. Song, D. L. Chen, and R. F. Ismagilov, "Reactions in droplets in microfluidic channels," *Angew. Chemie - Int. Ed.*, vol. 45, no. 44, pp. 7336–7356, 2006.

[104] L. Shui, A. van den Berg, and J. C. T. Eijkel, "Interfacial tension controlled W/O and O/W 2-phase flows in microchannel.," *Lab Chip*, vol. 9, no. 6, pp. 795–801, 2009.

[105] J. D. Tice, R. F. Ismagilov, and B. Zheng, "Forming droplets in microfluidic channels with alternating composition and application to indexing concentrations in droplet-based assays," *Anal. Chem.*, vol. 76, no. 17, pp. 4977–4982, 2004.

[106] T. Nisisako and T. Torii, "Microfluidic large-scale integration on a chip for mass production of monodisperse droplets and particles," *Lab Chip*, vol. 8, no. 2, pp. 287–293, 2008.

[107] J. K. Nunes, S. S. H. Tsai, J. Wan and H. A. Stone , "Dripping and jetting in microfluidic multiphase flows applied to particle and fibre synthesis," *J. Phys. D: Appl. Phys*, vol. 46, pp. 114002, 2013.

[108] S. L. Anna, N. Bontoux, and H. A. Stone, "Formation of dispersions using 'flow focusing' in microchannels," *Appl. Phys. Lett.*, vol. 82, no. 3, pp. 364–366, 2003.

[109] Z. Nie, M. Seo, S. Xu, P. C. Lewis, M. Mok, E. Kumacheva, G. M. Whitesides, P. Garstecki, and H. A. Stone, "Emulsification in a microfluidic flow-focusing device: Effect of the viscosities of the liquids," *Microfluid. Nanofluidics*, vol. 5, no. 5, pp. 585–594, 2008.

[110] T. Cubaud and T. G. Mason, "Capillary threads and viscous droplets in square microchannels," *Phys. Fluids*, vol. 20, no. 5, 2008.

[111] W. Lee, L. M. Walker, and S. L. Anna, "Role of geometry and fluid properties in droplet and thread formation processes in planar flow focusing," *Phys. Fluids*, vol. 21, no. 3, 2009.

[112] J. Collins and A. P. Lee, "Control of serial microfluidic droplet size gradient by step-wise ramping of flow rates," *Microfluid. Nanofluidics*, vol. 3, no. 1, pp. 19–25, 2007.

[113] T. Ward, M. Faivre, M. Abkarian, and H. A. Stone, "Microfluidic flow focusing: Drop size and scaling in pressure versus flow-rate-driven pumping," *Electrophoresis*, vol. 26, no. 19, pp. 3716–3724, 2005.

[114] M. M. Dupin, I. Halliday, and C. M. Care, "Simulation of a microfluidic flow-focusing device," *Phys. Rev. E - Stat. Nonlinear, Soft Matter Phys.*, vol. 73, no. 5, pp. 1–4, 2006.

[115] S. Takeuchi, P. Garstecki, D. B. Weibel, and G. M. Whitesides, "An axisymmetric flow-focusing microfluidic device," *Adv. Mater.*, vol. 17, no. 8, pp. 1067–1072, 2005.

[116] S.-H. Huang, W.-H. Tan, F.-G. Tseng, and S. Takeuchi, “A monolithically three-dimensional flow-focusing device for formation of single/double emulsions in closed/open microfluidic systems,” *J. Micromechanics Microengineering*, vol. 16, no. 11, pp. 2336–2344, 2006.

[117] L. Yobas, S. Martens, W.-L. Ong, and N. Ranganathan, “High-performance flow-focusing geometry for spontaneous generation of monodispersed droplets.,” *Lab Chip*, vol. 6, no. 8, pp. 1073–1079, 2006.

[118] P. B. Umbanhowar, V. Prasad, and D. A. Weitz, “Monodisperse emulsion generation via drop break off in a coflowing stream,” *Langmuir*, vol. 16, no. 2, pp. 347–351, 2000.

[119] C. Cramer, P. Fischer, and E. J. Windhab, “Drop formation in a co-flowing ambient fluid,” *Chem. Eng. Sci.*, vol. 59, no. 15, pp. 3045–3058, 2004.

[120] Y. Hong and F. Wang, “Flow rate effect on droplet control in a co-flowing microfluidic device,” *Microfluid. Nanofluidics*, vol. 3, no. 3, pp. 341–346, 2007.

[121] A. C. Hatch, A. Patel, N. R. Beer, and A. P. Lee, “Passive droplet sorting using viscoelastic flow focusing.,” *Lab Chip*, vol. 13, no. 7, pp. 1308–15, 2013.

[122] T. Glawdel, C. Elbuken, and C. Ren, “Passive droplet trafficking at microfluidic junctions under geometric and flow asymmetries,” *Lab Chip*, vol. 11, no. 22, p. 3774, 2011.

[123] C. Lee, J. Lee, H. H. Kim, S.-Y. Teh, A. Lee, I.-Y. Chung, J. Y. Park, and K. K. Shung, “Microfluidic droplet sorting with a high frequency ultrasound beam,” *Lab Chip*, vol. 12, no. 15, p. 2736, 2012.

[124] Z. Cao, F. Chen, N. Bao, H. He, P. Xu, S. Jana, S. Jung, H. Lian, and C. Lu, “Droplet sorting based on the number of encapsulated particles using a solenoid valve,” *Lab Chip*, vol. 13, no. 1, pp. 171–178, 2013.

[125] H. N. Joensson, M. Uhlén, and H. A. Svahn, “Droplet size based separation by deterministic lateral displacement-separating droplets by cell--induced shrinking.,” *Lab Chip*, vol. 11, no. 7, pp. 1305–1310, 2011.

[126] M. Yamada, M. Nakashima, and M. Seki, “Pinched flow fractionation: Continuous size separation of particles utilizing a laminar flow profile in a pinched microchannel,” *Anal. Chem.*, vol. 76, no. 18, pp. 5465–5471, 2004.

[127] Y.-C. Tan, J. S. Fisher, A. I. Lee, V. Cristini, and A. P. Lee, “Design of microfluidic channel

geometries for the control of droplet volume, chemical concentration, and sorting.,” *Lab Chip*, vol. 4, no. 4, pp. 292–298, 2004.

[128] Y. C. Tan, Y. L. Ho, and A. P. Lee, “Droplet coalescence by geometrically mediated flow in microfluidic channels,” *Microfluid. Nanofluidics*, vol. 3, no. 4, pp. 495–499, 2007.

[129] Y. Li, C. Dalton, H. J. Crabtree, G. Nilsson, and K. V. I. S. Kaler, “Continuous dielectrophoretic cell separation microfluidic device.,” *Lab Chip*, vol. 7, no. 2, pp. 239–48, 2007.

[130] S. Choi and J.-K. Park, “Microfluidic system for dielectrophoretic separation based on a trapezoidal electrode array.,” *Lab Chip*, vol. 5, no. 10, pp. 1161–1167, 2005.

[131] L. Wang, L. a Flanagan, E. Monuki, N. L. Jeon, and A. P. Lee, “Dielectrophoresis switching with vertical sidewall electrodes for microfluidic flow cytometry.,” *Lab Chip*, vol. 7, no. 9, pp. 1114–20, 2007.

[132] K. Ahn, C. Kerbage, T. P. Hunt, R. M. Westervelt, D. R. Link, and D. A. Weitz, “Dielectrophoretic manipulation of drops for high-speed microfluidic sorting devices,” *Appl. Phys. Lett.*, vol. 88, no. 2, pp. 1–3, 2006.

[133] C. Pei Yu, A. T. Ohta, and M. C. Wu, “Massively parallel manipulation of single cells and microparticles using optical images,” *Nature*, vol. 436, no. 7049, pp. 370–372, 2005.

[134] S.-Y. Park, S. Kalim, C. Callahan, M. a Teitell, and E. P. Y. Chiou, “A light-induced dielectrophoretic droplet manipulation platform.,” *Lab Chip*, vol. 9, no. 22, pp. 3228–3235, 2009.

[135] D. H. Lee, H. Hwang, and J. K. Park, “Generation and manipulation of droplets in an optoelectrofluidic device integrated with microfluidic channels,” *Appl. Phys. Lett.*, vol. 95, no. 16, pp. 2007–2010, 2009.

[136] K. Zhang, Q. Liang, S. Ma, X. Mu, P. Hu, Y. Wang, and G. Luo, “On-chip manipulation of continuous picoliter-volume superparamagnetic droplets using a magnetic force.,” *Lab Chip*, vol. 9, no. 20, pp. 2992–2999, 2009.

[137] A. A. Darhuber and S. M. Troian, “Principles of Microfluidic Actuation By Modulation of Surface Stresses,” *Annu. Rev. Fluid Mech*, vol. 37, pp. 425–55, 2005.

[138] N. R. Beer, K. A. Rose, and I. M. Kennedy, “Monodisperse droplet generation and rapid

trapping for single molecule detection and reaction kinetics measurement.," *Lab Chip*, vol. 9, no. 6, pp. 841–4, 2009.

[139] C. W. Lai, Y. H. Lin, and G. Bin Lee, "A microfluidic chip for formation and collection of emulsion droplets utilizing active pneumatic micro-choppers and micro-switches," *Biomed. Microdevices*, vol. 10, no. 5, pp. 749–756, 2008.

[140] M. A. Unger, "Monolithic Microfabricated Valves and Pumps by Multilayer Soft Lithography," *Science (80-.).*, vol. 288, no. 5463, pp. 113–116, 2000.

[141] O. Manneberg, S. Melker Hagsäter, J. Svennebring, H. M. Hertz, J. P. Kutter, H. Bruus, and M. Wiklund, "Spatial confinement of ultrasonic force fields in microfluidic channels," *Ultrasonics*, vol. 49, no. 1, pp. 112–119, 2009.

[142] T. Franke, S. Braunmuller, L. Schmid, A. Wixforth, and D. A. Weitz, "Surface acoustic wave actuated cell sorting (SAWACS)," *Lab Chip*, vol. 10, no. 6, pp. 789–794, 2010.

[143] X. Niu, M. Zhang, J. Wu, W. Wen, and P. Sheng, "Generation and manipulation of 'smart' droplets," *Soft Matter*, vol. 5, no. 3, p. 576, 2009.

[144] M. Zhang, J. Wu, X. Niu, W. Wen, and P. Sheng, "Manipulations of microfluidic droplets using electrorheological carrier fluid," *Phys. Rev. E - Stat. Nonlinear, Soft Matter Phys.*, vol. 78, no. 6, pp. 1–5, 2008.

[145] S.-H. Tan, N.-T. Nguyen, L. Yobas, and T. G. K. Kang, "Formation and manipulation of ferrofluid droplets at a microfluidic T -junction," *J. Micromechanics Microengineering*, no. 20, p. 45004, 2010.

[146] X. Niu, S. Gulati, J. B. Edel, and A. J. deMello, "Pillar-induced droplet merging in microfluidic circuits.," *Lab Chip*, vol. 8, no. 11, pp. 1837–1841, 2008.

[147] V. Chokkalingam, B. Weidenhof, M. Krämer, W. F. Maier, S. Herminghaus, and R. Seemann, "Optimized droplet-based microfluidics scheme for sol-gel reactions.," *Lab Chip*, vol. 10, no. 13, pp. 1700–5, 2010.

[148] G. F. Christopher, J. Bergstein, N. B. End, M. Poon, C. Nguyen, and S. L. Anna, "Coalescence and splitting of confined droplets at microfluidic junctions.," *Lab Chip*, vol. 9, no. 8, pp. 1102–1109, 2009.

[149] L. Bo-Chih and S. Yu-Chuan, "On-demand liquid-in-liquid droplet metering and fusion

utilizing pneumatically actuated membrane valves," *J. Micromechanics Microengineering*, vol. 18, no. 11, p. 115005, 2008.

[150] N. Bremond, A. R. Thiam, and J. Bibette, "Decompressing emulsion droplets favors coalescence," *Phys. Rev. Lett.*, vol. 100, no. 2, pp. 1–4, 2008.

[151] K. Liu, H. Ding, Y. Chen, and X. Z. Zhao, "Droplet-based synthetic method using microflow focusing and droplet fusion," *Microfluid. Nanofluidics*, vol. 3, no. 2, pp. 239–243, 2007.

[152] V. Chokkalingam, B. Weidenhof, M. Krämer, S. Herminghaus, R. Seemann, and W. F. Maier, "Template-free preparation of mesoporous silica spheres through optimized microfluidics," *ChemPhysChem*, vol. 11, no. 10, pp. 2091–2095, 2010.

[153] J. M. Köhler, T. Henkel, A. Grodrian, T. Kirner, M. Roth, K. Martin, and J. Metze, "Digital reaction technology by micro segmented flow - components, concepts and applications," *Chem. Eng. J.*, vol. 101, no. 1–3, pp. 201–216, 2004.

[154] C. Priest, S. Herminghaus, and R. Seemann, "Controlled electrocoalescence in microfluidics: Targeting a single lamella," *Appl. Phys. Lett.*, vol. 89, no. 13, pp. 2004–2007, 2006.

[155] M. Chabert, K. D. Dorfman, and J. L. Viovy, "Droplet fusion by alternating current (AC) field electrocoalescence in microchannels," *Electrophoresis*, vol. 26, no. 19, pp. 3706–3715, 2005.

[156] M. Zagnoni, C. N. Baroud, and J. M. Cooper, "Electrically initiated upstream coalescence cascade of droplets in a microfluidic flow," *Phys. Rev. E - Stat. Nonlinear, Soft Matter Phys.*, vol. 80, no. 4, pp. 1–9, 2009.

[157] K. Ahn, J. Agresti, H. Chong, M. Marquez, and D. A. Weitz, "Electrocoalescence of drops synchronized by size-dependent flow in microfluidic channels," *Appl. Phys. Lett.*, vol. 88, no. 26, pp. 2012–2015, 2006.

[158] C. N. Baroud, M. Robert de Saint Vincent, and J.-P. Delville, "An optical toolbox for total control of droplet microfluidics," *Lab Chip*, vol. 7, no. 8, p. 1029, 2007.

[159] T. Luong, N. Nguyen, and A. Sposito, "Thermocoalescence of microdroplets in a microfluidic chamber," vol. 254105, no. 2012, pp. 10–13, 2012.

[160] A. M. Leshansky, S. Afkhami, M. C. Jullien, and P. Tabeling, "Breakup of drops in a microfluidic T junction," *Phys. Rev. Lett.*, no. 21, p. 23303, 2009.

[161] T. Cubaud, “Deformation and breakup of high-viscosity droplets with symmetric microfluidic cross flows,” *Phys. Rev. E - Stat. Nonlinear, Soft Matter Phys.*, vol. 80, no. 2, pp. 3–6, 2009.

[162] J.-H. Choi, S.-K. Lee, J.-M. Lim, S.-M. Yang, and G.-R. Yi, “Designed pneumatic valve actuators for controlled droplet breakup and generation.,” *Lab Chip*, vol. 10, no. 4, pp. 456–61, 2010.

[163] S. Protière, M. Z. Bazant, D. a. Weitz, and H. a. Stone, “Droplet breakup in flow past an obstacle: A capillary instability due to permeability variations,” *EPL (Europhysics Lett.*, vol. 92, no. 5, p. 54002, 2010.

[164] A. R. Abate and D. a Weitz, “Faster multiple emulsification with drop splitting.,” *Lab Chip*, vol. 11, no. 11, pp. 1911–5, 2011.

[165] D. R. Link, S. L. Anna, D. A. Weitz, and H. A. Stone, “Geometrically mediated breakup of drops in microfluidic devices.,” *Phys. Rev. Lett.*, vol. 92, no. 5, p. 54503, 2004.

[166] A. T.-H. Hsieh, N. Hori, R. Massoudi, P. J.-H. Pan, H. Sasaki, Y. A. Lin, and A. P. Lee, “Nonviral gene vector formation in monodispersed picolitre incubator for consistent gene delivery.,” *Lab Chip*, vol. 9, no. 18, pp. 2638–43, 2009.

[167] B. T. Kelly, J. C. Baret, V. Taly, and A. D. Griffiths, “Miniaturizing chemistry and biology in microdroplets,” *Chem.Commun.(Camb.)*, no. 1359–7345 (Print), pp. 1773–1788, 2007.

[168] J.-C. Baret, O. J. Miller, V. Taly, M. Ryckelynck, A. El-Harrak, L. Frenz, C. Rick, M. L. Samuels, J. B. Hutchison, J. J. Agresti, D. R. Link, D. A. Weitz, and A. D. Griffiths, “Fluorescence-activated droplet sorting (FADS): efficient microfluidic cell sorting based on enzymatic activity.,” *Lab Chip*, vol. 9, no. 13, pp. 1850–8, 2009.

[169] L. Mazutis, J.-C. Baret, and A. D. Griffiths, “A fast and efficient microfluidic system for highly selective one-to-one droplet fusion.,” *Lab Chip*, vol. 9, no. 18, pp. 2665–2672, 2009.

[170] J. Wu and M. Gu, “Microfluidic sensing: state of the art fabrication and detection techniques.,” *J. Biomed. Opt.*, vol. 16, no. 8, p. 80901, 2011.

[171] M. He, J. S. Edgar, G. D. M. Jeffries, R. M. Lorenz, J. P. Shelby, and D. T. Chiu, “Selective encapsulation of single cells and subcellular organelles into picoliter- and femtoliter-volume droplets,” *Anal. Chem.*, vol. 77, no. 6, pp. 1539–1544, 2005.

[172] L. S. Roach, H. Song, and R. F. Ismagilov, “Controlling nonspecific protein adsorption in a

plug-based microfluidic system by controlling interfacial chemistry using fluorous-phase surfactants," *Anal. Chem.*, vol. 77, no. 3, pp. 785–796, 2005.

[173] F. Guo, M. I. Lapsley, A. A. Nawaz, Y. Zhao, S. S. Lin, Y. Chen, S. Yang, X. Zhao, and T. J. Huang, "A Droplet-Based, Optofl uidic Device for High-Throughput, Quantitative Bioanalysis," 2012.

[174] G. Cristobal, L. Arbouet, F. Sarrazin, D. Talaga, J.-L. Bruneel, M. Joanicot, and L. Servant, "On-line laser Raman spectroscopic probing of droplets engineered in microfluidic devices.," *Lab Chip*, vol. 6, no. 9, pp. 1140–1146, 2006.

[175] F. Sarrazin, J. B. Salmon, D. Talaga, and L. Servant, "Chemical reaction imaging within microfluidic devices using confocal raman spectroscopy: The case of water and deuterium oxide as a model system," *Anal. Chem.*, vol. 80, no. 5, pp. 1689–1695, 2008.

[176] S. E. Barnes, Z. T. Cygan, J. K. Yates, K. L. Beers, and E. J. Amis, "Raman spectroscopic monitoring of droplet polymerization in a microfluidic device.," *Analyst*, vol. 131, no. 9, pp. 1027–33, 2006.

[177] K. R. Strehle, D. Cialla, P. Rösch, T. Henkel, M. Köhler, and J. Popp, "A reproducible surface-enhanced Raman spectroscopy approach. Online SERS measurements in a segmented microfluidic system," *Anal. Chem.*, vol. 79, no. 4, pp. 1542–1547, 2007.

[178] M. P. Cecchini, J. Hong, C. Lim, J. Choo, T. Albrecht, J. Andrew, and J. B. Edel, "Ultrafast Surface Enhanced Resonance Raman Scattering Detection in," pp. 3076–3081, 2011.

[179] R. Lee, I. Jung, M. Park, H. Ha, and K. H. Yoo, "Real-time monitoring of adipocyte differentiation using a capacitance sensor array," *Lab Chip*, vol. 13, no. 17, pp. 3410–3416, 2013.

[180] M. C. Cole and P. J. A. Kenis, "Multiplexed electrical sensor arrays in microfluidic networks," *Sensors Actuators, B Chem.*, vol. 136, no. 2, pp. 350–358, 2009.

[181] K. C. Cheung, M. Di Berardino, G. Schade-Kampmann, M. Hebeisen, A. Pierzchalski, J. Bocsi, A. Mittag, and A. Tárnok, "Microfluidic impedance-based flow cytometry," *Cytom. Part A*, vol. 77, no. 7, pp. 648–666, 2010.

[182] J. Wei, C. Yue, M. Van Der Velden, Z. L. Chen, Z. W. Liu, K. A. A. Makinwa, and P. M. Sarro, "Design, fabrication and characterization of a femto-farad capacitive sensor for pico-

liter liquid monitoring,” *Sensors Actuators, A Phys.*, vol. 162, no. 2, pp. 406–417, 2010.

[183] M. Demori, V. Ferrari, D. Strazza, and P. Poesio, “A capacitive sensor system for the analysis of two-phase flows of oil and conductive water,” *Sensors Actuators, A Phys.*, vol. 163, no. 1, pp. 172–179, 2010.

[184] C. Elbuken, T. Glawdel, D. Chan, and C. L. Ren, “Detection of microdroplet size and speed using capacitive sensors,” *Sensors Actuators, A Phys.*, vol. 171, no. 2, pp. 55–62, 2011.

[185] A. Ernst, W. Streule, N. Schmitt, R. Zengerle, and P. Koltay, “A capacitive sensor for non-contact nanoliter droplet detection,” *Sensors Actuators, A Phys.*, vol. 153, no. 1, pp. 57–63, 2009.

[186] E. W. M. Kemna, L. I. Segerink, F. Wolbers, I. Vermes, and A. van den Berg, “Label-free, high-throughput, electrical detection of cells in droplets.,” *Analyst*, vol. 138, no. 16, pp. 4585–92, 2013.

[187] C. Luo, X. Yang, Q. Fu, M. Sun, Q. Ouyang, Y. Chen, and H. Ji, “Picoliter-volume aqueous droplets in oil: Electrochemical detection and yeast cell electroporation,” *Electrophoresis*, vol. 27, no. 10, pp. 1977–1983, 2006.

[188] S. Liu, Y. Gu, R. B. Le Roux, S. M. Matthews, D. Bratton, K. Yunus, A. C. Fisher, and W. T. S. Huck, “The electrochemical detection of droplets in microfluidic devices.,” *Lab Chip*, vol. 8, no. 11, pp. 1937–1942, 2008.

[189] J. B. Haun, T. J. Yoon, H. Lee, and R. Weissleder, “Magnetic nanoparticle biosensors,” *Wiley Interdiscip. Rev. Nanomedicine Nanobiotechnology*, vol. 2, no. 3, pp. 291–304, 2010.

[190] R. A. Kautz, W. K. Goetzinger, and B. L. Karger, “High-throughput microcoil NMR of compound libraries using zero-dispersion segmented flow analysis,” *J. Comb. Chem.*, vol. 7, no. 1, pp. 14–20, 2005.

[191] I. Giouroudi and F. Keplinger, “Microfluidic biosensing systems using magnetic nanoparticles,” *Int. J. Mol. Sci.*, vol. 14, no. 9, pp. 18535–18556, 2013.

[192] G. . Srivastava and V. . Gupta, *Microwave Devices and Circuit Design*. Prentice-Hall of India, 2006.

[193] I. Bahl and P. Bhartia, *Microwave Solid State Circuit Design*, 2nd Ed. John Wiley&Sons Inc., 2003.

[194] D. M. Pozar, *Microwave Engineering*, 4th ed. John Wiley&Sons Inc., 2012.

[195] B. T. Rosner and D. W. Van Der Weide, “High-frequency near-field microscopy,” *Rev. Sci. Instrum.*, vol. 73, no. 7, p. 2505, 2002.

[196] S. M. Anlage, D. E. Steinhaumer, B. J. Feenstra, C. P. Vlahacos, and F. C. Wellstood, “Near-Field Microwave Microscopy of Materials Properties,” *Microw. Supercond.*, pp. 239–269, 2001.

[197] H. J. Lee, J. H. Lee, and H. Il Jung, “A symmetric metamaterial element-based RF biosensor for rapid and label-free detection,” *Appl. Phys. Lett.*, vol. 99, no. 16, pp. 163701–163704, 2011.

[198] R. Joffe, E. O. Kamenetskii, and R. Shavit, “Novel microwave near-field sensors for material characterization, biology, and nanotechnology,” *J. Appl. Phys.*, vol. 113, no. 6, 2013.

[199] D. J. Rowe, A. Porch, D. A. Barrow, and C. J. Allender, “Microfluidic device for compositional analysis of solvent systems at microwave frequencies,” *Sensors Actuators, B Chem.*, vol. 169, pp. 213–221, 2012.

[200] D. J. Rowe, a Porch, D. a Barrow, and C. J. Allender, “Non-Contact Label-Free Dielectric Spectroscopy of Single- and Multi-Phase Microfluidic Systems,” pp. 891–893, 2011.

[201] G. R. Facer, D. A. Notterman, and L. L. Sohn, “Dielectric spectroscopy for bioanalysis: From 40 Hz to 26.5 GHz in a microfabricated wave guide,” *Appl. Phys. Lett.*, vol. 78, no. 7, pp. 996–998, 2001.

[202] N. Haase and A. F. Jacob, “Dielectric contrast measurements on biological substances with resonant microwave near-field sensors,” *Int. J. Microw. Wirel. Technol.*, vol. 5, no. 3, pp. 221–230, 2013.

[203] G. Gennarelli, S. Romeo, M. R. Scarfi, and F. Soldovieri, “A microwave resonant sensor for concentration measurements of liquid solutions,” *IEEE Sens. J.*, vol. 13, no. 5, pp. 1857–1864, 2013.

[204] I. Iramnaaz, Y. Xing, K. Xue, Y. Zhuang, and R. Fitch, “Graphene based RF / microwave impedance sensing of DNA,” *Technology*, pp. 1030–1034, 2011.

[205] H. Caglayan, S. Cakmakyapan, S. A. Addae, M. A. Pinard, D. Caliskan, K. Aslan, and E. Ozbay, “Ultrafast and sensitive bioassay using split ring resonator structures and microwave

heating," *Appl. Phys. Lett.*, vol. 97, no. 9, pp. 127–130, 2010.

[206] J. B. Pendry, A. J. Holden, D. J. Robbins, and W. J. Stewart, "Magnetism from conductors and enhanced nonlinear phenomena," *IEEE Trans. Microw. Theory Tech.*, vol. 47, no. 11, pp. 2075–2084, 1999.

[207] X. J. He, Y. Wang, J. M. Wang, and T. L. Gui, "Thin-film sensor based tip-shaped split ring resonator metamaterial for microwave application," *Microsyst. Technol.*, vol. 16, no. 10, pp. 1735–1739, 2010.

[208] W. T. S. Chen, K. M. E. Stewart, C. K. Yang, R. R. Mansour, J. Carroll, and A. Penlidis, "Wearable RF Sensor Array Implementing Coupling-Matrix Readout Extraction Technique," *IEEE Trans. Microw. Theory Tech.*, vol. 63, no. 12, pp. 4157–4168, 2015.

[209] H. J. Lee, H. S. Lee, K. H. Yoo, and J. G. Yook, "DNA sensing using split-ring resonator alone at microwave regime," *J. Appl. Phys.*, vol. 108, no. 1, 2010.

[210] K. Aydin and E. Ozbay, "Identifying magnetic response of split-ring resonators at microwave frequencies," *Opto-Electronics Rev.*, vol. 14, no. 3, pp. 193–199, 2006.

[211] A. Mason, O. Korostynska, M. Ortoneda-Pedrola, A. Shaw, and A. Al-Shamma'A, "A resonant co-planar sensor at microwave frequencies for biomedical applications," *Sensors Actuators, A Phys.*, vol. 202, pp. 170–175, 2013.

[212] K. Grenier, D. Dubuc, P. Poleni, and M. Kumemura, "Integrated Broadband Microwave and Microfluidic Sensor Dedicated to Bioengineering," vol. 57, no. 12, pp. 3246–3253, 2009.

[213] T. Chretiennot, D. Dubuc, and K. Grenier, "A Microwave and microfluidic planar resonator for efficient and accurate complex permittivity characterization of aqueous solutions," *IEEE Trans. Microw. Theory Tech.*, vol. 61, no. 2, pp. 972–978, 2013.

[214] C. Dalmay, M. Cheray, A. Pothier, F. Lalloué, M. O. Jauberteau, and P. Blondy, "Ultra sensitive biosensor based on impedance spectroscopy at microwave frequencies for cell scale analysis," *Sensors Actuators, A Phys.*, vol. 162, no. 2, pp. 189–197, 2010.

[215] L. Y. Zhang, C. Bounaix Morand Du Puch, C. Dalmay, A. Lacroix, A. Landoulsi, J. Leroy, C. Mélin, F. Lalloué, S. Battu, C. Lautrette, S. Giraud, A. Bessaudou, P. Blondy, M. O. Jauberteau, and A. Pothier, "Discrimination of colorectal cancer cell lines using microwave biosensors," *Sensors Actuators, A Phys.*, vol. 216, pp. 405–416, 2014.

[216] C. Dalmay, A. Pothier, P. Blondy, F. Lalloue, and M. O. Jauberteau, “Label free biosensors for human cell characterization using radio and microwave frequencies,” *Microw. Symp. Dig. 2008 IEEE MTT-S Int.*, pp. 911–914, 2008.

[217] C. Dalmay, J. Villemejane, V. Joubert, O. Franais, L. M. Mir, and B. Le Pioufle, “Design and realization of a microfluidic device devoted to the application of ultra-short pulses of electrical field to living cells,” *Sensors Actuators, B Chem.*, vol. 160, no. 1, pp. 1573–1580, 2011.

[218] C. Dalmay, M. a. De Menorval, O. Français, L. M. Mir, and B. Le Pioufle, “A microfluidic device with removable packaging for the real time visualisation of intracellular effects of nanosecond electrical pulses on adherent cells,” *Lab Chip*, vol. 12, no. 22, p. 4709, 2012.

[219] A. Mason, A. Shaw, and A. Al-Shamma’a, “A Co-planar microwave sensor for biomedical applications,” *Procedia Eng.*, vol. 47, pp. 438–441, 2012.

[220] Y. Il Kim, Y. Park, and H. K. Baik, “Development of LC resonator for label-free biomolecule detection,” *Sensors Actuators, A Phys.*, vol. 143, no. 2, pp. 279–285, 2008.

[221] Y. I. Kim, T. S. Park, J. H. Kang, M. C. Lee, J. T. Kim, J. H. Park, and H. K. Baik, “Biosensors for label free detection based on RF and MEMS technology,” *Sensors Actuators, B Chem.*, vol. 119, no. 2, pp. 592–599, 2006.

[222] M. Nikolic-Jaric, S. F. Romanuik, G. A. Ferrier, G. E. Bridges, M. Butler, K. Sunley, D. J. Thomson, and M. R. Freeman, “Microwave frequency sensor for detection of biological cells in microfluidic channels,” *Biomicrofluidics*, vol. 3, no. 3, pp. 1–15, 2009.

[223] H. J. Lee and J. G. Yook, “Biosensing using split-ring resonators at microwave regime,” *Appl. Phys. Lett.*, vol. 92, no. 25, pp. 127–130, 2008.

[224] H. J. Lee, J. H. Lee, H. S. Moon, I. S. Jang, J. S. Choi, J. G. Yook, and H. Il Jung, “A planar split-ring resonator-based microwave biosensor for label-free detection of biomolecules,” *Sensors Actuators, B Chem.*, vol. 169, pp. 26–31, 2012.

[225] W. Withayachumnankul, K. Jaruwongrungsee, A. Tuantranont, C. Fumeaux, and D. Abbott, “Metamaterial-based microfluidic sensor for dielectric characterization,” *Sensors Actuators, A Phys.*, vol. 189, pp. 233–237, 2013.

[226] G. A. Ferrier, A. N. Hladio, D. J. Thomson, G. E. Bridges, M. Hedayatipoor, S. Olson, and M. R. Freeman, “Microfluidic electromanipulation with capacitive detection for the mechanical

analysis of cells," *Biomicrofluidics*, vol. 2, no. 4, pp. 1–13, 2008.

[227] J. H. Goh, a Mason, a I. Al-Shamma'a, M. Field, M. Shackcloth, and P. Browning, "Non Invasive Microwave Sensor for the Detection of Lactic Acid in Cerebrospinal Fluid (CSF)," *J. Phys. Conf. Ser.*, vol. 307, p. 12017, 2011.

[228] A. Bababjanyan, H. Melikyan, S. Kim, J. Kim, K. Lee, and B. Friedman, "Real-time noninvasive measurement of glucose concentration using a microwave biosensor," *J. Sensors*, vol. 2010, 2010.

[229] Z. Hua, J. L. Rouse, A. E. Eckhardt, V. Srinivasan, V. K. Pamula, W. A. Schell, J. L. Benton, T. G. Mitchell, and M. G. Pollack, "Multiplexed real-time polymerase chain reaction on a digital microfluidic platform," *Anal. Chem.*, vol. 82, no. 6, pp. 2310–2316, 2010.

[230] S. Mahjoob, K. Vafai, and N. R. Beer, "Rapid microfluidic thermal cycler for polymerase chain reaction nucleic acid amplification," *Int. J. Heat Mass Transf.*, vol. 51, no. 9–10, pp. 2109–2122, 2008.

[231] G. Maltezos, A. Gomez, J. Zhong, F. A. Gomez, and A. Scherer, "Microfluidic polymerase chain reaction," *Appl. Phys. Lett.*, vol. 93, no. 24, pp. 127–130, 2008.

[232] T. Matsui, J. Franzke, A. Manz, and D. Janasek, "Temperature gradient focusing in a PDMS/glass hybrid microfluidic chip," *Electrophoresis*, vol. 28, no. 24, pp. 4606–4611, 2007.

[233] D. Ross and L. E. Locascio, "Microfluidic temperature gradient focusing," *Anal. Chem.*, vol. 74, no. 11, pp. 2556–2564, 2002.

[234] B. Selva, J. Marchalot, and M.-C. Jullien, "An optimized resistor pattern for temperature gradient control in microfluidics," *J. Micromechanics Microengineering*, vol. 19, no. 6, p. 65002, 2009.

[235] A. a Darhuber, J. P. Valentino, and S. M. Troian, "Planar digital nanoliter dispensing system based on thermocapillary actuation," *Lab Chip*, vol. 10, no. 8, pp. 1061–1071, 2010.

[236] Z. Jiao, N. T. Nguyen, X. Huang, and Y. Z. Ang, "Reciprocating thermocapillary plug motion in an externally heated capillary," *Microfluid. Nanofluidics*, vol. 3, no. 1, pp. 39–46, 2007.

[237] Z. Jiao, X. Huang, N. T. Nguyen, and P. Abgrall, "Thermocapillary actuation of droplet in a planar microchannel," *Microfluid. Nanofluidics*, vol. 5, no. 2, pp. 205–214, 2008.

[238] Y. Tanaka, M. N. Slyadnev, A. Hibara, M. Tokeshi, and T. Kitamori, “Non-contact photothermal control of enzyme reactions on a microchip by using a compact diode laser,” *J. Chromatogr. A*, vol. 894, no. 1–2, pp. 45–51, 2000.

[239] H. F. Arata, Y. Rondelez, H. Noji, and H. Fujita, “Temperature alternation by an on-chip microheater to reveal enzymatic activity of B-galactosidase at high temperatures,” *Anal. Chem.*, vol. 77, pp. 4810–4814, 2005.

[240] S. J. Kim, F. Wang, M. A. Burns, and K. Kurabayashi, “Temperature-programmed natural convection for micromixing and biochemical reaction in a single microfluidic chamber,” *Anal. Chem.*, vol. 81, no. 11, pp. 4510–4516, 2009.

[241] G. Maltezos, M. Johnston, and A. Scherer, “Thermal management in microfluidics using micro-Peltier junctions,” *Appl. Phys. Lett.*, vol. 87, no. 15, pp. 1–3, 2005.

[242] G. Velve-Casquillas, C. Fu, M. Le Berre, J. Cramer, S. Meance, A. Plecis, D. Baigl, J.-J. Greffet, Y. Chen, M. Piel, and P. T. Tran, “Fast microfluidic temperature control for high resolution live cell imaging.,” *Lab Chip*, vol. 11, no. 3, pp. 484–489, 2011.

[243] M. S. Munson, G. Danger, J. G. Shackman, and D. Ross, “Temperature gradient focusing with field-amplified continuous sample injection for dual-stage analyte enrichment and separation,” *Anal. Chem.*, vol. 79, no. 16, pp. 6201–6207, 2007.

[244] A. J. A. de Mello, M. Habgood, N. L. N. Lancaster, T. Welton, and R. R. C. R. Wootton, “Precise temperature control in microfluidic devices using Joule heating of ionic liquids,” *Lab Chip*, vol. 4, no. 5, pp. 417–419, 2004.

[245] B. Selva, V. Miralles, I. Cantat, and M.-C. Jullien, “Thermocapillary actuation by optimized resistor pattern: bubbles and droplets displacing, switching and trapping,” *Lab Chip*, vol. 10, no. 14, pp. 1835–1840, 2010.

[246] H. Kim, S. Vishniakou, and G. W. Faris, “Petri dish PCR: laser-heated reactions in nanoliter droplet arrays,” *Lab Chip*, vol. 9, no. 9, pp. 1230–1235, 2009.

[247] M. Robert De Saint Vincent, R. Wunenburger, and J. P. Delville, “Laser switching and sorting for high speed digital microfluidics,” *Appl. Phys. Lett.*, vol. 92, p. 154105, 2008.

[248] B. C. Giordano, J. Ferrance, S. Swedberg, A. F. R. Hühmer, and J. P. Landers, “Polymerase Chain Reaction in Polymeric Microchips: DNA Amplification in Less Than 240 Seconds,”

Anal. Biochem., vol. 291, no. 1, pp. 124–132, 2001.

[249] J. J. Shah, S. G. Sundaresan, J. Geist, D. R. Reyes, J. C. Booth, M. V Rao, and M. Gaitan, "Microwave dielectric heating of fluids in an integrated microfluidic device," *J. Micromechanics Microengineering*, vol. 17, no. 11, pp. 2224–2230, 2007.

[250] D. J. Marchiarullo, A. H. Sklavounos, K. Oh, B. L. Poe, N. S. Barker, and J. P. Landers, "Low-power microwave-mediated heating for microchip-based PCR," *Lab Chip*, vol. 13, no. 17, p. 3417, 2013.

[251] C. O. Kappe, D. Dallinger, and S. S. Murphree, *Practical Microwave Synthesis for Organic Chemists*. Wiley-VCH Verlag Co., 2009.

[252] C. O. Kappe and A. Stadler, *Microwaves in Organic and Medicinal Chemistry*. Wiley-VCH Verlag Co., 2005.

[253] J. P. Tierney and P. Lidstrom, *Microwave Assisted Organic Synthesis*. Blackwell Publishing, 2005.

[254] A. Loupy, *Microwaves in Organic and Synthesis*, 2nd ed. VCH Verlag GmbH&Co., 2006.

[255] M. V. Rao, J. J. Shah, J. Geist, and M. Gaitan, "Microwave Dielectric Heating of Fluids in Microfluidic Devices," in *The Development and Application of Microwave Heating*, W. Cao, Ed. InTech, 2012.

[256] J. J. Shah, J. Geist, and M. Gaitan, "Microwave-induced adjustable nonlinear temperature gradients in microfluidic devices," *J. Micromechanics Microengineering*, vol. 20, no. 10, p. 105025, 2010.

[257] A. Kempitiya, D. A. Borca-Tasciuc, H. S. Mohamed, and M. M. Hella, "Localized microwave heating in microwells for parallel DNA amplification applications," *Appl. Phys. Lett.*, vol. 94, no. 6, pp. 127–130, 2009.

[258] K. Shaw, P. Docker, and J. Yelland, "Rapid PCR amplification using a microfluidic device with integrated microwave heating and air impingement cooling," *Lab Chip*, vol. 10, no. 13, pp. 1725–8, 2010.

[259] D. Issadore, K. J. Humphry, K. A. Brown, L. Sandberg, D. A. Weitz, and R. M. Westervelt, "Microwave dielectric heating of drops in microfluidic devices.," *Lab Chip*, vol. 9, no. 12, pp. 1701–6, 2009.

[260] M. S. Boybay, A. Jiao, T. Glawdel, and C. L. Ren, “Microwave sensing and heating of individual droplets in microfluidic devices,” *Lab Chip*, vol. 13, no. 19, pp. 3840–3846, 2013.

[261] L. Li, Q. Wang, J. Feng, L. Tong, and B. Tang, “Highly sensitive and homogeneous detection of membrane protein on a single living cell by aptamer and nicking enzyme assisted signal amplification based on microfluidic droplets,” *Anal. Chem.*, vol. 86, no. 10, pp. 5101–5107, 2014.

[262] X. Ding, Z. Peng, S.-C. S. Lin, M. Geri, S. Li, P. Li, Y. Chen, M. Dao, S. Suresh, and T. J. Huang, “Cell separation using tilted-angle standing surface acoustic waves,” *Proc. Natl. Acad. Sci.*, vol. 111, pp. 12992–12997, 2014.

[263] Y. Chen, P. Li, P.-H. Huang, Y. Xie, J. D. Mai, L. Wang, N.-T. Nguyen, and T. J. Huang, “Rare cell isolation and analysis in microfluidics.,” *Lab Chip*, vol. 14, no. 4, pp. 626–45, 2014.

[264] H. Zhu, G. Wang, D. Xie, B. Cai, Y. Liu, and X. Zhao, “Au nanoparticles enhanced fluorescence detection of DNA hybridization in picoliter microfluidic droplets,” *Biomed. Microdevices*, vol. 16, no. 3, pp. 479–485, 2014.

[265] M. T. Guo, A. Rotem, J. a. Heyman, and D. a. Weitz, “Droplet microfluidics for high-throughput biological assays,” *Lab Chip*, vol. 12, no. 12, p. 2146, 2012.

[266] N. Wu, F. Courtois, R. Surjadi, J. Oakeshott, T. S. Peat, C. J. Easton, C. Abell, and Y. Zhu, “Enzyme synthesis and activity assay in microfluidic droplets on a chip,” *Eng. Life Sci.*, vol. 11, no. 2, pp. 157–164, 2011.

[267] L. Mazutis, J.-C. Baret, P. Treacy, Y. Skhiri, A. F. Araghi, M. Ryckelynck, V. Taly, and A. D. Griffiths, “Multi-step microfluidic droplet processing: kinetic analysis of an in vitro translated enzyme.,” *Lab Chip*, vol. 9, no. 20, pp. 2902–2908, 2009.

[268] H. Zhou, G. Li, and S. Yao, “A droplet-based pH regulator in microfluidics.,” *Lab Chip*, vol. 14, no. December 2013, pp. 1917–22, 2014.

[269] E. Brouzes, M. Medkova, N. Savenelli, D. Marran, M. Twardowski, J. B. Hutchison, J. M. Rothberg, D. R. Link, N. Perrimon, and M. L. Samuels, “Droplet microfluidic technology for single-cell high-throughput screening.,” *Proc. Natl. Acad. Sci. U. S. A.*, vol. 106, no. 34, pp. 14195–200, 2009.

[270] R. Sista, Z. Hua, P. Thwar, A. Sudarsan, V. Srinivasan, A. Eckhardt, M. Pollack, and V.

Pamula, “Development of a digital microfluidic platform for point of care testing,” *Lab Chip*, vol. 8, no. 12, p. 2091, 2008.

[271] Foudeh et al., “Microfluidic designs and techniques using lab-on-a-chip devices for pathogen detection for point-of-care diagnostics.,” *Lab Chip*, vol. 12, no. 18, pp. 3249–66, 2012.

[272] M. R. de Saint Vincent, S. Cassagnere, J. Plantard, and J. P. Delville, “Real-time droplet caliper for digital microfluidics,” *Microfluid. Nanofluidics*, vol. 13, pp. 261–271, 2012.

[273] J. Lim, P. Gruner, M. Konrad, and J.-C. Baret, “Micro-optical lens array for fluorescence detection in droplet-based microfluidics.,” *Lab Chip*, vol. 13, no. 8, pp. 1472–5, 2013.

[274] M. Fukuyama, Y. Yoshida, J. C. T. Eijkel, A. Van Den Berg, and A. Hibara, “Time-resolved electrochemical measurement device for microscopic liquid interfaces during droplet formation,” *Microfluid. Nanofluidics*, vol. 14, no. 6, pp. 943–950, 2013.

[275] G. D. M. Jeffries, R. M. Lorenz, and D. T. Chiu, “Ultrasensitive and high-throughput fluorescence analysis of droplet contents with orthogonal line confocal excitation,” *Anal. Chem.*, vol. 82, no. 23, pp. 9948–9954, 2010.

[276] N. M. iguel M. Pires, T. Dong, U. Hanke, and N. Hoivik, “Recent developments in optical detection technologies in lab-on-a-chip devices for biosensing applications,” *Sensors (Basel).*, vol. 14, no. 8, pp. 15458–15479, 2014.

[277] J. Sochor, J. Dobes, O. Krystofova, B. Ruttkay-Nedecky, P. Babula, M. Pohanka, T. Jurikova, O. Zitka, V. Adam, B. Klejdus, and R. Kizek, “Electrochemistry as a tool for studying antioxidant properties,” *Int. J. Electrochem. Sci.*, vol. 8, no. 6, pp. 8464–8489, 2013.

[278] K. Mitton and J. Trevithick, “High-performance liquid chromatography-electrochemical detection of antioxidants in vertebrate lens: glutathione, tocopherol, and ascorbate,” *Methods Enzym.*, no. 233, pp. 523–539, 1994.

[279] N. Wongkaew, P. He, V. Kurth, W. Surareungchai, and A. J. Baeumner, “Multi-channel PMMA microfluidic biosensor with integrated IDUAs for electrochemical detection,” *Anal. Bioanal. Chem.*, vol. 405, no. 18, pp. 5965–5974, 2013.

[280] E. V. Moiseeva, A. A. Fletcher, and C. K. Harnett, “Thin-film electrode based droplet detection for microfluidic systems,” *Sensors Actuators, B Chem.*, vol. 155, no. 1, pp. 408–414, 2011.

[281] G. Yesiloz, M. S. Boybay, and C. L. Ren, “Label-free high-throughput detection and content sensing of individual droplets in microfluidic systems,” *Lab Chip*, vol. 15, no. 20, pp. 4008–4019, 2015.

[282] N. Suwan, “Investigation of RF Direct Detection Architecture Circuits for Metamaterial Sensor Applications,” University of Waterloo, 2011.

[283] G. F. Engen, “The Six-Port Reflectometer: An Alternative Network Analyzer,” *IEEE Transactions on Microwave Theory and Techniques*, vol. 25, no. 12. pp. 1075–1080, 1977.

[284] F. Ghannouchi and A. Mohammadi, *The Six-Port Technique with Microwave and Wireless Applications*. Artech House Publishers, 2009.

[285] J. Ardizzoni and D. Falls, “A Practical Guide to High-Speed Printed Circuit Board Layout,” 2005.

[286] J. Kim, A. J. deMello, S.-I. Chang, J. Hong, and D. O’Hare, “Thermoset polyester droplet-based microfluidic devices for high frequency generation,” *Lab Chip*, vol. 11, no. 23, p. 4108, 2011.

[287] T. Glawdel and C. L. Ren, “Droplet formation in microfluidic T-junction generators operating in the transitional regime. III. Dynamic surfactant effects,” *Phys. Rev. E - Stat. Nonlinear, Soft Matter Phys.*, vol. 86, no. 2, pp. 1–9, 2012.

[288] T. Mohamed, T. Hoang, M. Jelokhani-Niaraki, and P. P. N. Rao, “Tau-derived-hexapeptide 306VQIVYK311 aggregation inhibitors: Nitrocatechol moiety as a pharmacophore in drug design,” *ACS Chem. Neurosci.*, vol. 4, no. 12, pp. 1559–1570, 2013.

[289] S. Haydar, H. Yun, R. Staal, and W. Hirst, “Small-Molecule Protein-Protein Interaction Inhibitors as Therapeutic Agents for Neurodegenerative Diseases: Recent Progress and Future Directions,” *Annu. Rep. Med. Chem.*, vol. 44, pp. 51–69, 2009.

[290] A. J. L. Morgan, J. Naylon, S. Gooding, C. John, O. Squires, J. Lees, D. A. Barrow, and A. Porch, “Efficient microwave heating of microfluidic systems,” *Sensors Actuators, B Chem.*, vol. 181, pp. 904–909, 2013.

[291] E. Samiei, M. Diaz de Leon Derby, A. van den Berg, and M. Hoorfar, “An electrohydrodynamic technique for rapid mixing in stationary droplets on digital microfluidic platforms,” *Lab Chip*, pp. 227–234, 2016.

[292] M. S. Boybay, “Behavior of metamaterial-based microwave components for sensing and heating of nanoliter-scale volumes,” *Turkish J. Electr. Eng. Comput. Sci.*, vol. 24, pp. 3503–3512, 2016.

[293] AnsoftCorporation, “High Frequency Structure Simulator,” Pittsburgh, PA, 2005.

[294] F. T. Ulaby, *Fundamentals of Applied Electromagnetics*. Prentice Hall, 2007.

[295] R. Harrington, *Time-harmonic Electromagnetic Fields*. New York: McGraw-Hill Co., 1961.

[296] A. Ozcelik, D. Ahmed, Y. Xie, N. Nama, Z. Qu, A. Nawaz, and T. J. Huang, “An Acoustofluidic Micromixer via Bubble Inception and Cavitation from Microchannel Sidewalls,” *Anal. Chem.*, no. 86, pp. 5083–5088, 2014.

[297] M. Muradoglu and H. A. Stone, “Mixing in a drop moving through a serpentine channel: A computational study,” *Phys. Fluids*, vol. 17, no. 7, pp. 1–9, 2005.

[298] R. O. Grigoriev, “Chaotic mixing in thermocapillary-driven microdroplets,” *Phys. Fluids*, vol. 17, no. 3, 2005.

[299] R. O. Grigoriev, M. Schatz, and V. Sharma, “Chaotic mixing in microdroplets,” *Lab Chip*, no. 6, pp. 1369–1372, 2006.

[300] C. Y. Wen, C. P. Yeh, C. H. Tsai, and L. M. Fu, “Rapid magnetic microfluidic mixer utilizing AC electromagnetic field,” *Electrophoresis*, vol. 30, no. 24, pp. 4179–4186, 2009.

[301] C. Chang, L. Fu, and R. Yang, “Active Mixer,” in *Encyclopedia of Microfluidics and Nanofluidics*, D. Li, Ed. Sipringer:Berlin: Springer, 2015, pp. 40–47.

[302] C. Y. Lee, C. L. Chang, Y. N. Wang, and L. M. Fu, “Microfluidic mixing: A review,” *Int. J. Mol. Sci.*, vol. 12, no. 5, pp. 3263–3287, 2011.

[303] N.-T. Nguyen and Z. Wu, “Micromixers—a review,” *J. Micromechanics Microengineering*, vol. 15, no. 2, pp. R1–R16, 2005.

[304] S. Wang, X. Huang, and C. Yang, “Mixing enhancement for high viscous fluids in a microfluidic chamber.,” *Lab Chip*, vol. 11, no. 12, pp. 2081–2087, 2011.

[305] C.-Y. Chen, C.-Y. Chen, C.-Y. Lin, and Y.-T. Hu, “Magnetically actuated artificial cilia for optimum mixing performance in microfluidics.,” *Lab Chip*, vol. 13, no. 14, pp. 2834–9, 2013.

[306] M. Viefhues, R. Eichhorn, E. Fredrich, J. Regtmeier, and D. Anselmetti, “Continuous and

reversible mixing or demixing of nanoparticles by dielectrophoresis.," *Lab Chip*, vol. 12, no. 3, pp. 485–94, 2012.

[307] A. Salmanzadeh, H. Shafiee, R. V. Davalos, and M. A. Stremler, "Microfluidic mixing using contactless dielectrophoresis," *Electrophoresis*, vol. 32, no. 18, pp. 2569–2578, 2011.

[308] I. F. Cheng, S. C. Chiang, C. C. Chung, T. M. Yeh, and H. C. Chang, "Ripple structure-generated hybrid electrokinetics for on-chip mixing and separating of functionalized beads," *Biomicrofluidics*, vol. 8, no. 6, pp. 15–18, 2014.

[309] M. L. Y. Sin, Y. Shimabukuro, and P. K. Wong, "Hybrid electrokinetics for separation, mixing, and concentration of colloidal particles.," *Nanotechnology*, vol. 20, no. 16, p. 165701, 2009.

[310] J. K. Chen and R. J. Yang, "Electroosmotic flow mixing in zigzag microchannels," *Electrophoresis*, vol. 28, no. 6, pp. 975–983, 2007.

[311] L. Lu, K. S. Ryu, and C. Liu, "A Magnetic Microstirrer and Array for Microfluidic Mixing," vol. 11, no. 5, pp. 462–469, 2002.

[312] T. G. Kang, M. A. Hulsen, P. D. Anderson, J. M. J. Den Toonder, and H. E. H. Meijer, "Chaotic mixing induced by a magnetic chain in a rotating magnetic field," *Phys. Rev. E - Stat. Nonlinear, Soft Matter Phys.*, vol. 76, no. 6, pp. 1–11, 2007.

[313] G. Kitenbergs, E. Kaspars, R. Perzynski, and C. Andrejs, "Journal of Magnetism and Magnetic Materials Magnetic particle mixing with magnetic micro-convection for micro fl uidics," vol. 380, pp. 227–230, 2015.

[314] R. Ganguly, T. Hahn, and S. Hardt, "Magnetophoretic mixing for in situ immunochemical binding on magnetic beads in a microfluidic channel," *Microfluid. Nanofluidics*, vol. 8, no. 6, pp. 739–753, 2010.

[315] J. Tsai and L. Lin, "Active microfluidic mixer and gas bubble filter driven by thermal bubble micropump," *Sensors And Actuators*, vol. 98, pp. 665–671, 2002.

[316] B. Xu, T. N. Wong, N. T. Nguyen, Z. Che, and J. C. K. Chai, "Thermal mixing of two miscible fluids in a T-shaped microchannel," *Biomicrofluidics*, vol. 4, no. 4, pp. 1–13, 2010.

[317] I. Glasgow and N. Aubry, "Enhancement of microfluidic mixing using time pulsing.," *Lab Chip*, vol. 3, no. 2, pp. 114–120, 2003.

[318] F. Okkels and P. Tabeling, “Spatiotemporal Resonances in Mixing of Open Viscous Fluids,” *Phys. Rev. Lett.*, no. January, pp. 1–4, 2004.

[319] G. G. Yaralioglu, I. O. Wygant, T. C. Marentis, and B. T. Khuri-Yakub, “Ultrasonic mixing in microfluidic channels using integrated transducers,” *Anal. Chem.*, vol. 76, no. 13, pp. 3694–3698, 2004.

[320] Z. Yang, Z. Yang, S. Matsumoto, S. Matsumoto, H. Goto, H. Goto, M. Matsumoto, M. Matsumoto, R. Maeda, and R. Maeda, “Ultrasonic micromixer for microfuidic systems,” *Sensors And Actuators*, vol. 93, pp. 266–272, 2001.

[321] H. Van Phan, M. B. Coşkun, M. Şeşen, G. Pandraud, A. Neild, and T. Alan, “Vibrating membrane with discontinuities for rapid and efficient microfluidic mixing,” *Lab Chip*, pp. 4206–4216, 2015.

[322] D. Ahmed, X. Mao, J. Shi, B. Juluri, and T. Huang, “A millisecond micromixer via single-bubble-based acoustic streaming,” *Lab Chip*, vol. 9, no. 18, p. 2738, 2009.

[323] D. Ahmed, X. Mao, B. K. Juluri, and T. J. Huang, “A fast microfluidic mixer based on acoustically driven sidewall-trapped microbubbles,” *Microfluid. Nanofluidics*, vol. 7, no. 5, pp. 727–731, 2009.

[324] H. Kinoshita, S. Kaneda, T. Fujii, and M. Oshima, “Three-dimensional measurement and visualization of internal flow of a moving droplet using confocal micro-PIV,” *Lab Chip*, vol. 7, no. 3, pp. 338–346, 2007.

[325] D. Malsch, M. Kielpinski, R. Merthan, J. Albert, G. Mayer, J. M. Köhler, H. Süße, M. Stahl, and T. Henkel, “u-PIV-Analysis of Taylor flow in micro channels,” *Chem. Eng. J.*, vol. 135, no. SUPPL. 1, pp. 166–172, 2007.

[326] S. Ma, J. M. Sherwood, W. T. S. Huck, and S. Balabani, “On the flow topology inside droplets moving in rectangular microchannels,” *Lab Chip*, vol. 14, no. 18, p. 3611, 2014.

[327] H. Song, M. R. Bringer, J. D. Tice, C. J. Gerdts, and R. F. Ismagilov, “Experimental test of scaling of mixing by chaotic advection in droplets moving through microfluidic channels,” *Appl. Phys. Lett.*, vol. 83, no. 22, pp. 4664–4666, 2003.

[328] D. Wong, G. Yesiloz, M. S. Boybay, and C. L. Ren, “Microwave temperature measurement in microfluidic devices,” *Lab Chip*, vol. 16, no. 12, pp. 2192–2197, 2016.

[329] G. Yesiloz, M. S. Boybay, and C. L. Ren, "Effective Thermo-Capillary Mixing in Droplet Microfluidics Integrated with a Microwave Heater," *Anal. Chem.*, p. acs.analchem.6b04520, 2017.

[330] Z. B. Stone and H. A. Stone, "Imaging and quantifying mixing in a model droplet micromixer," *Phys. Fluids*, vol. 17, no. 6, pp. 1–11, 2005.

[331] Y. A. Cengel and J. M. Cimbala, *Fluid Mechanics: Fundamentals and Applications*. McGraw-Hill Co., 2006.

[332] E. Buckingham, "On Physically Similar Systems: Illustrations of the Use of Dimensional Equations," *Phys. Rev.*, vol. 4, pp. 345–376, 1914.

[333] F. White, *Fluid Mechanics*. McGraw-Hill Co., 2011.

[334] J. Braga, J. Desterro, and M. Carmo-Fonseca, "Intracellular macromolecular mobility measured by fluorescence recovery after photobleaching with confocal laser scanning microscopes," *Mol. Biol. Cell*, vol. 15, no. 10, pp. 4749–4760, 2004.

[335] M. L. Cordero, H. O. Rolfsnes, D. R. Burnham, P. A. Campbell, D. McGloin, and C. N. Baroud, "Mixing via thermocapillary generation of flow patterns inside a microfluidic drop," *New J. Phys.*, vol. 11, pp. 0–15, 2009.

[336] S. Wiggins and J. M. Ottino, "Foundations of chaotic mixing.," *Philos. Trans. A. Math. Phys. Eng. Sci.*, vol. 362, no. 1818, pp. 937–970, 2004.

[337] Y. Li, Y. Xu, X. Feng, and B. F. Liu, "A rapid microfluidic mixer for high-viscosity fluids to track ultrafast early folding kinetics of G-quadruplex under molecular crowding conditions," *Anal. Chem.*, vol. 84, no. 21, pp. 9025–9032, 2012.

[338] R. Samy, T. Glawdel, and C. L. Ren, "Method for Microfluidic Whole-Chip Temperature Measurement Using Thin-Film Poly (dimethylsiloxane)/ Rhodamine B," *Measurement*, vol. 80, no. 2, pp. 4117–4123, 2008.

[339] X. Fang, M. Adams, and J. Pawliszyn, "A model of thermally generated pH gradients in tapered capillaries," *Analyst*, no. 124, pp. 335–341, 1999.

[340] T. Huang and J. Pawliszyn, "Microfabrication of a tapered channel for isoelectric focus," pp. 1–7, 2002.

[341] D. Ross and L. E. Locascio, “Microfluidic Temperature Gradient Focusing Microfluidic Temperature Gradient Focusing,” *Anal. Chem.*, vol. 74, no. April, pp. 2556–2564, 2002.

[342] M. K. Sun, G. J. Sommer, M. A. Burns, and E. F. Hasselbrink, “Low-power concentration and separation using temperature gradient focusing via Joule heating,” *Anal. Chem.*, vol. 78, no. 23, pp. 8028–8035, 2006.

[343] D. Mao, X. Liu, Q. Qiao, W. Yin, M. Zhao, J. M. Cole, J. Cui, and Z. Xu, “Coumarin 545: an emission reference dye with a record-low temperature coefficient for ratiometric fluorescence based temperature measurements,” *Analyst*, vol. 140, no. 4, pp. 1008–1013, 2015.

[344] Y. Y. Chen and A. W. Wood, “Application of a temperature-dependent fluorescent dye (Rhodamine B) to the measurement of radiofrequency radiation-induced temperature changes in biological samples,” *Bioelectromagnetics*, vol. 30, no. 7, pp. 583–590, 2009.

[345] L. Gui and C. L. Ren, “Temperature measurement in microfluidic chips using photobleaching of a fluorescent thin film,” *Appl. Phys. Lett.*, vol. 92, no. 2, pp. 23–25, 2008.

[346] K. M. Schreiter, T. Glawdel, J. A. Forrest, and C. L. Ren, “Robust thin-film fluorescence thermometry for prolonged measurements in microfluidic devices,” *RSC Adv.*, vol. 3, no. 38, pp. 17236–17243, 2013.

[347] M. a. Bennet, P. R. Richardson, J. Arlt, A. McCarthy, G. S. Buller, and A. C. Jones, “Optically trapped microsensors for microfluidic temperature measurement by fluorescence lifetime imaging microscopy.,” *Lab Chip*, vol. 11, no. 22, pp. 3821–8, 2011.

[348] C. Dames, “Resistive Temperature Detectors,” in *Encyclopedia of Microfluidics and Nanofluidics*, D. Li, Ed. Springer US, 2008, pp. 1782–1790.

[349] D. Ross, M. Gaitan, and L. E. Locascio, “Temperature Measurement in Microfluidic Systems Using a Temperature-Dependent Fluorescent Dye,” *Anal. Chem.*, vol. 73, no. 17, pp. 4117–4123, 2010.

[350] C. Gosse, C. Bergaud, and P. Low, “Molecular Probes for Thermometry in Microfluidic Devices,” in *Thermal Nanosystems and Nanomaterials*, S. Volz, Ed. Springer Berlin Heidelberg, 2009, pp. 301–341.

[351] T. Glawdel, Z. Almutairi, S. Wang, and C. Ren, “Photobleaching absorbed Rhodamine B to improve temperature measurements in PDMS microchannels,” *Lab Chip*, vol. 9, no. 1, pp.

171–174, 2009.

[352] G. W. Walker, V. C. Sundar, C. M. Rudzinski, A. W. Wun, M. G. Bawendi, and D. G. Nocera, “Quantum-dot optical temperature probes,” *Appl. Phys. Lett.*, vol. 83, no. 17, pp. 3555–3557, 2003.

[353] S. Senapati and K. K. Nanda, “Red emitting Eu:ZnO nanorods for highly sensitive fluorescence intensity ratio based optical thermometry,” *J. Mater. Chem. C*, pp. 1074–1082, 2017.

[354] J. Sakakibara and R. J. Adrian, “Whole field measurement of temperature in water using two-color laser induced fluorescence,” *Exp. Fluids*, vol. 26, no. 1–2, pp. 7–15, 1999.

[355] V. K. Natrajan and K. T. Christensen, “Two-color laser-induced fluorescent thermometry for microfluidic systems,” *Meas. Sci. Technol.*, vol. 20, no. 1, p. 15401, 2008.

[356] K. Okabe, N. Inada, C. Gota, Y. Harada, T. Funatsu, and S. Uchiyama, “Intracellular temperature mapping with a fluorescent polymeric thermometer and fluorescence lifetime imaging microscopy.,” *Nat. Commun.*, vol. 3, p. 705, 2012.

[357] R. K. P. Benninger, Y. Koç O. Hofmann, J. Requejo-Isidro, M. A. A. Neil, P. M. W. French, and A. J. DeMello, “Quantitative 3D mapping of fluidic temperatures within microchannel networks using fluorescence lifetime imaging,” *Anal. Chem.*, vol. 78, no. 7, pp. 2272–2278, 2006.

[358] A. M. Chaudhari, T. M. Woudenberg, M. Allin, and K. E. Goodson, “Transient liquid crystal thermometry of microfabricated PCR vessel arrays,” *J. Microelectromechanical Syst.*, vol. 7, no. 4, pp. 345–354, 1998.

[359] A. Iles, R. Fortt, and A. J. de Mello, “Thermal optimisation of the Reimer-Tiemann reaction using thermochromic liquid crystals on a microfluidic reactor.,” *Lab Chip*, vol. 5, pp. 540–544, 2005.

[360] D. Dabiri and M. Gharib, “Digital Particle Image Thermometry: The Method and Implementation,” *Exp. Fluids*, no. 11, pp. 77–86, 1991.

[361] V. Hohreiter, S. Wereley, M. Olsen, and J. Chung, “Cross-Correlation Analysis for Temperature Measurement,” *Meas. Sci. Technol.*, no. 13, pp. 1072–1078, 2002.

[362] R. Kuriyama and Y. Sato, “Two-wavelength Raman imaging for non-intrusive monitoring of

transient temperature in microfluidic devices," *Meas. Sci. Technol.*, vol. 25, p. 95203, 2014.

[363] G. Yaralioglu, "Ultrasonic heating and temperature measurement in microfluidic channels," *Sensors Actuators, A Phys.*, vol. 170, no. 1–2, pp. 1–7, 2011.

[364] C. J. Easley, L. A. Legendre, M. G. Roper, T. A. Wavering, J. P. Ferrance, and J. P. Landers, "Extrinsic Fabry-Perot interferometry for noncontact temperature control of nanoliter-volume enzymatic reactions in glass microchips," *Anal. Chem.*, vol. 77, no. 4, pp. 1038–1045, 2005.

[365] M. E. Lacey, A. G. Webb, and J. V. Sweedler, "Monitoring temperature changes in capillary electrophoresis with nanoliter-volume NMR thermometry," *Anal. Chem.*, vol. 72, no. 20, pp. 4991–4998, 2000.

[366] A. Chandramohan, J. A. Weibel, and S. V. Garimella, "Spatiotemporal infrared measurement of interface temperatures during water droplet evaporation on a nonwetting substrate," *Appl. Phys. Lett.*, vol. 110, no. 4, p. 41605, 2017.

[367] A. A. Abduljabar, H. Choi, D. A. Barrow, and A. Porch, "Adaptive Coupling of Resonators for Efficient Microwave Heating of Microfluidic Systems," *IEEE Trans. Microw. Theory Tech.*, vol. 63, no. 11, pp. 3681–3690, 2015.

[368] A. A. Abduljabar, "Compact microwave microfluidic sensors and applicator," Cardiff University, 2016.

[369] E. M. Ahmed, "Hydrogel: Preparation, characterization, and applications: A review," *J. Adv. Res.*, vol. 6, no. 2, pp. 105–121, 2015.

[370] Y. Jiang, J. Chen, C. Deng, E. J. Suuronen, and Z. Zhong, "Click hydrogels, microgels and nanogels: Emerging platforms for drug delivery and tissue engineering," *Biomaterials*, vol. 35, no. 18, pp. 4969–4985, 2014.

[371] D. Seliktar, "Designing Cell-Compatible Hydrogels for Biomedical Applications," *Science (80-.).*, vol. 336, pp. 1124–1129, 2012.

[372] R. Censi, P. Di, T. Vermonden, and W. E. Hennink, "Hydrogels for protein delivery in tissue engineering," *J. Control. Release*, vol. 161, no. 2, pp. 680–692, 2012.

[373] T. Nochi, Y. Yuki, H. Takahashi, S. Sawada, M. Mejima, T. Kohda, N. Harada, I. G. Kong, A. Sato, N. Kataoka, D. Tokuhara, S. Kurokawa, Y. Takahashi, H. Tsukada, S. Kozaki, K. Akiyoshi, and H. Kiyono, "Nanogel antigenic protein-delivery system for adjuvant-free

intranasal vaccines.," *Nat. Mater.*, vol. 9, no. 7, pp. 572–578, 2010.

[374] L. A. Lyon, Z. Meng, N. Singh, C. D. Sorrell, and A. St. John, "Thermoresponsive microgel-based materials," *Chem. Soc. Rev.*, vol. 38, no. 4, p. 865, 2009.

[375] C. He, S. W. Kim, and D. S. Lee, "In situ gelling stimuli-sensitive block copolymer hydrogels for drug delivery," *J. Control. Release*, vol. 127, no. 3, pp. 189–207, 2008.

[376] L. Yu and J. Ding, "Injectable hydrogels as unique biomedical materials.," *Chem. Soc. Rev.*, vol. 37, no. 8, pp. 1473–81, 2008.

[377] X. Cheng, Y. Jin, T. Sun, R. Qi, B. Fan, and H. Li, "Oxidation- and thermo-responsive poly(N-isopropylacrylamide-co-2-hydroxyethyl acrylate) hydrogels cross-linked via diselenides for controlled drug delivery," *RSC Adv.*, vol. 5, no. 6, pp. 4162–4170, 2015.

[378] A. K. Bajpai, S. K. Shukla, S. Bhanu, and S. Kankane, "Responsive polymers in controlled drug delivery," *Prog. Polym. Sci.*, vol. 33, no. 11, pp. 1088–1118, 2008.

[379] A. Döring, W. Birnbaum, and D. Kuckling, "Responsive hydrogels--structurally and dimensionally optimized smart frameworks for applications in catalysis, micro-system technology and material science.," *Chem. Soc. Rev.*, vol. 42, no. 17, pp. 7391–420, 2013.

[380] Y. Liu, Z. Li, and D. Liang, "Behaviors of liposomes in a thermo-responsive poly(N-isopropylacrylamide) hydrogel," *Soft Matter*, vol. 8, no. 16, pp. 4517–4523, 2012.

[381] L.-W. Xia, R. Xie, X.-J. Ju, W. Wang, Q. Chen, and L.-Y. Chu, "Nano-structured smart hydrogels with rapid response and high elasticity.," *Nat. Commun.*, vol. 4, p. 2226, 2013.

[382] A. Nemethy, K. Solti, L. Kiss, B. Gyarmati, M. A. Deli, E. Csanyi, and A. Szilagyi, "pH- and temperature-responsive poly(aspartic acid)-l-poly (N-isopropylacrylamide) conetwork hydrogel," *Eur. Polym. J.*, vol. 49, pp. 2392–2403, 2013.

[383] X. Gao, Y. Cao, X. Song, Z. Zhang, C. Xiao, C. He, and X. Chen, "pH- and thermo-responsive poly(N-isopropylacrylamide-co-acrylic acid derivative) copolymers and hydrogels with LCST dependent on pH and alkyl side groups," *J. Mater. Chem. B*, vol. 1, no. 41, p. 5578, 2013.

[384] B. Kim, H. Soo Lee, J. Kim, and S.-H. Kim, "Microfluidic fabrication of photo-responsive hydrogel capsules," *Chem. Commun.*, vol. 49, no. 18, pp. 1865–7, 2013.

[385] A. Servant, C. Bussy, K. Al-Jamal, and K. Kostarelos, “Design, engineering and structural integrity of electro-responsive carbon nanotube- based hydrogels for pulsatile drug release,” *J. Mater. Chem. B*, vol. 1, no. 36, pp. 4593–4600, 2013.

[386] Y. Li, G. Huang, X. Zhang, B. Li, Y. Chen, T. Lu, T. J. Lu, and F. Xu, “Magnetic hydrogels and their potential biomedical applications,” *Adv. Funct. Mater.*, vol. 23, no. 6, pp. 660–672, 2013.

[387] M. Dadsetan, Z. Liu, M. Pumberger, C. V. Giraldo, T. Ruesink, L. Lu, and M. J. Yaszemski, “A stimuli-responsive hydrogel for doxorubicin delivery,” *Biomaterials*, vol. 31, no. 31, pp. 8051–8062, 2010.

[388] S. Zhou, A. Bismarck, and J. H. G. Steinke, “Ion-responsive alginate based macroporous injectable hydrogel scaffolds prepared by emulsion templating,” *J. Mater. Chem. B*, vol. 1, no. 37, pp. 4736–4745, 2013.

[389] C. Legros, M.-C. De Pauw-Gillet, K. C. Tam, S. Lecommmandoux, and D. Taton, “pH and redox responsive hydrogels and nanogels made from poly(2-ethyl-2-oxazoline),” *Polym. Chem.*, vol. 4, no. 17, p. 4801, 2013.

[390] M. F. Maitz, U. Freudenberg, M. V Tsurkan, M. Fischer, T. Beyrich, and C. Werner, “Bio-responsive polymer hydrogels homeostatically regulate blood coagulation,” *Nat. Commun*, vol. 4, p. 2168, 2013.

[391] C. Rivest, D. W. . Morrison, B. Ni, J. Rubin, V. Yadav, A. Mahdavi, J. . Karp, and A. Khademhosseini, “Microscale hydrogels for medicine and biology:synthesis, characteristics and applications,” *J. Mech. Mater. Struct.*, vol. 2, no. 6, pp. 1103–1119, 2007.

[392] J. Guzowski, P. M. Korczyk, S. Jakiela, and P. Garstecki, “Automated high-throughput generation of droplets,” *Lab Chip*, vol. 11, no. 21, p. 3593, 2011.

[393] N. Wen, Z. Zhao, B. Fan, D. Chen, D. Men, J. Wang, and J. Chen, “Development of droplet microfluidics enabling high-throughput single-cell analysis,” *Molecules*, vol. 21, no. 7, pp. 1–13, 2016.

[394] T. Wu, Y. Mei, T. Cabral, C. Xu, and K. L. Beers, “A New Synthetic Method for Controlled Polymerization Using a Microfluidic System,” pp. 9880–9881, 2004.

[395] T. D. Dang, Y. H. Kim, H. G. Kim, and G. M. Kim, “Preparation of monodisperse PEG

hydrogel microparticles using a microfluidic flow-focusing device," *J. Ind. Eng. Chem.*, vol. 18, no. 4, pp. 1308–1313, 2012.

[396] D. Steinhilber, T. Rossow, S. Wedepohl, F. Paulus, S. Seiffert, and R. Haag, "A microgel construction kit for bioorthogonal encapsulation and pH-controlled release of living cells," *Angew. Chemie - Int. Ed.*, vol. 52, no. 51, pp. 13538–13543, 2013.

[397] T. N. Glasnov and C. O. Kappe, "Microwave-assisted synthesis under continuous-flow conditions," *Macromol. Rapid Commun.*, vol. 28, no. 4, pp. 395–410, 2007.

[398] R. Hoogenboom and U. S. Schubert, "Microwave-assisted polymer synthesis: Recent developments in a rapidly expanding field of research," *Macromol. Rapid Commun.*, vol. 28, no. 4, pp. 368–386, 2007.

[399] S. Sinnwell and H. Ritter, "Recent advances in microwave-assisted synthesis," *Aust. J. Chem.*, no. 60, pp. 729–743, 2007.

[400] F. Wiesbrock, R. Hoogenboom, and U. S. Schubert, "Microwave-assisted polymer synthesis: State-of-the-art and future perspectives," *Macromol. Rapid Commun.*, vol. 25, pp. 1739–1764, 2004.

[401] A. de la Hoz and A. Loupy, *Microwaves in Organic Synthesis*, 3rd ed. Wiley-VCH Verlag Co., 2012.

[402] N. Lorber, B. Pavageau, and E. Mignard, "Droplet-based millifluidics as a new miniaturized tool to investigate polymerization reactions," *Macromolecules*, vol. 43, no. 13, pp. 5524–5529, 2010.

[403] N. Lorber, F. Sarrazin, P. Guillot, P. Panizza, A. Colin, B. Pavageau, C. Hany, P. Maestro, S. Marre, T. Delclos, C. Aymonier, P. Subra, L. Prat, C. Gourdon, and E. Mignard, "Some recent advances in the design and the use of miniaturized droplet-based continuous process: applications in chemistry and high-pressure microflows.," *Lab Chip*, vol. 11, no. 5, pp. 779–87, 2011.

[404] B. R. Saunders and B. Vincent, "Microgel particles as model colloids: theory, properties and applications," *Adv. Colloid Interface Sci.*, vol. 80, no. 1, pp. 1–25, 1999.

[405] S. O. Kelley, C. a Mirkin, D. R. Walt, R. F. Ismagilov, M. Toner, and E. H. Sargent, "Advancing the speed, sensitivity and accuracy of biomolecular detection using multi-length-

scale engineering," *Nat. Publ. Gr.*, vol. 9, no. 12, pp. 969–980, 2014.

[406] P. Kara, D. Ariksoysal, and M. Ozsoz, "Electrochemical Nucleic Acid Biosensors Based on Hybridization Detection for Clinical Analysis," in *Electrochemical DNA Biosensors*, M. Ozsoz, Ed. Pan Stanford Pusblishing, 2012.

[407] J. Kafka, O. Pänke, B. Abendroth, and F. Lisdat, "A label-free DNA sensor based on impedance spectroscopy," *Electrochim. Acta*, vol. 53, no. 25, pp. 7467–7474, 2008.

[408] H. Ben-yoav, P. H. Dykstra, W. E. Bentley, and R. Ghodssi, "Biosensors and Bioelectronics A controlled microfluidic electrochemical lab-on-a-chip for label-free diffusion-restricted DNA hybridization analysis," vol. 64, pp. 579–585, 2015.

[409] A. Li, F. Yang, Y. Ma, and X. Yang, "Electrochemical impedance detection of DNA hybridization based on dendrimer modified electrode," *Biosens. Bioelectron.*, vol. 22, no. 8, pp. 1716–1722, 2007.

[410] H. Ben-Hoav, P. H. Dykstra, T. Gordonov, W. E. Bentley, and R. Ghodssi, "A Microfluidic-based Electrochemical Biochip for Label-free DNA Hybridization Analysis," *J. Vis. Exp.*, vol. 91, no. e51597, pp. 1–8, 2014.

[411] A. B, A. Johnson, J. Lewis, D. Morgan, M. Raff, K. Roberts, and P. Walter, *Molecular Biology of the Cell*, 6th Ed. Garland Science, 2014.

[412] F. Caruso, E. Rodda, D. N. Furlong, K. Niikura, and Y. Okahata, "Quartz crystal microbalance study of DNA immobilization and hybridization for nucleic Acid sensor development.," *Anal. Chem.*, vol. 69, pp. 2043–9, 1997.

[413] J. Reichert, A. Cskai, J. Kohler, and W. Fritzsche, "Chip-Based Optical Detection of DNA Hybridization by Means of Nanobead Labeling," *Anal. Chem.*, vol. 72, pp. 6025–6029, 2000.

[414] T. A. Taton, G. Lu, and C. A. Mirkin, "Two-Color Labeling of Oligonucleotide Arrays via Size-Selective Scattering of Nanoparticle Probes," *J. Am. Chem. Soc.*, no. 123, pp. 5164–5165, 2001.

[415] B. Nelson, T. Grimsrud, M. Liles, R. Goodman, and R. Corn, "Surface plasmon resonance imaging measurements of DNA and RNA hybridization adsorption onto DNA microarrays," *Anal. Chem.*, vol. 73, pp. 1–7, 2001.

[416] H. Peng, C. Soeller, M. B. Cannell, G. A. Bowmaker, R. P. Cooney, and J. Travas-Sejdic,

"Electrochemical detection of DNA hybridization amplified by nanoparticles," *Biosens. Bioelectron.*, vol. 21, no. 9, pp. 1727–1736, 2006.

[417] V. N. Goral, N. V. Zaytseva, and A. J. Baeumner, "Electrochemical microfluidic biosensor for the detection of nucleic acid sequences," *Lab Chip*, vol. 6, pp. 414–421, 2006.

[418] M. Salazar-Alvarez, O. Korostynska, A. Mason, A. Al-Shamma'a, J. C. Cooney, E. Magner, and S. A. M. Tofail, "Label free detection of specific protein binding using a microwave sensor," *Analyst*, vol. 139, no. 21, pp. 5335–8, 2014.

Appendix A

Calibration with Fluorescence Thermometry and RTD

Attempts were made to measure working fluid temperature directly for calibration purposes. Figure A1 shows the intensity vs. temperature calibration obtained for a fluorescein and Tris-HCL solution. Fluorescence properties of fluorescein are pH dependent, while pH properties of Tris-HCL are temperature dependent, allowing temperature to be measured from its fluorescing intensities. However, local concentration difference, lamp intensity fluctuation, and CCD camera noise resulted in error in the range of ±3°C, which is higher than what the microwave sensor can achieve, and therefore is not suitable for calibrating the microwave sensor. In contrast, the hotplate correction method is much more accurate. Resistance Temperature Detector was also considered for use in calibrating the microwave sensor in the single-phase experiment, Figure A2, but fabricating both the RTD and microwave sensor on the same chip has proved to be problematic.

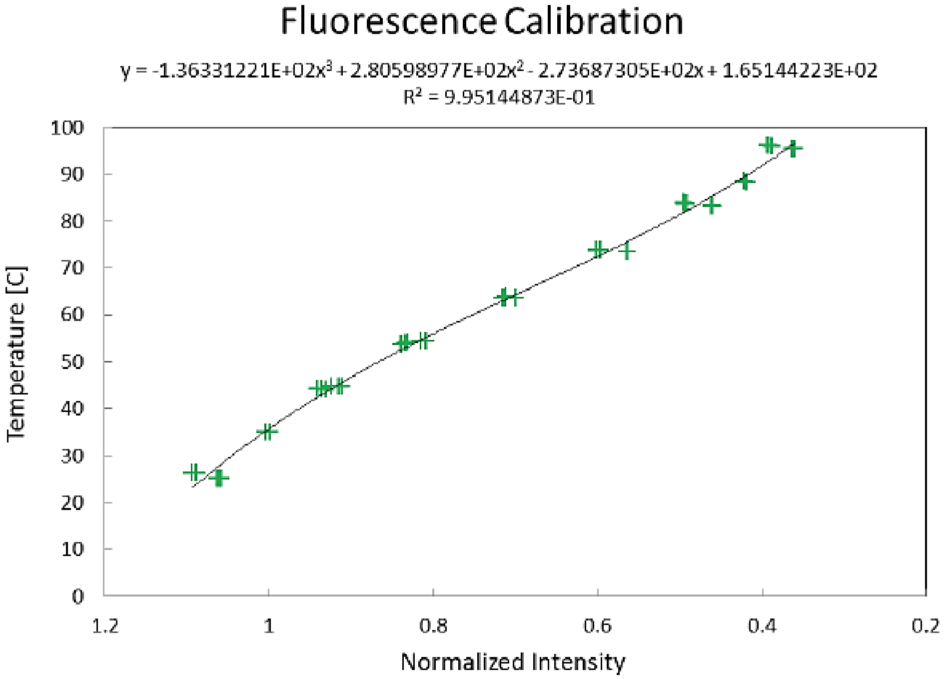

Figure A1. Fluorescence Thermometry using 100uM fluorescein and 10mM Tris-HCL buffer adjusted to pH 7.1 at 22 ^{o}C.

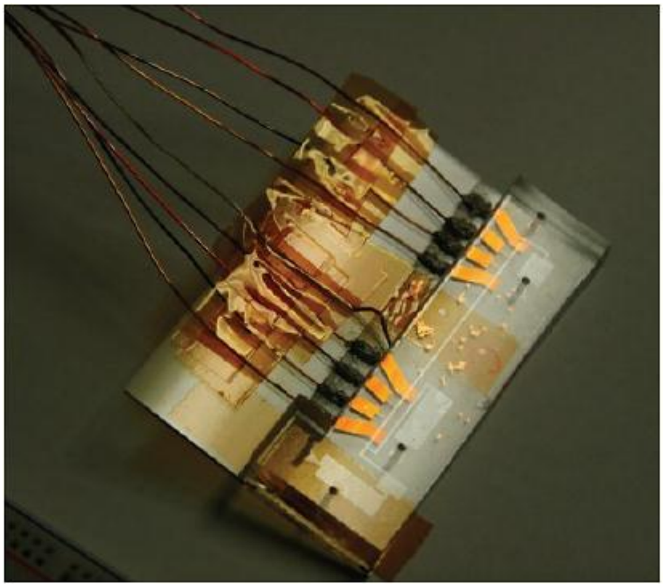

Figure A2. The RTD sensor.

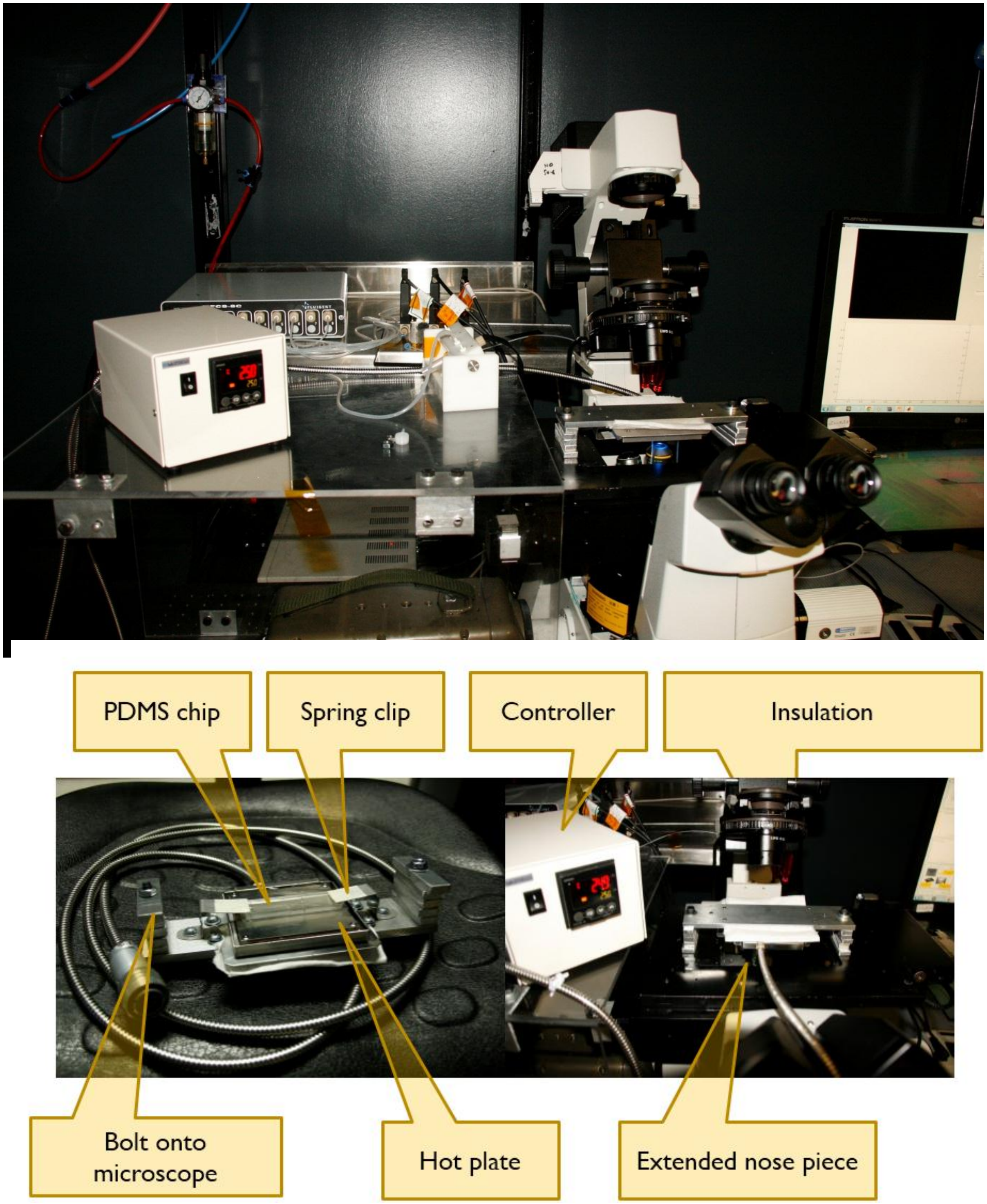

Figure A3. Picture of the temperature measurement setup and components used in detail.

Appendix B

Poly (Acrylamide-co-Sodium Acrylate) Copolymer Hydrogel Particle Synthesis

B1. On-chip Polymerization of Droplets

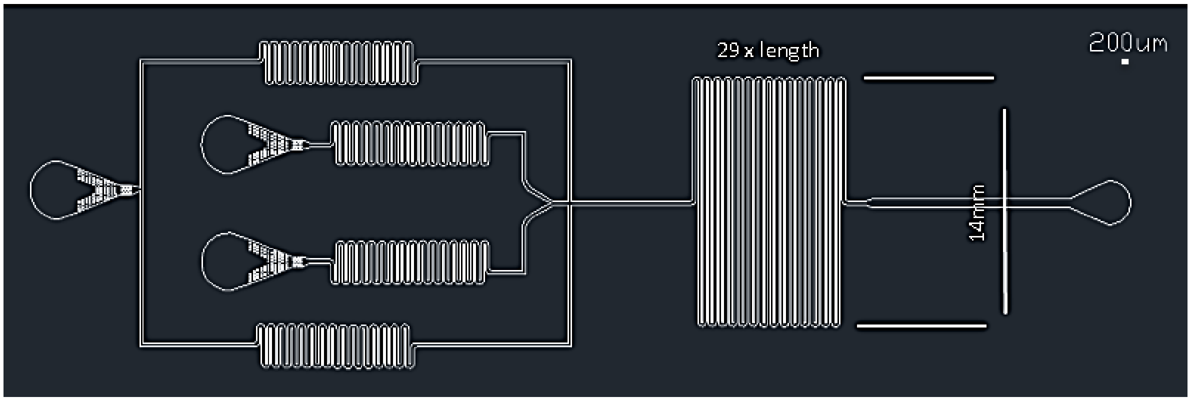

Figure B1.1. The serpentine channel design for increasing the reaction time.

Figure B1.1 shows the long serpentine channel configuration for increased reaction time of droplets. The residence time (UV exposure time) of a droplet inside the serpentine section is calculated based on the flow rate and geometry.

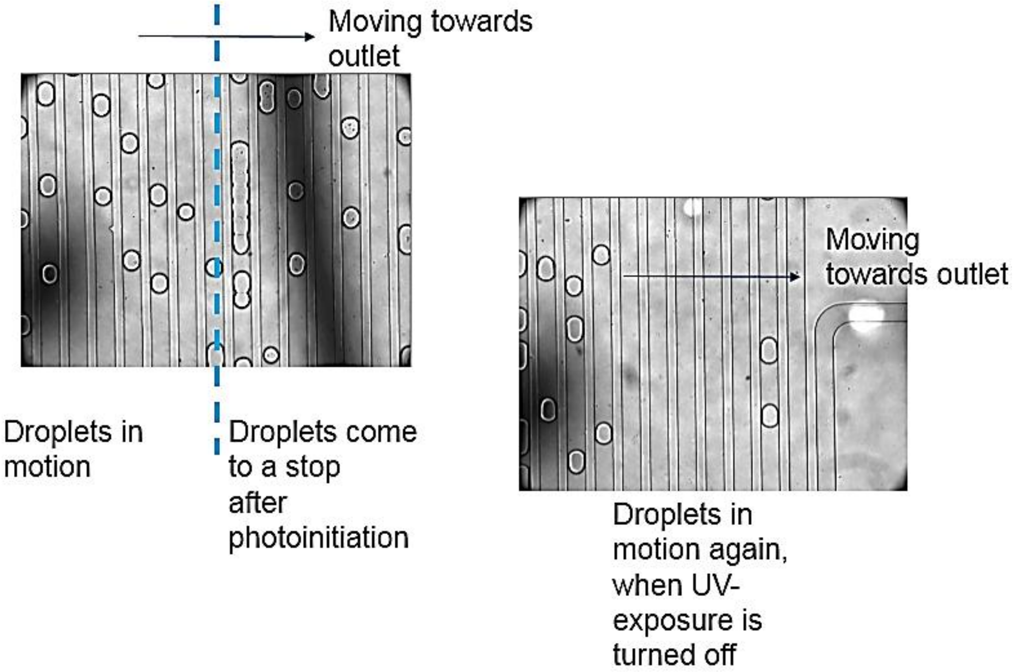

Figure B1.2. Polymerized droplets merge each other and come to a stop. When UV-exposure is turned off droplets start to move again.

B2. Semi-on-chip Polymerization of Droplets

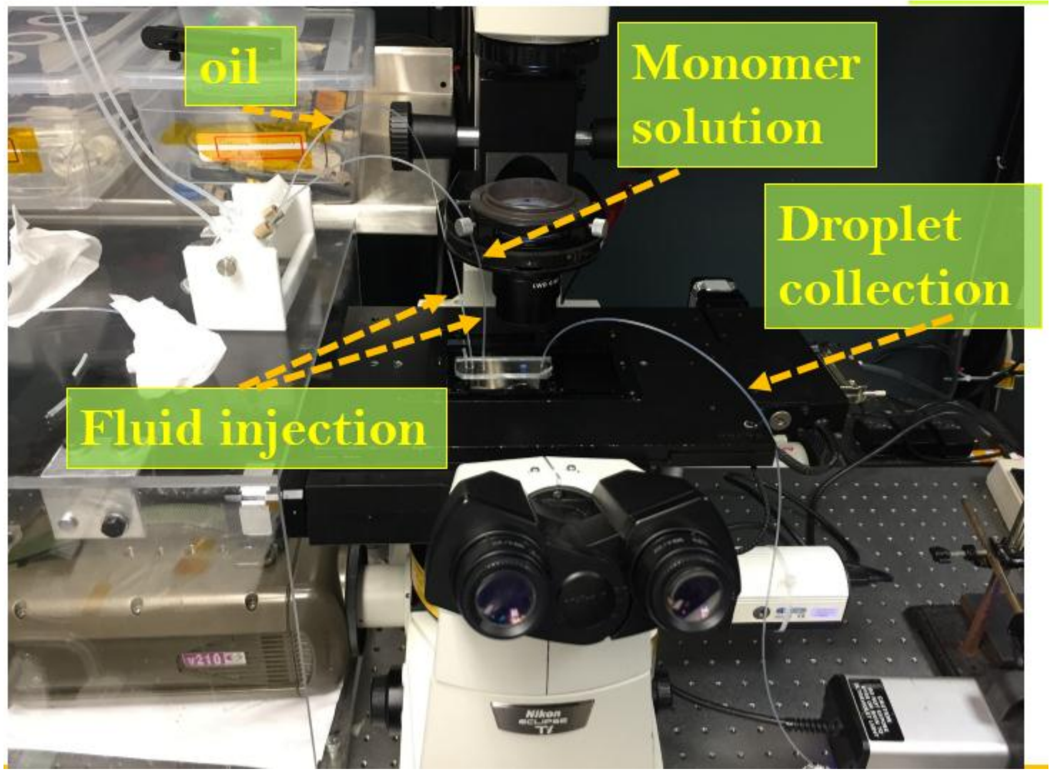

Figure B2.1. The experimental setup for semi-on-chip polymerization of droplets. Droplets are generated inside microfluidic chip and transported with a capillary tubing for UV exposure.

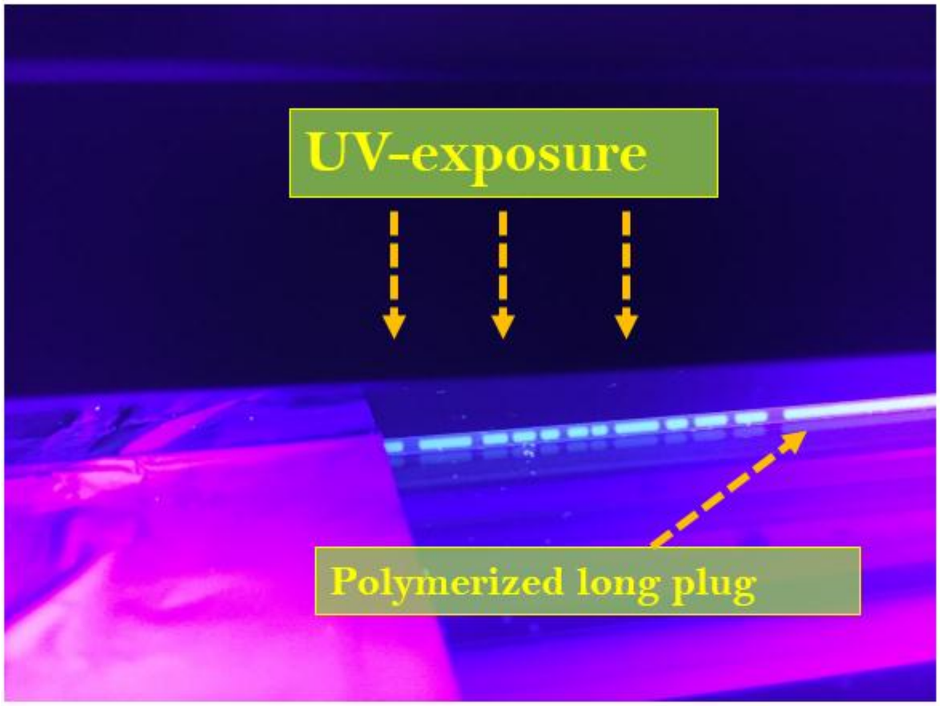

Figure B2.2. Due to bending of the tubing at the outlet and gravitational force on droplets, the spacing between droplets are non-uniform, which causes long plugs of polymerized droplets in capillary tubing.

B3. Off-chip Polymerization of Droplets

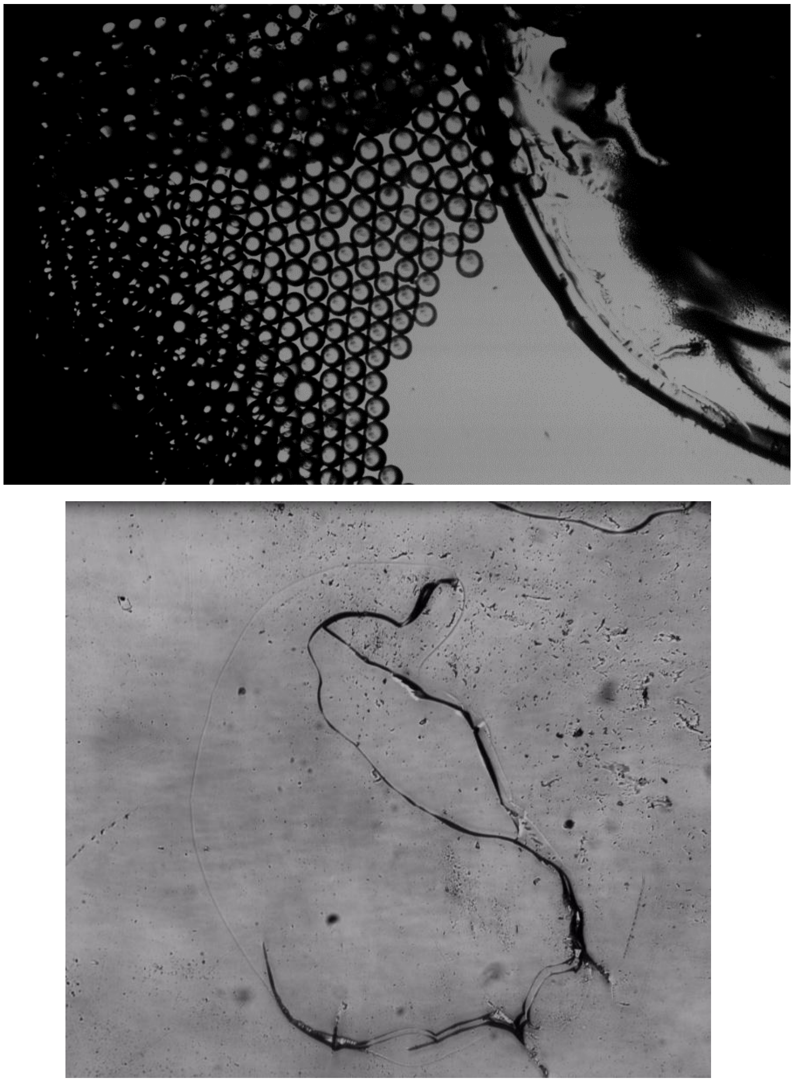

Figure B3. Off-chip polymerization. Droplets form a thin polymer film after reaction. Since the spacing among droplets is small, droplets are merged and cross-linked together during polymerization. A thin film of hydrogel was synthesized instead of individual micro-particles.

Appendix C

Video: Droplet Pair

This appendix is a video of the generation of droplet pairs used in Chapter 4.

The file name of this video file is “Appendix C_droplet pair.avi”.

If you accessed this thesis from a source other than the University of Waterloo, you may not have access to this file. You may access it by searching for this thesis at http://uwspace.uwaterloo.ca .

Appendix D

Video: Microwave Thermocapillary Droplet Mixing

This appendix is videos of the microwave based thermocapillary droplet mixing used in Chapter 6.

The file name of this video file is “Appendix D_Microwave Mixing-Gly75_L1.avi”,

and

The file name of this video file is “Appendix D_Microwave Mixing-Gly75_L2.avi”,

If you accessed this thesis from a source other than the University of Waterloo, you may not have access to this file. You may access it by searching for this thesis at http://uwspace.uwaterloo.ca .